Enabling astrophotonics: adaptive optics and photonic lanterns for coupling starlight into the single-mode regime

Thesis by
Momen Diab

In Partial Fulfillment of the Requirements for the
Degree of
"Doctor rerum naturalium"
(Dr. rer. nat.)
in Physics

Submitted to the Faculty of Science
Institute of Physics and Astronomy
of the University of Potsdam
and
the Leibniz Institute for Astrophysics Potsdam (AIP)

Defended 20.12.2021

Betreuer: Prof. Dr. Martin M. Roth, Dr. Kalaga Madhav, Dr. Stefano Minardi
1. Gutachter: Prof. Dr. Martin M. Roth
Leibniz Institute for Astrophysics Potsdam/University of Potsdam

2. Gutachter: apl. Prof. Dr. Carsten Denker
Leibniz Institute for Astrophysics Potsdam/University of Potsdam

3. Gutachter: Prof. Sergio Leon-Saval
The University of Sydney

Published online on the
Publication Server of the University of Potsdam:
https://doi.org/10.25932/publishup-53901
https://nbn-resolving.org/urn:nbn:de:kobv:517-opus4-539012

Momen Diab
ORCID: 0000-0001-6556-9378

ABSTRACT

Ground-based astronomy is set to employ next-generation telescopes with apertures larger than 25 m in diameter before this decade is out. Such giant telescopes observe their targets through a larger patch of turbulent atmosphere, demanding that most of the instruments behind them must also grow larger to make full use of the collected stellar flux. This linear scaling in size greatly complicates the design of astronomical instrumentation, inflating their cost quadratically. Adaptive optics (AO) is one approach to circumvent this scaling law, but it can only be done to an extent before the cost of the corrective system itself overwhelms that of the instrument or even that of the telescope. One promising technique for miniaturizing the instruments and thus driving down their cost is to replace some, or all, of the free space bulk optics in the optical train with integrated photonic components.

Photonic devices, however, do their work primarily in single-mode waveguides, and the atmospherically-distorted starlight must first be efficiently coupled into them if they are to outperform their bulk optic counterparts. This is doable by two means: AO systems can again help control the angular size and motion of seeing disks to the point where they will couple efficiently into astrophotonic components, but this is only feasible for the brightest of objects and over limited fields of view. Alternatively, tapered fiber devices known as photonic lanterns — with their ability to convert multimode into single-mode optical fields — can be used to feed speckle patterns into single-mode integrated optics. They, nonetheless, must conserve the degrees of freedom, and the number of output waveguides will quickly grow out of control for uncorrected large telescopes. An AO-assisted photonic lantern fed by a partially corrected wavefront presents a compromise that can have a manageable size if the trade-off between the two methods is chosen carefully. This requires end-to-end simulations that take into account all the subsystems upstream of the astrophotonic instrument, i.e., the atmospheric layers, the telescope, the AO system, and the photonic lantern, before a decision can be made on sizing the multiplexed integrated instrument.

The numerical models that simulate atmospheric turbulence and AO correction are presented in this work. The physics and models for optical fibers, arrays of waveguides, and photonic lanterns are also provided. The models are on their own useful in understanding the behavior of the individual subsystems involved and are also used together to compute the optimum sizing of photonic lanterns for feeding

astrophotonic instruments. Additionally, since photonic lanterns are a relatively new concept, two novel applications are discussed for them later in this thesis: the use of mode-selective photonic lanterns (MSPLs) to reduce the multiplicity of multiplexed integrated instruments and the combination of photonic lanterns with discrete beam combiners (DBCs) to retrieve the modal content in an optical waveguide.

ZUSAMMENFASSUNG

In der erdbasierten Astronomie sollen noch in diesem Jahrzehnt Teleskope der nächsten Generation mit Öffnungen von mehr als 25 Metern in Betrieb genommen werden. Mit derart riesigen Aperturen werden die Zielobjekte durch einen größeren Ausschnitt turbulenter Atmosphäre beobachtet, weswegen die meisten die dahinterliegenden Instrumente entsprechend größer werden müssen, um die aufgefangene Strahlungsleistung vollständig nutzen zu können. Die lineare Skalierung der Größe erschwert das Design astronomischer Instrumente erheblich und führt zu einem quadratischen Anstieg der Kosten. Die adaptive Optik (AO) ist ein Ansatz, diese Skalierung zu umgehen. Allerdings ist dies nur bis zu einem gewissen Grad möglich, bevor die Kosten des Korrektursystems die des Instruments oder sogar des Teleskopes übersteigen. Eine vielversprechende Methode, das Instrument zu miniaturisieren und damit die Kosten zu reduzieren besteht darin, einige oder sogar alle der voluminösen Freistrahloptiken im Strahlengang durch photonische Komponenten zu ersetzen.

Photonische Bauteile arbeiten jedoch in erster Linie mit Einzelmoden-Wellenleitern. Damit sie eine bessere Leistung erbringen als die entsprechenden Freistrahloptiken muss das durch die atmosphärischen Störungen verformte Sternenlicht zunächst effizient in die Wellenleiter eingekoppelt werden. Dies kann auf zwei Wegen erreicht werden: AO Systeme können Winkelausdehnung und Bewegung der Bildunschärfe der Sternscheibchen stark genug korrigieren, um diese effizient in astrophotonische Komponenten einzukoppeln. Dies ist aber nur für die hellsten Objekte und über ein begrenztes Sichtfeld möglich. Alternativ können photonische Laternen genutzt werden, um Multimoden des optischen Feldes in Einzelmoden umzuwandeln und somit die Specklemustern in die Einzelmoden-Wellenleiter der integrierten Optiken zu injizieren. Da hierbei die Anzahl der Freiheitsgrade trotzdem erhalten bleiben muss, wird die Zahl der Ausgangswellenleiter für nicht-korrigierte große Teleskope schnell unkontrollierbar anwachsen. Durch sorgfältiges Abwägen kann ein Kompromiss zwischen diesen beiden Methoden gewählt werden, bei dem man eine AO-assistierte photonische Laterne mit überschaubarer Größe erhält, in die eine partiell korrigierte Wellenfront gespeist wird. Dieser Prozess erfordert durchgehende Simulationen unter Einbeziehung aller Subsysteme vor dem astrophotonischen Instrument -Atmosphäre, Teleskop, AO System und photonische Laterne- bevor eine Entscheidung über die Dimensionierung des integrierten Multiplex-Instruments getroffen

werden kann.

Die numerischen Modelle, die die atmosphärischen Störungen und AO Korrekturen simulieren, werden in dieser Arbeit präsentiert. Die Physik und Modelle für optische Fasern, Wellenleiter-Arrays und photonische Laternen werden ebenfalls dargestellt. Jedes Modell für sich ist nützlich, um die Auswirkung des jeweiligen Subsystems nachzuvollziehen. In Kombination werden die Modelle verwendet, um die optimale Konfiguration und Größe der photonischen Laterne für die Einspeisung astrophotonischer Instrumente zu berechnen. Da photonische Laternen ein relativ neues Konzept sind, werden im weiteren Verlauf der Arbeit zusätzlich zwei neuartige Anwendungen erörtert: der Einsatz modenselektiver photonischer Laternen (MSPLs) zur Verringerung der Anzahl von Multiplex-Instrumenten sowie die Kombination photonischer Laternen mit diskreten Strahlkombinierern („Discrete Beam Combiners“: DBCs), um die Moden in einem Lichtwellenleiter zu erfassen.

PUBLISHED CONTENT AND CONTRIBUTIONS

Peer-reviewed articles

Diab, M., Dinkelaker, A. N., Davenport, J., Madhav, K., & Roth, M. M. (2021). Starlight coupling through atmospheric turbulence into few-mode fibres and photonic lanterns in the presence of partial adaptive optics correction. *Monthly Notices of the Royal Astronomical Society*, *501*(2), 1557–1567. https://doi.org/10.1093/mnras/staa3752

Diab, M., Tripathi, A., Davenport, J., Dinkelaker, A. N., Madhav, K., & Roth, M. M. (2021). Simulations of mode-selective photonic lanterns for efficient coupling of starlight into the single-mode regime. *Applied Optics*, *60*(19), D9–D14. https://doi.org/10.1364/AO.421799

Diab, M., & Minardi, S. (2019). Modal analysis using photonic lanterns coupled to arrays of waveguides. *Optics Letters*, *44*(7), 1718–1721. https://doi.org/10.1364/OL.44.001718

Davenport, J., Diab, M., Deka, P., Tripathi, A., Madhav, K., & Roth, M. (2021). Photonic lanterns: A practical guide to filament tapering. *Optical Materials Express*. https://doi.org/10.1364/OME.427903

Davenport, J. J., Diab, M., Madhav, K., & Roth, M. M. (2021). Optimal SMF packing in photonic lanterns: Comparing theoretical topology to practical packing arrangements. *JOSA B*, *38*(7), A7–A14. https://doi.org/10.1364/JOSAB.413640

Conference proceedings

Diab, M., Dinkelaker, A. N., Davenport, J., Madhav, K., & Roth, M. M. (2020). Testbed for coupling starlight into fibers and astrophotonic instruments. *Advances in Optical and Mechanical Technologies for Telescopes and Instrumentation IV*, *11451*, 114516G. https://doi.org/10.1117/12.2564720

Diab, M., & Minardi, S. (2018). On the modal throughput of photonic lanterns in the presence of partial adaptive optic correction. *Advances in Optical and Mechanical Technologies for Telescopes and Instrumentation III*, *10706*, 107064T. https://doi.org/10.1117/12.2309657

Minardi, S., Diab, M., Pedretti, E., Shankar-Nayak, A., Saviauk, A., Piacentini, S., Corrielli, G., Osellame, R., Diener, R., Tepper, J., Labadie, L., Dreisow, F., Grafe, M., Pertsch, T., Nolte, S., Errmann, R., Stoffel, D., & Chakrova, N. (2019). Discrete beam combiners from astronomy to lasers. *Integrated Optics: Devices, Materials, and Technologies XXIII*, *10921*, 1092110. https://doi.org/10.1117/12.2512276

Davenport, J. J., Diab, M., Tripathi, A., Madhav, K., & Roth, M. M. (2020). Optical fibre pseudo-slits for astronomy. *Advances in Optical and Mechanical Technologies for Telescopes and Instrumentation IV*, *11451*, 1145123. https://doi.org/10.1117/12.2562652

Patents

Minardi, S., & Diab, M. (2019). *Device for analyzing modes of multimode optical fibers* (EP3572857A1). Retrieved May 7, 2021, from https://patents.google.com/patent/EP3572857A1/en

CONTENTS

LIST OF FIGURES

LIST OF TABLES

GLOSSARY

B Complex amplitude of the magnetic flux density. 38, 158

D_x Structure function of random varaible x. 11

D Complex amplitude of the electric flux density. 38, 158

E Complex amplitude of the electric field. 38, 39, 76, 150–154, 157, 158

H Complex amplitude of the magnetic field. 38, 39, 157, 158

I Intensity. 21, 29, 30, 59, 153, 154

J Bessel function of the first kind. 42–44, 59, 66, 153

K Modified Bessel function of the second kind. 42–44

N Refractivity. xii, 7, 12–20

P Pressure. 7

Q Potential. 52, 53

S étendue. 60, 61

T_{aper} Aperture function. 20, 21

T_{tele} Telescope transfer function. 21, 22, 154

T Temperature. 7, 12

V Normalized frequency or V-number. xiii, xiv, 43–46, 48, 51–53, 55, 60, 61, 66, 67

Δ Refractive index constrast. 36, 39, 52, 53, 158

Λ Aberration function. 154

Φ Energy spectrum per unit mass. 9, 10, 16, 70, 71, 149

$\vec{r}_T$ Transverse position vector. 12–14, 21

$\vec{r}$ Position vector. 11–14, 16, 17, 21, 38, 39, 76, 156–158

β Propagation constant. xiii, xiv, 40–44, 48, 49, 51, 52, 57, 67, 158, 159

χ Fiber cladding parameter. 41–44, 66

ϵ_0 Electric permittivity of free space. 156, 159

ϵ Electric permittivity. 38, 39, 157, 158

η Coupling efficiency. 57, 58

γ Zenith angle. 15, 17

κ Coupling coefficient. xiii, 49, 50, 68

λ Wavelength. xii, xiv, 7, 12, 19–22, 29, 30, 33, 37, 52, 58–61, 69, 73, 74, 76, 82, 84, 87, 150, 153, 154

$\mathcal{B}$ Magnetic flux density. 157

$\mathcal{D}$ Electric flux density. 157

$\mathcal{E}$ Electric field. 38, 156, 157

$\mathcal{H}$ Magnetic field. 38, 156, 157

$\mathcal{L}_0$ Outer scale. 8–10, 16, 71–73, 149

$\mathcal{R}$ Resolving power of an optical system. 21, 22

$\mathfrak{E}$ Energy. 9, 52

NA Numerical aperture. 37, 42, 43, 60, 87

Re Reynolds number. 8, 149

SR Strehl ratio. 24, 91, 154, 155

μ_0 Magnetic permeability of free space. 156, 159

μ Magnetic permeability. 38, 39, 157, 158

ν Kinematic viscosity. 8

ω Temporal angular frequency. 38, 39, 150–153, 157–159

ϕ Phase of the electric field. 12–15, 17, 24, 25, 30–33, 70, 71, 73, 75, 76, 151, 154, 155

ψ Wavefront. 13–15, 20–22, 24, 75, 76, 154, 155

$r_\perp$ Distance between planes. 59, 151–154

r_s Distance between source and observation point. 150, 151

v Velocity. 8, 9, 11, 12, 16, 17, 73

w_0 Mode field radius. 45, 46, 58, 59

ACRONYMS

4QD four-quadrant detector. 29

ADU analog to digital unit. 75

AO adaptive optics. iv, x–xii, xv, xix, 1, 3–5, 7, 17, 26–28, 34, 35, 62, 63, 66, 73–75, 85–89, 91–93, 144–147

ARPA advanced research projects agency. 26

AWG arrayed waveguide grating. xiii, 62

BPM beam propagation method. 48, 54, 68, 145, 146

CCD charge-coupled device. 29

CFHT Canada-France-Hawaii telescope. 26

CMT coupled mode theory. xiv, 48, 51, 68, 69

CoG center of gravity. 29, 30

CW continuous wave. 2

DBC discrete beam combiner. v, xiii, 36, 62, 63, 68, 147

DFB distributed feedback. 82

DM deformable mirror. xi, xiv, xv, 27, 28, 31–34, 74, 75, 78–80, 85–92, 145

DWDM dense wavelength division multiplexing. 62

EE encircled energy. 91

ELT extremely large telescope. 1

EM-CCD electron multiplying charge-coupled device. 86

EMI electromagnetic Interference. 2

ESO European southern observatory. 26

ExAO extreme adaptive optics. 4, 18, 34, 144

FBG fiber Bragg grating. 3, 36, 63, 64

FFT fast Fourier transform. 66, 74, 76

FMF few-mode fiber. xi, 38, 45, 51, 66, 87, 146

FoV field of view. 3, 26–28, 34, 59, 144

FRD focal ratio degradation. 37, 47

FSO free space optical communication. 147

FWHM full width half maximum. 82

GLAO ground layer adaptive optics. 28

IO integrated optic. 2

LD laser diode. xiv, 82, 83, 90, 91

LGS laser guide star. 26, 28

LMA large mode area fiber. 147

LOAO low-order adaptive optics. x, 34, 35, 81, 85, 87, 145

LP linearly polarized. xiii, xiv, 39, 45, 66, 67, 146

LTAO laser tomography adaptive optics. 28

MCAO multi-conjugate adaptive optics. 27, 28

MEMS microelectro-mechanical systems. 33

MLA microlens array. 29, 30, 74–76, 86, 91

MMF multimode fiber. 3, 38, 40, 45–47, 50, 51, 55, 59, 61, 64, 144

MOAO multi-object adaptive optics. 28

MSPL mode-selective photonic lantern. v, 64, 147

NCPA non-common path aberration. 88, 147

NEP noise equivalent power. 88, 91

NIM near index matched. xiv, 84

NOAO national optical astronomy observatories. 26

OPD optical path difference. xiv, 24, 27, 84, 85, 154, 155

OTF optical transfer function. 21, 28, 154

PBL planetary boundary layer. xii, 6, 19, 20

PD photodiode. 88, 91, 92

PIAA phase-induced amplitude apodizer. 59

PIC photonic integrated circuit. 2

PMN lead magnesium niobate. 33

PSD power spectral density. 70, 71

PSF point spread function. xii, xiii, xv, 15, 22, 23, 28–30, 59–61, 64, 87, 91, 92, 147, 154

PZT lead zirconate titanate. 33

QE quantum efficiency. 28, 75, 77, 86

RON readout noise. 75, 146

RTAC real-time atmospheric compensator. 26

RTC real time computer. 35

SCAO single-conjugate adaptive optics. 27, 34, 145

SMF single-mode fiber. xiv, 4, 38, 45–47, 51, 54–56, 58, 61, 63–66, 82, 87, 144, 146–148

SNR signal-to-noise ratio. 87, 91, 145–147

STP standard temperature and pressure. 6

SVD singular value decomposition. 79

TEM transverse electromagnetic. 39

ULI ultrafast laser inscription. 55, 56

VLT very large telescope. 63

VLTI very large telescope interferometer. 63

VRO Vera C. Rubin observatory. 59

WFS wavefront sensor. xi, xiv, xv, 27–32, 34, 74, 75, 77–80, 85, 87, 88, 90, 92, 145, 147, 148

Chapter 1

INTRODUCTION

1.1 Astrophysics and instrumentation

Astronomy concerns the investigation of celestial bodies and phenomena through the analysis of the particles, the electromagnetic waves, and the gravitational waves they give off. The vast majority of the objects of interest are faint and far away, making astronomy a photon-starved business that requires the use of large optics to collect as many photons as possible if any informative signals are to be detected. In most scientific discoveries, an advancement in instrumentation was behind new measurements that caused a paradigm shift in thinking, leading to new physics. It was, after all, thanks to a new instrument at the time that Galileo could convert the scientific community from Aristotelian cosmology to Copernicanism.

With the upcoming commissioning of three extremely large telescopes (ELTs), some of the most interesting science goals can finally be addressed. Namely, the direct detection of an Earth-like exoplanet around a nearby star with biosignatures in its atmosphere and the detection of the earliest and most distant star-forming regions from the reionization epoch (Bland-Hawthorn et al., 2009). Identifying an Earth-like candidate has been the holy grail since the confirmed discovery of the first exoplanet in 1992 (Mayor et al., 1995). One way this could be achieved is by tracking the Doppler shift of the stellar spectrum caused by an orbiting companion which requires high-resolution spectrographs with resolving powers in the $\sim 10^5$ range and a stable calibration source to suppress systematic noise. Once identified, direct imaging of the planet will require a diffraction-limited performance with a sub-milliarcsecond resolution to resolve the highly contrasted faint companion (Labadie et al., 2016). For a monolithic ELT, this is only possible with adaptive optics (AO) while for a telescope array, single-mode long baselines are needed.

On the other hand, studying extragalactic objects requires high sensitivity and the ability to simultaneously disperse light from many objects distributed across a wide field of view. Thus, the distribution of matter within them could be mapped, and their kinematics could be understood. In doing so, constraints on proposed cosmological models can be properly placed.

1.2 Photonics and integrated optics

With the invention of lasers in the 1960s came a source of high-intensity coherent light. Soon after, *integrated optics (IOs)* emerged as means to process optical signals in waveguides rather than in free space. After the introduction of low-loss optical fibers, the CW laser diodes, and photolithography, the telecommunication industry was fast to replace electrical currents and radio waves with light as a data carrier (Hunsperger, 2009). In such optical networks, fibers connected the transmitter to the receiver while *photonic integrated circuits (PICs)* processed the signals at both ends. Compared to metallic wires, fibers are lighter, immune from EMI, made of less expensive materials, and most importantly have a large bandwidth. PICs must replace electrical integrated circuits once fibers are used as transmission media, and they further offer additional advantages like lower power consumption and are typically smaller in size.

The platform, i.e., the substrate material on which a PIC is fabricated, depends on the functionality. A generic circuit would have a material of high refractive index, the *core*, impeded in another of a slightly lower refractive index, the *cladding*, through which light is guided from one point to another. Structures of varying refractive indices and compositions manipulate the light en route through the waveguides. A few examples of the materials considered for the platforms are silicon (Si), silicon nitride (Si_3N_4), lithium niobate ($LiNbO_3$), and silica (SiO_2). Active materials capable of emitting light have also been used to integrate laser diodes and amplifiers in PICs.

In astronomical instruments, fused silica is by far the most used substrate when operating at the visible or the near-IR. It has a low refractive index of 1.4 ensuring low Fresnel losses at the free space interfaces, and it is highly stable chemically. Fluoride glasses like ZBLAN and chalcogenide glasses like GLS can be used for longer wavelengths, but unlike silica, the photonic functionalities possible with these materials are limited by the immaturity of the technologies developed to fabricate structures in them.

For the purposes of this work, a distinction is made between the terms: *optics* and *photonics*. Optics is used to refer to bulk components, e.g., lenses, gratings, and mirrors, that manipulate light by refracting or reflecting it at air-glass interfaces. Photonics, on the other hand, is used for situations where the processing is done via structures of contrasting refractive indices inside waveguides. Moreover, fibers are distinguished from waveguides in general by their cylindrical geometry and their

index profile of only two functional materials.

1.3 Astrophotonics

Applying photonic technologies to astronomical instrumentation that process starlight is known as *astrophotonics*. This approach leads to various benefits. Photonic components are significantly smaller than their bulk optic counterparts and can therefore miniaturize the instruments they are employed in (Ellis et al., 2019). Smaller instruments require a simpler vacuum and thermal control, directly cutting the cost. The smaller footprint and the mass production capacity furthermore mean that astrophotonic devices are modular and can be easily multiplexed in an efficient manner. Additionally, advantages like better detector utilization are also possible due to the mechanical flexibility of photonic components (Leon-Saval et al., 2012). In the future, space missions, be it telescopes or roving vehicles, could benefit from compact components that are less sensitive to vibrations and harsh environmental conditions.

Astrophotonics emerged at the turn of the century when AO systems allowed for efficient coupling of light into the narrow input waveguides of photonic devices. This is in contrast to the large multimode fibers (MMFs) that have been in use since the 1970s to deliver light from the focal plane of the telescope to spectrographs (Parry, 1998) and interferometers (Coudé du Foresto, 1994) that are desired to be kept motionless in a controlled environment away from the focus. MMFs as means for light transport have also been used to maximize the utility of spectrographs and detectors, allowing for spectra to be measured for each pixel of an extended object's image (Roth et al., 2005) and various objects spread across the field of view (FoV) of a fiber unit (Roth et al., 2018) simultaneously.

Some of the most advanced photonic technologies proposed so far to perform a variety of functionalities on starlight are photonic spectrographs, integrated beam combiners, fiber Bragg grating (FBG)-based OH-suppression filters, and photonic lanterns.

1.4 Synopsis

The introduction of astrophotonics given above alluded to the main reason their application to astronomical instrumentation has been limited. Specifically, the need to operate at the single-mode regime and the poor coupling via seeing-limited telescopes into them. The foremost challenge for these technologies, therefore,

remains the efficient coupling of starlight into single- and few-mode waveguides over broader spectral ranges.

The theoretical maximum of the coupling efficiency with which starlight can be coupled at the diffraction limit into a single-mode fiber (SMF) was first calculated by Shaklan and Roddier (Shaklan et al., 1988) as 0.78. Seeing conditions can obviously reduce this attainable efficiency severely. On-sky experiments at the 3.60-m obscured telescope in La Silla measured an average of 0.05 coupling efficiency without AO correction (Coudé du Foresto et al., 2000). Recently, $> 60\%$ of the light gathered by the 10-m Subaru telescope was coupled into an SMF, but this was only possible thanks to the facility's extreme adaptive optics (ExAO) system and the use of a pupil apodizer to eliminate the effect of the central obscuration and the spiders (Jovanovic, Cvetojevic, et al., 2017).

This work revisits the theory of starlight coupling through atmospheric turbulence into optical waveguides and explores the application of AO systems, photonic lanterns, and a combination thereof to enable the use of astrophotonic instrumentation in large astronomical telescopes.

The thesis is organized as follows: the next three chapters introduce the required physics and mathematical background before presenting some numerical models, while the three chapters afterward present the results and some novel concepts examined with the developed numerical tools. Chapter 2 introduces the theory of atmospheric turbulence and the basic principles of AO systems. Chapter 3 presents aspects of the theory of optical waveguides relevant to astronomical instruments and discusses how the coupling of starlight is affected by the atmosphere. In Ch. 4, details are given on how the numerical models apply the theoretical concepts in Ch. 2 and 3 to simulate scenarios of coupling starlight into optical waveguides through AO-corrected telescopes.

An experimental setup that was used to verify the constructed models is detailed in Ch. 5, and both the theoretical and experimental results are given as a published article in that chapter. Additionally, in the form of published articles, Ch. 6 and 7 present new concepts that use astrophotonic components to optimize coupling and analyze optical modes, respectively.

Chapter 2

THEORY OF ATMOSPHERIC TURBULENCE AND ADAPTIVE OPTICS

In ground-based astronomy, targets are always observed from behind a turbulent layer of air, complicating the process in various manners. This chapter discusses the theory of atmospheric turbulence with an introduction to AO systems. Section 2.1 presents the mathematical formulation of Kolmogorov's theory of turbulence and how it applies to optical wavefronts and stellar images. Section 2.2 explains the concept of AO with a description of its basic elements.

2.1 Impact of Earth's atmosphere on observations

Light waves carrying information from distant celestial objects travel unchanged through the vastness of space only to get distorted during the last few kilometers of their journey when they pass through Earth's atmosphere. To the naked eye, the effect of the atmosphere manifests itself by the colors of sunsets at day and the twinkling of stars at night. For modern-day astronomical observatories, the images formed by ground-based telescopes are blurred, setting a limit on the resolution that can be achieved (see Fig. 2.1), complicating the design of spectrographs and similar bulk optics instruments, and reducing the efficiency of astrophotonic devices. The latter of these effects is the main concern of this work.

In 1609, Galileo was the first to use a telescope to observe a celestial object, but it was not until Huygens around 1656 that the increase in size and quality of the optics made it clear that the atmosphere was affecting the observations. In 1704, Newton wrote in his *Opticks* (Newton, 1730)

> . . . For the Air through which we look upon the Stars, is in a perpetual Tremor; as may be seen by the tremulous Motion of Shadows cast from high Towers, and by the twinkling of the fix'd Stars. . . .
>
> . . . The only Remedy is a most serene and quiet Air, such as may perhaps be found on the tops of the highest Mountains above the grosser Clouds.

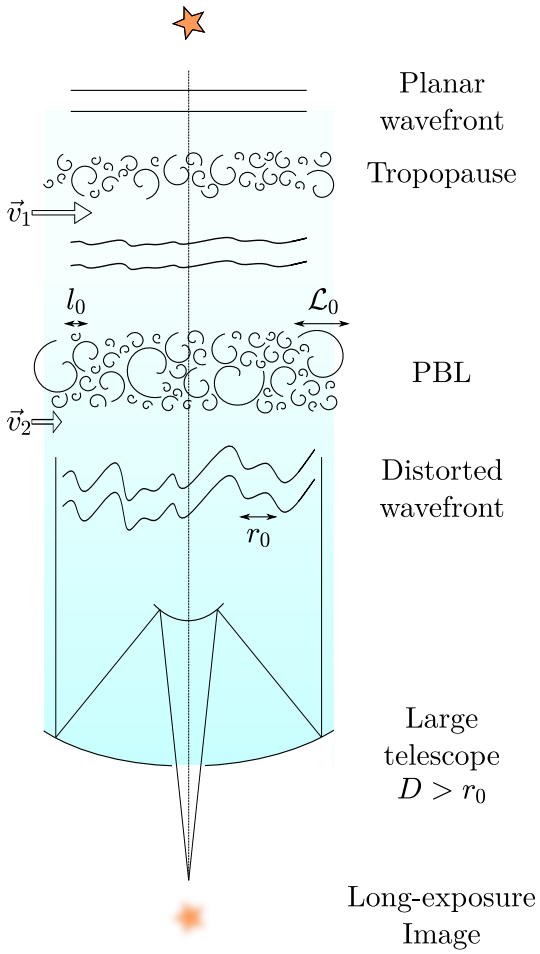

Figure 2.1: Wavefronts arriving from celestial sources pass through turbulent layers before they are collected by ground-based telescopes.

2.1.1 Refractive index fluctuations

The atmosphere is a dielectric medium that absorbs and re-emits when radiation propagates through it. With a refractive index of about $n = 1.00029$ at STP, it can also refract light waves when fluctuations in the refractive index (a few parts in a million for a vertical path) are encountered by the propagating waves. The strength of this effect is not uniform at all altitudes. The part of the atmosphere closest to the ground, i.e., the planetary boundary layer (PBL), is a turbulent layer a few hundred meters thick. From there up, turbulence falls off exponentially with altitude in the higher volume, known as the free atmosphere, with an exceptional local maximum at the tropopause (see Fig. 2.4).

With a temperature gradient developing between the lower and upper parts of the atmosphere, convective cells of air rise up. Wind shear caused by the velocity

difference between the layers mixes the cells of different temperatures when the Kelvin-Helmholtz instability sets in, and therefore temperature inhomogeneities ensue. The refractivity of air, N — defined as the departure from unity in parts per million — depends linearly on the pressure, P, and temperature, T. At optical wavelengths, the following approximation holds (Hardy, 1998):

$$N = (n-1) \times 10^6 \approx 77.6\frac{P}{T}, \tag{2.1}$$

where n is air's index of refraction. At 15°C and 1 bar, the dispersion is given by the Cauchy formula

$$n(\lambda) = 1 + \left(272.6 + \frac{1.22}{\lambda^2}\right) \times 10^{-6}. \tag{2.2}$$

This weak wavelength, λ, dependence of refractivity (Edlén, 1966) means that air is practically achromatic in the visible and the near-infrared resulting in wavefronts having the same shape across the two bands. An important property that AO systems exploit, as seen later in Sec. 2.2.

Apart from the atmosphere, dome seeing — caused by heat sources inside the telescope enclosure and the temperature gradient between the mirror and the air above — is easily mitigated by air-conditioning the dome and wind-flushing the mirror continuously.

2.1.2 Turbulence mechanics

An agreed-upon definition of turbulence does not exist but comparing it to laminar flow and listing some of its features help identify it. In a laminar flow, the individual layers of the fluid flow parallel to each other without any mixing between the parts of each layer and its neighbors. In turbulent flow, different parts of the fluid move in vortices in directions away from, even opposite to, the overall flow direction of the fluid. This mixing causes the good diffusivity of turbulent flow that works on homogenizing the fluid properties, and it leads the kinetic energy of the large-scale vortices of the turbulent fluid to dissipate at the molecular level as heat by viscous friction.

The problem of describing the mechanics of airflow in space and time above a telescope aperture is a complex one. The flow of incompressible fluids is governed

by Navier-Stokes equations, but their applicability to turbulent flow is limited. These partial differential equations are notoriously computationally expensive at the length scales involved in a turbulent flow. They are not yet proven to have a well-behaved solution, either. Moreover, turbulent flow is chaotic, meaning that a small change to the initial conditions results in a large deviation in the final state. This again limits the usefulness and applicability of deterministic models to real-world problems.

A statistical treatment of this random phenomenon is, however, still possible. Richardson, Stokes, and others gave a qualitative description. They noticed that the vortices in a turbulent flow have a maximum large scale, i.e., the *outer scale* ($\mathcal{L}_0$), when the energy is supplied to the fluid, be it by heating or stirring, which then break down into ever smaller-scale motions down to a minimum spatial scale, i.e., the *inner scale* (l_0). At that scale, the viscosity of the fluid prevents further cascading. Richardson summarized this process in the verse (Richardson, 1922)

> Big whirls have little whirls that feed on their velocity,
>
> and little whirls have lesser whirls and so on to viscosity.

Reynolds experimentally identified the fluid properties that cause turbulence to kick in. The dimensionless Reynolds number

$$Re = \frac{L_0 v_0}{\nu}, \tag{2.3}$$

gauges turbulence, where L_0 is the characteristic scale of the problem, say the pipe diameter or the layer thickness, v_0 is the characteristic velocity at that scale, and ν is the kinematic viscosity of the fluid.[1] The flow is turbulent when Re exceeds a critical value. Air, with its low viscosity at $\nu = 1.5 \times 10^{-6}$ m^{2}s^{-1}, flows in a fully developed turbulent regime when driven with wind speeds as slow as a few ms^{-1} at scales of only several meters (Glindemann, 1997).

Kolmogorov's theory of turbulence

Next comes Andrey Kolmogorov, who worked out how to quantify the distribution of kinetic energy in Richardson's whirls within the inertial range between the inner

[1] Notice that the English letter v is used for velocity, while the Greek letter nu (ν) is used for the kinematic viscosity.

and outer scales (Kolmogorov, 1991). He suggested that the kinetic energy of the largest vortices gets redistributed continuously to smaller and smaller vortices under the assumption that the motions are isotropic and homogeneous. Conservation of energy hence demands that for this stationary process, the energy input rate per unit mass, ε, at the outer scale must equal the dissipation rate of energy as heat. With this restriction and the postulate that the inner scale vortices are statistically isotropic, dimensional analysis is possible to derive the power law governing the spectral distribution of energy. In the reciprocal space, i.e., k-space, the energy, $\mathfrak{E}$, cascades from low spatial frequencies to high spatial frequencies.

The energy injection rate per unit mass is by definition (Frisch, 1995; Glindemann, 1997)

$$\varepsilon = \frac{\mathfrak{E}(\mathcal{L}_0)}{mt(\mathcal{L}_0)} = \frac{\mathfrak{E}(l_0)}{mt(l_0)} = \frac{v^2}{2t(l)} = const., \tag{2.4}$$

where m is the mass, t is the vortex turnover time, and v is the velocity.[2] The kinetic energy transfer time through a vortex of size l is l/v which yields

$$\varepsilon \propto \frac{v^3}{l} \rightarrow v \propto (\varepsilon l)^{1/3}. \tag{2.5}$$

Since the energy is proportional to v^2, one gets

$$\mathfrak{E}(l) \propto (\varepsilon l)^{2/3}. \tag{2.6}$$

In reciprocal space, the energy spectrum $\Phi(k)$ in the spatial frequency range $[k, k + \mathrm{d}k]$

$$\Phi(k)\mathrm{d}k \propto k^{-2/3}, \tag{2.7}$$

with $k = 2\pi/l$ the angular spatial frequency. The energy is only governed by the scale size k and the injection rate ε in the inertial range. Integrating Eq. (2.7) and using Eq. (2.6) gives

$$\Phi(k) \propto \varepsilon^{2/3} k^{-5/3}. \tag{2.8}$$

[2]The velocity v is not the total velocity of the vortex which is mainly driven by advection, but it is rather the velocity difference across the distance l (Frisch, 1980).

Which is Kolmogorov's $5/3$ law that is valid within the inertial range, $\mathcal{L}_0 \ll l \ll l_0$. This is true for the modes in one dimension. Tatarski (Tatarski, 2016) applied Kolmogorov's work on velocity fields to refractive index fluctuations and extended this power spectrum into three dimensions. To get the three-dimensional spectrum, one needs to integrate over the unit sphere. The relation

$$\Phi(\vec{k}) = \frac{-\mathrm{d}\Phi/\mathrm{d}k}{2\pi k}, \tag{2.9}$$

holds. This gives

$$\Phi(k) = 4\pi k^2 \Phi(\vec{k}), \tag{2.10}$$

which, together with Eq. (2.8), leads to

$$\Phi(\vec{k}) \propto k^{-11/3}. \tag{2.11}$$

Again, this power spectrum of refractive index variations is only valid within the inertial range ${\mathcal{L}_0}^{-1} \ll k \ll {l_0}^{-1}$. The bounds of the inertial range vary with altitude and from site to site. The inner scale at which dissipation starts lays between 1 mm near the ground and 1 cm at the tropopause (F. Roddier, 1981). The outer scale varies over a larger range, between a few meters close to the ground and the thickness of the entire turbulent layer in the free atmosphere, which can reach a few hundred meters (Colavita, 1990). For large telescopes and long-baseline interferometers, the outer scale quantifies the magnitude of tip/tilt in the distorted wavefront, which means that the actual overall tilt is smaller than that predicted by Kolmogorov's spectrum. To account for this finite outer scale, von Kármán proposed the following modification to Kolmogorov's spectrum (Welsh, 1997)

$$\Phi(\vec{k}) \propto \left(|\vec{k}|^2 + \frac{1}{{\mathcal{L}_0}^2} \right)^{-11/6}. \tag{2.12}$$

One step further is to incorporate the inner scale, hence the modified von Kármán spectrum (Hardy, 1998)

$$\Phi(\vec{k}) \propto \left(|\vec{k}|^2 + \frac{1}{{\mathcal{L}_0}^2} \right)^{-11/6} e^{-|\vec{k}|^2/|\vec{k}_i|^2}, \tag{2.13}$$

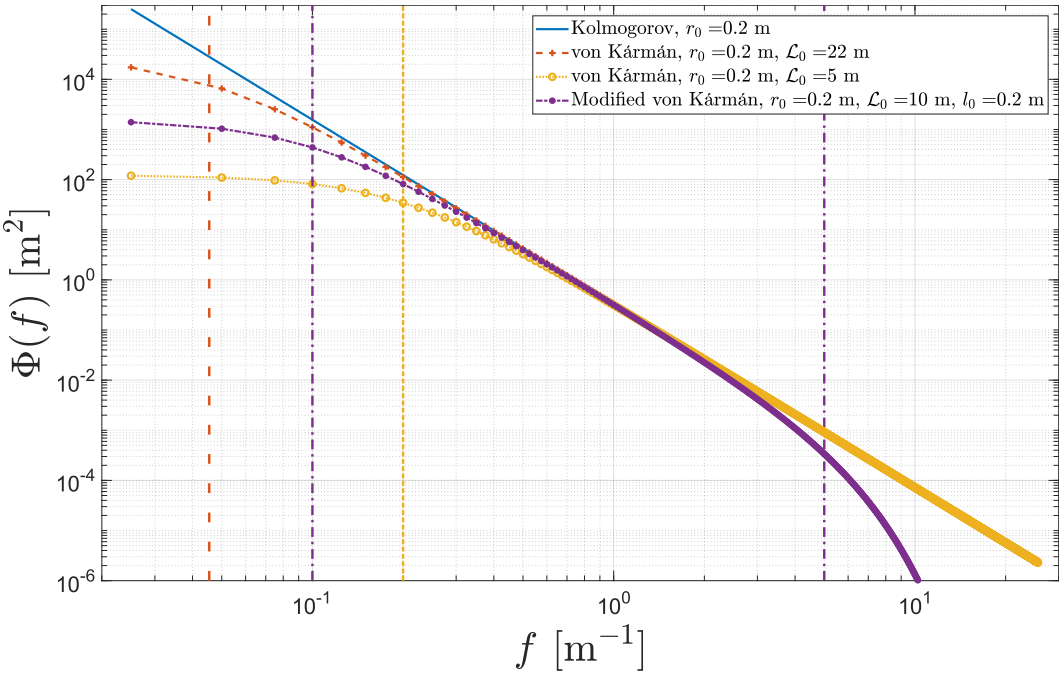

Figure 2.2: Log-log plots of Kolmogorov, von Kármán, and modified von Kármán spectra. Vertical lines on the left indicate the outer scales, while the vertical line on the right indicates the inner scale for the modified von Kármán spectrum. Here, the spectra are functions of the linear, f, rather than the angular, k, spatial frequency.

where $\vec{k}_i = 5.92/l_0$. Figure 2.2 shows Kolmogorov and von Kármán spectra for varying outer scales.[3]

A mathematical tool introduced by Kolmogorov to describe the spatial structure of a random process is the *structure function* that measures the expectation of the difference of the values of a random variable at two points in space (or time). For a random variable x, the structure function measured at positions $\vec{r}_1$ and $\vec{r}_2$ is defined as

$$D_x(\vec{r}_1, \vec{r}_2) = \langle |x(\vec{r}_1) - x(\vec{r}_2)|^2 \rangle. \tag{2.14}$$

The $\langle \cdot \rangle$ represents an ensemble average. The structure function for isotropic homogeneous turbulence (and all higher statistical moments) must depend on the separation between the two points, $r_{12} = |\vec{r}_2 - \vec{r}_1|$ rather than their absolute locations. Since energy per unit mass ($v^2/2$) has a $2/3$ power-law dependence on the

[3] An alternative derivation of Kolmogorov's law based on a units-matching argument is given in App. A.

spatial scale (Eq. (2.6)), the structure function of the velocity field (also $\propto v^2$) must follow the same, i.e.,

$$D_{\vec{v}}(r_{12}) = \left\langle |\vec{v}(\vec{r}) - \vec{v}(\vec{r} + r_{12})|^2 \right\rangle = C_v^2 {r_{12}}^{2/3}. \tag{2.15}$$

The velocity structure constant C_v^2 determines the turbulence strength. Specifically, how well correlated the velocities between two points separated by r_{12} are. The variations in the velocity field, however, do not produce optical aberrations on their own. It is because the stirring of air involves mixing pockets from layers of different altitudes, ergo layers with temperature inhomogeneities, that the wavefronts get distorted. At a pressure equilibrium, the different temperatures translate into different densities and eventually different indices of refraction (see Eq. (2.1)). Since the mechanical turbulence drives the variations in temperature and refractive index, they also follow Kolmogorov's law for the velocity field, albeit with a different proportionality constant. The temperature structure function is, therefore,

$$D_T(r_{12}) = \left\langle |T(\vec{r}) - T(\vec{r} + r_{12})|^2 \right\rangle = C_T^2 {r_{12}}^{2/3}. \tag{2.16}$$

With the refractivity dependence on temperature as given by Eq. (2.1), the structure function of the refractive index is

$$D_n(r_{12}) = D_N(r_{12}) = \left\langle |N(\vec{r}) - N(\vec{r} + r_{12})|^2 \right\rangle = C_N^2 {r_{12}}^{2/3}. \tag{2.17}$$

This is Obukhov's law (Hardy, 1998). Of interest here are the statistics of the phase, $\phi(x, y)$, rather than the refractive index fluctuations. For a monochromatic plane wave traveling downward from a star at zenith through a turbulent layer of thickness δh with the telescope at height h, the phase shift introduced by the refractive index field $n(x, y)$ into the plane wave is

$$\phi(\vec{r}_T) = k \int_h^{h+\delta h} \mathrm{d}z n(\vec{r}_T, z), \tag{2.18}$$

where $k = 2\pi/\lambda$ is the wavenumber, and $\vec{r}_T = (x, y)$ is the position vector in the transverse plane. The turbulence layer is assumed to be thin enough for diffraction effects to take place but at the same time larger than the correlation length of the refractive index distortions. The auto-correlation function of the wavefront

$\psi(\vec{r}) = \exp[i\phi(\vec{r})]$, known as the coherence function (a measure of how well related is the field at one position to its value at neighboring positions), is given by

$$B_\psi(\vec{r}_T) = \langle \psi(\vec{r} + \vec{r}_T)\psi^*(\vec{r})\rangle, \tag{2.19}$$

where * indicates a complex conjugate. When the turbulence layers are much thicker than the vortices (the *Markov approximation*), independent variables from different altitudes through the layer contribute to the phase shift of the emerging wavefront. This allows the use of the central limit theorem to deduce that the phase has Gaussian statistics. With $\psi^*(\vec{r}) = \exp[-i\phi(\vec{r})]$,

$$\begin{aligned} B_\psi(\vec{r}_T) &= \langle \exp\left[i\left(\phi\left(\vec{r}\right) - \phi\left(\vec{r} + \vec{r}_T\right)\right)\right]\rangle \\ &= \exp\left[-\frac{1}{2}\left\langle \left|\phi(\vec{r}) - \phi(\vec{r} + \vec{r}_T)\right|^2 \right\rangle\right], \end{aligned} \tag{2.20}$$

where the fact that the expectation value of a Gaussian signal is also a Gaussian, i.e., $\langle \exp(iax)\rangle = \exp\left(-a^2\langle x^2\rangle/2\right)$, was used. The term in the argument of the exponential in Eq. (2.20) is recognized as the structure function of the phase $D_\phi(\vec{r})$ which yields

$$B_\psi(\vec{r}_T) = \exp\left[-\frac{1}{2}D_\phi(\vec{r}_T)\right]. \tag{2.21}$$

In general, a structure function of any variable x can be expressed in terms of the coherence function by expanding the square in the structure function definition (Eq. (2.14)). For a real function $\phi(\vec{r})$,

$$D_\phi(\vec{r}) = 2[B_\phi(0) - B_\phi(\vec{r})]. \tag{2.22}$$

The auto-correlation of the phase is

$$\begin{aligned} B_\phi(\vec{r}_T) &\equiv \langle \phi(\vec{r})\phi(\vec{r} + \vec{r}_T)\rangle \\ &= k^2 \int_h^{h+\delta h} \int_h^{h+\delta h} \mathrm{d}z' \mathrm{d}z'' \langle n(\vec{r}, z')n(\vec{r} + \vec{r}_T, z'')\rangle \\ &= k^2 \int_h^{h+\delta h} \mathrm{d}z' \int_{h-z'}^{h+\delta h-z'} \mathrm{d}z B_N(\vec{r}_T, z), \end{aligned} \tag{2.23}$$

where the dummy integration variable z'' was substituted by $z + z'$ to introduce the refractive index auto-correlation function $B_N(\vec{r}_T, z) = \langle n(\vec{r}, z')n(\vec{r} + \vec{r}_T, z + z')\rangle$. The first integral amounts to the thickness of the layer and again making use of the fact that the turbulence layer thickness δh is much larger than the correlation scale (the Markov approximation), the integration can be taken over all of space to get

$$B_\phi(\vec{r}_T) = k^2 \delta h \int_{-\infty}^{\infty} \mathrm{d}z B_N(\vec{r}_T, z). \tag{2.24}$$

Back to Eq. (2.22) with a substitution

$$\begin{aligned} D_\phi(\vec{r}_T) &= 2\left[B_\phi(\vec{0}) - B_\phi(\vec{r}_T)\right] \\ &= 2k^2\delta h \int_{-\infty}^{\infty} \mathrm{d}z \left[B_N(\vec{0}, z) - B_N(\vec{r}_T, z)\right] \\ &= 2k^2\delta h \int_{-\infty}^{\infty} \mathrm{d}z \left[\Big(B_N(\vec{0}, \vec{0}) - B_N(\vec{r}_T, z)\Big) - \Big(B_N(\vec{0}, \vec{0}) - B_N(\vec{0}, z)\Big)\right] \\ &= k^2\delta h \int_{-\infty}^{\infty} \mathrm{d}z \left[\Big(D_N(\vec{r}_T, z) - D_N(\vec{0}, z)\Big)\right]. \end{aligned} \tag{2.25}$$

But from Obukhov's law $D_N(r_{12}, z) = C_N^2 |\vec{r}_T|^{2/3} = C_N^2 ({r_{12}}^2 + z^2)^{1/3}$, where $r_{12} = |\vec{r}_T|$. This reads

$$\begin{aligned} D_\phi(r_{12}) &= k^2\delta h C_N^2 \int_{-\infty}^{\infty} \mathrm{d}z \left[({r_{12}}^2 + z^2)^{1/3} - |z|^{2/3}\right] \\ &= \frac{2}{5} \frac{\Gamma\left(\frac{1}{2}\right)\Gamma\left(\frac{1}{6}\right)}{\Gamma\left(\frac{2}{3}\right)} k^2\delta h C_N^2 {r_{12}}^{5/3} \\ &= 2.914 k^2 \delta h C_N^2 {r_{12}}^{5/3}, \end{aligned} \tag{2.26}$$

where $\Gamma(\cdot)$ is the gamma function. Substituting for the phase structure function $D_\phi(r_{12})$ in Eq. (2.22), one gets the wavefront coherence function as

$$B_\psi(r_{12}) = \exp\left[-\frac{1}{2}\left(2.914 k^2 \delta h C_N^2 {r_{12}}^{5/3}\right)\right]. \tag{2.27}$$

This is the wavefront coherence function for an infinitesimal layer of thickness δh. An integration is in order to get the coherence function over the whole of the

atmosphere. With the refractive index structure constant, $C_N^2 = C_N^2(z)$, dependant on position along the propagation path in general,

$$B_\psi(r_{12}) = \exp\left[-\frac{1}{2}\left(2.914k^2{r_{12}}^{5/3}\int \mathrm{d}z C_N^2(z)\right)\right], \tag{2.28}$$

where the integral is along the line of sight. Making use of the fact that the atmosphere is generally stratified in parallel horizontal layers, C_N^2 is only dependent on altitude h and does not vary horizontally (F. Roddier, 1999). This yields

$$B_\psi(r_{12}) = \exp\left[-\frac{1}{2}\left(2.914k^2{r_{12}}^{5/3}\sec\gamma\int \mathrm{d}h C_N^2(h)\right)\right], \tag{2.29}$$

where γ is the zenith angle of the source and therefore $\sec\gamma$ accounts for the airmass, i.e., the apparent increased thickness of the layers.

The next development is due to Fried (Fried, 1966), who studied the effect of turbulence on the structure of the images formed by telescopes. The factor in the exponent in Eq. (2.29)

$$r_0 \equiv \left[0.423k^2\sec\gamma\int \mathrm{d}h C_N^2(h)\right]^{-3/5}, \tag{2.30}$$

is defined as *Fried's parameter*. It sums up the strength of the turbulence along the layer, accounting for the airmass and the wavelength. The phase structure function and the wavefront coherence function can be then simply expressed in terms of r_0 as

$$D_\phi(r_{12}) = 6.88\left(\frac{r_{12}}{r_0}\right)^{5/3}, \tag{2.31}$$

$$B_\psi(r_{12}) = \exp\left[-3.44\left(\frac{r_{12}}{r_0}\right)^{5/3}\right]. \tag{2.32}$$

Fried chose the proportion factor in Eq. (2.30) such that a telescope of diameter $D = r_0$ will have an equal contribution from atmospheric seeing and diffraction to the image resolution as explained later in Sec. 2.1.3. The near-Gaussian form of the wavefront coherence function means that the seeing-limited PSF, i.e., the seeing disk, is also nearly Gaussian in shape since the PSF is the Fourier transform of the coherence function as shown later in Sec. 2.1.3.

At this point, the formulation is mature enough to set the proportion factors of the Kolmogorov (Eq. (2.11)) and von Kármán (Eq. (2.12)) spectra. The refractive index fluctuations are driven by kinetic energy and, therefore, follow the same spatial frequency statistics. For Kolmogorov's spectrum

$$\Phi_N(\vec{k}) = 0.033 C_N^2 k^{-11/3}, \tag{2.33}$$

and in terms of Fried's parameter

$$\Phi_N(\vec{k}) = 0.023 {r_0}^{-5/3} k^{-11/3}. \tag{2.34}$$

The von Kármán spectrum becomes

$$\Phi_N(\vec{k}) = 0.033 C_N^2 \left(|\vec{k}|^2 + \frac{1}{{\mathcal{L}_0}^2} \right)^{-11/6}. \tag{2.35}$$

Temporal correlation of the refractive index inhomogeneities

The treatment so far has concerned the spatial distribution of the refractive index inhomogeneities at a fixed time. The index is, nevertheless, also changing with time, t, and a temporal structure function can be used to describe the temporal evolution of such fluctuations. At a fixed point in space $\vec{r}$, over a time period τ

$$D_N(\tau) = \left\langle \left| n(\vec{r}, t) - n(\vec{r}, t+\tau) \right|^2 \right\rangle. \tag{2.36}$$

An approximation attributed to Taylor (Taylor, 1938), known as the *frozen flow hypothesis*, states that the lifetimes of the intrinsic changes in the temperature inhomogeneities are much longer than the time it takes the wind to carry the turbulence pattern downstream over the aperture, i.e.,

$$n(\vec{r}, t+\tau) = n(\vec{r} - \vec{v}\tau, t). \tag{2.37}$$

This is to say that the refractive index at a given point $\vec{r}$, a time τ later is related to the index at the current time, at a point $\vec{v}\tau$ away where $\vec{v}$ is the wind velocity. Therefore, the temporal evolution is directly related to the spatial fluctuations and

the statistics developed so far holds with a simple substitution of r_{12} by $|\vec{v}\tau|$. The temporal structure function for refractivity becomes

$$D_N(\tau) = \left\langle \left| n(\vec{r},t) - n(\vec{r}-\vec{v}\tau,t) \right|^2 \right\rangle = C_N^2 |\vec{v}\tau|^{2/3}. \tag{2.38}$$

Similar to Eq. (2.26), the temporal phase structure function is

$$D_\phi(\tau) = 2.914 k^2 \sec\gamma \tau^{5/3} \int_0^\infty \mathrm{d}h C_N^2 \overline{v}^{5/3}, \tag{2.39}$$

where $\overline{v}$ is the modulus of the mean propagation velocity. In terms of r_0,

$$D_\phi(\tau) = 6.88 \left(\frac{\overline{v}\tau}{r_0} \right)^{5/3} = \left(\frac{\tau}{\tau_0} \right)^{5/3}, \tag{2.40}$$

where $\tau_0 = 0.314 r_0/\overline{v}$ is the atmospheric coherence timescale. This sets the most stringent limitation on any system that attempts to correct for atmospheric turbulence, as seen later in Sec. 2.2.3. A characteristics bandwidth of an AO system was defined by Greenwood as the frequency at which the residual phase variance equals 1 rad^2 (Greenwood, 1977) and he calculated it as

$$f_G = \left[0.102 k^2 \sec\gamma \int_0^\infty \mathrm{d}h C_N^2(h) v^{5/3}(h) \right]^{3/5}. \tag{2.41}$$

For a single layer or a constant velocity profile, i.e., $v(h) = v$, *Greenwood's frequency* can be given in terms of r_0 (Eq. 2.30) as

$$f_G = 0.426 \frac{v}{r_0}. \tag{2.42}$$

Scintillation

So far the focus has been on phase fluctuations but the size of the refractive index inhomogeneities involved and the distances traversed by wavefronts between the atmospheric layers and the telescope inevitably give rise to amplitude distortions as well.

For planar waves, the amplitude of the field is uniform all over the wavefront, and the local energy flow is in the direction perpendicular to the wavefront, i.e., the direction

of the rays. Atmospheric distortion leads to a redistribution of energy, which means that the amplitude will vary from one position to another on the wavefront. Once the intensity fluctuations set in the wavefront, they will keep growing with distance even after passing the turbulence layer, and therefore the greatest contribution to the effect is due to the higher layers. The stochastic temporal variation of the intensity of a point source as seen by an observer behind a turbulence layer is the cause of the familiar phenomenon of stars twinkling and changing color, known in the literature as *scintillation*.

Both phase and amplitude variations of the wavefront contribute to the degradation of the image quality and coupling, but the fluctuations in amplitude contribute much less to that degradation. The loss in Strehl ratio due to amplitude variations is only a few percent in the infrared (F. Roddier et al., 1986). The effect is clearly reduced when the telescope is close to the turbulence layers. Moreover, apertures larger than the Fresnel radius average the inhomogeneities out over multiple uncorrelated patches, further reducing the impact of scintillation in an effect known as *aperture averaging*. Figure 2.3 shows the scintillation resulting from phase fluctuations propagating to a distant aperture. Only turbulence layers 10 km or higher would have an appreciable scintillation effect when a large r_0 is present, and a large aperture is used.

Scintillation is therefore only relevant to high-performance ExAO systems used for direct detection of exoplanets and is therefore incorporated in the numerical models of Ch. 4 but omitted in the results of Ch. 5. Including the effect would lead to high computational costs without a discernible impact on the results. When high-precision photometry is being considered, the effect needs to be included as the change of 0.01 to 1.0 percent in intensity due to scintillation might limit the sensitivity of a transit detection instrument (Osborn, 2015).

Structure constant profile

Several groups have modeled the nighttime profile C_N^2 as a function of height h. One is the modified Hufnagel-Valley (Roggemann et al., 2018; Valley, 1980)

$$C_N^2(h) = 8.16 \times 10^{-54} h^{10} e^{-h/1000} + 3.02 \times 10^{-17} e^{-h/1500} + 1.90 \times 10^{-15} e^{-h/100}. \tag{2.43}$$

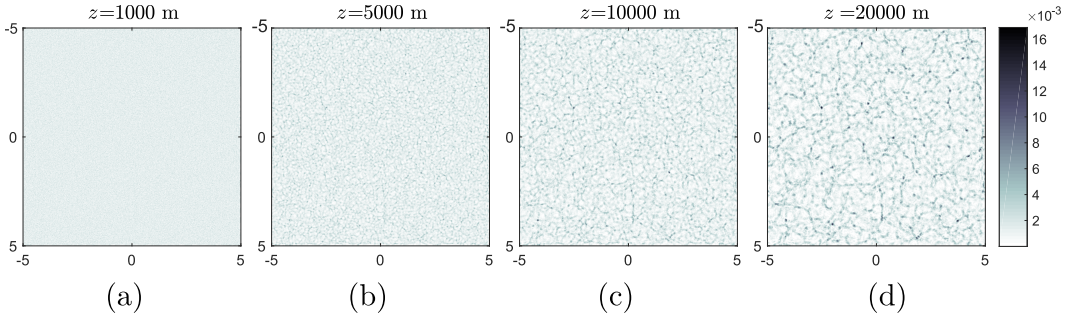

Figure 2.3: Simulated scintillation (intensity fluctuations) in arbitrary units at $\lambda = 1550$ nm due to an atmospheric layer (a) 1, (b) 5, (c) 10, and (d) 20 km above the aperture. The simulated phase screen is 10×10 m^2 with $r_0 = 0.2$ m.

A generalized model with free parameters in place of the constants in Eq. (2.43) can be adjusted to match measured C_N^2 values at specific sites (Hardy, 1998).The model's main features are the two distinct maxima at two turbulence layers, one near the ground and the other at about 10 km in the tropopause, as shown in Fig. 2.4. Observatories at high altitudes on narrow summits, e.g., Mauna Kea, have to deal with the weaker tropopause as the dominant layer while lower telescopes, e.g., Calar Alto, need to contend with both the PBL and the higher layer. For a site above sea level that has little relief from surrounding terrain, the profile would have an extended tail for the PBL caused by the topography.

2.1.3 Image formation through turbulence

Coupling into waveguides, similar to imaging, requires having the point source forming as small as possible an image in terms of angular size at the focal plane. The argument and mathematical formulation established in this section for image formation, therefore, hold for coupling correspondingly.

While the functions in Eq. (2.31) and (2.40) give statistical insight into the impact of r_0 on the phase at the aperture of a telescope, imaging and coupling occur at the focal plane. Waves passing through apertures get diffracted and form patterns that deviate from the geometric shadow of that aperture at the far-field.

Diffraction theory

Huygens' principle states that each point in the aperture opening acts as a source of spherical wavelets that mutually interfere while propagating to the observation plane. The resulting pattern is therefore simply given by the superposition of those

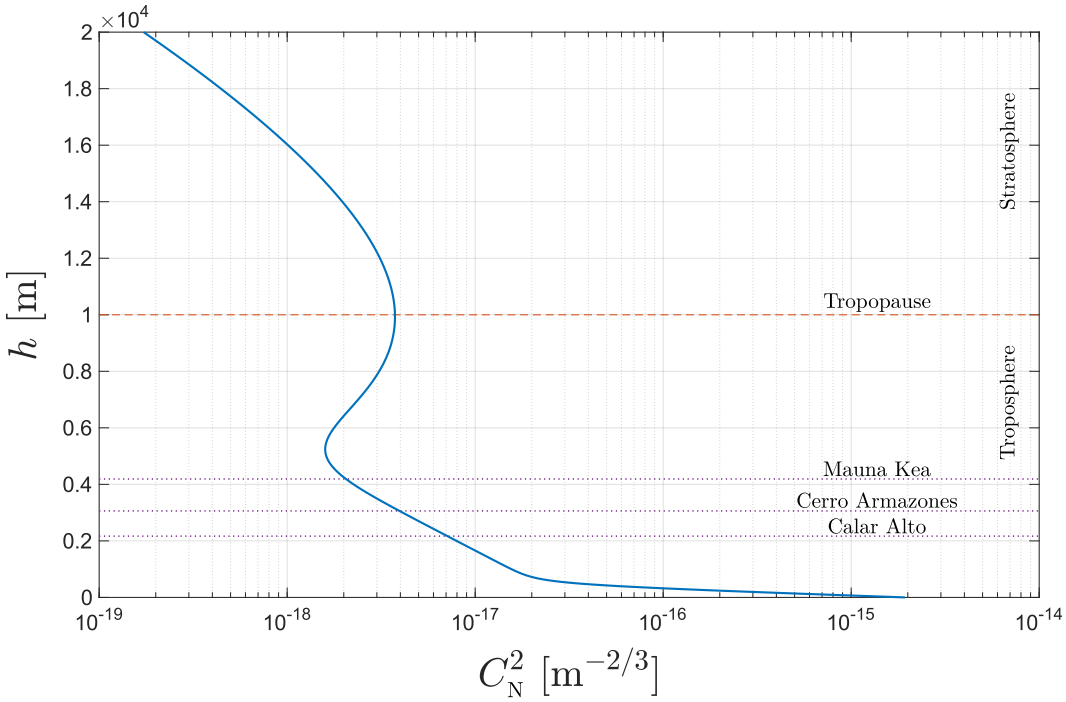

Figure 2.4: The modified Hufnagel-Valley profile of C_N^2 plotted in semi-log scale. The altitudes and the relative strength of the two dominant layers are evident by the local maxima in the curve at the PBL and the tropopause. This profile results in an $r_0 = 17.8$ cm at $\lambda = 500$ nm.

wavelets. Although an approximation of the phenomenon, the principle works very well in predicting images formed by apertures of much larger dimensions than the wavelength. The Fraunhofer diffraction formula goes further and takes advantage of the fact that the spherical wavelets are effectively plane waves in the far-field and at the focal plane of a converging optic to express the complex amplitude, i.e., the time-independent part of the wave function, at the focal plane as a Fourier transform of any fully transmissive aperture function. Appendix B lays out the derivation of the Fraunhofer diffraction formula, the Fourier transform relation between the aperture and the focal fields, and the diffraction pattern of circular apertures.

Turbulence effects on imaging

Eq. (B.16) may be used to calculate the structure of the image at the focal plane given the optical field at the aperture plane but to gain insight into the statistics of how turbulence degrades the images, the concept of transfer functions is now in order. If $T_{aper}(\vec{r_n})$ is the aperture function and $\psi(\vec{r_n})$ is the incident wavefront, then $T_{aper}(\vec{r_n})\psi(\vec{r_n})$ is the field at the pupil. For a clear aperture, $T_{aper}(\vec{r_n})$ is unity inside

the pupil and zero everywhere else. The coordinate $\vec{r}_n = \vec{r}_T/\lambda$ is the normalized spatial coordinate in the aperture plane. The intensity on the focal plane as given by Eq. (B.9) is

$$I(\vec{f}) \propto \left|\mathcal{F}\left[\psi(\vec{r}_n)T_{aper}(\vec{r}_n)\right]\right|^2 = \mathcal{F}\left[\int \mathrm{d}\vec{r}_n \psi(\vec{r}_n)\psi^*(\vec{r}_n+\vec{f})T_{aper}(\vec{r}_n){T_{aper}}^*(\vec{r}_n+\vec{f})\right], \tag{2.44}$$

where the Wiener-Khinchin-Einstein theorem was utilized to express the power spectrum of the pupil optical field as the Fourier transform of the autocorrelation function of the same field and f is the spatial frequency. The spatial frequency composition of a long exposure image is calculated by taking the expectation value over many realizations of the atmosphere

$$\begin{aligned}\langle I(\vec{f})\rangle &= \left\langle \int \mathrm{d}\vec{r}_n \psi(\vec{r}_n)\psi^*(\vec{r}_n+\vec{f})T_{aper}(\vec{r}_n){T_{aper}}^*(\vec{r}_n+\vec{f})\right\rangle \\ &= \int \mathrm{d}\vec{r}_n \langle\psi(\vec{r}_n)\psi^*(\vec{r}_n+\vec{f})\rangle T_{aper}(\vec{r}_n){T_{aper}}^*(\vec{r}_n+\vec{f}) = B_\psi(\vec{f})T_{tele}(\vec{f}),\end{aligned} \tag{2.45}$$

where $B_\psi(\vec{f})$ is recognized as the coherence function of the atmosphere in Eq. (2.32) evaluated at $\vec{r} = \vec{f}\lambda$ and since it is independent of the spatial coordinate as argued in Sec. 2.1.2, it could be taken out of the integral and serves as the atmospheric transfer function. The telescope transfer function $T_{tele}(\vec{f})$ was introduced as the autocorrelation of the pupil function. Equation (2.45) is the optical transfer function (OTF) for long exposure images and can therefore be used to gain some insight into the anatomy of such images.

A more general definition of the resolving power of an optical system, such as the atmosphere-telescope system under study here, is given by (Fried, 1966)

$$\mathcal{R} \equiv \int \mathrm{d}\vec{f} B_\psi(\vec{f})T_{tele}(\vec{f}). \tag{2.46}$$

At the diffraction limit, the wavefront is well correlated and $B_\psi(\vec{f}) = 1$. The resolving power is

$$\mathcal{R} = \int \mathrm{d}\vec{f} T_{tele}(\vec{f}) = \frac{\pi}{4}\left(\frac{D}{\lambda}\right)^2, \tag{2.47}$$

where D is the aperture diameter. In the limit of strong turbulence, i.e., a large aperture, $T_{tele}(\vec{f}) = 1$ whereas $B_\psi(\vec{f})$ is non-zero

$$\mathcal{R} = \int \mathrm{d}\vec{f} B_\psi(\vec{f}) = \int \mathrm{d}\vec{f} \exp\left[-3.44\left(\frac{\lambda\vec{f}}{r_0}\right)^{5/3}\right]$$
$$= \frac{6\pi}{5}\Gamma\left(\frac{6}{5}\right)\left[3.44\left(\frac{\lambda}{r_0}\right)^{5/3}\right]^{-6/5} = \frac{\pi}{4}\left(\frac{r_0}{\lambda}\right)^2. \quad (2.48)$$

where one arrives at the fact that the two transfer functions, the atmosphere's and the telescope's, become equal when $D = r_0$. Not a coincidence since this is by definition what Fried's parameter is. The factor 0.423 in the definition of r_0 in Eq. (2.30) was chosen by Fried for this equality to hold.

Therefore, the structure of the image formed is dependent on both, the diameter of the telescope D and r_0. The ratio D/r_0, known as the *turbulence strength*, determines what one sees at the focal plane. For small telescopes with $D/r_0 < 1$, the Airy disc $\sim \lambda/D$ is larger than the seeing disc $\sim \lambda/r_0$ and the broadening caused by turbulence is not seen because the wavefront is fairly correlated within the aperture. An overall tilt, however, still exists which can shift the centroid of the PSF randomly by $\sim \lambda/r_0$ over time scales longer than the coherence time, τ_0. This is known as *image motion*, and it causes images taken over exposure times longer than τ_0 to be smeared over an area of a diameter of $\sim \lambda/r_0$. For $D/r_0 < 0.5$ this would still be smaller than the Airy disk, and no correction is necessary, but when $0.5 < D/r_0 < 3$, a simple tip/tilt correction of the wavefront can stabilize the long exposure images. This is particularly important for coupling into waveguides. As turbulence strength increases, the wavefront within the aperture is stitched from uncorrelated patches of diameter r_0 that interfere to form a diffraction pattern at the focal plane composed of speckles spread over a distance of $\sim \lambda/r_0$ and each having an angular size $\sim \lambda/D$. Figure 2.5 shows the short and long exposure PSFs for different scenarios of turbulence strength.

Since energy is conserved, smearing the image over a larger seeing disc will necessarily reduce the peak value of the PSF. A useful measure to quantify the image quality is the *Strehl ratio*. It is defined as the ratio of the on-axis intensity of the seeing-limited PSF to that of a hypothetical diffraction-limited PSF. It could be defined for either on-axis or peak intensity values, but both definitions yield the same result for tip/tilt corrected wavefronts.

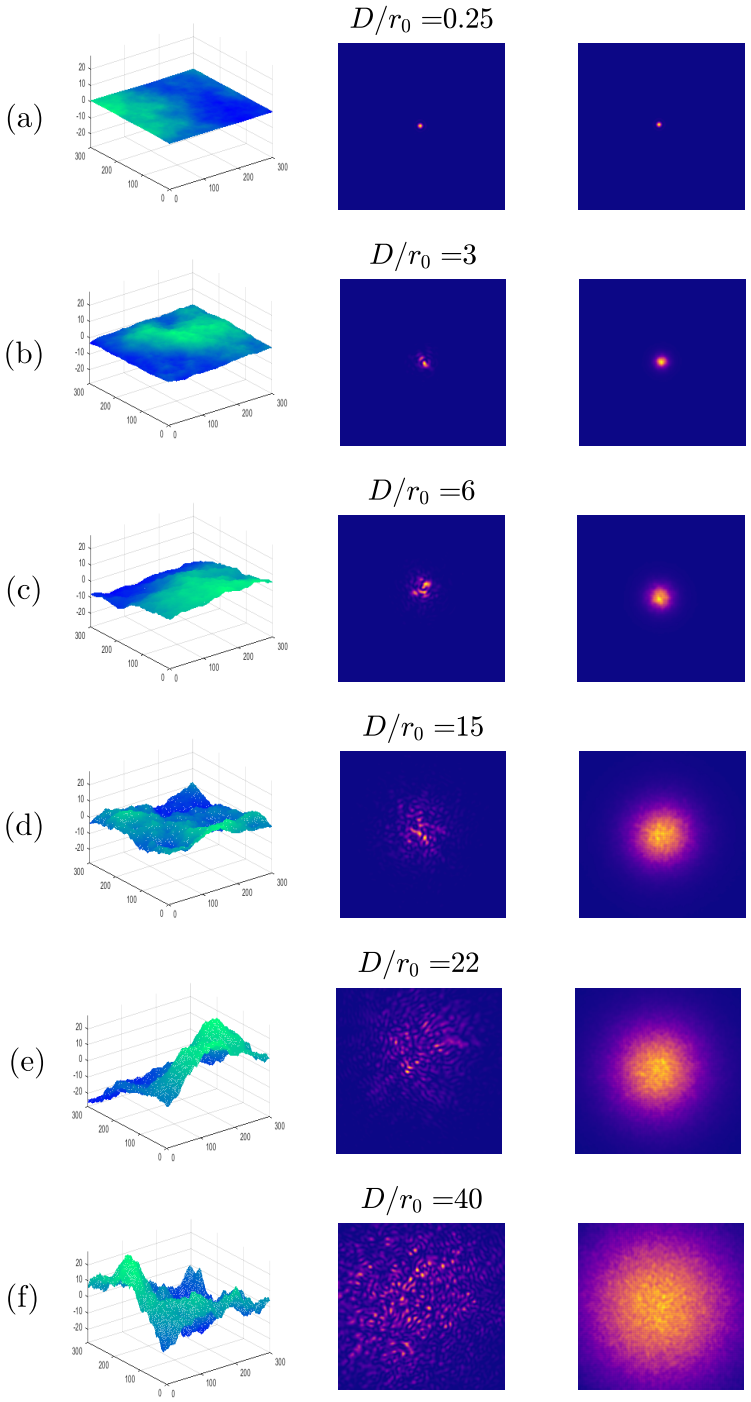

Figure 2.5: Wavefronts and PSFs at increasing D/r_0. Left panels are the wavefronts, middle panels show the short exposure ($t < \tau_0$) image, and right panels show the normalized long exposure ($t \gg \tau_0$) images.

To derive the formula for the Strehl ratio, the Fresnel-Kirchhoff diffraction integral is required (Born et al., 2013), and the derivation is given in App. B. When the phase is random, and only its statistics are known, the following approximation

$$SR \approx e^{-\sigma_\phi^2}, \tag{2.49}$$

known as the *extended Maréchal approximation* (Maréchal, 1947) holds for rms phase errors $\sigma_\phi = \langle(\phi - \overline{\phi})^2\rangle < 2$ rad. The phase rms, σ_ϕ, is related to the rms OPD error by $\sigma_\phi \equiv k\sigma_\psi$. The Strehl ratio, therefore, takes values $SR \in [0, 1]$. For a plane wavefront with $\phi = const.$, $SR = 1$. Equation 2.49 shows how the image quality degrades exponentially with the mean square error of the phase.

2.1.4 Wavefront representation

With full knowledge of a distorted wavefront, one has a choice on how to represent it mathematically for further processing. A zonal representation presents the local gradient values on a discrete grid, while modal representations decompose the wavefront into a sum of familiar basis functions over the aperture. For low-order distortions, modal representations are more accurate in describing the wavefront when an equivalent number of free parameters is considered for both approaches.

Because of the energy cascade of Kolmogorov's spectrum, the distorted wavefronts are smoothly varying within the inertial range. This allows their expansion in a series of orthogonal basis functions. Physicists and optical engineers use *Zernike polynomials* (Zernike et al., 1934) to decompose complex wavefronts since they are orthogonal on a unit disk and the lowest order polynomials of that family correspond to the common optical aberrations.

Noll presented a normalization that made the polynomials suitable for representing atmospheric turbulence (Noll, 1976). In an unobscured circular aperture, the Zernike modes are

$$Z_n^m(\rho, \theta) = \sqrt{\frac{2(n+1)}{1+\delta_{m0}}} R_n^m(\rho) \begin{cases} \cos(m\theta), \\ \sin(m\theta), \end{cases} \tag{2.50}$$

where

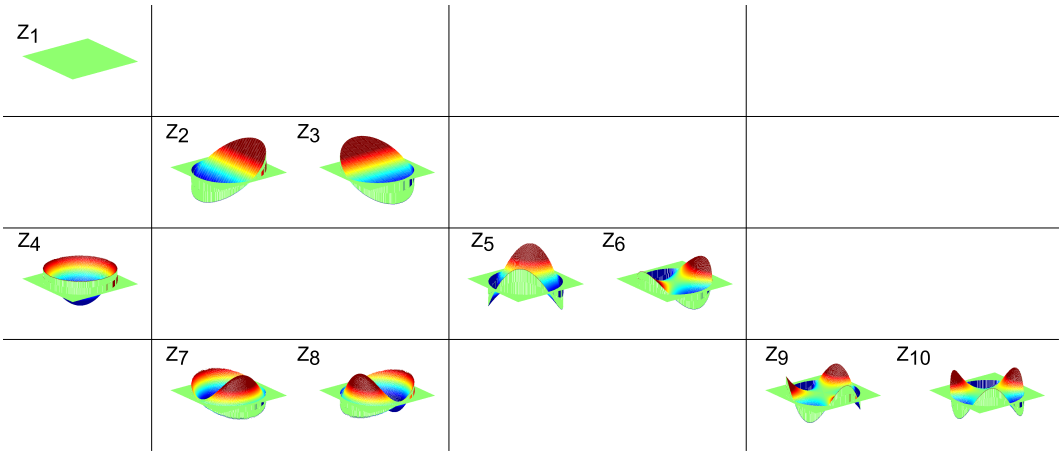

Figure 2.6: The first ten Zernike modes, arranged in groups according to their common radial and azimuthal orders. The indices follow Noll's single indices convention. The optical aberrations associated with the polynomials, in order, are piston, tip, tilt, defocus, oblique astigmatism, vertical astigmatism, vertical coma, horizontal coma, vertical trefoil, and oblique trefoil.

$$R_n^m(\rho) = \sum_{s=0}^{(n-m)/2} \frac{(-1)^s (n-s)! \rho^{n-2s}}{s! \left(\frac{n+m}{2} - s\right)! \left(\frac{n-m}{2} - s\right)!}, \tag{2.51}$$

and δ_{m0} is the Kronecker delta. Any arbitrary phase distortion $\phi(\rho, \theta)$ over a unit disk can be decomposed as a series of Zernike modes

$$\phi(\rho, \theta) = \sum_{j=0}^{\infty} a_j Z_j(\rho, \theta). \tag{2.52}$$

Given the orthogonality property, the coefficients $\{a_j\}$ are given by

$$a_j = \iint \rho \mathrm{d}\rho \mathrm{d}\theta \phi(\rho, \theta) Z_j(\rho, \theta). \tag{2.53}$$

The normalization under the square root in Eq. (2.50) is such that the rms value is unity over the unit disk. The integer index n is the radial order that determines the degree of the radial polynomial R_n^m, while m determines the azimuthal frequency. The effect of a central obscuration on the accuracy of the representations is negligible, making it more suitable for representing aberrations in astronomical telescopes. Figure 2.6 shows the first ten Zernike polynomials.

Zernike polynomials are, however, not strictly statistically independent. A set that has statistically independent coefficients is the Karhunen-Loéve expansion. For low-

order terms, the difference is small, and the simplicity of the Zernike polynomials outweighs the accuracy and the economy of the Karhunen-Loéve functions. They are therefore used for the numerical models in Sec. 4.5.

2.2 Adaptive optics (AO)

Modern-day ground-based astronomy is dominated by large and very large telescopes that are affected by the properties of the atmosphere. Systematic properties like refraction and dispersion can be easily counteracted through the careful optical design of the telescope itself and additional corrective static optics behind it. Dynamic random distortions due to turbulence, however, require real-time compensation by an optomechanical system that adapts to the ever-changing state of the atmosphere.

2.2.1 Historical context and state of the art of AO systems

Babcock was the first to propose using adaptive control to correct images degraded by atmospheric turbulence. He proposed a system that employs an active optical element that corrects phase distortions based on signals received from a wavefront sensing device (Babcock, 1953). The cost of implementing his suggestion prevented its adoption at the time until the defense agencies got interested in using segmented mirrors for pre-correcting laser beams to focus them on far targets and image the newly launched artificial satellites during the space race. In 1972, Hardy and his colleagues at Itek Optical Systems, commissioned by ARPA, started building the first AO system (Hardy, 1998). The real-time atmospheric compensator (RTAC) had a 21 actuators deformable mirror, a shearing interferometer as a wavefront sensor, and an analog computer to reconstruct the wavefront. Upon declassification, astronomers started looking into applying AO to astronomy where the fainter targets presented a challenge for the wavefront sensors. ESO and NOAO led the efforts of developing low-order, more sensitive AO systems suitable for IR astronomy where ESO's effort culminated with the prototype instrument 'COME-ON' (Rigaut et al., 1991) on the 3.6 m telescope at La Silla while NOAO's first prototype was successfully tested at the CFHT in 1993.

To overcome the limitation on the degrees of freedom set by the brightness of the reference star, laser guide stars (LGSs) were proposed (Foy et al., 1985) to create artificial light sources anywhere in the telescope's FoV. Thus opening the sky to AO systems.

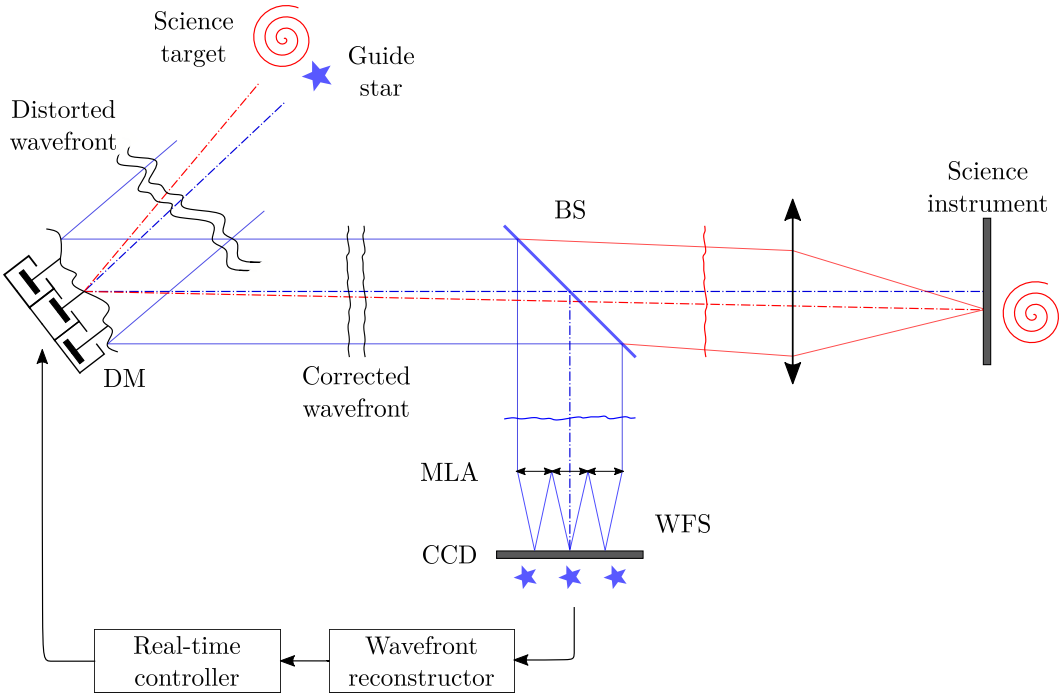

Figure 2.7: Elements of a basic AO system configured in a closed loop.

2.2.2 Elements of an AO system

The simplest AO system consists of a wavefront corrector, usually a deformable mirror (DM), a wavefront sensor (WFS), and a control system, as depicted in Fig. 2.7. The light from a reference star, known as the *guide star*, reflects off the DM and is directed towards the WFS which measures the wavefront error. The control system uses the WFS measurements to generate the commands that are actively sent to the DM with the target of minimizing the error. The DM compensates for the error by introducing equal but opposite path lengths to the wavefront. When the loop has closed, the images of the guide start, and all the objects whose light has traversed the same turbulence volume are corrected. Being a point source, the guide star is spatially coherent but not necessarily temporally coherent. However, sending a narrow band only towards the WFS is still possible since air's dispersion is too weak to cause a difference between the OPD and the phase across different bands (see Eq. (2.2)).

The classical AO system is known as single-conjugate adaptive optics (SCAO) since it uses a single DM and a single guide star to correct for one layer. Other more involved configurations of AO systems have been proposed to overcome some of the limitations of SCAO. Multi-conjugate adaptive optics (MCAO) systems (Beckers, 1988) help to expand the FoV beyond the isoplanatic angle. They do so using

multiple DMs and multiple WFSs. One DM/WFS pair is optically conjugated to the ground turbulence layer, while the extra pairs are conjugated to high-altitude layers, thereby expanding the size of the isoplanatic patch. Multiple LGSs are almost always required to place more than one reference around the target.

Multi-object adaptive optics (MOAO) uses multiple DMs and WFSs, each pair for a separate target, with each WFS tracking a guide star near its designated object. The corrected FoV is, therefore, composed of small patches centered on the guide stars rather than a single large patch like in MCAO.

Ground layer adaptive optics (GLAO) (Hubin et al., 2005) has a single DM conjugated to the ground layer but several WFSs and guide stars from which a combined correction signal is computed for the DM. Lastly, Laser tomography adaptive optics (LTAO) (Tallon et al., 1990) also uses one DM and multiple laser guide stars to evade the cone effect caused by the finite altitude of LGSs.

Wavefront sensing

Wavefront sensors that measure the phase distortion across the wavefront predate AO systems. Characterizing optical aberrations in the lab requires WFSs with a high spatial resolution. However, no particular demand is placed on the sensitivity of the detector since illumination is provided by coherent laser sources that can be made brighter, and each measurement can be done over relatively long exposures. AO systems have to work with faint sources and need to perform the measurements within times comparable to the coherence times of the atmosphere. The measurement's spatial resolution, and in turn the degrees of freedom of the AO system, are therefore limited by the brightness of the guide star and the available coherence time. These two limitations are nowadays alleviated, to some degree, by using detectors with a high quantum efficiency (QE) and low noise.

Unlike radio, optical waves have fields that oscillate at fast temporal frequencies, and there are not yet detectors that can respond at such a pace. There are, however, photodetectors, which are square-law devices, that respond to the intensity instead of the field, and any information about the phase has to be indirectly inferred from intensity measurements.

One is interested in the phase at the entrance pupil of the telescope, but given the Fourier transform relation between the field at the focal plane, i.e., the PSF, and the field at the pupil plane, i.e., the OTF (cf. Eq. (B.9)), phase retrieval is possible from

the intensity at the focal plane. Since both the phase and the sign of the field are lost at the focal detector, the problem is underdetermined, and multiple solutions for the pupil field can produce the same intensity pattern. With an *a priori* assumption that the amplitude is constant at the pupil plane, an iterative algorithm can be used to find a unique solution. One example of such an algorithm is the Gerchberg-Saxton algorithm (Fienup, 1982; Maeda et al., 1981). The need for the focal images to be monochromatic and the computation time required to reach convergence, however, prevent the use of such methods in astronomy.

The techniques used mainly in astronomy are the lateral shearing interferometer, the curvature sensor, the pyramid sensor, and the Shack-Hartmann WFS. The latter is the most common and the one used in the experimental part of this work, and therefore, further considerations focus mainly on its working principle and modeling.

At the pupil plane of a Shack-Hartmann WFS, conjugated to the turbulence layer being sensed, is an array of positive lenslets, known as the microlens array (MLA). The array samples the wavefront spatially and an image of the guide star is formed behind each of the lenslets. With a planar wave, the images formed at the detector are all on the optical axes of their respective subapertures, as shown in Fig. 2.8b. If each subaperture is smaller than r_0 of the distorted wavefront, then each lenslet receives a planar segment of that wavefront but at a tilt angle. The images in the grid are no longer aligned on the optical axes of the lenslets but rather shifted by an amount proportional to the slope of the wavefront over that subaperture (see Fig. 2.8c). Measurements of the average local slopes are also possible when the subapertures are larger than r_0 by evaluating the center of gravity (CoG), i.e., the weighted centroid, of the images and even though one four-quadrant detector (4QD) per subaperture is enough to estimate the displacements in the spots, high-resolution CCDs are used nowadays since CoG estimates get better with increased resolution.

The lenslets are usually square in shape to capture all the light incident on the subapertures. The PSF of such geometry of side length d at focal length f is (Born et al., 2013)

$$I(x,y) = I_0 \left(\frac{\sin(\pi dx/\lambda f)}{\pi dx/\lambda f} \right)^2 \left(\frac{\sin(\pi dy/\lambda f)}{\pi dy/\lambda f} \right)^2 . \tag{2.54}$$

The width of the central lobe of this pattern (shown in Fig. 2.8a) is $2\lambda f/d$. The size of this spot together with the geometry of the CCD array determines the sensitivity and dynamic range of the WFS. Furthermore, detectors are never free of noise and

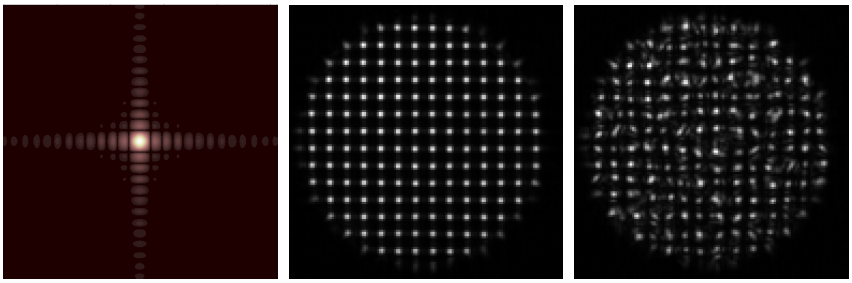

(a) (b) (c)

Figure 2.8: (a) PSF of a square subaperture. (b) SH spots pattern corresponding to a planar wavefront. (c) SH spots pattern measured for a $D/r_0 = 8$ wavefront.

thus the number of photons reaching each pixel within the exposure time needs to exceed a certain threshold to avoid noise corrupting the measurements. A trade-off, therefore, exists between the resolution of the measurement determined by the number of subapertures (and/or the detector pixels) and the brightness of the guide star that can still deliver enough flux to each subaperture before noise dominates.

The first moment, i.e., the CoG, of the intensity pattern $I(x,y)$ with respect to the transverse directions determines the slope of the wavefront at the pupil according to (Gross et al., 2012)

$$c_x = \frac{\iint_R \mathrm{d}x\mathrm{d}y x I(x,y)}{\iint_R \mathrm{d}x\mathrm{d}y I(x,y)} = \frac{\lambda f}{2\pi} \iint_A \mathrm{d}x\mathrm{d}y \partial_x \phi(x,y), \tag{2.55a}$$

$$c_y = \frac{\iint_R \mathrm{d}x\mathrm{d}y y I(x,y)}{\iint_R \mathrm{d}x\mathrm{d}y I(x,y)} = \frac{\lambda f}{2\pi} \iint_A \mathrm{d}x\mathrm{d}y \partial_y \phi(x,y), \tag{2.55b}$$

where the integration domains, R and A, are the subaperture areas at the focal plane and the MLA, respectively.

Higher spatial resolution at the detector with further processing of the image's shape, e.g., ellipticity due to astigmatism and broadening due to defocus, allows higher moments to be sensed, but this path is not pursued in Ch. 3.

Wavefront reconstruction and control

Since WFSs only measure the local gradient of the wavefront, the absolute phase value is lost, and a reconstruction computation is necessary before the commands for

the DM can be generated. Assuming that the local gradients of the wavefront within the subapertures are corrected, disregarding the relative phase relation between them, the wavelets from the subapertures would add incoherently, and a speckle pattern will form at the focal plane.

If the WFS is noise-free, the gradients can be summed over a spatial integration path to produce a smoothly varying surface. In a two-dimensional wavefront, all integration paths would give the same output. The phase at a point p is (Herrmann, 1980)

$$\phi(p) = \int_C \nabla\phi \cdot \mathrm{d}S + \phi(p_0), \tag{2.56}$$

where the phase at a reference point p_0 is given and C is any path connecting the points p and p_0. Since noise in the detector used by the WFS is inevitable, the reconstruction process is dependent on the choice of the integration path. A method of minimizing the mean-square error between the reconstructed wavefront and the gradient measurements is thus needed. This is not trivial. After the exposure time required to integrate enough photons from the guide star, the processing time to reconstruct the wavefront is the second most stringent bottleneck in the control loop.

Two approaches have been used for estimating the wavefront from the gradient measurements, the zonal and the modal methods. In the zonal methods, the phase is evaluated on a network of nodes that may or may not be similar to the geometric configuration of the DM actuators. Modal methods, on the other hand, (Southwell, 1980) define the wavefront in terms of modes, e.g., Zernike modes, over the entire aperture (see Eq. (2.50)). The weights of the basis functions are to be determined and are dependent on the WFS measurements.

In the modal method, the wavefront as a superposition of N basis functions is

$$\phi(x,y) = \sum_{k=1}^{N} a_k Z_k(x,y), \tag{2.57}$$

and the measured wavefront gradients in both dimensions are

$$g_i^x = \partial_x \phi(x,y) = \sum_{k=1}^{N} a_k \partial_x Z_{ki}, \tag{2.58a}$$

$$g_i^y = \partial_y \phi(x,y) = \sum_{k=1}^{N} a_k \partial_y Z_{ki}. \tag{2.58b}$$

Collapsing the equations system (2.58) into a matrix form with **D** containing both the derivatives of the Zernike functions in x- and in y-directions concatenated into one matrix yields

$$\vec{g} = \mathbf{D}\vec{a}. \tag{2.59}$$

With a multiplication of both sides from the left by $\mathbf{D}^{-1}$

$$\vec{a} = \mathbf{D}^{-1}\vec{g}, \tag{2.60}$$

the coefficients $\{a_k\}$ are obtained. Slope measurements are performed inside subapertures that are not necessarily aligned with the DM actuators. In a Fried geometry (Hardy, 1998), the corners of the subapertures coincide with the actuators. This geometry is insensitive to the piston mode, like the others, and additionally insensitive to the waffle mode (checkerboard-like pattern) (Gavel, 2003). A fact that can be utilized to align the system. Once aligned by having the WFS generating no signal when a waffle command is sent to the DM, the influence matrix can be experimentally measured. A command of unit amplitude is applied to each actuator one by one, and the slopes S_x and S_y of the WFS are registered. Practical considerations to solving the system in Eq. (2.60) are discussed in Sec. 4.5.1.

Wavefront corrector

With the knowledge acquired from the wavefront reconstruction process, the proper shape of the mirror to counteract the distortion in the wavefront can be determined. Therefore, the arrangement of the actuators behind the DM's facesheet and the shapes that the DM can take need to be considered. The DM introduces a temporally and spatially varying optical path difference $\delta(x,y;t)$ to the wavefront which results in a phase shift

$$\phi(x,y;t) = k\delta(x,y;t) = \frac{2\pi}{\lambda} nd(x,y;t), \tag{2.61}$$

where d is the physical path difference. Introducing an optical path difference by varying the refractive index is possible with birefringent electro-optical materials, but inertial devices that change shape, e.g., mechanical DMs, have been the method of choice in astronomy given their fast response times and wide spectral bands. The number of needed actuators grows as the square of the turbulence strength $\sim (D/r_0)^2$, which is a function of the wavelength itself, but the stroke required is wavelength-independent thanks to the inverse dependence of phase on wavelength as seen in Eq. (2.61). This required stroke is usually reduced by first correcting the overall tip/tilt in the wavefront by means of a fast steering tip/tilt mirror.

In nature, several effects have been discovered that can transform an electrical voltage into a displacement (F. Roddier, 1999). The ferroelectric effect occurs in permanently polarized piezoelectric ceramics like PZT that generate mechanical strain when an electric field is applied. This was one of the earliest methods used. The electrostriction effect, on the other hand, occurs in all dielectrics where in non-piezoelectric materials, e.g., PMN, the displacement is proportional to the square of the applied field. Magnetostriction is the magnetic analog in ferromagnetic materials where the shape changes in response to a magnetic field. Microelectro-mechanical systems (MEMS) fabricated in Si by lithographic masks can also be used to make DMs with a high density of actuators. A segmented mirror with independent segments, each actuated by three actuators for tip/tilt and piston is used for large DMs that are meant to move fast. Non-ferroelectric actuators can also be used where voice coils produce a magnetic field that displaces electrodes in contact with a facesheet continuous reflective membrane. This is the technology behind the DM used for the experiments in Sec.5.1.1.

To model a DM, its influence functions are needed. The influence functions are the spatial distributions $D_i(x,y)$ of the deformation due to one actuator being poked to one unit of stroke at a time. Assuming linearity and minimum coupling between the actuators, the shape a DM with M actuators activated takes is

$$D(x,y) = \sum_{i=1}^{M} a_i D_i(x,y), \tag{2.62}$$

where a_i is the command sent to actuator i. Once the number of usable subapertures of the WFS, N, is set depending on the brightness of available guide stars, the number of degrees of freedom of the DM, M, needs to be chosen such that $M \geqslant N$ to make use of all the information acquired by the sensor.

Worth mentioning is that, even with a high actuator count, facesheet mirrors have eigenmodes different from those of a turbulent wavefront, i.e., Karhunen-Loéve polynomials (see Sec. 2.1.4). The mismatch will cause a fitting error that depends on the modes of the mirror.

2.2.3 Performance metrics and low-order adaptive optics (LOAO)

Given the turbulence strength D/r_0, two parameters dictate the specifications of the AO system to be used. Namely, the coherence time τ_0 and the isoplanatic angle θ_0.

An AO system is limited by the number of subapertures it can correct for and its sky coverage. While the limit on the degrees of freedom was set in the past by the computational power accessible to the controller and the wavefront reconstructor, it is now the brightness of the guide star available near targets of interest that determines how much correction is attainable. Laser guide stars can help overcome the isoplanatism limit when the demanded FoV is small enough, but the cone effect restricts a full correction unless multiple stars are used. ExAO systems are therefore limited to observing narrow fields like circumstellar discs with bright enough host stars to guide the correction. The correction possible with an SCAO system is consequently, most of the time, only partial. With only tip and tilt corrected, the residual mean square error in the corrected wavefront is (Noll, 1976; N. A. Roddier, 1990)

$$\sigma_3^2 = 0.134 \left(\frac{D}{r_0}\right)^{5/3}. \tag{2.63}$$

With the first N Zernike modes corrected, the error is

$$\sigma_N^2 \approx 0.2944 N^{-\sqrt{3}/2} \left(\frac{D}{r_0}\right)^{5/3}, \tag{2.64}$$

for large N, where the index N follows Noll's convention. The rms residual error, therefore, becomes negligible ($\sigma < 1$ rad) when the number of corrected modes $N \geqslant (D/r_0)^2$.

Essentially, the control loop rejects the low temporal frequency fluctuations where the frequency f_C at which this rejection reaches one-half of its maximum power is defined as the loop's bandwidth. The temporal error due to this limited bandwidth is a function of the ratio of f_G to that bandwidth

$$\sigma_\tau^2 = \alpha \left(\frac{f_G}{f_C} \right)^{5/3}, \tag{2.65}$$

where the constant α depends on the design of the control loop. It has a value $\alpha = 1$ for a simple RC circuit and $\alpha = 0.191$ for an ideal filter with a sharp cutoff.

Available nowadays are general-purpose AO systems that are pre-engineered with generic control software and can operate with real time computers (RTCs) running at 5 kHz speed. Such low-cost LOAO systems make it possible for mid-size telescopes to become partially adaptive ($\sigma \sim 2$ rad after correction) and thus host astrophotonic instruments where the bridging from the few-mode to the single-mode regime can be achieved with a reasonably sized photonic lantern as further discussed in the next chapters.

Chapter 3

THEORY OF WAVEGUIDES, INTEGRATED OPTICS AND COUPLING

As introduced in Sec. 1.3, astrophotonics concerns instruments that manipulate starlight in and between optical waveguides made of dielectric structures of contrasting refractive indices that confine and carry electromagnetic energy. This is possible by virtue of total internal reflection. A typical waveguide has a medium of refractive index n_1 embedded in a medium of refractive index $n_2 < n_1$. A light ray entering the waveguide can remain trapped inside the high index medium before it emerges at the opposite end.

In astronomical instruments, the delivery of starlight from the focal plane to astrophotonic components is done using cylindrical step-index optical fibers. Furthermore, many astrophotonic devices involve cylindrical waveguides as well, e.g., DBCs, photonic lanterns, and FBG OH filters. Therefore, the light phenomenon in such structures is the focus of the following two sections.

3.1 Ray picture of multimode waveguides

An optical fiber is a cylindrical waveguide composed of highly transparent dielectric materials like fused silica glass (SiO_2) of high purity. The inner-most layer is a central core surrounded by cladding with a lower refractive index. Layers of polymer for mechanical protection follow as required by the application. In geometrical optics, rays incident on the core-cladding interface at angles greater than a certain critical angle undergo multiple total internal reflections and are, therefore, guided through the structure.

The geometry of a step-index fiber is shown in Fig. 3.1. The core is circularly symmetric of radius a, surrounded by the cladding, which is usually large enough to be assumed unbounded. In most widely used fibers, the refractive index contrast

$$\Delta \equiv \frac{n_1^2 - n_2^2}{2n_1^2} \approx \frac{n_1 - n_2}{n_1} \ll 1, \tag{3.1}$$

since the indices of the two materials differ only slightly. Doping by materials like boron or germanium has been the industry's method of choice for altering the

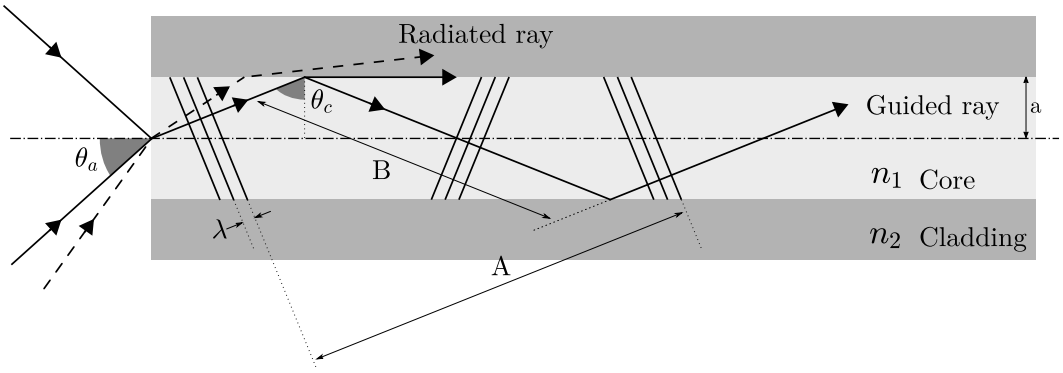

Figure 3.1: Total internal reflection in one dimension in an optical fiber. Only the waves that interfere constructively with their reflections are sustained throughout the structure. The distance A, the original wave travels before it reaches its twice reflected counterpart, needs to differ by exactly an integer multiple of 2π from the distance B, traveled by the reflected wave for that set of waves to be guided.

refractive index.

A ray entering the fiber at the air-core interface with an angle θ_a gets refracted and reaches the core-cladding interface making an angle θ_c with the optical axis. Since $n_1 > n_2$, the ray incident at the core-cladding interface will refract away from the normal towards the surface, and when the incidence angle is large enough, total internal reflection takes place. Snell's law is applied to calculate the critical angle beyond which the reflection occurs and the acceptance angle θ_a at the air-core interface below which the rays are guided. With air's refractive index taken equal to one, $\sin\theta_a = n_1 \sin\overline{\theta_c} = n_1\sqrt{1-\cos^2\overline{\theta_c}}$. The refraction angle at total internal reflection is 90°, which leads to $\cos\overline{\theta_c} = \sin\theta_c = n_2/n_1$ and therefore $\sin\theta_a = \sqrt{n_1^2 - n_2^2}$. This is defined as the numerical aperture of the fiber

$$NA \equiv \sqrt{n_1^2 - n_2^2}, \tag{3.2}$$

in analogy with the light-gathering angle of bulk optics. Ideally, for straight undisturbed fibers, the light exiting the fiber is also within a cone of angle θ_a. However, effects like focal ratio degradation (FRD) and modal noise cause an increase in the exit angle, as discussed later in Sec. 3.2.1.

This ray picture, being a geometrical theory of light, is surely approximate and only valid, strictly speaking, as $\lambda \to 0$. It also becomes complicated when extended into the third dimension since only the rays that cross the fiber axis, i.e., meridional rays, remain confined to the same plane. Skew rays rotate every time they reflect,

making it harder to track their phase progression. A wave theory of optical fibers is, therefore, necessary and is presented in the next section.

3.2 Wave picture of waveguides

The ray optics picture in Sec. 3.1 is very helpful for getting an insight into the propagation of light through fibers, but it fails at explaining the propagation through SMFs and relatively small MMFs.[1] Taking a closer look, one finds that only a discrete set rather than all angles inside an acceptance cone results in sustained waves propagating throughout. The spatial distributions in the transverse plane of the fields associated with these angles are the modes of the fiber. The modes are solutions of the source-free Maxwell equations that satisfy the boundary conditions set by the geometry as derived below.

In the electromagnetic theory of light, the field is described by two temporally and spatially varying vector fields, i.e., the electric $\vec{\mathcal{E}}(\vec{r},t)$ and the magnetic $\vec{\mathcal{H}}(\vec{r},t)$ fields. Based on the experimental findings of pioneers before him, Maxwell formulated four partial differential equations that relate the functions of these fields in space and time to each other. Appendix C gives a quick reference to Maxwell's equations in free space and source-free media. The derivation of the scalar wave equation is also given.

The partial time derivatives of the fields are simplified in the case of linear, nondispersive, homogeneous, and isotropic media. The monochromatic Maxwell's equations of the complex amplitudes are

$$\nabla \times H = i\omega\epsilon E, \tag{3.3}$$

$$\nabla \times E = -i\omega\mu H, \tag{3.4}$$

$$\nabla \cdot D = 0, \tag{3.5}$$

$$\nabla \cdot B = 0. \tag{3.6}$$

Differentiating Eq. (C.13) twice with respect to time and substituting in the wave equation Eq. (C.12), the *Helmholtz equation* (Born et al., 2013) is obtained

$$\nabla^2 U(\vec{r}) + k^2 U(\vec{r}) = 0, \tag{3.7}$$

[1] Known henceforth as few-mode fibers (FMFs).

where $U(\vec{r})$ can be the complex amplitude of any of the components of $\vec{E}$ or $\vec{H}$ and $k = \omega\sqrt{\epsilon\mu} = nk_0$ is the wavenumber in the medium. The factor by which light slows down in a medium, $n = c_0/c$, is recognized as the refractive index of that medium.

3.2.1 Weak guidance and circular fibers

The solutions to Eq. (3.7) that satisfy the boundary conditions are the sought-after modes of the fiber. Those are six equations, one for each of the three components of E and H. The exact solutions of these equations give the mode configurations known as TE, TM, HE, and EH. Since Eq. (3.7) is a vector partial differential equation that couples the x and y components of U (U_x and U_y), the solutions do not have simple polarization states. They require a lengthy algebraic manipulation with messy labeling that is listed in specialized books and are, in general, quite involved.[2] A useful approximation is possible for the case of weakly guiding fibers, i.e., $\Delta \ll 1$, which is the case for most fibers in astronomy. The components U_x and U_y detach and solutions for the resulting scalar wave equation, known as the linearly polarized (LP) modes, can be found for each one separately. For this case, the superposition of four modes of the TE, TM, HE, and EH families that have nearly identical propagation constants and cutoff frequencies under the weak guidance condition results in a two-fold or a four-fold degenerate mode (Gloge, 1971).

In the ray picture, the guided rays are paraxial in such a fiber. In the wave picture, this means that the guided waves are approximately transverse electromagnetic (TEM), with the longitudinal components of the fields much smaller than the transverse components. Additionally, in a cylindrical fiber, the refractive index n is azimuthally invariant and changes only in the radial direction, i.e., $n = n(\rho)$. For a step-index fiber, Eq. (3.7) is obeyed in each of the two regions, the core and the cladding. The use of cylindrical coordinates is now in order, given the symmetry of the problem. In cylindrical coordinates, $U = U(\rho, \phi, z)$ and the Helmholtz equation becomes

$$\partial_{\rho\rho}U + \frac{1}{\rho}\partial_{\rho}U + \frac{1}{\rho^2}\partial_{\phi\phi}U + \partial_{zz}U + n^2k_0^2U = 0. \tag{3.8}$$

The dependencies of the fields components on the spatial coordinates could be constrained by the symmetries of the situation at hand. The waves are propagating in the z direction along the fiber axis, and therefore U would have a harmonic

[2] See, for instance, Black et al. (2010).

dependence of the form $e^{-i\beta z}$, where β is the rate of phase accumulation in z known as the *propagation constant*. In an MMF, each field component is, in fact, a sum of modes

$$U(\rho,\phi,z)=\sum_i u_{\rho,i}(\rho)u_{\phi,i}(\phi)e^{-i\beta_i z}, \tag{3.9}$$

where the dependencies of U on ρ, ϕ, and z were separated into $u_{\rho,i}$,$u_{\phi,i}$ and $e^{-i\beta_i z}$, respectively. Given the linearity, each mode in Eq. (3.9) is by itself a solution to Eq. (3.8). Additionally, for paraxial waves, the field is not dependent on z, and the term $\partial_{zz}U$ drops from the Helmholtz equation. This gives

$$u_\phi\frac{\mathrm{d}^2u_\rho}{\mathrm{d}\rho^2}+\frac{1}{\rho}u_\phi\frac{\mathrm{d}u_\rho}{\mathrm{d}\rho}+\frac{1}{\rho^2}u_\rho\frac{\mathrm{d}^2u_\phi}{\mathrm{d}\phi^2}+n^2k_0^2u_\rho u_\phi=0, \tag{3.10}$$

which can be rearranged to get

$$\frac{\rho^2}{u_\rho}\frac{\mathrm{d}^2u_\rho}{\mathrm{d}\rho^2}+\frac{\rho}{u_\rho}\frac{\mathrm{d}u_\rho}{\mathrm{d}\rho}+\rho^2n^2k_0^2=-\frac{1}{u_\phi}\frac{\mathrm{d}^2u_\phi}{\mathrm{d}\phi^2}. \tag{3.11}$$

Since one side of Eq. (3.11) depends only on ρ while the other depends only on ϕ, the two sides must equal a constant as they vary independently. This separates Eq. (3.11) into two equations (Buck, 2004)

$$\frac{\mathrm{d}^2u_\phi}{\mathrm{d}\phi^2}+l^2u_\phi=0, \tag{3.12}$$

and

$$\frac{\mathrm{d}^2u_\rho}{\mathrm{d}\rho^2}+\frac{1}{\rho}\frac{\mathrm{d}u_\rho}{\mathrm{d}\rho}-\left(\frac{l^2}{\rho^2}-n^2k_0^2\right)u_\rho=0, \tag{3.13}$$

where l^2 is the designation given to the constant that both sides equal. Equation (3.12) has the solutions

$$u_\phi=\begin{cases}\cos(l\phi)\\ \sin(l\phi)\end{cases}\quad l=0,\pm1,\pm2,\ldots \tag{3.14}$$

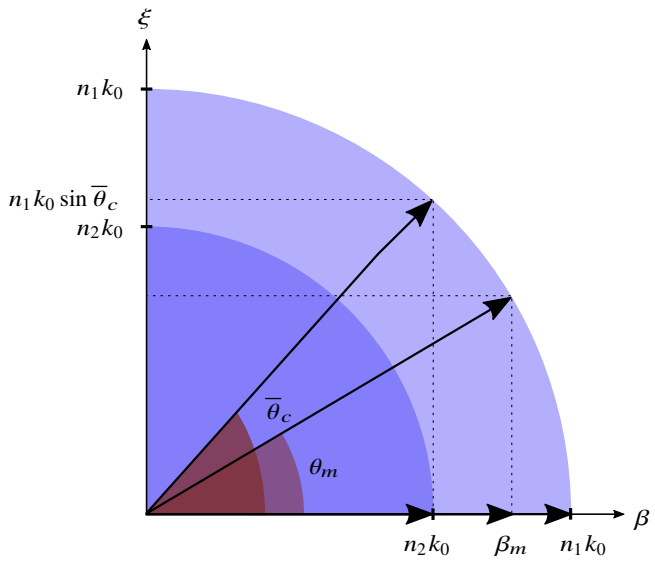

Figure 3.2: Simplified picture of the propagation vectors of guided modes. Propagation constants, $\beta_m = n_1 k_0 \cos\theta_m$, take values between $n_1 k_0$ for the fundamental mode and $n_2 k_0$ for the highest order mode. For weakly guiding fibers, the shell between the two quarter circles is thin leading all modes to have paraxial wavevectors with a small transverse component.

where l must be an integer because the fields must close onto themselves azimuthally after a rotation of 2π.

Solutions to Eq. (3.13) would give the radial form of the mode, but a range within which the free parameters are allowed to vary must be identified first. In the wave picture, the rays serve the purpose of defining the propagation direction of the waves. From the diagram in Fig. 3.2, $\beta = n_1 k_0 \cos\theta$, where θ is the angle the ray makes with the fiber axis. For the waves to be guided, $0 < \theta < \overline{\theta_c}$. Hence, the propagation constant must lay between the wavenumbers in the cladding and the core, i.e., $k_2 = n_2 k_0 < \beta < n_1 k_0 = k_1$. These two conditions may be rewritten by first defining (Snyder, 1974)

$$\xi^2 = k_1^2 - \beta^2, \tag{3.15}$$

$$\chi^2 = \beta^2 - k_2^2. \tag{3.16}$$

The guiding condition then demands that ξ^2 and χ^2 are both positive. The differential equation Eq. (3.13) is separated into two parts, one for the core and the other for the cladding

$$\begin{aligned}\frac{\mathrm{d}^2 u_\rho}{\mathrm{d}\rho^2} + \frac{1}{\rho}\frac{\mathrm{d}u_\rho}{\mathrm{d}\rho} + \left(\xi^2 - \frac{l^2}{\rho^2}\right) u_\rho = 0, \quad \rho \leqslant a, \\ \frac{\mathrm{d}^2 u_\rho}{\mathrm{d}\rho^2} + \frac{1}{\rho}\frac{\mathrm{d}u_\rho}{\mathrm{d}\rho} - \left(\chi^2 + \frac{l^2}{\rho^2}\right) u_\rho = 0, \quad \rho \geqslant a,\end{aligned} \tag{3.17}$$

where a is the core radius. These differential equations have solutions in the family of Bessel functions that do not diverge at the center or as $\rho \to \infty$. The solutions are hence of the form

$$u_\rho(\rho) = \begin{cases} AJ_l(\xi\rho), & \rho \leqslant a \\ BK_l(\chi\rho), & \rho \geqslant a, \end{cases} \tag{3.18}$$

where $J_l(\cdot)$ is the Bessel function of the first kind and order l while $K_l(\cdot)$ is the modified Bessel function of the second kind and order l. The scaling constants ξ and χ are chosen such that the solution is continuous across the core-cladding interface. The parameter ξ determines the oscillation rate of the radial component of the field distribution, $u(\rho)$, in the core, while χ serves a similar purpose in the cladding. Bringing in the axial and azimuthal dependencies, the complete field in the core is

$$U_1(\rho,\phi,z) = \begin{cases} AJ_l(\xi\rho)\cos(l\phi)e^{-i\beta z}, & \rho \leqslant a, \\ AJ_l(\xi\rho)\sin(l\phi)e^{-i\beta z}, & \rho \leqslant a, \end{cases} \tag{3.19}$$

and in the cladding

$$U_2(\rho,\phi,z) = \begin{cases} BK_l(\chi\rho)\cos(l\phi)e^{-i\beta z}, & \rho \geqslant a, \\ BK_l(\chi\rho)\sin(l\phi)e^{-i\beta z}, & \rho \geqslant a. \end{cases} \tag{3.20}$$

Summing Eq. (3.15) and Eq. (3.16), one gets a constant

$$\xi^2 + \chi^2 = (n_1^2 - n_2^2)k_0^2 = NA^2 k_0^2, \tag{3.21}$$

that is independent of the mode in question. This implies that, for each mode, the rate of oscillations of $u(\rho)$ in the core is inversely proportional to that in the cladding. The two scaling parameters can now be normalized as

$$\xi' = a\xi, \tag{3.22}$$

$$\chi' = a\chi, \tag{3.23}$$

to give their values in units of core radii. The sum of their squares is again a constant for any given fiber at a given wavelength whose square root

$$V = \sqrt{\xi'^2 + \chi'^2} = ak_0NA, \tag{3.24}$$

has significant importance. This is the *normalized frequency* or the V-number of a fiber that controls the number of modes supported at any given wavelength. In terms of the normalized constants, the fields are

$$U_1(\rho,\phi,z) = \begin{cases} AJ_l\left(\frac{\xi'\rho}{a}\right)\cos(l\phi)e^{-i\beta z}, & \rho \leqslant a, \\ AJ_l\left(\frac{\xi'\rho}{a}\right)\sin(l\phi)e^{-i\beta z}, & \rho \leqslant a, \end{cases} \tag{3.25}$$

$$U_2(\rho,\phi,z) = \begin{cases} BK_l\left(\frac{\chi'\rho}{a}\right)\cos(l\phi)e^{-i\beta z}, & \rho \geqslant a, \\ BK_l\left(\frac{\chi'\rho}{a}\right)\sin(l\phi)e^{-i\beta z}, & \rho \geqslant a. \end{cases} \tag{3.26}$$

The scaling factors A and B are not necessarily the same for the electric and the magnetic fields, but each is linearly related to its other field counterpart. To determine their values, the continuity conditions at the interface

$$U_1(\rho = a,\phi) = U_2(\rho = a,\phi) \tag{3.27}$$

$$\partial_\rho U_1(\rho,\phi)|_{\rho=a} = \partial_\rho U_2(\rho,\phi)|_{\rho=a}, \tag{3.28}$$

are imposed. Substituting for $U_1(a,\phi)$ and $U_2(a,\phi)$ from Eq. (3.25) and (3.26)

$$AJ_1\left(\xi'\right) = BK_1\left(\chi'\right), \tag{3.29}$$

$$A\frac{\xi'}{a}J_1'\left(\xi'\right) = B\frac{\chi'}{a}K_1'\left(\chi'\right). \tag{3.30}$$

Now dividing Eq. (3.30) by Eq. (3.29) to get

$$\frac{\xi' J_1'(\xi')}{J_1(\xi')} = \frac{\chi' K_1'(\chi')}{K_1(\chi')}. \tag{3.31}$$

Applying the identities

$$J_l'(x) = \pm J_{l\mp1}(x) \mp l\frac{J_l(x)}{x}, \tag{3.32}$$

$$K_l'(x) = -K_{l\mp1}(x) \mp l\frac{K_l(x)}{x}, \tag{3.33}$$

yields the *characteristic equation*

$$-\frac{\xi' J_{l+1}(\xi')}{J_l(\xi')} + \frac{\chi' K_{l+1}(\chi')}{K_l(\chi')} = 0. \tag{3.34}$$

With ξ' and χ' related to V by $V^2 = \xi'^2 + \chi'^2$, the characteristic equation is a function of one unknown for a given fiber's V and mode's azimuthal order l. Equation (3.34) may be solved numerically or graphically to find the values of ξ' that satisfy it for each value of l. With all the values of ξ' known, the scaling parameters ξ and χ, the propagation constant β and therefore the spatial distribution of the modes may all be determined using Eq. (3.21), Eq. (3.22), and Eq. (3.23).

A proof that all six fields components are attained, given only two, by the formulation above is presented in App. C.

The modes of weakly guiding fibers

From the χ' versus ξ' plots of the two terms of Eq. (3.34), one sees that more solutions, i.e., intersections, for the characteristics equation exist as V increases. The J term consists of multiple branches intersecting the abscissa at the roots of $J_{l+1}(\chi')$ while the K term is a monotonically decreasing curve that intersects the branches of the J term until it reaches the $\chi' = 0$ axis at $\xi' = V$. The number of supported modes is, therefore, limited by the number of roots in the interval $0 < \xi' < V$ (see Fig. 3.3 for the case of $l = 0$). The maximum value of V below which a given mode is not supported is known as the *cutoff frequency* of that mode. For $l = 0$, the J_1 term has its smallest root at $\xi' = 0$. This is the fundamental mode of the fiber, and it is always supported for any non-vanishing V. For an arbitrarily small $V \to 0$, $\beta \to k_0 n_2$ and the wave becomes poorly guided with most of the

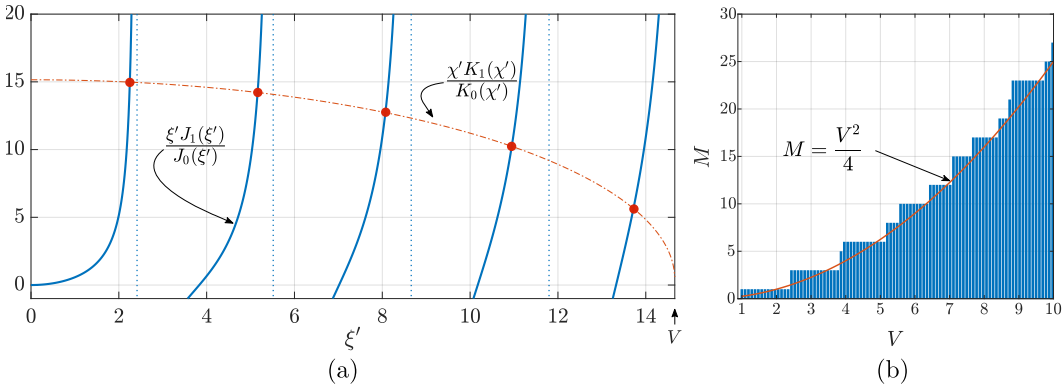

Figure 3.3: (a) The two arms of the characteristics equation (Eq. (3.34)) for $l = 0$ and $V = 14.67$. Every intersection is a solution and, therefore, a fiber mode. (b) Number of LP modes plotted against V. Only one polarization state is accounted for. Also plotted is the approximation formula for $V \gg 1$.

field distribution in the cladding. With V increasing, only this fundamental mode is supported as long as $V \leqslant 2.405$ (for step-index fibers). After that, the next solution corresponding to a higher-order mode exists.

Each mode, including the fundamental mode, has two polarization states, e_x and e_y, and must therefore be counted twice. Furthermore, for MMFs, every mode with $l > 0$ must be counted twice to account for the corresponding mode with $\sin(l\phi)$ (see Eq. (3.25) and Eq. (3.26)). In the ray picture, the $l = 0$ modes correspond to meridional rays that pass through the fiber axis upon every reflection, while the $l \neq 0$ modes correspond to skew rays.

The regime where the fiber supports a number of modes $\in [2, \sim 100]$ is designated as the few-mode regime. Most geometrical approximations followed for large MMFs do not hold for FMFs justifying their special classification. This is the case for the fibers considered in this work.

Single-mode fibers (SMFs)

The fundamental mode of an SMF is the first solution that has $l = 0$ (leftmost solution in Fig. 3.3a), and it can be fairly approximated by a Gaussian function for fibers with $V > 1.2$. The approximation is accurate to within 1% of error at $V = 2.4$ (Marcuse, 1978)

$$u(\rho) = \sqrt{\frac{2}{\pi {w_0}^2}} \exp\left(-\frac{\rho^2}{{w_0}^2}\right), \tag{3.35}$$

where w_0, the *mode field radius*, is the radial distance from the core center to the point where the field drops to $1/e$ of its peak value. A useful formula that approximates the mode field radius in terms of a and V is the empirical Marcuse expression

$$w_0 \approx a\left(0.65 + \frac{1.619}{V^{3/2}} + \frac{2.879}{V^6}\right). \tag{3.36}$$

Marcuse's Gaussian fit is the one with the maximum inner product with the exact mode. Other more accurate approximations were given by Yang et al., 2013. From Eq. (3.36) one sees that the spot radius decreases with increasing V resulting in a field of increasing confinement in the core.

With only one supported mode, SMFs act as spatial filters admitting only normally incident plane waves to propagate throughout. No extra modes means that there is not a chance for the coupled light to change its state, and it always exists in the fiber as a coherent plane wave regardless of the conditions along the fiber. This is not the case for MMFs.

Multimode fibers (MMFs)

In an MMF, the number of modes increases with V, and for small V values, all the modes could be found in reasonable computing time. Otherwise, for fibers with much larger V that support thousands of modes or more, one is often interested in estimating the modes count. A formula that approximates the number of modes for fibers with $V \gg 1$ (as shown in Fig. 3.3b) is

$$M = \frac{V^2}{2}, \tag{3.37}$$

where multiplicities due to both degeneracy and polarization states are accounted for.

Compared to SMFs, the several modes of an MMF have diverse field distributions and accumulate phase at different propagation constants. This causes a pseudorandom interference between the modes, known as *modal noise*, when certain factors, e.g., strain, temperature, and composition, which can shift the phase of each mode differently vary along the fiber. Light initially coupled into a certain mode can then couple into a neighboring mode after undergoing a random phase shift causing the

superposition of the fields at the output to have a random pattern uncorrelated to that at the input. A field coupled into the lowest order modes at the input can populate all the supported modes as it propagates causing the output beam's focal ratio to degrade in an effect called FRD. The dependence of these fluctuations on wavelength generates a spectral noise if the output pattern of the fiber is to be dispersed. This presents a problem for high-resolution spectroscopy that needs to be addressed using scramblers or photonic lanterns (Benoit et al., 2020).

3.3 Losses in optical fibers

Aside from modal noise, many other non-uniformities can cause the behavior of light in a fiber to deviate from that predicted by the theory. Bends in an SMF cause the wavefronts, which are otherwise normal to the fiber axis all over the fiber cross-section, to rotate, inducing a phase velocity gradient between the parts closer and the parts further from the center of curvature (Snyder et al., 2012). When the bending exceeds a certain limit where the phase velocity in the cladding away from the center of curvature becomes larger than the speed of light, the mode must become radiative. For MMFs, this is easily modeled by considering the ray picture and taking all modes that do not locally satisfy the condition for the total internal reflection to be radiation modes.

Another effect overlooked in the theory presented so far is that of *leaky modes*. A leaky mode is one that enters the fiber below its cutoff frequency and therefore undergoes partial reflections at the core-cladding interface radiating away its energy as it propagates. Within a short distance near the fiber input, the inclusion of these modes is necessary to calculate the complete field inside and outside the fiber structure (Snyder et al., 1974).

Furthermore, guided modes are also attenuated in straight fibers by impurities and irregularities in the material. Scatterers redistribute the energy between the guided and radiative modes leading to losses, as well as noise, that increases with the length of the fiber (Snyder, 1974). These effects are not included in the models of Ch. 4, but they explain the deviations seen in the experiments of Ch. 5 as presented later.

3.4 Waveguide arrays

As seen in Sec. 3.2, the wave picture of the total internal reflection phenomenon reveals that the field always has a non-zero magnitude in the cladding as demanded

by Maxwell's equations and the continuity conditions. For the sustained modes, this transmitted wave across the interface, known as the *evanescent wave*, has limited spatial penetration that decays exponentially depending on the V-number and the mode in question.[3] Therefore, when the cores of two waveguides are brought sufficiently close together, their modes overlap even though their cores do not, and the field in one can excite a wave in the other transferring optical power between them.

Several astrophotonic devices, e.g., discrete beam combiners, transition regions of photonic lanterns, and reformatters, feature an array of waveguides — usually all of which are single mode — that are in close proximity such that their modes overlap. Light in one waveguide in the array can then couple to the others via evanescent coupling. One way to analyze such structures is to consider them as a bulk of different index regions and solve Maxwell's equations under the boundary conditions set by symmetry and continuity similar to what has been done for standalone fibers. The modes of the entire structure, known as the *supermodes*, are in this case different from the fundamental modes of the isolated waveguides. Except for the simplest cases, no analytical solutions exist, and specialized computer algorithms, e.g., the *beam propagation method (BPM)*, are required to solve the equations numerically on a grid of discrete points.

When dealing with identical weakly guiding single-mode waveguides that are weakly coupled to each other, a simplified approach, known as the *coupled mode theory (CMT)* (Little et al., 1995), can approximate the solutions. Here the effect that one waveguide has on the mode profile of a nearby one is neglected, and the mode is assumed to maintain its distribution with only the amplitude changing due to power being transferred to the neighborhood. Under these assumptions, a system of first-order differential equations can be written that describes the axial evolution of the amplitudes of the modes at each waveguide. For the simplest case of two single-mode waveguides, the coupled-mode equations are (Saleh et al., 2019; Snyder et al., 2012)

$$\frac{\mathrm{d}a_1}{\mathrm{d}z} = -iC_{21}e^{i(\beta_1-\beta_2)z}a_2(z), \tag{3.38a}$$

$$\frac{\mathrm{d}a_2}{\mathrm{d}z} = -iC_{12}e^{-i(\beta_1-\beta_2)z}a_1(z), \tag{3.38b}$$

[3] More accurately, it follows a modified Bessel function of the second kind as shown in Eq. (3.26).

where a_1 and a_2 are the peak field amplitudes while C_{21} and C_{12} are the coupling coefficients given by

$$C_{21} = \frac{k_0^2}{2\beta_1}(n_2^2 - n^2) \iint \mathrm{d}x\mathrm{d}y u_1(x,y)u_2(x,y), \tag{3.39a}$$

$$C_{12} = \frac{k_0^2}{2\beta_2}(n_1^2 - n^2) \iint \mathrm{d}x\mathrm{d}y u_2(x,y)u_1(x,y), \tag{3.39b}$$

where each integration is evaluated over the entire plane and the fields u_1 and u_2 are appropriately normalized. For identical waveguides with $n_1 = n_2$ and $\beta_1 = \beta_2$, $C_{21} = C_{12} = C$. The solution to Eq. (3.38) can be immediately guessed

$$a_1(z) = a_1(0)\cos(Cz) - ia_2(0)\sin(Cz), \tag{3.40a}$$

$$a_2(z) = -ia_1(0)\sin(Cz) + a_2(0)\cos(Cz). \tag{3.40b}$$

The algebraic formulation becomes complicated for arrays of more than two waveguides, but if they are all identical and arranged symmetrically, matrix algebra could be used to write and solve the differential equations. This takes the form

$$\frac{\mathrm{d}\vec{A}}{\mathrm{dz}} = -i\kappa\mathbf{C}\vec{A}, \tag{3.41}$$

where κ is the coupling coefficient, $\vec{A}$ is an $N \times 1$ vector that contains the amplitudes of the fields at the N waveguides of the array and $\mathbf{C}$ is an $N \times N$ coupling matrix that only depends on the arrangement and has the information on how the waveguides are related to each other in the array. In an array where coupling is only between each waveguide and its nearest neighbor, e.g., a hexagonal array (see Fig. 3.4b), the matrix $\mathbf{C}$ has ones only in the entries $\mathbf{C}_{i,j}$ where waveguides i and j are nearest neighbors and zeros everywhere else. If the arrangement has next-nearest neighbors, e.g., a square array (see Fig. 3.4a), for which coupling is weaker than that between nearest neighbors, then a coefficient $0 < \kappa_1/\kappa_2 < 1$ needs to be entered for these pairs. Numerically, the system of differential equations is approximated by a system of difference equations that can be solved using a Crank-Nicolson scheme. This is left for Sec. 4.2 on modeling matters.

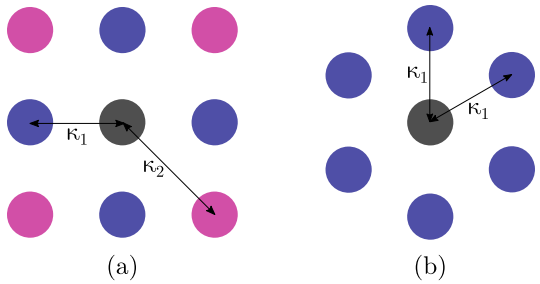

Figure 3.4: Coupling in a waveguide array. (a) In a square array, two coupling coefficients κ_1 and κ_2 for nearest neighbors and next-nearest neighbors, respectively, characterize the array. (b) In a hexagonal array, only one coefficient is required since next-nearest neighbor coupling is negligible.

3.5 Slowly varying waveguides and tapers

Born and Fock formulated the adiabatic theorem in quantum mechanics as (Born et al., 1928; Faddeev, 2019)

> A physical system remains in its instantaneous eigenstate if a given perturbation is acting on it slowly enough and if there is a gap between the eigenvalue and the rest of the Hamiltonian's spectrum.

The transition region of a photonic lantern exhibits a wave guiding structure that is longitudinally variant. Along the taper, the core diameter varies continuously with distance z. In the ray picture, the power associated with a bound ray remains constant, but the axial distance between successive reflections is no longer constant (Snyder et al., 2012). A rays treatment of MMFs is possible as long as the continuous non-uniformity is slowly varying over distances of the order of the wavelength. Moreover, if the non-uniformity varies sufficiently slowly over a ray half-period, the *adiabatic invariant* remains approximately constant along the fiber. The invariant is given by

$$\int_{z_p(z)} \mathrm{d}\rho n(\rho, z) \frac{\mathrm{d}\rho}{\mathrm{d}s}, \tag{3.42}$$

where the integration path is over a ray half-period, $z_p(p)$, and $\mathrm{d}s$ is the component of length along the ray path. In general, the adiabatic invariant of a physical system is that property that remains approximately constant when a slow perturbation is introduced between two endpoints. This is true even when the ratio of the core radii of a taper is arbitrarily large, but the taper angle needs to be small everywhere.

For SMFs and FMFs, a wave optics treatment is necessary. In general, exact solutions of Maxwell's equations for these tapers do not exist but, as intuition suggests, the modes of the longitudinally uniform fiber should be accurate approximations to the solution of Maxwell's equations if the taper is varying slowly enough (Snyder et al., 2012) in accordance with the adiabatic theorem. These are known as the *local modes* and while they change profile, the power of each is conserved along the taper. The phase accumulation rate is not constant, but since the variation is slow, it can be approximated by an integral. The local mode has the spatial dependence

$$U = u_j\left(\rho, \beta_j(z)\right) \exp\left[i \int_0^z \mathrm{d}z' \beta_j(z')\right], \tag{3.43}$$

where β_j is the local propagation constant of the jth mode and u_j is the solution of the wave equation with the refractive index profile at z. The power in a local mode is approximately conserved since the change in the mode profile occurs over large distances. This is why the argument above is known as the *adiabatic approximation*.

The slow variation condition needs to be quantified. This is given by the total field in an equivalent uniform fiber. The total field is a superposition of the modes and, therefore, it changes over a distance due to the phase differences between the constituent modes. The largest beat length (or coupling length) occurs between the two nearest neighboring modes that have the two closest propagation constants since the beat length between modes 1 and 2 is given by

$$z_b = \frac{2\pi}{\beta_1 - \beta_2}. \tag{3.44}$$

The taper length thus must be long compared to z_b for the local mode approximation to hold. The high order modes in an MMF have the closest separation in terms of propagation constants, and separation decreases as V increases. However, the ray optics treatment given above suffices to determine the maximum taper angle before adiabaticity is destroyed. The change in the local mode distribution varies as $z_b \partial_z n^2$ and qualitatively, using Eq. (3.44), the adiabaticity criterion is (Black et al., 2010)

$$\left|\frac{2\pi}{\beta_1(z) - \beta_2(z)} \frac{1}{n^2} \partial_z n^2\right| \ll 1. \tag{3.45}$$

An exact criterion can be derived using an adaptation of the CMT (cf. Eq. (3.38)) known as the *coupled local-mode theory* that determines the exchange of power between each local mode and the radiation field (Snyder et al., 2012)

$$\left|\frac{2\pi}{\beta_1-\beta_2}\frac{\mathrm{d}\rho}{\mathrm{d}z}\int_A \mathrm{d}A U_1\partial_z U_2\right| \ll 1, \tag{3.46}$$

where the non-uniformity in the refractive index profile here is only due to the change in core diameter. This is the mathematical form of Born and Fock's adiabatic theorem in the context of waveguide modes.

In light of the quantum mechanical analogy, the propagation constants are the eigenvalues of the modes. The adiabatic theorem then states that slowness is when (Martínez-Garaot et al., 2017)

$$\left|\frac{\langle U_1|\partial_z U_2\rangle}{\beta_1-\beta_2}\right| \ll 1, \tag{3.47}$$

where the Hamiltonian here is space- rather than time-dependent as in the original theorem.

This analogy can be taken even further to develop an intuition about the working principle of photonic lanterns. While photons are fundamentally different from electrons, the wavelike behavior of electrons at atomic scales has similarities with that of a photon. A conduction electron in a 1-D periodic lattice experiences a potential caused by the electromagnetic field of the positive ions. They have a wavefunction described by the Bloch function. In the Kronig-Penney model, the potential wells are simplified and made rectangular (Kronig et al., 1931), similar to the index profile of a step-index waveguide array.

The scalar wave equation (Eq. (3.7)) can be rewritten as (Black et al., 1985)

$$\left[\nabla^2 + 2k^2 n_1^2 \Delta\left(\frac{\xi'^2}{V^2} - f(\rho)\right)\right]\psi(\rho) = 0, \tag{3.48}$$

where $k = 2\pi/\lambda, \xi' = ak(n_1^2 - n_{eff}^2)^{1/2}, V = ak(n_1^2 - n_2^2)^{1/2}$, and $\Delta = \left(1 - n_2^2/n_1^2\right)/2$. The effective index n_{eff} of the mode equals β/k. In comparison, the time-independent Schrödinger equation for a unit mass particle of energy $\mathfrak{E}$ reads

$$\left[\nabla^2 + \frac{2}{\hbar^2}\left(\mathfrak{E} - Q(\rho)\right)\right]\psi(\rho) = 0, \tag{3.49}$$

where $Q(\rho)$ is the potential well and $\hbar \equiv h/2\pi$. Planck's constant h is therefore analogous to λ, and the energy $\mathfrak{E}$ is analogous to

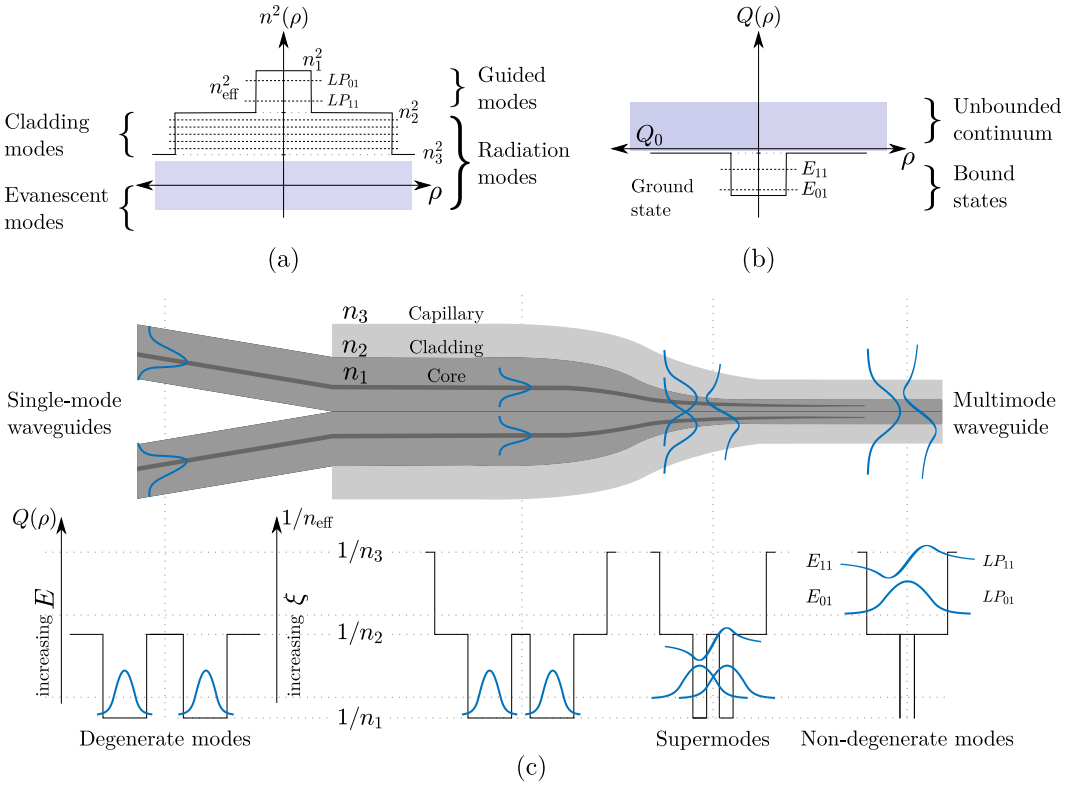

Figure 3.5: Analogy between (a) the refractive index profile in a step-index waveguide structure that supports two non-degenerate modes and (b) the potential in a 1D quantum well. (c) The analogy in (a) and (b) applied to the three regions of a 1×2 photonic lantern.

$$n_1^2 \Delta \xi'^2 / V^2 = \frac{1}{2}[n_1^2 - n_{eff}^2], \tag{3.50}$$

while the potential $Q(\rho)$ is analogous to

$$n_1^2 \Delta f(\rho) = \frac{1}{2}[n_1^2 - n^2(\rho)], \tag{3.51}$$

where $n(\rho) = n_1 \left[1 - 2\Delta f(\rho)\right]^{1/2}$ is the refractive index profile. The quantity in Eq. (3.51) decreases as one approaches $\rho = 0$ in the core from either side, forming a well. The potential energy is therefore analogous to the reciprocal of the refractive index profile, $1/n$.

In the spirit of this analogy, guided modes can take discrete effective index, n_{eff}, values between the index of the cladding and that of the core. Cladding or radiation modes take values from the continuum below the cladding index in the case of an infinite cladding fiber. Values of $n_{eff}^2 < 0$ (n_{eff} is imaginary) correspond to the

leaky modes discussed in Sec. 3.3 analogous to the metastable states of a quantum mechanical system. Figure 3.5 illustrates the analogy between the two systems.

It is now appropriate to explain the working principle of photonic lanterns using this analogy.

3.5.1 Photonic lanterns and adiabatic mode transformation

In its standard form, the single-mode end of the photonic lantern has an array of M decoupled identical SMFs. Collectively, the array is a structure that supports M spatial degenerate modes, known also as the supermodes (Ladouceur et al., 1990). A gradual transition after that, when adiabatic, will allow the supermodes of the array to evolve into the modes of the multimode end. A lossless transition is theoretically possible if the degrees of freedom, i.e., the entropy, do not decrease along the propagation direction. These are, nonetheless, necessary but not sufficient conditions for lossless transformation. One more condition is the correct geometric arrangement of the waveguides, as seen later.

Maxwell's equations do indeed apply to light propagating through structures like photonic lanterns. Solvers that numerically calculate the field at each point on a defined grid based on the initial conditions and propagate it forward in discrete steps using the BPM exist (Spaleniak et al., 2013; Synposys and RSoft Design Group, 1993-2018) but an analogy based on the introduction in Sec. 3.5 can be given to develop an intuition of how photonic lanterns work.

The analogy in Fig. 3.5 is made between a mode-matched photonic lantern and a quantum mechanical system that has M separated narrow potential wells brought together into one wider well that has M energy levels. When operated with monochromatic light, all photons in the photonic lantern have the same energy, unlike the electrons in a potential well. However, the analogy is not made between the energies of the two systems but rather between the energies of the electrons in the wells and the transverse components of the wavevectors ξ of the modes in the waveguides (Leon-Saval et al., 2010). The higher the order of the mode, the longer is its transverse wavevector, as depicted in Fig. 3.2.

The fundamental mode of a single-mode waveguide is analogous to the ground state of the electron in a narrow well. This mode has a high effective index value close to that of the core, and its transverse wavevector ξ is therefore short. When the wells are brought closer together while made narrower, as is the case for the waveguides

in a photonic lantern, the wavefunctions become less localized and spread further beyond the wall (since the well depth is finite). The energy increases all the way to the point where the wavefunctions start to overlap, and the electrons become conduction electrons shared by the atoms of the periodic lattice. The electrons are no longer confined to their initial wells but occupy the energy levels of a single broader potential well. In the photonic case, the fields spread further into the cladding as the core radius (and in turn the V-number) decreases in the transition region. At the multimode end, the energy levels of a lattice are similar to the modes of the larger multimode waveguide, which, when fabricated with fibers, has a lower refractive index of the multimode end core than that of the single-mode end.

Geometry and arrangement of cores

Along the propagation direction in the transition region of a photonic lantern, the cores of the waveguides need to align with the local modes for the adiabatic condition in Eq. (3.47) to hold. Without the waveguides evolving into a geometric arrangement compatible with the local modes upstream, the overlap is poor and light would not couple into the local (super)modes of the structure ahead leading to losses.

For a circular step-index MMF that supports the linearly polarized modes LP_{nm}, the SMFs arrangement that eliminates losses is one with $max(m)$ concentric rings, with $2p+1$ SMFs in each ring where $p = max(n)$ for each radial order m (Fontaine et al., 2012).

Depending on the fabrication method of choice, the SMFs may not be freely arrangeable, and modal losses would be unavoidable for arrangements with large numbers of SMFs as seen below. The large number of modes, however, means that a loss of only a few of the modes might be negligible.[4]

Photonic lanterns fabrication

Photonic lanterns could and have been made by all different fabrication methods that can realize waveguides that exhibit the conditions above for lossless transition. This excludes methods restricted to 2-dimensional planes, e.g., photolithography, but techniques like ULI (Harris et al., 2015) and tapering (Noordegraaf et al., 2009) have been used successfully to fabricate them.

[4]Several works in the literature explored this compatibility further for a wide range of specific arrangements. See, for instance, Fontaine et al. (2012) and J. J. Davenport et al. (2021).

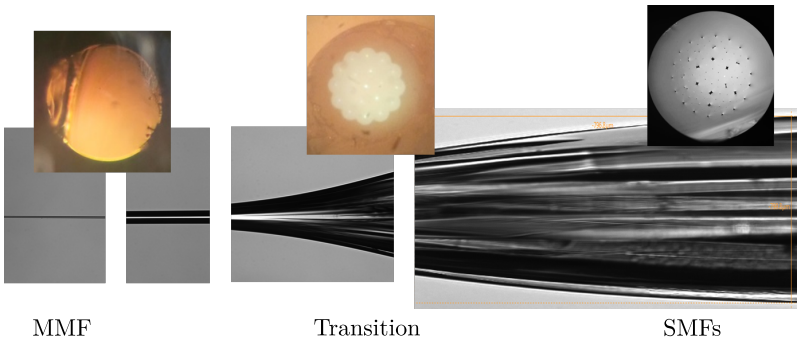

Figure 3.6: Micrographs showing side views and cross-sections of the main regions of a photonic lantern fabricated by a filament fusion splicer.

When tapered in a fusion splicer, the SMFs are stripped down to the cladding and inserted inside an F-doped Si capillary with refractive index n_3 slightly lower than the refractive index of the claddings as depicted in Fig. 3.9. The stack is then heated either by a tungsten filament (Noordegraaf et al., 2012) or a ring CO_2 laser beam before tension is applied from both ends. As shown in Fig. 3.6, the SMFs fuse together as the stack diameter decreases to the point where the cores become too narrow to couple light, and the fused claddings act as the core of the multimode end of the photonic lantern (J. Davenport et al., 2021). The capillary is now the cladding of the multimode end. The arrangement of SMFs inside the capillary needs to be optimized to ensure that they are tightly packed with a high fill factor and therefore will maintain order in accordance with the geometrical requirements above as they are tapered (J. J. Davenport et al., 2021). The same tapering approach has also been used to taper multicore fibers into photonic lanterns where a capillary might not be required (Haynes et al., 2018).

ULI focuses ultrashort laser pulses inside a glass substrate to modify the glass at the focus, increasing the refractive index and hence writing optical waveguides (Thomson et al., 2011). Usually, the substrate is precisely translated relative to the focus to realize waveguides in three dimensions. The dimensions and the design parameters of such a component are given in Ch. 6.

3.6 Coupling theory

Quantifying the amount of light that can be injected (and guided) into a waveguide given the properties of the excitation source is known as the *coupling efficiency*. Coupling from free space using a telescope and how it is affected by the geometry of the aperture and the atmosphere above it are discussed next.

3.6.1 Free space coupling

In general, the optical field propagating in a waveguide is a superposition of the modes supported by the said waveguide. The complex amplitude is (Neumann, 2013)

$$u(x,y,z) = \sum_m a_m u_m(x,y) e^{-i\beta_m z}, \tag{3.52}$$

where u_m is the transverse distribution of the mode m, a_m is its weight, and β_m is its propagation constant. Here the weights $\{a_m\}$ depend on the correlation between the exciting source and the mode m. If only one mode is to be excited with 100% efficiency, the source must perfectly match the distribution of that mode. Since the modes are orthogonal functions, the weight of mode m is given by

$$a_m = \iint \mathrm{d}x\mathrm{d}y u(x,y) u_m(x,y). \tag{3.53}$$

With the proper normalization, the coupling efficiency, defined as the fraction of the total power available at the entrance pupil that couples power into the waveguide, is given by the sum of the power weights $|a_m|^2$, i.e.,

$$\eta_m = \frac{\left|\iint \mathrm{d}x\mathrm{d}y u^*(x,y) u_m(x,y)\right|^2}{\iint \mathrm{d}x\mathrm{d}y \left|u(x,y)\right|^2 \iint \mathrm{d}x\mathrm{d}y \left|u_m(x,y)\right|^2}, \tag{3.54}$$

where * denotes complex conjugation. The integral in the numerator, known as the *overlap integral*, quantifies the correlation between the mode and the exciting field, while the integrals in the denominator are simply the total powers of the two fields since they are not necessarily normalized to unity. The modes are nearly transverse, while the exciting field is purely transverse. When polarization is ignored, the products in Eq. (3.54) can be written as inner products (Horton et al., 2007)

$$\eta_m = \frac{|\langle u|u_m\rangle|^2}{\langle u|u\rangle \langle u_m|u_m\rangle}, \tag{3.55}$$

where $\langle\cdot|\cdot\rangle$ is the inner product of the two arguments. Conservation of energy means that coupling efficiency is preserved along the propagation direction. This allows for the overlap integral to be evaluated at any convenient transversal plane. Therefore, the waveguide modes may be back-propagated from the focal plane to

the entrance pupil of the telescope, where the overlap with the aperture function produces an equal result due to the linearity of Maxwell's equations if the optical system is lossless (Haffert, 2021).

A case of particular interest, for which an analytical solution exists, is the coupling via a diffraction-limited telescope into an SMF. The exciting field, in this case, is the Airy pattern in Eq. (B.16), while the mode is the fundamental one approximated by Eq. (3.35). The clear mismatch between the two distributions prohibits a 100% coupling. The size of the Airy pattern needs to be optimized to the Gaussian mode by choosing the focal ratio that leads to the maximum correlation. At the entrance pupil, the exciting field is a plane wavefront, and the mode remains a Gaussian whose parameters are determined by Gaussian beam optics (Neumann, 2013). The distribution of the mode at the aperture is

$$u'_m(\rho) = \sqrt{\frac{2}{\pi w_1^2}} e^{-\frac{\rho^2}{w_1^2}}, \tag{3.56}$$

where polar coordinates are used for the circular fiber and w_1 is the $1/e$ radius, i.e., the *mode field radius*, of the Gaussian beam at the pupil related to the radius at the focus by $w_1 = \lambda f/\pi w_0$ with f being the focal length of the focusing optic. Both fields have planar wavefronts at the aperture, and thus $u^* u_m$ reduces to $|u||u_m|$. The numerator in Eq. (3.54) becomes

$$\eta_m = \frac{4}{\pi D^2} \left| \sqrt{\frac{2}{\pi w_1^2}} \int_0^{2\pi} \int_0^{D/2} \rho \mathrm{d}\rho \mathrm{d}\theta e^{-\frac{\rho^2}{w_1^2}} \right|^2 \tag{3.57}$$

$$= 8 \left(\frac{\lambda f}{\pi w_0 D} \right) \left[1 - \exp\left(- \left(\frac{\pi w_0 D}{2\lambda f} \right)^2 \right) \right]^2, \tag{3.58}$$

where w_1 was expressed in terms of its focal plane counterpart, w_0, and the integral at the denominator was recognized to be simply the area of the aperture. When η in Eq. (3.58) is plotted against $\pi w_0 D/2\lambda f$ similar to the plot shown later in Fig. 5.11, [5] one finds that it has its maximum equal to 0.816 at $\pi w_0 D/2\lambda f = 1.121$. This is the maximum coupling efficiency that one can get from plane waves diffracted by circular apertures into step-index SMFs. The optimum focal ratio, $f/\# = f/D$,

[5] Actually, the plot in Fig. 5.11 is calculated at the focal plane with the true mode rather than its Gaussian approximation, and it is, therefore, more accurate than the formula in Eq. (3.58).

for maximum coupling into a given fiber should be chosen such that it equals $\pi w_0/(2\lambda \times 1.121)$. Worth mentioning is that the actual maximum calculated with the exact mode rather than its Gaussian approximation is a bit lower at $\sim 79\%$ (see Fig. 5.11).

Effect of obscuration and spiders

Most astronomical telescopes do not have pupils that are clear circular apertures but are instead obscured by a secondary mirror and its spiders. Both of which adversely affect the coupling of light into waveguides (Coudé du Foresto, 1994). Structures like these diffract light away from the focus, effectively reducing the Airy disk's peak amplitude and carrying the power to the outer rings and the spikes, as shown in Fig. 3.7. In the case of a secondary mirror with negligible spiders, the PSF deviates from the Airy pattern in Eq. (B.16) and takes the form (Everhart et al., 1959)

$$I(\rho', \phi') = \frac{2A^2(2\pi a^2)^2}{{r_\perp}^2} \left[\frac{J_1(ka\rho'/r_\perp)}{ka\rho'/r_\perp} - \zeta^2 \frac{2J_1(\zeta ka\rho'/r_\perp)}{\zeta ka\rho'/r_\perp} \right]^2, \tag{3.59}$$

where ζ is the obscuration ratio. The effect is extreme for telescopes designed for wide FoV surveys with a large obscuration ratio, e.g., VRO at $\zeta = 0.62$. One way of mitigation is to apodize the pupil by shifting the light at the edges of the pupil towards the center to transform the intensity from a uniform distribution into a Gaussian-like one by optics that modulate the phase to redistribute the amplitude across the pupil. A phase-induced amplitude apodizer (PIAA) that brings the outer rays into the middle before collimating the beam can perform better than a Gaussian apodizer in terms of coupling if tailored to its host telescope (Calvin et al., 2021; Jovanovic, Schwab, et al., 2017).

Coupling through turbulence

The effect of turbulence on coupling is the main point that this work is trying to address and numerical results calculated with attention paid to the contributing phenomena detailed so far are presented in Sec. 5.2. Some insights are, however, possible at this point and can help develop an intuition without the need for intricate computations.

This involves the brightness theorem and the concept of étendue to relate the turbulence strength to the modes of a large MMF. According to the brightness theorem,

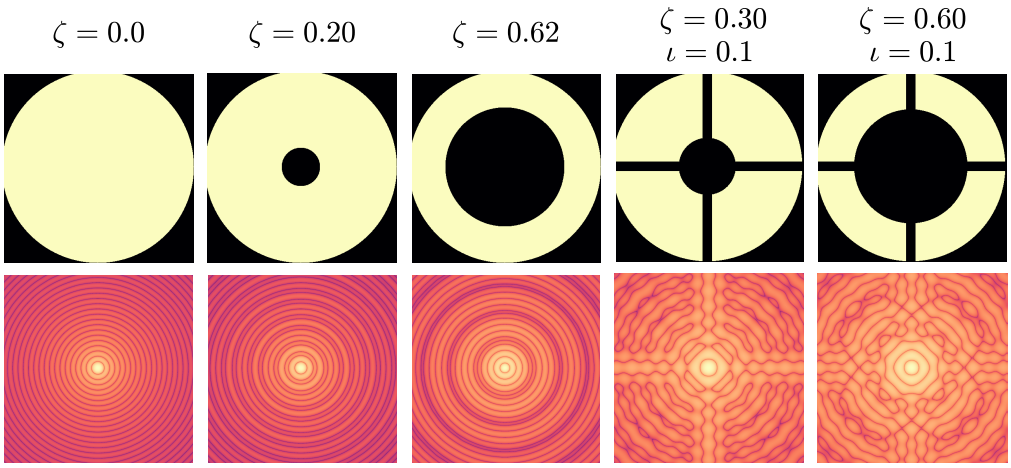

Figure 3.7: Top panels: aperture functions of various telescope configurations. The parameter ζ is the obscuration ratio, while ι is the spider width as a fraction of the whole diameter. Bottom panels: their respective normalized PSFs in base 10 logarithmic.

the étendue, S, is conserved for light traversing an ideal passive optical system. In an imperfect system, however, it can only increase since entropy must also increase. In free space, the étendue of a source is given by (Minardi et al., 2021)

$$S = A\Omega, \tag{3.60}$$

where A is the source area normal to the line of sight and Ω is the solid angle of the emission. The étendue of light that couples into a fiber

$$S_F = \pi^2 a^2 NA^2 = \frac{\lambda^2 V^2}{4}, \tag{3.61}$$

where a is the fiber radius, NA is its numerical aperture, and V its normalized frequency. The approximation $\Omega = \pi\alpha^2$ for the solid angle was used. The seeing disk, as seen from the aperture, has the area

$$A = \pi \left(\theta_S f\right)^2, \tag{3.62}$$

where θ_S is the seeing and f is the focal length. The solid angle seen by the telescope is

$$\Omega = \pi \left(\frac{1}{2f_\#}\right)^2, \tag{3.63}$$

where the solid angle approximation was used once more. The étendue of the telescope is, therefore,

$$S_T = \frac{\pi^2 {\theta_S}^2 D^2}{4}, \tag{3.64}$$

where the definition $f = D f_{\#}$ with D being the diameter of the telescope was used. Imposing the conservation of étendue

$$\frac{\lambda^2 V^2}{4} = \frac{\pi^2 {\theta_S}^2 D^2}{4}, \tag{3.65}$$

one reaches the formula for the number of modes contained in the seeing disk

$$M \approx \frac{V^2}{4} = \left(\frac{\pi D}{2 r_0}\right)^2, \tag{3.66}$$

where the approximation for the number of modes in terms of the V-number (Eq. (3.37)) and the angular size of the seeing disk in terms of Fried's parameter $\theta_S \sim \lambda / r_0$ (Sec. 2.1.3) were utilized. Note that this formula only counts one polarization state.

Although an approximation, this is a significant result. The number of modes that an MMF needs to support in order to couple the seeing disk is given simply in terms of the turbulence strength D/r_0. Note that $(D/r_0)^2$ is the count of coherent wavefront patches at the aperture and roughly the count of speckles in the PSF. One, therefore, arrives at the elegant conclusion that efficient coupling requires a mode (or an SMF) per speckle in the focal plane.

3.7 Integrated optics and astrophotonics

The photonic advantage that integrated optics bring to astronomical instrumentation was touched on in Sec. 1.3. Some of the most advanced photonic technologies that have been proposed to perform a variety of functionalities on starlight are discussed next. A brief description is given, demonstrating their superiority over bulk optics while stressing the necessity for them to operate in the single-mode regime. Note that this list is by no means exhaustive.

3.7.1 Photonic spectrographs

Next to interferometry, spectroscopy stands to benefit the most from photonic technologies. For typical slit spectrographs with bulk optics dispersers, e.g., gratings

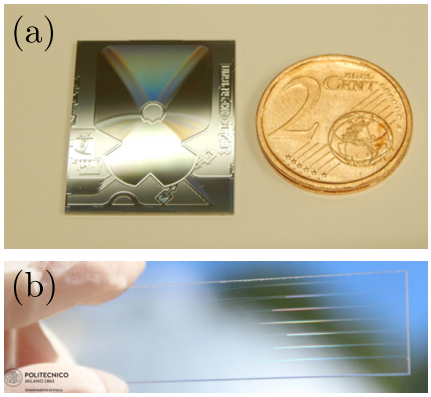

Figure 3.8: Pictures of (a) an AWG shown next to a 2 euro cent coin [adapted from Stoll et al., 2020] and (b) multiple four-telescopes DBCs inscribed in a glass substrate held between two fingers [image credit: A. N. Dinkelaker (AIP)], highlighting the scale.

and prisms, the plate scale defines the slit width given the seeing, which in turn constrains the size of the optics required for the spectrograph. The size of the instrument, therefore, grows linearly with the diameter of the aperture. The costs of both, the telescope and the instruments, grow even faster as the aperture square (Belle et al., 2004; Blind et al., 2017). Some form of AO will consequently be indispensable to control the size of the seeing disk and maintain a practical size of the spectrograph. With AO correction, coupling into a single-mode waveguide is viable, and the use of a photonic spectrograph becomes even more attractive.

Several technologies have been identified as candidates for photonic spectroscopy. One example is arrayed waveguide gratings (AWGs) which are high-resolution planar spectrometers developed originally for DWDM. The light delivered by the input fiber is allowed to diverge in one dimension in a slab waveguide known as the free propagation zone before before an on-chip phased array of waveguides picks it up. The beams propagating out of the array waveguides, having accumulated progressive phase shifts, then interfere to produce a dispersed output because the interference is constructive for different wavelengths at different output angles. AWGs are fully integrated with all the segments on the same platform (see Fig. 3.8a), but the spectral orders may overlap if the free spectral range is too small. Cross dispersion can be introduced after that to separate the orders but that would add an additional stage and increase the size.

3.7.2 Beam combiners

In an array of 4 telescopes or more, the flux reaching the detector after combination is only a few percent of its initial value because of the multiple reflections it undergoes in the delay lines and the beam splitters (Labadie et al., 2016). Using an integrated optics beam combiner is one way to mitigate this light loss. The need for the combiner waveguides to operate at the single-mode regime (Perraut et al., 2018) contributes to the losses as the coupling is never total, but AO can be used to tip the scale in favor of the photonic approach.

Long-baseline interferometry was the first application of astrophotonics. The prototype FLOUR (Coudé du Foresto et al., 1992) instrument used SMF couplers to combine a pair of telescopes on Kitt Peak observatory before becoming a facility instrument at IOTA (Coudé du Foresto et al., 1998). Soon after, the VLTI followed suit with PIONIER and GRAVITY. Planar photonic chips admitted active phase shifting allowing the derivation of visibility amplitudes and closure phases using the ABCD scheme. GRAVITY, operating in the K-band, combines the light from the four 8-m VLT telescopes using a planar lithographic chip. It has been used successfully to uncover the orbital motions of stars in the crowded Galactic Center and led to, among other achievements, the discovery of a supermassive object at Sgr A* (Abuter et al., 2018).

DBCs like the one shown in Fig. 3.8b use a 3D array of nonoverlapping single-mode waveguides to combine multiple telescopes. They are discussed further in Sec. 4.2 and Ch. 7.

3.7.3 OH suppression filters

A series of high refractive index regions inscribed in the core of an SMF, known as an FBG, have the capability of reflecting back the light of a selected wavelength via Fresnel reflections. The reflections from all the interfaces between the different index regions interfere constructively when the grating period matches an integer multiple of half-wavelength, and the grating, therefore, acts as a notch filter. In IR ground-based astronomy, this can be exploited to develop complex filters to suppress the problematic hundreds of telluric OH lines. One complication is that these background lines are not periodically spaced and vary in depth. Nevertheless, the filter spectrum could be controlled by precisely tuning the spacings and depths of the index modulations, which can be laser-inscribed into the core. OH suppression

should allow the observation of faint, high redshift objects like the cosmic noon galaxies that can only be reliably observed from the ground upon filtering the IR sky background.

If written in MMFs, each mode would experience a slightly different periodicity resulting in the periodic filter rejecting multiple lines instead of one. Fortunately, photonic lanterns can help overcome this difficulty by feeding the multimode seeing disk to several SMFs before the downstream half of the lantern converts them back to a single MMF. This was first done for the GNOSIS spectrograph (Ellis et al., 2012) and next-generation designs continue to be developed (Rahman et al., 2020).

3.7.4 Mode converters (photonic lanterns)

Unlike many of the other astrophotonic technologies developed first for the communication industry, photonic lanterns were originally conceived to increase the throughput of FBGs, which only operate efficiently in SMFs (Leon-Saval, 2015) as mentioned above. They have since made the leap and found applications in telecommunications and sensing, and are now commercially traded. Photonic lanterns transform, in theory without loss, the multimode light in a multimode waveguide into multiple single-mode waveguides and vice versa (see Fig. 3.9). This breakthrough has a substantial significance for astronomical instruments. It means that starlight distorted by the atmosphere, composed of numerous modes, can be transformed into Gaussian-like coherent beams. No matter how much distorted the wavefront is, the input port of the photonic lantern can be made large enough for all the constituents of the PSF to find modes in the plethora of guided modes offered to couple into. The drawback, however, is that the degrees of freedom must be matched. This is to say, the system's entropy must be conserved as demanded by the second law of thermodynamics. Any design of an instrument that utilizes photonic lanterns has to navigate this limitation.

The symmetry between the identical SMFs of the photonic lantern could interestingly be broken to make a mode-selective photonic lantern (MSPL) that has a one-to-one correspondence between the modes and the SMFs. This is discussed in detail in Ch. 6 where the potential advantages it could bring to astronomy are pointed out.

Other astrophotonic technologies that have been studied but are of less relevance to this work include pupil remappers, reformatters, microring resonators, phase chronographs, and frequency converters.

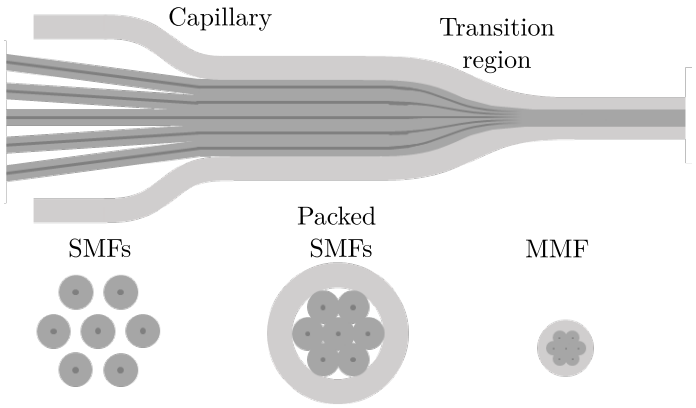

Figure 3.9: A 1 $\times$ 7 photonic lantern fabricated by tapering a stack of SMFs. The greyscale also reveals the refractive index profile from the dark grey of the SMFs cores being the highest index to the light grey of the capillary representing the lowest [adapted from J. J. Davenport et al., 2021].

Chapter 4

NUMERICAL MODELS FOR COUPLING THROUGH TURBULENCE

The theoretical concepts presented in Ch. 2 for turbulence mechanics and AO and in Ch. 3 for waveguides describe the physics, but the mathematical equations need to be formulated in a manner more suitable for implementation on a computer. The numerical models for these concepts are presented here. Section 4.1 gives the considerations necessary for simulating SMFs and FMFs, while Sec. 4.2 does the same for waveguide arrays. Section 4.3 shows how phase screens for the atmospheric layers are generated using matrix algebra and FFT. Section 4.4 discusses the use of FFT to model free space propagation. Finally, Sec. 4.5 presents the models for the components of an AO system.

4.1 Modeling few-mode fibers (FMFs)

To find the LP modes of weakly guiding step-index fibers, the characteristics equation (Eq. (3.34)) is solved numerically. For a given azimuthal index l and a maximum radial order m, the first m positive zeros of the Bessel function J_{l-1} are found by applying Halley's iterative method (Alefeld, 1981; Traub, 1982). The least-square fits of the first three zeros are used to get approximate initial values that will cause the method to converge to the correct zeros. The fact that the zeros of Bessel functions are regularly spaced is used to find the initial values for the subsequent zeros starting from the third. Tabulated values are not used here but could lead to a faster computation if the iterations involved in Halley's method are identified as a bottleneck in the calculations pipeline.

Next, the characteristic equation is solved by looking for the point where the equation changes signs within the interval defined by the zeros of the Bessel function. The solution represents the ξ' value of the found mode and χ' can be calculated using $\chi' = \sqrt{V^2 - \xi'^2}$. The field distributions in the core and the cladding are then given by Eq. (3.25) and (3.26). The process is repeated for increasing values of the indices l and m until no more modes could be found. The first 15 LP modes found using this algorithm are shown in Fig. 4.1. Figure 4.2 shows how more modes become supported as V increases.

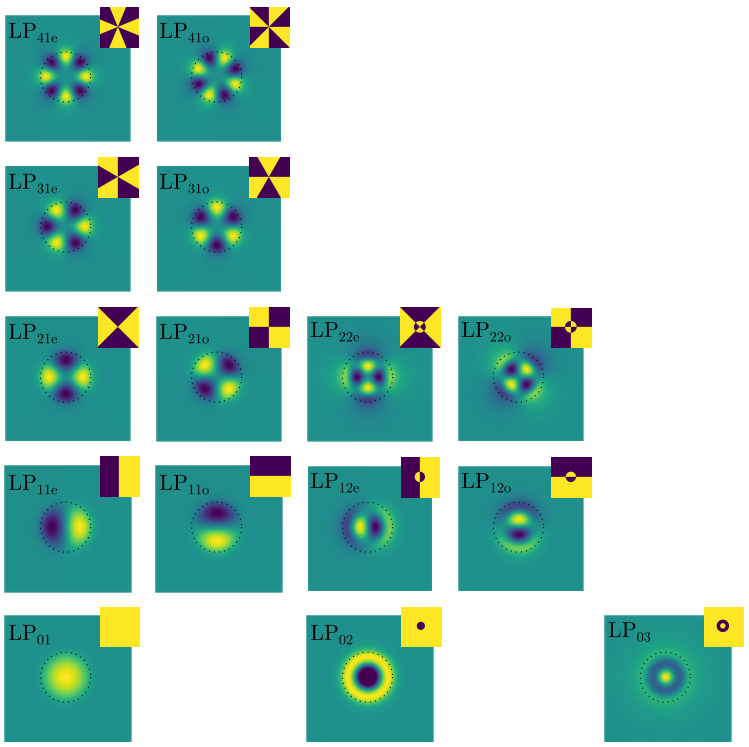

Figure 4.1: The first 15 LP modes of a weakly guiding step-index fiber with the dotted circles marking the core-cladding interface. The subscript e denotes even while o denotes odd for the degenerate modes. The insets show the phase profile, which only flips between 0 and π for the LP modes.

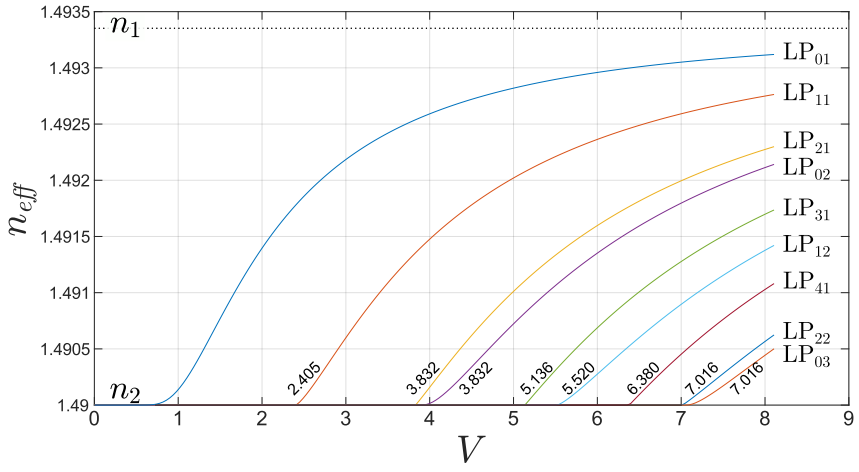

Figure 4.2: The increase in the effective indices of the modes in Fig. 4.1 as V increases. The effective indices, $n_{\text{eff}} = \beta/k_0$, take values between that of the core, n_1, and that of the cladding, n_2. The cutoff frequencies are at the crossings on the cladding index value on the x axis.

4.2 Modeling waveguide arrays

To solve the differential equations of the CMT in Sec. 3.4, the Crank-Nicolson method (Crank et al., 1947) is applied. The discrete approximation of Eq. (3.41) has the form

$$\frac{\vec{A}^{(k+1)} - \vec{A}^{(k)}}{\Delta z} = \frac{i}{2}\kappa\mathbf{C}\left[\vec{A}^{(k+1)} + \vec{A}^{(k)}\right], \tag{4.1}$$

where Δz is the size of the differentiation step and k is the index of the step. Grouping all terms from the same step in z together, one gets

$$\left(\mathbf{1} + \frac{i}{2}\kappa\Delta z\mathbf{C}\right)\vec{A}^{(k+1)} = \left(\mathbf{1} - \frac{i}{2}\kappa\Delta z\mathbf{C}\right)\vec{A}^{(k)}, \tag{4.2}$$

where $\mathbf{1}$ is the identity matrix. Using the notations $\mathbf{L} = \mathbf{1} + \frac{i}{2}\kappa\Delta z\mathbf{C}$ and $\mathbf{R} = \mathbf{1} - \frac{i}{2}\kappa\Delta z\mathbf{C}$, one gets

$$\vec{A}^{(k+1)} = \mathbf{L}^{-1}\mathbf{R}\vec{A}^{(k)}. \tag{4.3}$$

Evolving the field forward to the next step in an array of N identical waveguides is therefore reduced to a problem of inverting and multiplying an $N \times N$ matrix by another. Figure 4.3 shows the results of propagating an initial field through a hexagonal waveguide array using CMT.

When waveguide arrays are used for phase retrieval, like in DBCs and mode analyzers, their geometrical configuration and the choice of the excitation sites make a difference on how sensitive the system is to noise, as further discussed in Ch. 7.[1] This is characterized by the condition number of the transfer matrix of the said system. Therefore, a fast numerical algorithm is essential when a large number of configurations is to be tested. BPMs, although more accurate than the CMT, are far too slow for testing all the possible permutations of excitation sites in a given waveguide array.

Together with the local modes assumptions of slowly varying waveguides given in Sec. 3.5, CMT could also be used to model the transition regions of photonic lanterns. As mentioned, BPM, although demanding in terms of computing power, is superior in terms of accuracy, and it is used for the photonic lanterns modeled in

[1] Put differently, the geometry determines how chaotic the resulting system will be.

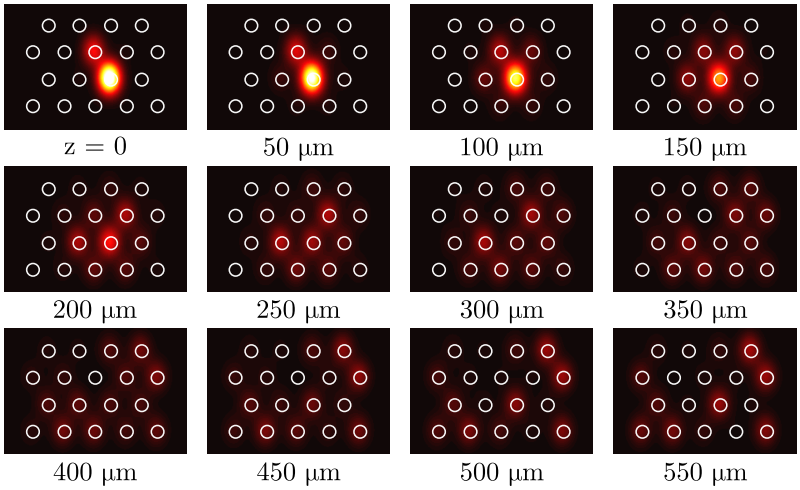

Figure 4.3: Evolution of the field in a hexagonal array of identical waveguides. Only two waveguides are initially excited, and steps of 50 μm are calculated using the CMT are shown. Wavelength is $\lambda = 1.55$ μm, and coupling length $L_C = 1$ mm.

this works whenever the number of simulation runs planned could be accomplished inside a reasonable time frame.

4.3 Modeling the atmosphere with phase screens

When simulating atmospherically distorted starlight, a key tool is the *phase screen generator*. The generator produces random realizations of the wavefront phase after propagation through an atmospheric layer that have the correct spatial statistics, e.g., the Kolmogorov (Eq. (2.34)) or the von Kármán (Eq. (2.35)) spectra. The temporal evolution of the turbulence can then be easily simulated by shifting a large phase screen over the aperture following Taylor's frozen flow hypothesis (see Eq. (2.37)).

Methods for creating phase screens generally fall under two categories. In the sample-based method, a matrix of random Gaussian numbers is filtered with Kolmogorov's spectrum. The filtered matrix is inverse Fourier transformed to get the phase (Welsh, 1997). The resolution of the matrix limits the representation of low spatial frequencies in the wavefront, which are the main contributors according to the 5/3rds law (Louthain et al., 1998). The second category is the modal-based method where the phase is decomposed into an infinite set of orthogonal functions over the aperture. The basis functions are assigned coefficients that are random Gaussian numbers with zero mean and variances that satisfy the desired statistics. The underrepresentation of low-frequency components is therefore avoided in doing so.

The approach proposed by Welsh, 1997 is a modal method that uses a Fourier series as the expansion of the wavefront. The phase $\phi(\vec{\rho})$ is assumed to be a stochastic process that is Gaussian and has zero mean. According to the Wiener–Khinchin–Einstein theorem, the PSD of the process is given by the Fourier transform of the autocorrelation function. The autocorrelation of the phase is

$$B_\phi(\vec{\rho}_0) = \langle \phi(\vec{\rho})\phi(\vec{\rho} - \vec{\rho}_0)\rangle, \tag{4.4}$$

which is independent of the absolute position $\vec{\rho}$ due to the process being a spatial wide sense stationary process, i.e., its mean and variance do not change when shifted in space. The PSD is

$$\Phi(\vec{f}) = \int \mathrm{d}\vec{\rho}_0 B_\phi(\vec{\rho}_0) \exp\left(-2\pi i \vec{f}\cdot\vec{\rho}_0\right), \tag{4.5}$$

where $\vec{f}$ is the vector spatial frequency coordinate. If the screen is being generated over an area of dimension D_p, then the phase will have a period of D_p in both directions. The Fourier series expansion of the generated phase is

$$\phi'(\vec{\rho}_0) = \sum_{i=-\infty}^{\infty}\sum_{j=-\infty}^{\infty} c_{i,j} \exp\left[2\pi i\left(\frac{ix}{D_p} + \frac{jy}{D_p}\right)\right], \tag{4.6}$$

where x and y are the orthogonal components of $\vec{\rho}_0$. and $c_{i,j}$ are the coefficients to be determined for the spatial frequencies $\vec{f} = i\hat{x}/D_p + j\hat{y}/D_p$. The coefficients are independent random complex numbers that have a Gaussian distribution with the mean square

$$\left\langle |c_{i,j}|^2 \right\rangle = \frac{1}{D_p^2}\Phi\left(\frac{i}{D_p}, \frac{j}{D_p}\right). \tag{4.7}$$

Furthermore, the symmetry of the problem requires that the coefficients are Hermitian, i.e., $c_{i,j} = c^*_{-i,-j}$. Both the generated and the true phases have approximately the same autocorrelation function within a distance of D_p from the origin. With D_p chosen larger than the outer scale and in general much larger, the autocorrelation approaches zero as $D_p \to \infty$ and it decreases to negligible values for $\rho_0 \geqslant D_p/2$. The expansion over a finite number, N, of basis functions is

$$\begin{aligned}\phi'(\vec{\rho}) &= \sum_{i=-(N-1)}^{N-1}\sum_{j=-(N-1)}^{N-1} c_{i,j}\exp\left[2\pi i\left(\frac{ix}{D_p}+\frac{jy}{D_p}\right)\right] \\ &= 2\,\mathrm{Re}\left\{\sum_{i=0}^{N-1}\sum_{j=0}^{N-1} c_{i,j}\exp\left[2\pi i\left(\frac{ix}{D_p}+\frac{jy}{D_p}\right)\right]\right. \\ &\qquad \left. + \sum_{i=1}^{N-1}\sum_{j=-(N-1)}^{-1} c_{i,j}\exp\left[2\pi i\left(\frac{ix}{D_p}+\frac{jy}{D_p}\right)\right]\right\} \quad (4.8)\end{aligned}$$

The pseudocode for generating a phase screen with a von Kármán spectrum proceeds as follows:

For N sampling points in the frequency domain in each direction and a period D_p of the Fourier series, the spatial frequency column vector is

$$f = \left[0, \frac{1}{D_p}, \cdots, \frac{N}{D_p}\right]^{\mathsf{T}}. \quad (4.9)$$

The elements $c_{i,j}$ in Eq. (4.8) have the variances

$$\begin{aligned}\sigma_1^2 &= \frac{1}{D_p^2}\Phi\left(\frac{k-1}{D_p}, \frac{l-1}{D_p}\right), \\ \sigma_2^2 &= \frac{1}{D_p^2}\Phi\left(\frac{k-1}{D_p}, \frac{-l+1}{D_p}\right),\end{aligned} \quad (4.10)$$

where 1 and 2 designate the variances associated with the first and the second terms in Eq. (4.8), respectively. The spatial frequencies for each term are

$$\begin{aligned}|f_1|^2(k,l) &= \left(\frac{k-1}{D_p}\right)^2 + \left(\frac{l-1}{D_p}\right)^2, \\ |f_2|^2(k,l) &= \left(\frac{k-1}{D_p}\right)^2 + \left(\frac{-l+1}{D_p}\right)^2.\end{aligned} \quad (4.11)$$

In terms of the spatial frequency, the von Kármán PSD has the form

$$\Phi(\vec{f}) = \frac{0.023\left(\frac{D_p}{r_0}\right)^{5/3} D_p^2}{\left(|\vec{f}|^2 D_p^2 + \left(\frac{D_p}{\mathcal{L}_0}\right)^2\right)^{11/6}}. \quad (4.12)$$

Substituting in Eq. (4.10) with f as defined in Eq. (4.11)

$$\begin{aligned}\sigma_1^2 &= \frac{0.023\left(\frac{D_p}{r_0}\right)^{5/3}}{\left[f_1^2 D_p^2 + \left(\frac{D_p}{\mathcal{L}_0}\right)^2\right]^{11/6}},\\ \sigma_2^2 &= \frac{0.023\left(\frac{D_p}{r_0}\right)^{5/3}}{\left[f_2^2 D_p^2 + \left(\frac{D_p}{\mathcal{L}_0}\right)^2\right]^{11/6}}.\end{aligned} \tag{4.13}$$

The amplitudes of C_1 and C_2 have the values

$$\begin{aligned}A_1 &= \sigma_1 R_1,\\ A_2 &= \sigma_2 R_2,\end{aligned} \tag{4.14}$$

where R is an $N+1$ square matrix of normally (Gaussian) distributed random numbers of zero mean and variance 1. The angles of the complex coefficients are

$$\begin{aligned}\theta_1 &= 2\pi R_1',\\ \theta_2 &= 2\pi R_2',\end{aligned} \tag{4.15}$$

where R' is an $N+1$ square matrix of uniformly distributed random numbers in the interval $(0,1)$.The coefficients therefore are

$$\begin{aligned}C_1 &= A_1 e^{i\theta_1},\\ C_2 &= A_2 e^{i\theta_2}.\end{aligned} \tag{4.16}$$

The first row and the first column of C_1 are set to zero since the second sum in Eq. (4.8) starts from $i = 1, j = -(N-1)$

The pupil sampling in both dimensions is defined by the vectors

$$\begin{aligned}x &= \left[0 : \frac{D}{M-1} : D\right],\\ y &= \left[0 : \frac{D}{M-1} : D\right],\end{aligned} \tag{4.17}$$

where x and y are row vectors of length M that contain the x- and y-coordinates of the grid points, respectively.

Wavelength	λ
Aperture diameter	D
Size of the spectrum period	D_p
Sampling of the spatial frequency	N
Sampling of the phase screen	M
Fried's parameter	r_0
Outer scale	$\mathcal{L}_0$
Velocity vector	$\vec{v} = (v_x, v_y)$
Time delay	τ

Table 4.1: Simulation parameters used for modeling the atmospheric layer.

Substituting in Eq. (4.8), the generated phase screen is

$$\hat{\phi} = 2\,\mathrm{Re}\left\{\left[e^{2\pi i f x}\right]^{\intercal}\left[\mathbf{C_1}e^{2\pi i f y} + \mathbf{C_2}e^{-2\pi i f y}\right]\right\}, \tag{4.18}$$

where $^{\intercal}$ indicates a transpose. This is the matrix form of Eq. (4.6). Table 4.1 lists the input parameters required for simulating an atmospheric layer.

4.4 Free space propagation

Once atmospheric turbulence is modeled and a phase screen generator is at hand, one needs to calculate the optical field at the focus and at intermediate planes where certain AO operations take place. This is done by propagating the phase screen through free space using Fraunhofer diffraction as detailed in App. B. If scintillation is to be modeled (see Sec. 2.1.2), the phase screen from the highest atmospheric layer is propagated by a Fresnel diffraction integral (Eq. 4.21) to the next layer and so on to the aperture to get both the phase and the amplitude of the wavefront (Osborn, 2015). Simulations that do not involve AO correction require a single propagation from the aperture to the focal plane where a waveguide is placed. Some numerical considerations are necessary before Eq. (B.9) is applied.

When the aim is to calculate the overlap integral in Eq. (3.54) to estimate the coupling efficiency, the integral may be evaluated at either the focal or the pupil plane. The number of phase screens required to obtain ensemble averages is normally more than the number of modes involved, and therefore, the waveguide modes are back-propagated to the pupil plane for computing economy.

The modes $\mathbf{M_i}$ calculated as described in Sec. 3.2.1 are zero-padded by adding an equal number of zero-containing rows and columns in all directions, effectively

increasing the size of the matrix. This is done for two reasons. First, to increase the size of the matrix to have a power-of-two dimension, allowing the FFT codes to apply the extremely efficient radix-2 algorithm (Kelly, 2014). Secondly, since the size of the FFT output matrix equals that of the input, increasing the input size by adding zeros also increases the FFT resolution. This is not to say that the frequency resolution, given by $1/N$ where N is the length of the data-containing matrix $\mathbf{M_i}$, increases. Zero-padding, however, ensures that no information is lost in the FFT output because of poor sampling.

The zero-padded modes are back-propagated to the pupil plane via an inverse FFT

$$\mathbf{M}_i' = FFTshift^{-1}\left[FFT^{-1}\left(FFTshift^{-1}\left(i\lambda f \exp\left(-\frac{2\pi i}{\lambda}\left(f + \frac{x^2+y^2}{2f}\right)\right)\mathbf{M}_i^z\right)\right)\right], \tag{4.19}$$

where $\mathbf{M}_i^z$ is the zero-padded mode, and x and y are vectors that contain the x- and y-coordinates of the grid over which M_i^z is defined. $FFT^{-1}(\cdot)$ returns the two-dimensional discrete inverse FFT of its argument while $FFTshift^{-1}(\cdot)$ rearranges its argument by swapping its first with its third quadrants and its second with its fourth quadrant such that it is consistent with the requirement of $FFT^{-1}(\cdot)$ (Breckinridge et al., 2011). In Eq. (4.19), f is the focal length of the focusing optic, i.e., the telescope. The resulting pupil field is then properly truncated and interpolated to match the dimensions of the wavefront that it needs to be overlapped with.

4.5 Modeling AO correction

To include the effect of AO correction on wavefronts before coupling, the three main elements of an AO system, i.e., the WFS, the DM, and the wavefront constructor, need to be modeled. Each component is defined by several parameters and performance specifications, as shown in Table 4.2.

4.5.1 WFS model

The model here assumes a WFS of the Shack-Hartmann type introduced in Sec. 2.2.2. The MLA is defined by the number of microlenses along each direction, its pitch, and focal length. The focal length determines the linear size of the spots on the detector and the amount of shift per unit tilt, setting the limits on the dynamic range of the sensor. Since the MLA is placed at the exit pupil of the

WFS		Controller	DM
MLA	Number (N_{ML}) and arrangement of microlenses	Reconstruction modes	Number and arrangement of actuators
	Size (d) and subaperture pitch	Pure delay	Actuators pitch
	Focal length (f)		Influence functions
Detector	QE		Response time
	RON		Stroke
	Dark current (σ_{dark})		Pupil diameter
	Gain (ADU)		
	Pixel pitch		
	Exposure time (T_{exp})		

Table 4.2: AO system parameters relevant to modeling.

telescope, the wavefront it intercepts is the same as the wavefront at the aperture apart from a multiplication factor equal to the magnification of the afocal system formed by the telescope's primary and the collimator. The detector behind the MLA is characterized by its QE, dark current, pixel pitch, discretization levels, i.e., analog to digital units (ADUs), and exposure time.[2]

The wavefront phase is that of the generated phase screen in Sec. 4.3, and its amplitude is assumed to be uniform and normalized to unity unless scintillation effects are included. The shape of the telescope aperture, i.e., primary mirror and secondary obscuration, is accounted for by appropriate masking. The resulting wavefront is

$$\psi = A_N M_T T_{ML} \exp(i\phi), \tag{4.20}$$

[2]Or the frame rate if it happens to be the limiting factor.

where A_N is an amplitude normalizing factor, M_T is the telescope aperture mask, ϕ is the phase screen, and T_{ML} is the transmission function of the MLA. For a square MLA of N_{ML} microlenses in each direction, the transmission function is a concatenation of $N_{ML} \times N_{ML}$ single-lens transmission functions, which are simply spherical wavefronts for spherical lenslets, i.e., $\exp\left(-\pi i \vec{r}^2/\left(f\lambda\right)\right)$, where f is the focal length and $\vec{r}$ is the position. The phase modulation of the lenslets array is illustrated in Fig. 4.4a. The piston component can be removed by subtracting the mean value from the wavefront. The Fraunhofer condition $d^2/(\lambda f) \ll 1$, where d is the side length of the array, does not hold here and cannot be used for the optical propagation through the array to its focal plane. Furthermore, the incoming wavefront modulated by the short focal length array differs from the planar wavefront by multiple wavelengths over the extent of the aperture. Such an arrangement calls for Fresnel's diffraction

$$E(x', y') = \mathcal{F}^{-1}\left\{\mathcal{F}\left\{\psi(x, y)\right\} Y(k_x, k_y)\right\}, \tag{4.21}$$

where the propagator transfer function Y is given by

$$Y(k_x, k_y) = e^{ikf} e^{-i\pi\lambda f(k_x^2 + k_y^2)}. \tag{4.22}$$

This is implemented numerically using FFTs as follows

$$\mathbf{E}(x', y') = \text{FFTshift}^{-1}\left[\text{FFT}^{-1}\left(\text{FFTshift}^{-1}\left(\mathbf{Y}(k_x, k_y)\text{FFT}\left(\text{FFTshift}^{-1}\left(\psi(x, y)\right)\right)\right)\right)\right]. \tag{4.23}$$

The pattern forming on the detector due to this optical field is

$$\mathbf{I} = \frac{1}{2Z_0}|\mathbf{E}(x', y')|^2, \tag{4.24}$$

where Z_0 is the impedance of the free space. The reference locations of the spots are obtained by propagating a plane wave using the same Eq. (4.23). The photons count per pixel is calculated using

$$n_{\text{ph}} = \frac{\lambda A_{\text{px}} I T_{\text{exp}}}{hc}, \tag{4.25}$$

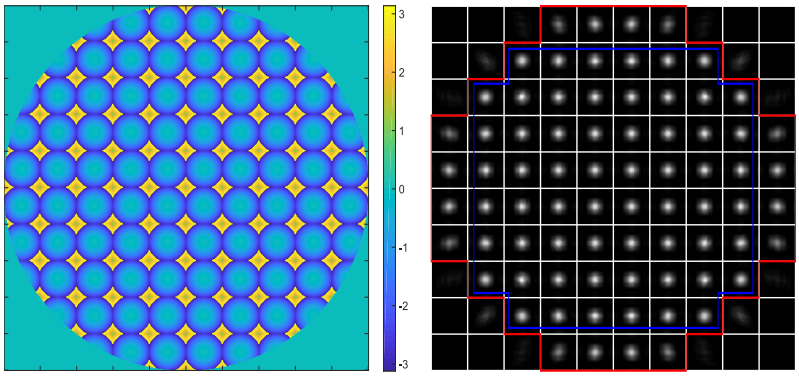

(a) (b)

Figure 4.4: Lenslets array of the SH sensor. (a) Phase of the array. (b) Simulated spots pattern due to a circular planar wavefront. Red line encircles $> 25\%$ illuminated subapertures, and blue line encircles spots with 99% illumination threshold.

where A_{px} is the area of a single pixel and T_{exp} is the total exposure time. Shot noise is included by adding a term $\sqrt{n_{\text{ph}}} \times \text{R}$ to each pixel value where R is a normally distributed random scalar. Finally, the number of photoelectrons is found by accounting for the QE of the detector. Dark current may be included by adding a term $\sigma_{\text{dark}} \times R$ to the number of photoelectrons where σ_{dark} is the rms dark current noise.

A centroiding algorithm is run next on this WFS image. Within each subaperture, a check is carried out to ensure that it is well illuminated. This is always the case for the central subapertures when a circular beam is illuminating a square lenslets array but not for the outer ring, as shown in Fig. 4.4b. Subapertures with a fill factor below a defined threshold are considered noisy and not used for calculating local slopes. The centroid coordinates for a subaperture that has N pixels are given by Eq. (2.55) which has the discrete form

$$c_x = \frac{\sum_{i,j} x_{i,j} I_{i,j}}{\sum_{i,j} I_{i,j}}, \tag{4.26a}$$

$$c_y = \frac{\sum_{i,j} y_{i,j} I_{i,j}}{\sum_{i,j} I_{i,j}}, \tag{4.26b}$$

where $I_{i,j}$ is the number of photoelectrons of pixel i, j while $x_{i,j}$ and $y_{i,j}$ are the x- and y-coordinates of that pixel, respectively. The indices (i, j) run over all the pixels in the region of interest behind the subaperture. These centroids could be

arranged in two vectors O_x and O_y, one for each coordinate, and the local slopes measured by the WFS are, therefore, given by

$$S_x = \frac{(O_x - R_x)\delta}{fM_T}, \tag{4.27}$$

$$S_y = \frac{(O_y - R_y)\delta}{fM_T}, \tag{4.28}$$

where δ is the pixel pitch of the detector and M_T is the magnification of the telescope-collimator system that reduces the received beam size to that of the lenslets array. The vectors R_x and R_y are the reference centroids due to a plane wave. The two vectors S_x and S_y are concatenated into one vector $S = [S_x S_y]^\intercal$ for the use of further wavefront reconstruction computations in Sec. 4.5.3.

4.5.2 DM model

Formulas for calculating the influence functions of generic DMs have been reported in the literature (Ealey et al., 1992). The simplest of these models approximate the shape by a Gaussian and assume that the functions are axisymmetrical. They also model all the actuators by the same function regardless of position (F. Roddier, 1999).

The use of influence functions assumes that the DM is linear and that its actuators are fairly decoupled, i.e., the response due to two actuators poked by some commands a_1 and a_2 is simply the sum of the unit step responses of each actuator weighted by a_1 and a_2, respectively. The DM parameters relevant to modeling are the number of actuators and their arrangement, the stroke, i.e., the maximum extent an actuator can reach from its nominal position before its behavior deviates from linearity, and the response time it takes an actuator to reach within $\pm 10\%$ of the set point. Artifacts like creep and hysteresis are neglected in this modeling but tended to in the experimental work in Sec. 5.2. The measured influence functions of all 97 actuators of an ALPAO DM97-15 mirror are shown in Fig. 5.4.

When one knows the make of the DM one plans to use, measured influence functions are usually available from the vendor (Garcia et al., 1978). The influence functions used in this work were provided by ALPAO SAS (Bouquin et al., 2018).

4.5.3 Wavefront reconstruction

To perform a modal reconstruction, a matrix that has the WFS response to the first M Zernike modes is filled. The WFS slopes are acquired as in Sec. 2.1.4, except that the propagated wavefront is a Zernike mode (Eq. (2.50)) instead of a phase screen. This results in an $N \times M$ matrix $\mathbf{D}$ whose columns are the gradients of the different Zernike modes. Equation (2.59) is then used to find the Zernike coefficients of the measured wavefront where $\vec{g}$ is acquired as in Sec. 2.2.2. To find the modal control matrix of the DM, i.e., the matrix that produces the correct DM commands given the Zernike coefficients, the WFS responses to the influence functions are required. This is obtained by propagating the functions through the WFS to get the matrix $\mathbf{B}$. The modal control matrix is then given by

$$\vec{C}_Z = \mathbf{B}^+ \vec{g}, \tag{4.29}$$

where $\mathbf{B}^+$ denotes the Moore-Penrose pseudoinverse of $\mathbf{B}$ which is computed by performing an SVD on the matrix $\mathbf{B} = \mathbf{U\Sigma V}^*$ to get $\mathbf{B}^+ = \mathbf{V\Sigma}^+\mathbf{U}^*$. The pseudoinverse of the rectangular diagonal matrix $\mathbf{\Sigma}$ is obtained by taking the reciprocal of the nonzero elements larger than some set threshold on the diagonal. The DM commands are

$$\vec{C} = \vec{C}_Z \mathbf{a}. \tag{4.30}$$

When a correction by a limited number rather than all of the modes is desired, the higher-order modes coefficients in $\mathbf{a}$ (see Eq. (2.60)) are set to zero and to account for the limited stroke of the DM, the values in $\vec{C}$ are capped at ± 1. Figure 4.5 shows one example of a wavefront reconstruction calculation.

The major results obtained from the simulations run using the models detailed here are reported in Ch. 5. The computational burden involved in running such models calls for the use of a multicore processor, especially when a large number of waveguide modes and a large number of phase screens are involved. The simulation results obtained in this work were possible thanks to a multicore processor with 88 cores that runs parallel computing codes.

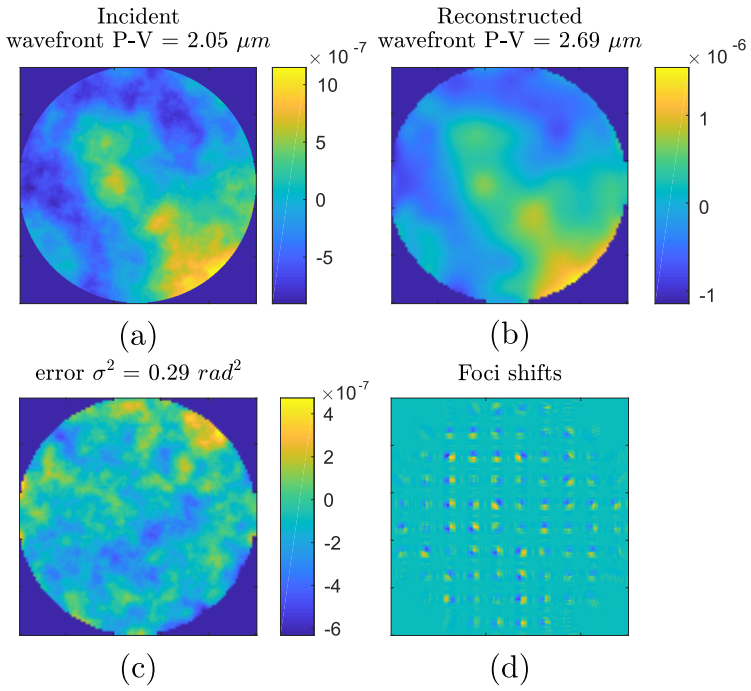

Figure 4.5: A reconstruction of a $D/r_0 = 5$ wavefront with 97 modes. (a) The incident wavefront. (b) The reconstructed wavefront that matches the best fit the DM can produce. (c) The difference between (a) and (b). (d) The resultant shifts in the SH-WFS.

Chapter 5

EXPERIMENTS AND SIMULATIONS RESULTS

Section 5.1 of this chapter is an adapted version of the proceeding

Diab, M., Dinkelaker, A. N., Davenport, J., Madhav, K., & Roth, M. M. (2020). Testbed for coupling starlight into fibers and astrophotonic instruments. *Advances in Optical and Mechanical Technologies for Telescopes and Instrumentation IV*, *11451*, 114516G. https://doi.org/10.1117/12.2564720

Section 5.2 was published as

Diab, M., Dinkelaker, A. N., Davenport, J., Madhav, K., & Roth, M. M. (2021). Starlight coupling through atmospheric turbulence into few-mode fibres and photonic lanterns in the presence of partial adaptive optics correction. *Monthly Notices of the Royal Astronomical Society*, *501*(2), 1557–1567. https://doi.org/10.1093/mnras/staa3752

The mathematical models detailed in Ch. 4 are only possible because of the assumptions made to simplify the problem under study and are, therefore, merely an approximation to the physical reality they attempt to describe. To assess the impact of these approximations on the accuracy of the models, experimental results are needed. An on-sky test that uses an astronomical telescope to collect starlight from point sources archetypal of science targets suitable for astrophotonic technologies would be the ultimate verification. Professional observatories are, however, heavily overbooked and enough time to conduct experiments and troubleshoot arising issues on a $D > 4$ m class telescope is hard to come by. An alternative is to recreate the conditions of an observation run in the lab. Section 5.1 gives the specifications of the testbed built to run the experiments, while Sec. 5.2 presents the main results obtained, followed by a discussion on their agreement with theoretical predictions.

5.1 Testbed subsystems

5.1.1 Optics and hardware

The testbed is illustrated in Fig. 5.1. At its core is an ALPAO LOAO system that corrects wavefronts distorted by an atmosphere emulator upstream. Two laser

sources are used, one in the visible to simulate a guide star and one in the near-IR to simulate a science target. A pigtailed DFB LD with a center wavelength $\lambda = 1550$ nm and an FWHM linewidth $\Delta f = 1$ MHz simulates the science target. Wavelength tunability over a small range, $\Delta\lambda = 8$ nm, is possible with a temperature controller allowing limited spectral response measurements. A Fabry-Pérot single-mode LD with a central wavelength $\lambda = 785$ nm and maximum FWHM linewidth $\Delta\lambda = 2$ nm is used to simulate the guide star. Both beams, launched from SMFs, are collimated and then expanded to 24 mm diameters using achromats and Galilean telescopes, respectively. A beam splitter overlaps the two beams before a phase distortion is introduced in the wavefronts.

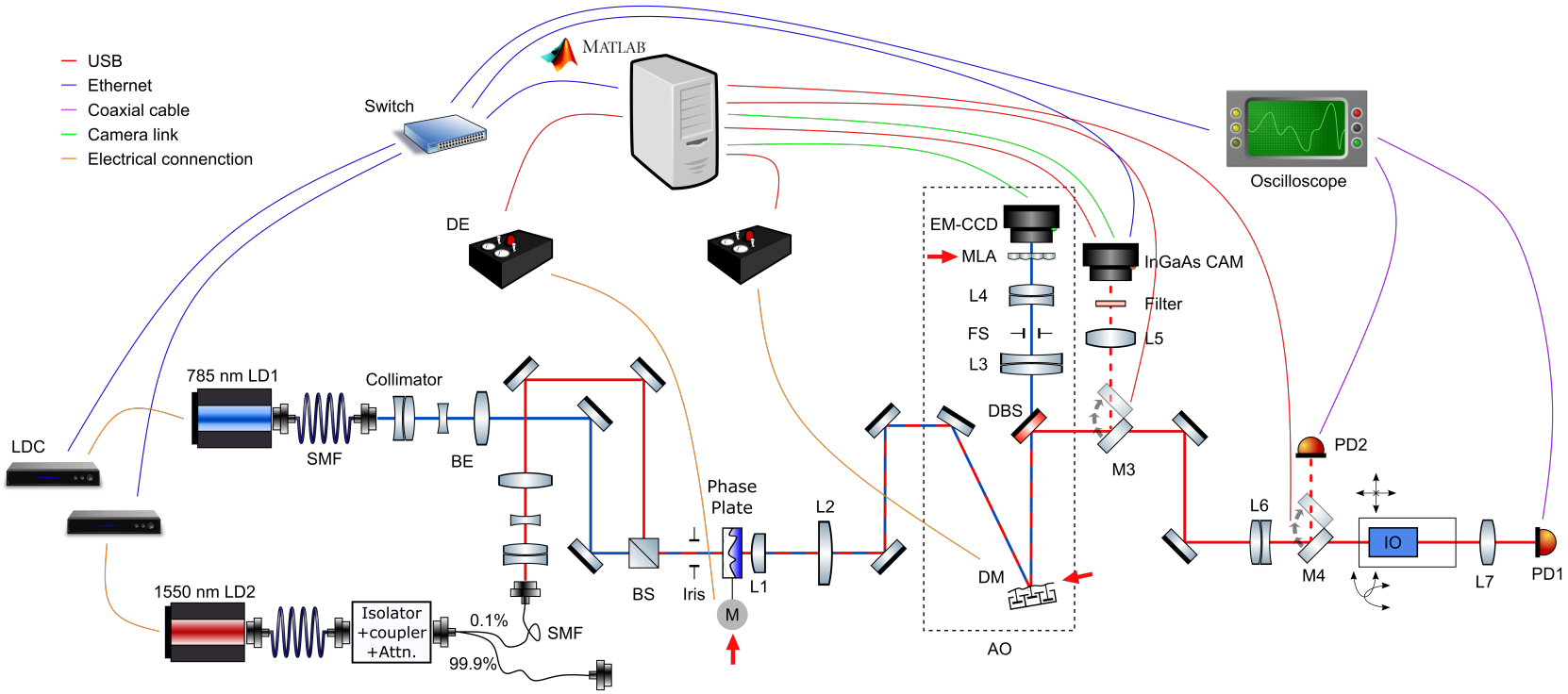

Figure 5.1: Schematic of the testbed. LDC: LD controller, DE: drive electronics, BE: beam expander, BS: beam splitter, M: stepper motor, DBS: dichroic beamsplitter, FS: field stop. Red arrows indicate conjugated pupil planes. The fiber coupler for the 1550 nm LD provides a high power beam that can be launched from either end to ease alignment.

Atmosphere emulator

The combined beams are passed through a phase screen that emulates an atmospheric turbulence layer. The phase screen from LEXITEK (Ebstein, 1996) is a sandwich of 4 optical disks (see Fig. 5.2). The outer 2 are protective windows, while the inner 2 are polymers of nearly matched refractive indices ($\Delta n < 0.001$). The exterior surfaces are planar, meaning that an optical plane wave propagating through the plate will have an optical path difference (OPD) defined by the relief height of the inner interface and the refractive index mismatch

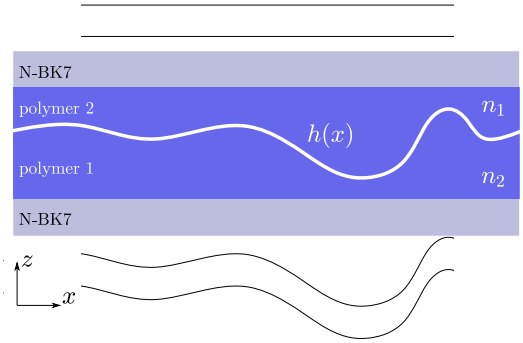

Figure 5.2: Structure of the NIM phase plate. The plate reshapes a planar wavefront propagating downward to have the required statistics.

$$OPD(x) = h(x)(n_1 - n_2) = h(x)\Delta n. \tag{5.1}$$

The near index match between the two materials means that the physical profile variation across the screen to produce a given optical path difference is coarser than that for an air-glass interface. Such relaxation results in a profile difference as high as 75 μm being required to introduce a phase shift of only 1 wave on an incoming planar wavefront at 1550 nm. This allows for engraving the phase pattern using typical CNC machining techniques, greatly reducing fabrication costs. The sandwich is itself cemented between two $\lambda/10$ N-BK7 windows with AR coating. All materials are transparent between 600 nm and 1600 nm, and the dispersion in the refractive index difference Δn of the two polymers is less than 0.001 between 785 nm and 1550 nm. The phase pattern is impressed on an outer annulus of width 24 mm, and thus a maximum beam diameter of 24 mm can be passed through the plate. The plate is mounted off-center to overlap the outer annulus with the beam path, and different pattern realizations can be attained by translating and rotating the plate about its axis.

A pattern that has Kolmogorov statistics with a Fried's parameter $r_0 = 0.6$ mm is impressed on the two polymers before they are bonded. Turbulence strength D/r_0 can be controlled by clipping the emerging beam by an iris down to the required size. The plate is mounted on a rotary stage that can rotate at a maximum of 100 rpm to allow for measurements at different realizations from the screen and simulate wind velocities, in accordance with Taylor's frozen flow hypothesis. Fig. 5.3 shows the phase plate mounted on the rotary stage and the OPD structure used.

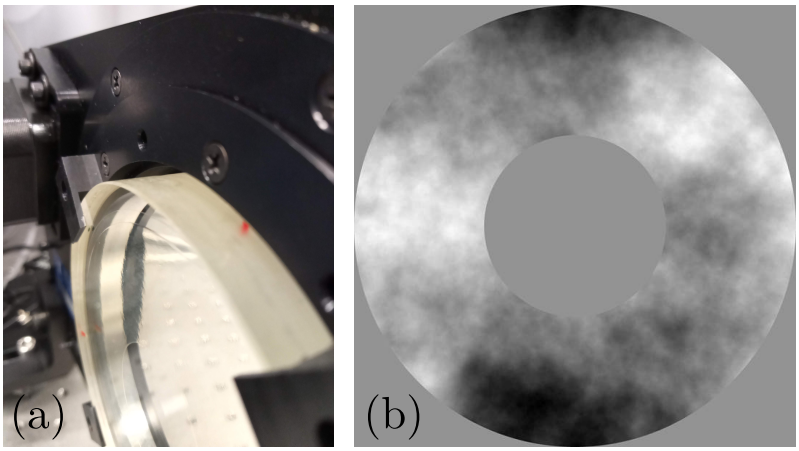

Figure 5.3: (a) Phase plate mounted on a rotary stage. (b) OPD pattern engraved on the screen in (a).

For the smaller beams, a translation stage moves the plate laterally to make use of most of the screen area. An afocal system (L1 - L2) is then needed to image the phase screen with the correct magnification on the DM of the AO system. The telescope lenses are uncoated singlets, and lens pairs that produce the minimum total Seidel aberrations were selected from off-the-shelf catalogs using Zemax. Folding mirrors on kinematic mounts allow for independently realigning the beam to the optical axis every time the afocal system is replaced to vary the turbulence strength, and a removable cage system facilitates the replacement of the lenses.

ALPAO LOAO

The AO setup employed is a turn-key system integrated and supplied by ALPAO SAS. The pre-aligned optical setup consists of the DM, the WFS, and the relay optics necessary to conjugate the two pupils to each other. A PC connected to the WFS and the drive electronics of the DM acts as a controller.

In a closed-loop configuration, the distorted beam is first reflected off the DM toward a dichroic mirror that passes the visible beam through to a beam reducer (L3 - L4) which resizes the beam to match the pupil at the MLA as shown in Fig. 5.1. The MLA is placed at the DM's conjugate plane with the detector at the focal plane of the MLA, 7 mm away. The AO setup is aligned by the vendor and no realignment, except for tip/tilt adjustments of the DM, is necessary upon varying the turbulence strength. The DM, however, must be at the exit pupil, i.e., the conjugate plane of the phase screen, and the afocal system (L1 - L2) is placed appropriately depending on the magnification with the exact distances obtained from Zemax calculations (see Fig. 5.5).

The 13.5 mm DM from ALPAO has a continuous face sheet membrane controlled by 97 magnetic voice coils arranged in a square array inside an octagon, as shown in Fig. 5.4a. The DM can achieve a tip/tilt (P-V) stroke of 60 μm and an inter-actuator stroke > 3 μm. It can attain a flatness of 2.89 nm rms in closed-loop mode and can be driven at a frequency up to 1 kHz before the first resonance sets in. Figure 5.4 shows the measured influence functions of the DM97-15 of the AO setup and the working principle of the voice coils.

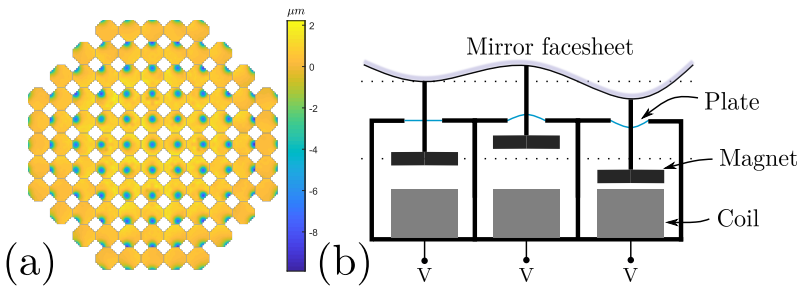

Figure 5.4: (a) Influence functions of the ALPAO DM used in the AO setup, each depicted on the location of its respective actuator. (b) Construction of the magnetic voice coils.

Wavefront sensing is performed downstream of the DM in a closed-loop architecture by a Shack-Hartmann type sensor that consists of a 16×16 MLA with an EM-CCD camera. The EM-CCD from Nüvü has a quantum efficiency QE $> 75\%$ between 500 and 800 nm and a full-frame rate of 1 kHz. The system features a dichroic mirror to split the science beam from the guide star beam, which is resized by a beam reducer (a Keplerian telescope of 2 achromats) to match the size of the lenslet array (2.75 mm). The beam reducer also conjugates the DM pupil to the lenslet

array placed at the exit pupil of the system. A field stop at the image plane between the telescope lenses baffles the light from all sources other than the guide star beam.

The loop is controlled with a PC driven by an Intel i5-8500, 3.0 GHz, 6 cores processor, and 16 GB RAM running a Matlab-based engine developed by ALPAO. The pure delay, i.e., the time it takes the PC to have the DM commands ready after the end of an exposure, is 1.38 ms (as measured by ALPAO). The loop can be closed at 500 Hz with the WFS camera operating at maximum frame rate with sufficient photons available for each frame to guarantee a high SNR (camera requires 3 photons/frame/subaperture for SNR $= 1$). The rejection (correction) bandwidth, i.e., the maximum Greenwood frequency that can be corrected for, is the figure of merit most significant here, and for this system, it is about 20 Hz. The partial correction nature of the LOAO system is clear from the limited number of modes (97) it can correct for (spatial limitation) and the maximum Greenwood frequency it can track (temporal limitation) compared to the needs of large and very large telescopes.

Relay and coupling optics

The corrected science beam reflected out of the AO system can be directed toward a focusing lens where the PSF is imaged with a C-RED2 InGaAs camera (Feautrier et al., 2017). The focusing lens (L5) has a long focal length $f = 1$ m to enlarge the PSF on the detector and thus increase the resolution. With the diameter of the DM, $\phi = 13.5$ mm, the Airy disk of the diffraction-limited PSF has a linear size of 0.28 mm at $\lambda = 1550$ nm. This is sampled by $\sim 19 \times 19$ pixels on the detector, guaranteeing that larger speckle patterns are well sampled for further calculations. The corrected beam can also be passed to a coupling lens with a 6-axis positioner at the focal plane. Fibers and integrated optics components can be precisely aligned to the optical axis at the focus with a LUMINOS nano-positioner. A 10 nm resolution can be achieved for x and y alignment, while 50 nm is possible for the less stringent z axis. Pitch and yaw can be adjusted with a resolution of 0.2 arcsec. The same $f = 75$ mm lens is used for all fibers. With the beam diameter at the lens equal to the DM aperture, i.e., $d = 13.5$ mm, an $f/5.56$ beam results, close to the optimum for coupling into an $NA = 0.1$ SMF at $\lambda = 1550$ nm as shown in Fig. 5.11. The optimum $f/\#$ for coupling into SMFs of a different NA or FMFs is different, but 5.5 is roughly the midpoint where sufficient coupling is expected for all the cases considered. The spot at the output of the component under test is imaged by a coated

convex lens (L6) onto a PD. This arrangement allows for measuring the total output power of the diverging beam out of the waveguide without the need to place the PD arbitrarily close to the component. By choosing the right lens, the imaged spot can be made small enough to fit inside the active area of the PD within the limits allowed by conservation of étendue. Such an arrangement is necessary because the femto-watt PD has a small active area (0.2 mm^2), making it difficult to entirely capture the diverging beam directly after the fiber. The highly sensitive InGaAs PD has a noise equivalent power (NEP)= 7.5 fW and bandwidth $BW = 25$ Hz. The two PDs were calibrated against each other using the fiber port-lens-PD setup across their dynamic range, i.e., 10 fW - 100 pW.

To measure the total power available for coupling at the aperture, a flip mirror (M4) reflects the converging beam behind L6 toward a second PD aligned at the focus. Coupling efficiency can thus be quantified. Flip mirrors instead of beam splitters are used to avoid NCPA and the chromatic response of BSs with regard to split ratios. A 200 MHz, 8 bits oscilloscope is used to average and digitize the voltages of the PDs.

Realignment of tip/tilt and defocus are usually required before a measurement run. The DM mount is adjusted to reduce tip/tilt to lower than 0.1 μm rms, and the afocal system (L1 - L2) is adjusted to correct defocus. Calibration is then performed to record the influence functions and calculate the eigenvalues of the influence matrix. A realignment is required anytime the largest and the smallest eigenvalues differ by more than an order of magnitude (condition number > 10).

A feedback loop is closed between the C-RED2 camera and the DM (on top of the main AO loop) to correct for temperature-induced tip and tilt in the IR arm only and hence not seen by the WFS. Wavefront error, temperature, and humidity are logged for the open-loop case to ensure that creep and memory effects as reported by Bitenc et al., 2014 do not introduce measurement artifacts.

Testbed ray traces (Zemax models)

To decide on the off-the-shelf optics needed for the experimental setup (see Fig. 5.1), the optical train is designed sequentially using Zemax. The science and the guide star arms are simulated separately at their respective nominal wavelengths. Moreover, since the set of lenses for the Keplerian telescope (L1 - L2) are different for each desired D/r_0 point, the ray tracing is repeated for each set. The optics are

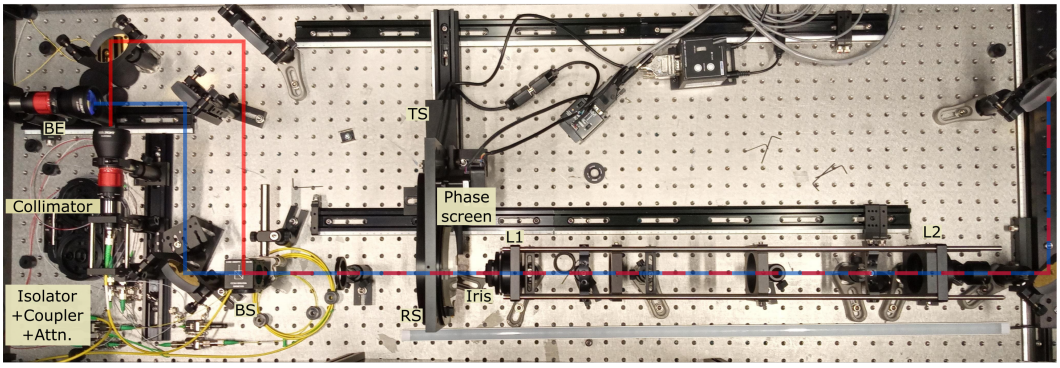

(a)

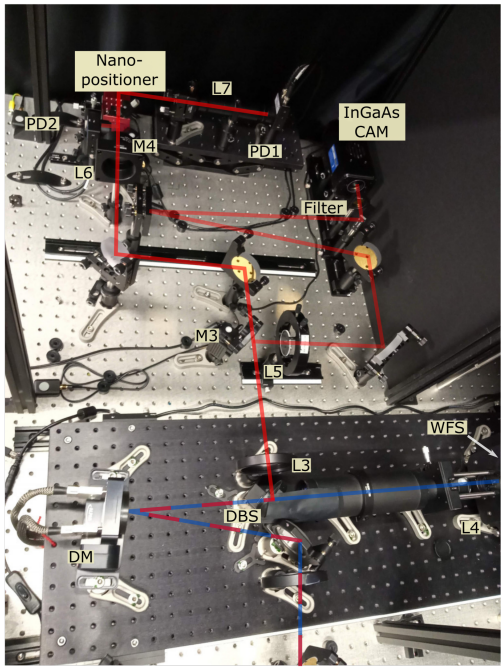

(b)

Figure 5.5: Pictures of the testbed. (a) Sources and atmospheric emulation setup. RS: rotary stage. TS: translation stage. (b) AO, coupling, and imaging setups.

chosen such that the coupling efficiency is maximized, which is the case when the f-number is optimized (see Sec. 3.6.1 and Sec. 5.2.4), and the total aberrations are minimized. The boundary conditions for the design are the wavelengths and the diameter of the DM, i.e., the system's aperture stop. The design of the AO subsystem was shared by ALPAO upon delivering the setup.

Apart from helping with the selection of the optics, the ray traces were crucial for aligning the components. The most problematic to align is having the DM at

the image plane of the phase screen, and Zemax was used to get the correct axial separations. Fig. 5.6 shows the ray trace of one instance along with its Seidel aberrations.

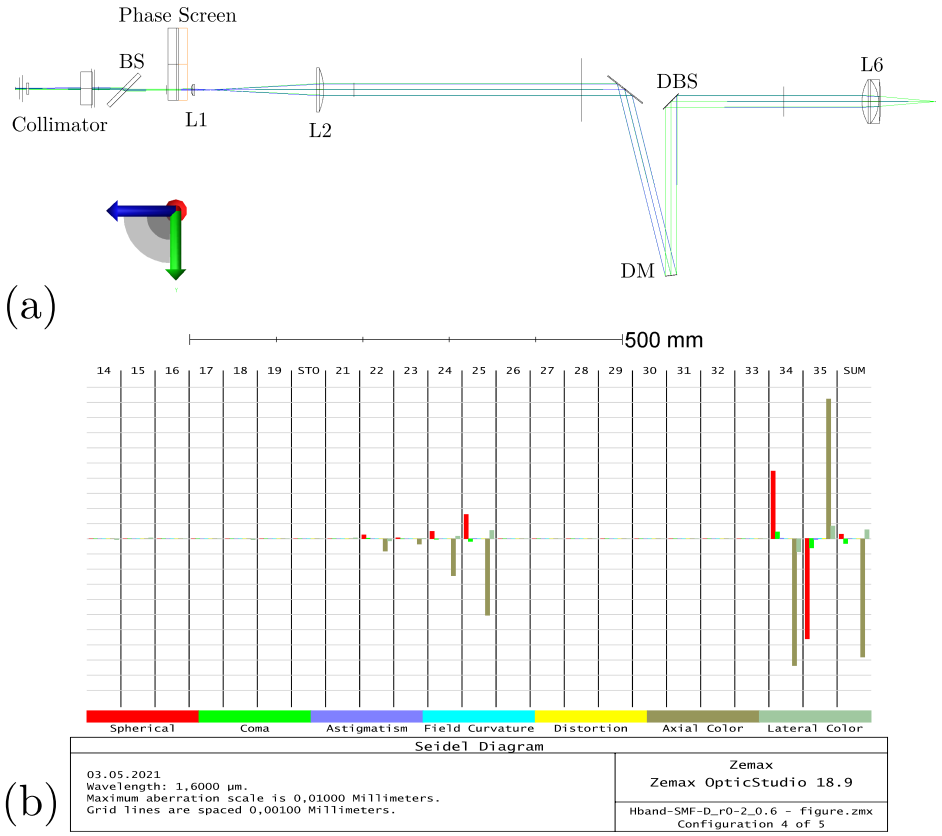

Figure 5.6: (a) Ray trace of one configuration of the science arm of the testbed. 5 configurations were designed to emulate 5 different D/r_0 scenarios. (b) Seidel diagram showing the primary aberration contributions of the optics in the testbed (24/25 surfaces belong to L2 and 34/35 surfaces belong to L6) .

5.1.2 Control software

Closing the loop and driving the DM is done using ALPAO Core Engine (ACE) (Schimpf et al., 2014). ACE is a Matlab environment, object-oriented toolbox that provides classes for interfacing the DM and the WFS and allows different modes of operation, e.g., closed-loop, feed-forward with Zernikes, zonal and modal reconstruction. Data acquisition and control of the rest of the equipment, i.e., LDs, rotary stage, InGaAs camera, flip mirrors, translation stage, and oscilloscope, are also done through Matlab.

Matlab scripts were written to automate measurements of coupling efficiencies, capture PSF images and collect relevant wavefront information. Due to the stochastic nature of atmospheric turbulence, one is usually interested in metrics averaged over an ensemble of phase screens for variables sensitive to atmospheric effects, e.g., the number of speckles in the PSF, wavefront error, or coupling efficiency of light into a waveguide. The script, therefore, rotates and translates the phase screen in steps and records the measurements from the 2 PDs and the 2 cameras, consequently.

Objects from ACE classes are used to control the AO system as desired. The effects of closing the loop, compensating for tip/tilt only or correcting with a limited number of modes on coupling, and the anatomy of the PSF can all be tested seamlessly. Post-processing the PSF images yields additional information about the *SR*, EE, and the centroid shift, i.e., image motion. Additionally, wavefront measurements are also recorded.

The LDs currents are adapted by the software to maximize the PDs utilization, i.e., make full use of their dynamic range. The integration time of the InGaAs camera is then automatically set to prevent saturation while maintaining the highest possible SNR. Moreover, the software performs the necessary dark current and background subtractions for the PDs and the InGaAs camera.

Besides analyzing the PSF, the InGaAs camera can also be used to provide feedback for correcting the residual tip/tilt errors in the IR beam induced by temperature variations after alignment. Temperature and humidity at the DM, the nano-positioner, and the MLA are monitored in case creep and memory effects in the DM (Bitenc et al., 2014) are suspected of causing any anomalies seen in long-term open-loop experiments.

5.1.3 Testbed limitations

To give an impression of the capabilities of the testbed, presented here are examples of the results one can obtain for a turbulence strength of $D/r_0 = 8.3$ and the FG025LJA multimode fiber from THORLABS. Figure 5.7 shows an example of the data collected for one measurement point. The trends in Fig. 5.8 show the variations in coupling efficiency and wavefront rms errors across the phase screen.

The PDs are the highly sensitive PDF10C from THORLABS. With an NEP of 7.5 fW, they can measure coupling efficiencies as small as 75×10^{-6}. The calibration table of the PDs is made available for the coupling calculations script. Optical power

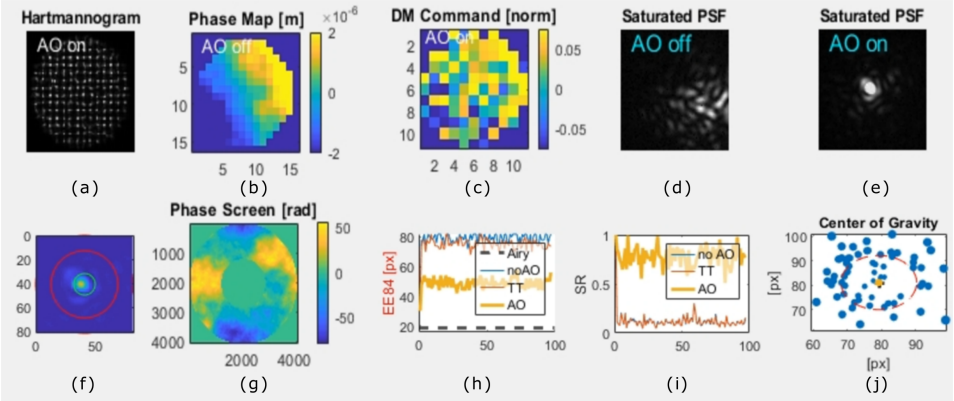

Figure 5.7: Cameras images and calculated parameters for one instance. (a) and (b) WFS image and the calculated phase, respectively. (c) commands sent to the DM by ACE. (d) and (e) PSFs before and after correction, respectively. (f) PSF containment within the fiber core. (g) phase screen. (h) 84% encircled energy. (i) Strehl ratio. (j) scatter plot of PSFs centroids distribution around the fiber before tip/tilt correction.

measurements, taken for one instance of a phase screen, are averaged for a few seconds in the oscilloscope to minimize the effect of electronic noise in the PDs.

For cases of high turbulence strength ($D/r_0 > 15$), the loop might diverge due to the highest order modes having too low eigenvalues, i.e., the influence matrix being ill-conditioned, or the wavefront error being greater than the maximum DM stroke. The software optimizes the number of modes accordingly by filtering as many higher-order modes as necessary to prevent the loop from diverging.

The largest unobstructed beam diameter that can be passed through the atmosphere emulator is 24 mm, limiting the turbulence strength to $D/r_0 = 40$. The complete aperture of the screen with a diameter of 83 mm can, in theory, be used but with an obscuration of $\sim 40\%$. For small beams, the limiting factor is the magnification (L2/L1) that one requires to enlarge the beam to match the aperture of the DM. The testbed components are optimized for the whole H-band, but a tunable or a broadband NIR light source is required to perform spectral measurements. For temporal response measurements, the phase screen can be spun continuously by the rotary stage, but the limitation of the control loop bandwidth is set by the 6 cores, 3 GHz PC used to close the loop. Astronomy-grade AO systems, in contrast, have real-time computers with pure delays in the order of $\sim 100\ \mu$s.

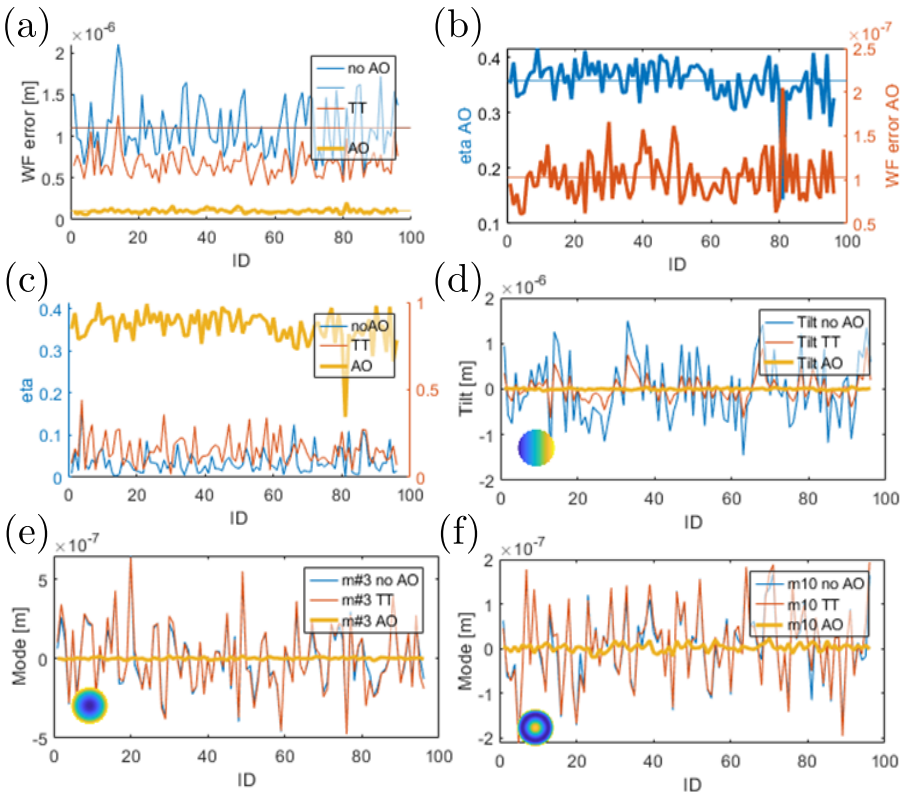

Figure 5.8: Testbed results for the coupling efficiency for a circular, step-index 6 modes fiber and wavefront errors across the phase screen. (a) rms wavefront error for the uncorrected case (blue), tip/tilt compensated (orange), and AO corrected case (yellow); (b) coupling efficiency and rms wavefront error for the AO corrected case; (c) coupling efficiency for the uncorrected, tip/tilt corrected, and the AO-corrected cases; (d), (e), and (f) variations of tilt, defocus, and spherical aberrations around the screen, respectively.

5.2 Simulations and experimental results

This section was published as

Diab, M., Dinkelaker, A. N., Davenport, J., Madhav, K., & Roth, M. M. (2021). Starlight coupling through atmospheric turbulence into few-mode fibres and photonic lanterns in the presence of partial adaptive optics correction. *Monthly Notices of the Royal Astronomical Society*, *501*(2), 1557–1567. https://doi.org/10.1093/mnras/staa3752

5.2.1 Abstract

Starlight corrupted by atmospheric turbulence cannot couple efficiently into astronomical instruments based on integrated optics as they require light of high spatial coherence to couple into their single-mode waveguides. Low-order adaptive optics in combination with photonic lanterns offer a practical approach to achieve efficient coupling into multiplexed astrophotonic devices. We investigate, aided by simulations and an experimental testbed, the trade-off between the degrees of freedom of the adaptive optics system and those of the input waveguide of an integrated optic component leading to a cost-effective hybrid system that achieves a signal-to-noise ratio higher than a standalone device fed by a single-mode fiber.

5.2.2 Introduction

As telescope apertures increase in diameter, optical instruments at their foci such as spectrographs need to proportionally expand in size to make use of the additional flux without compromising performance, e.g. resolving power or sensitivity (Spanò et al., 2006; Spanò et al., 2008). This results in costly instruments with large physical dimensions, making them more sensitive to vibrational and environmental changes. Photonic technologies offer an opportunity to avoid bulk optics, thus limiting the increase in size. Using integrated optics (IO) to manipulate starlight in astronomical instruments before detection– an emerging field known as astrophotonics– has the potential of reducing the footprint and mass of astronomical instruments, cutting costs owing to simpler vacuum and thermal control, enhancing performance, and enabling multiplexing (Minardi et al., 2020).

Photonic spectrographs (Blind et al., 2017), e.g. arrayed waveguide gratings (AWGs) (Bland-Hawthorn et al., 2006), fiber Bragg gratings for OH suppression (Bland-Hawthorn et al., 2011; Rahman et al., 2020), and photonic beam combiners, e.g. GRAVITY (Eisenhauer et al., 2008) and discrete beam combiners (DBCs) (Minardi, 2012; Minardi, 2015), need to operate in the single mode regime in order to deliver their promised spectral resolution, filter characteristics and phase retrieval capabilities, respectively, while avoiding modal noise and focal ratio degradation. Coupling a seeing-limited point spread function (PSF) at the focus of a large telescope into a single mode waveguide is challenging and typically results in low efficiency. Two mitigation techniques can be applied to enable the use of a photonic instrument behind a ground-based telescope: On the one hand, an extreme adaptive optics (ExAO) system may be used to entirely correct for the atmospheric aberra-

tions present in the received wavefronts, and in doing so convert the focal speckle pattern into a diffraction-limited spot that couples efficiently into a single-mode fiber (SMF). On the other hand, a photonic lantern can be employed to split the optical power coupled from the telescope into multiple SMFs (Leon-Saval et al., 2005). ExAO systems have more degrees of freedom and run faster than conventional AO systems to deliver high Strehl ratios ($SR > 0.8$ in NIR) but can only do so for bright objects that act as their own guide stars (Guyon, 2018). As a result, they are more suited to high-contrast imaging of exoplanets and circumstellar disks. They also tend to be notoriously expensive for midsize (2 – 4 m) telescopes and can overwhelm the cost of the telescope itself.

Photonic lanterns, conversely, are mode converting devices that redistribute multimodal light into multiple single-mode beams. They do so by guiding the light through an adiabatic taper from a multimode core to several single-mode cores. If the transition is gradual and the number of SMFs is equal to or greater than the number of modes supported by the multimode port, the conversion is theoretically lossless. Degrees of freedom are therefore conserved and the second law of thermodynamics (brightness theorem) is not violated (McMahon, 1975). A copy of the IO-based astrophotonic device, which tends to be inexpensive to replicate, is then needed at the output of every SMF in order to recover all the collected flux. The number of modes required to efficiently couple starlight at a telescope's focus scales as the square of the aperture diameter. This results in $\sim$ 100s of modes being required and consequently $\sim$ 100s of single-mode channels at the output of the photonic lantern (almost 1000 modes for a 4 m telescope at median seeing). While such complex lanterns can, in theory, be fabricated, the total flux divided among too many channels will result in every SMF having a fractional share of the total optical power comparable to, or even less than, the noise floor of the detector. Accumulating these noisy signals in post-processing would result in a signal-to-noise ratio (SNR) smaller than that had all the flux been collected by a sole SMF directly from the focal plane to the instrument.

An alternative approach is to combine the two techniques, i.e. AO and photonic lantern, as illustrated in Fig. 5.9. Here, the goal is to partially correct the incident wavefront using a low-order adaptive optics (LOAO) system first to reduce the modal content down to a manageable number ($\sim$ 10s) before coupling the starlight into the multimode port of a reasonably-sized photonic lantern where a multiplexed photonic spectrograph like the instrument suggested by Watson (1995) and PIMMS (Bland-

Hawthorn et al., 2010) can be used at the single-mode output ports. The same signal, e.g. spectrum, is thus measured multiple times. Such a hybrid solution is potentially less expensive than employing an ExAO system and amplifies the SNR compared to a standalone photonic lantern. To find the optimum trade-off between the complexity, i.e. degrees of freedom, of the LOAO system, and the number of modes, i.e. degrees of freedom, of the photonic lantern, a study of how an LOAO system affects the form of the PSF for various turbulence strengths and how coupling efficiency into fibers depends on the number of modes, is needed. The trade-off can vary for different instruments: depending on readout noise (RON) and other detector properties, an optimum number of SMFs exists for a given LOAO system such that the SNR of the accumulated signal is maximized.

Coupling through turbulence directly into SMFs has been studied for both astronomy and free-space optical (FSO) communication applications (Dikmelik et al., 2005; Ruilier, 1998; Shaklan et al., 1988). Horton et al. (2007) calculated coupling into FMFs numerically for the diffraction-limited case while Zheng et al. (2016) explored coupling via seeing-limited telescopes but only up to 4 modes. Coupling into a 1×7 photonic lantern of high Strehl ratio PSFs was demonstrated on-sky using the ExAO available at the Subaru telescope (Jovanovic, Schwab, et al., 2017) and experimentally without correction for FSO scenarios by Tedder et al. (2020).

Here we study systematically for the purposes of H-band astronomy the dependence of throughput and SNR on the turbulence strength, the extent of AO compensation, the number of modes sustained by the coupling waveguide, the setup geometry (its f-number) and the detector quality. Section 5.2.3 revisits the basic physics and the mathematical tools used to obtain the necessary models for the atmospheric layer, the AO system, and the waveguides considered. The simulations run utilizing those models to calculate the dependency of coupling efficiency on f-number and turbulence strength are described in Section 5.2.4. An experiment is devised around an LOAO setup to validate the simulation results and check for deviations in the models. Both the experimental setup and the results obtained are presented in Section 5.2.5.

5.2.3 Methodology

The mathematical models used to calculate the coupling efficiency of atmospherically-distorted starlight into fibers are discussed here. First, the wavefronts are propagated through a ground atmospheric layer before getting clipped by an entrance pupil. The

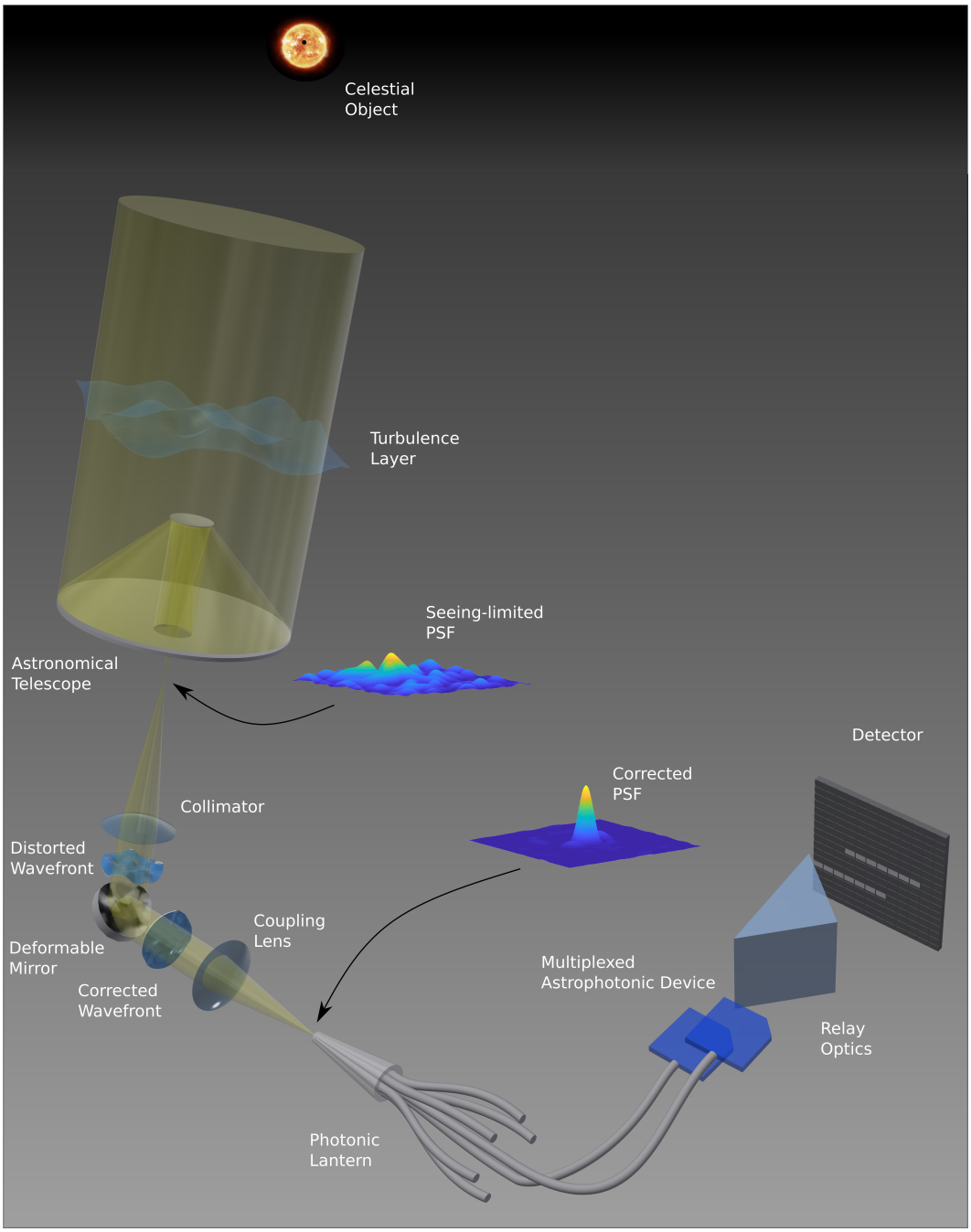

Figure 5.9: Concept overview. Starlight collected by an astronomical telescope is corrected by an AO system before getting coupled into a photonic lantern. Replicas of an astrophotonic device at the SMFs tips manipulate copies of the same signal to generate multiple images at the detector that can be stacked in post-processing.

corrugated wavefronts are then passed through an AO system to calculate the partially corrected beams and their residual error. Next, the corrected wavefronts are propagated to the focus where the coupling efficiency of the collected light into SMFs and FMFs is calculated using the supported modes of the waveguides.

Atmospheric turbulence

Distant celestial objects observed through apertures appear as point sources emitting electromagnetic waves of planar phase fronts and uniform intensities at the top of Earth's atmosphere. Upon propagating through the turbulent atmosphere, the optical field's phase and amplitude are distorted before reaching ground-based telescopes. The distortion in phase (F. Roddier, 2008) results in the deformation of the PSF from the diffraction-limited Airy pattern, where 84 per cent of the total power is within one central disk, into a speckle pattern where the collected power is spread among many loci, the number of which depends on the state of the atmosphere and the diameter of the collecting telescope (see Fig. 5.9). The weak overlap of such a speckle pattern with the first few modes of a step-index fiber means that coupling starlight efficiently into a narrow waveguide cannot be achieved without compensating for the atmospheric turbulence or increasing the number of modes that the fiber supports. An LOAO system can partially correct the corrugated wavefront prior to coupling because it has the effect of redistributing most of the optical power from the speckles back into a central core, albeit with a background halo, and thereby improving the coupling efficiency into FMFs.

To include the effects of turbulence on light propagating through the atmosphere and subsequent wavefront correction, mathematical models have to be identified and implemented in wavefront calculations. Realizations of the atmospheric-induced wavefront phase distortion, called phase screens, that have ensemble statistics matching those predicted by Kolmogorov's 1941 theory of turbulence (Kolmogorov, 1991) are computed (Welsh, 1997). This is a modal-based representation in which the wavefront is assumed to be a superposition over the aperture of infinite orthogonal basis functions or modes. The basis functions are assigned zero mean Gaussian pseudorandom coefficients that possess the desired variance. In doing so, the modal-based approach avoids the shortcomings of sample-based methods, namely the underrepresentation of low spatial frequencies.

An LOAO system is a single conjugate adaptive optics (SCAO) system of modest

capabilities. SCAOs are limited to corrections of a single atmospheric layer, which in this case is taken to be the ground layer at the pupil where most of the distortions occur. The phase screens simulating the ground turbulence layer are non stationary random functions that can be described by structure functions introduced by Kolmogorov

$$D_\phi(\rho) = \langle |\phi(\vec{r}) - \phi(\vec{r}+\vec{\rho})|^2 \rangle, \tag{5.2}$$

where $\phi(\vec{r})$ is the phase at a point located by the vector $\vec{r}$ and $\phi(\vec{r}+\vec{\rho})$ is the phase at a point a distance $\rho = |\vec{\rho}|$ away. The von Kármán power spectral density (PSD) associated with this structure function is (Hardy, 1998)

$$\Phi(\kappa) = 0.023 \left| \kappa^2 + \frac{1}{\mathcal{L}_0^2} \right|^{-11/6} r_0^{-5/3}, \tag{5.3}$$

where κ is the spatial frequency, $\mathcal{L}_0$ is the outer scale, and r_0 is the convenient Fried parameter (Fried, 1965) that quantifies the accumulated turbulence strength over the thickness of the turbulence layer, defined as

$$r_0 = \left[0.423 k^2 \sec\gamma \int_0^\infty C_n^2(h) dh \right]^{-3/5}, \tag{5.4}$$

where k is the wavenumber, γ is the zenith angle and $C_n^2(h)$ is the refractive index structure constant at height h above the aperture. The total wavefront variance σ_ϕ^2 in terms of turbulence strength is $1.03(D/r_0)^{5/3}$. Therefore r_0 defines the telescope aperture of diameter D over which the variance in phase $\sigma_\phi^2 \approx 1$ rad^2. The PSD of the von Kármán spectrum in Eq. (5.3) differs from Kolmogorov's in one aspect: it assumes a finite outer scale $\mathcal{L}_0$ and thus suppresses the contribution of frequencies lower than $1/\mathcal{L}_0$. In doing so, it avoids the infinite power in Kolmogorov turbulence as $\kappa \to 0$. Values for $\mathcal{L}_0$ differ for different observation sites and measurements in the literature disagree widely, but in general it has a value in the range $1 \sim 100$ m, meaning an exact value is superfluous for small telescopes as it only amounts to an overall tilt (Hardy, 1998). In this work we assume $\mathcal{L}_0 = 20$ m, an average of the values measured for the Mauna Kea Observatory (20 m), the Observatoire de Haute Provence (23 m) (Maire et al., 2007), and the Palomar Observatory sites (17.5 m) (Ziad et al., 2004). Due to the random nature of atmospheric turbulence, all calculations affected by it need to be taken as averages over a large number of

screens. Here, 85 screens are used which is found to produce a relative standard deviation in the metrics in question that is lower than unity. The fractal nature of Kolmogorov's phase screens allow for scaling the aperture size down to convenient diameters since the statistics remain the same inside the inertial range $[\ell_0, \mathcal{L}_0]$, apart from a scale factor (Lane et al., 1992).

Partial adaptive optics correction

To include the effect of partial AO correction on the corrugated wavefronts, the influence functions of an ALPAO DM97-15 are used to model the deformable mirror (DM). The DM is highly linear (Gorkom et al., 2018), i.e. its actuators are decoupled and the influence functions completely characterize its behavior. With 97 actuators arranged inside an octagon, 11 actuators are on the longest axis across the diameter. Projected on a midsize 4 m telescope, each DM segment would have a projected size $d = 0.36$ m on the entrance pupil. Since a DM only corrects for optical path delays between its actuators and cannot correct those within an actuator's action area, this configuration can only attain the diffraction limit, $\sigma_\phi < 1$ rad, for seeing conditions $r_0 > 0.36$ m. At median seeing conditions for H-band astronomy ($r_0 \sim 0.1$ m), the mean square fitting error is $\sigma^2 \approx 3$ rad^2 (for a continuous facesheet DM) (Miller et al., 2003); ergo, the correction is partial (Hardy, 1998). Qualitatively, the PSF of such a partially corrected wavefront has a central core with an angular radius $\sim \lambda/D$ and a background halo with an angular radius $\sim \lambda/r_0$.

To calculate the commands for the DM, the wavefront is propagated through a model of a Shack-Hartmann wavefront sensor (SH-WFS) that has 10×10 subapertures. With actuators at the corners of subapertures, this represents a Fried geometry. Instead of phase, local wavefront slopes inside the subapertures are sensed by the SH-WFS. A modal reconstruction is therefore necessary and is performed with the DM influence functions as a basis to calculate the actuators commands

$$\vec{c} = \mathbf{B}^{+}\vec{s}, \tag{5.5}$$

where $\vec{c}$ is a vector that contains the DM commands and $\mathbf{B}^{+}$ is the Moore-Penrose pseudoinverse of the matrix $\mathbf{B}$ that has the WFS response to the influence functions. The system in Eq. (5.5) is underdetermined and therefore lacks a unique solution. The pseudoinverse calculates the solution with the least square departure from a linear fit by performing a singular value decomposition (SVD) that sets the wavefront

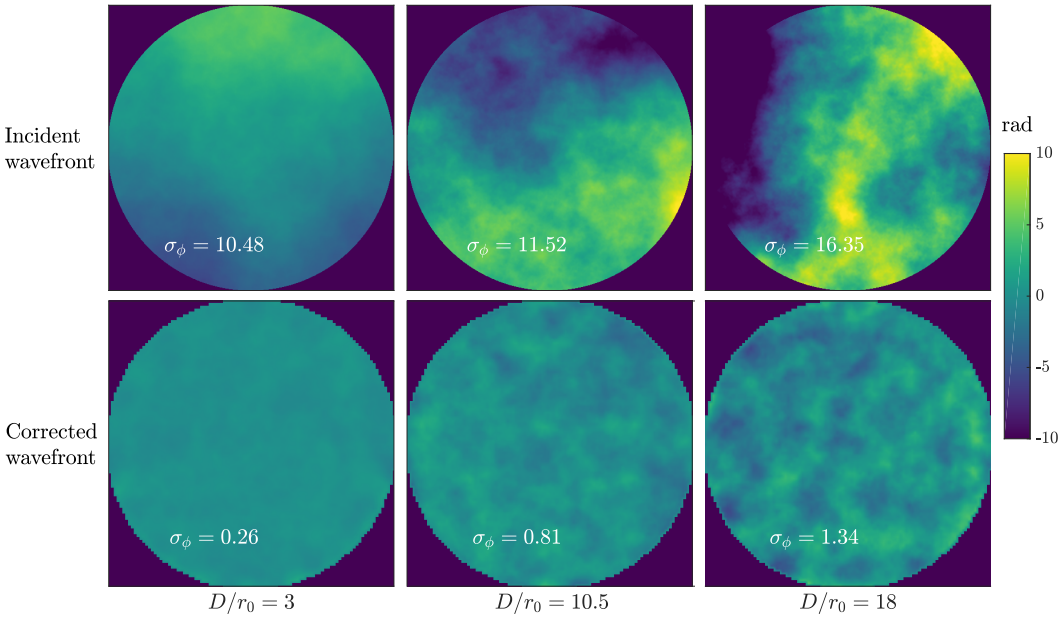

Figure 5.10: Top: piston-compensated phase screens that exhibit Kolmogorov statistics at varying turbulence strengths. Bottom: corresponding corrected wavefronts by a 97 degrees of freedom LOAO system.

modes that have a small WFS response to zero. The vector $\vec{s}$ contains the x and y slopes of the incident wavefront calculated from the center-of-gravity of the focal spots behind the microlens array (MLA). Taking advantage of the DM linearity, the shape of the DM due to the commands $\vec{c}$ can be calculated by

$$\vec{M} = \mathbf{I}^{\intercal}\vec{c}, \tag{5.6}$$

where $\mathbf{I}$ is the matrix containing the influence functions of the DM and $^{\intercal}$ denotes a transpose. Example realizations of wavefronts generated as described in Sec. 5.2.3 and their corrected counterparts are shown in Fig. 5.10.

To calculate the coupling into fibers and DM commands, the conjugate counterparts to the entrance pupil (aperture function) at the telescope focus and at the MLA focal plane are required. Propagating optical fields from pupil planes to focal planes (far-field) is performed by means of the Fraunhofer diffraction equation. A fast Fourier transform (FFT) of the pupil field produces the focal field apart from a coordinate transformation and a scaling phase pre-factor that needs to be included. The optical field at the focal plane, a distance f away, is given by (Goodman, 2004)

$$\psi_F(x,y) = \frac{1}{i\lambda f}\exp\left[i\frac{2\pi}{\lambda}\left(f+\frac{x^2+y^2}{2f}\right)\right]\mathfrak{F}\{\psi_P(x',y')\}_{k_x,k_y}, \tag{5.7}$$

where $\mathfrak{F}\{\psi_P(x',y')\}_{k_x,k_y}$ is the Fourier transform of the pupil field $\psi_P(x',y')$ evaluated at $k_x = x/(\lambda f)$ and $k_y = y/(\lambda f)$. To perform a back-propagation from the focal plane to the pupil plane, an inverse Fourier transform is calculated with the reciprocals of the phase pre-factor and the spatial frequencies instead.

Waveguides

The models for the SMFs and FMFs assume weakly guiding waveguides, i.e. low index contrast between the core (n_{co}) and the cladding (n_{cl}) such that $\Delta n = n_{co} - n_{cl} \ll n_{cl}$, where both the electric and magnetic fields are transverse to the optical axis. Furthermore, circularly symmetric, step-index waveguides are assumed which allow the approximation of the guided waves by the linearly polarized (LP) modes. Given the wavelength, the refractive indices, and the core diameter of the fiber, the LP modes are analytically calculable (Saleh et al., 2019) and represent a complete model for the straight fiber. The number of modes that the fiber supports depends on the normalized frequency $V = 2\pi aNA/\lambda$ where a is the core radius and NA is the numerical aperture, $NA = (n_{co}^2 - n_{cl}^2)^{1/2}$. An SMF has $V < 2.405$ and the number of modes p in a multimode fiber (MMF) scales with V according to $p \approx V^2/4$ for each polarization direction. While this approximation is better suited for larger fibers as FMFs adhere less to geometric optics, it can still be used to estimate the parameters of the fiber before solving for the exact modes.

Coupling of starlight collected by a telescope into fibers is calculated by evaluating the overlap integral between the fiber modes and the PSF. For an incident optical field $\psi_E(x,y)$ and the $i-$th fiber mode $\psi_i(x,y)$, the coupling efficiency is

$$\eta_i = \frac{|\iint dxdy\psi_i(x,y)\psi_E^*(x,y)|^2}{\iint dxdy|\psi_i(x,y)|^2\iint dxdy|\psi_E(x,y)|^2} = \frac{|\langle\psi_i|\psi_E\rangle|^2}{\langle\psi_i|\psi_i\rangle\langle\psi_E|\psi_E\rangle}, \tag{5.8}$$

where the integration window is the smallest area over which neither of the two fields vanishes and the normalization factors in the denominator are to compensate for the possibly unequal total powers contained in the fields.

Further losses, e.g. bending, insertion, and propagation losses, are accounted for in the experimental results but are not included in the models.

The number of modes p required to couple a seeing-limited PSF can be derived from the conservation of étendue (Minardi et al., 2020). In terms of turbulence strength

$$p \approx \left(\frac{\pi D}{2r_0}\right)^2, \tag{5.9}$$

a relation that is more accurate for highly multimode fibers having been derived from geometrical optics considerations. Notice that Eq. (5.9) is nothing but the area of the aperture in units of area elements $r_0 \times r_0$.

Besides SMFs and MMFs (including FMFs) we also consider photonic lanterns in our models. Here, we assume photonic lanterns with weakly-guiding circular step index profiles and the mathematical model described above applies to their multimode ports. The propagation of the field from the multimode port to the SMFs through the transition region depends on the modal content of the coupled field and the transversal geometry of the transition region. Beam propagation methods (BPMs) could be used to simulate the photonic lantern and calculate the distribution of the optical power among the SMFs. However the discrete step-by-step calculations involved in BPMs tend to be slow and it is hence unrealistic to run them for a large number of phase screens. Instead, the assumption that the optical power distributes equally among the SMFs is made to model the downstream segments of the photonic lantern. The SNR calculations given below (Sec. 5.2.4) are a good approximation as long as all SMFs are receiving comparable shares of the total power. Modal noise and scrambling are discussed further in Sec. 5.2.4

A number of different procedures have been considered to realize the necessary taper transition between the MMF and SMFs necessary for photonic lanterns (Birks et al., 2015). Inserting a bundle of stripped SMFs inside a capillary, whose index is lower than the refractive index of the cladding, and tapering the stack down using a glass processor (Davenport (in preparation)) is the method of choice in astronomy because throughput is not compromised. In contrast to lanterns made from multicore fibers (MCFs) or using ultrafast laser inscription (ULI) techniques, this method results in a single-mode section with free fibers that can be readily spliced to other components. This however requires the SMFs in the bundle to be arranged in a close pack to maintain symmetry along the taper. With an SMF at the center, 1, 2, and 3 rings of SMFs arranged in a hexagonal lattice, i.e. a centered hexagonal number, result in bundles that have $q = 7$, 19, and 37 SMFs, respectively (Davenport (in

preparation)). The number of modes sustained by an FMF, p, can be controlled by tuning the normalized frequency V where the modes count increments by 1 as V increases gradually, except for degenerate modes ($LP_{lm}, l \neq 0$) where 2 modes appear together. Opting for theoretically lossless lanterns with more SMFs than modes at the MM section ($p < q$), two of the FMFs considered for the simulations below have $p = 6$ and 36 modes, one mode short of the ideal design.

The LOAO system considered below assumes that tip/tilt are already corrected for by a fast steering mirror (FSM) and that the fiber is aligned at the focus. Aligning SMFs to images of celestial objects at the focal planes of very large telescopes has been achieved with the aid of guiding cameras and can nowadays be done with relative ease (Bechter et al., 2015).

5.2.4 Simulations

A calculations pipeline that propagates the wavefronts perturbed by the atmosphere from the telescope pupil, through the LOAO system to the focus where a fiber is placed, is built using the mathematical tools in Sec. 5.2.3. Estimates for the optimum setup geometry to couple into SMFs and FMFs under diffraction- or seeing-limited conditions can thus be calculated. The boost in coupling that an LOAO system provides as compared to the uncorrected case is studied for various turbulence strengths. The optimum number of channels in a multiplexed astrophotonic device fed by a photonic lantern can therefore be deduced from this pipeline.

In the following subsections, several free parameters are varied to study the dependencies of the coupling efficiency and the SNR before an optimum number of channels is selected for specific cases. The free parameters under study are the telescope properties in form of the f-number (Sec. 5.2.4) as well as turbulence properties (Sec. 5.2.4). The theoretical SNR of the stacked signal detected at the outputs of a photonic lantern is eventually calculated to estimate the optimum trade-off in the size of a multi-channel astrophotonic instrument (Sec. 5.2.4). Additionally, scrambling is discussed in further detail in Sec. 5.2.4.

Coupling dependence on f-number

Coupling of starlight into waveguides depends on the correlation between the PSF and the modes of the waveguide. The PSF is defined by the shape of the aperture and the optical field at the pupil. The linear extent of that pattern however is dependent

on the effective focal length f. As a result, the coupling efficiency depends on the f-number $f/\# = f/D$ of the coupling setup. For a large MMF, one simply considers the ray optics aspect and selects an $f/\#$ that gives a beam slow enough to fit within the acceptance angle, i.e. NA, of the fiber. Diffraction effects are still non-negligible for SMFs and FMFs, and calculating the coupling efficiency as a function of the $f/\#$ around the value predicted by geometric optics is necessary to optimize the system.

Fig. 5.11 shows the dependence of the coupling efficiency η on the f-number $f/\#$ for the SMF and FMFs sustaining $p = 6$, 19, and 36 modes at $\lambda = 1550$ nm. All fibers have $NA = 0.1$ from which the geometrically expected optimum value is $f/\# \approx (2NA)^{-1} = 5$. The efficiency increases rapidly and reaches its maximum values at $f/\#$ around the geometrically predicted values ($f/5.1$ for $p = 36$). For higher p, the efficiency curves plateau for slower beams, but with an additional oscillation. The maximum efficiency values increase with increasing p, from 0.78 for the SMF up to 0.91 and 0.92 for $p = 19$ and 36 modes, respectively. Fig. 5.11 (middle) shows the expected lower η for a seeing-limited case $D/r_0 = 15$ without AO correction. η increases gradually , and following a maximum, gradually decreases instead of plateauing. The position of the maxima for $p = 19$ and 36 mode FMFs, however, are very close to those in the diffraction-limited case (for $p = 36$ modes, the maximum efficiency is reached at $f/5.1$ and $f/4.9$ for the diffraction- and the seeing-limited case, respectively). The dependence of $f/\#_{opt}$ on D/r_0 for the fibers considered is also shown in Fig. 5.11. The optimum coupling $f/\#$ drops as D/r_0 increases due to the focal pattern spreading over a larger area and therefore requiring a faster beam to confine its linear extent. This gradual drop in optimum $f/\#$ and similarity between the curves suggests that a setup designed for the SMF and the diffraction limit may be used for the seeing-limited case with only little effect on coupling. The optimum $f/\#$ established here is used for all subsequent calculations of starlight coupling into fibers.

Coupling dependence on turbulence

The deterioration of coupling efficiency into an SMF and 3 FMFs as seeing worsens is shown in Fig. 5.12. An ensemble of 85 phase screens was used to calculate the overlap integral at each turbulence strength point between the diffraction limit and $D/r_0 = 30$. The improved coupling efficiency that the partial AO-compensation contributes is also plotted. Phase screens generated with the statistics discussed in Sec. 5.2.3 are corrected by the LOAO system described in Sec. 5.2.3 before

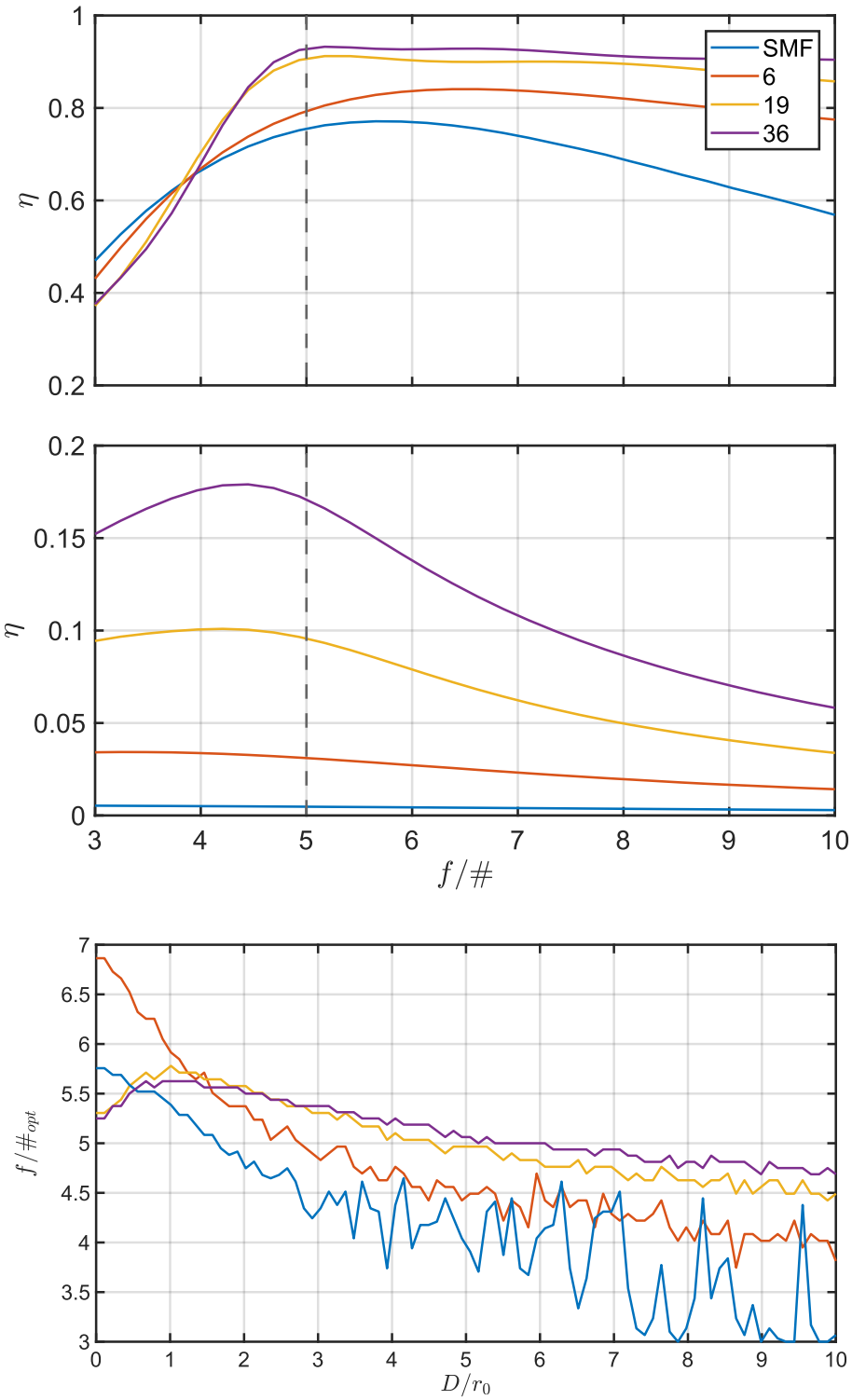

Figure 5.11: Top: coupling efficiency dependence on $f/\#$ for $NA = 0.1$ SMF, 6, 19, and 36 modes FMFs at the diffraction limit. Dashed line indicates the geometrically predicted optimum $f/\#$. Middle: shows the same efficiency dependence, but with added $D/r_0 = 15$ turbulence. Bottom: variation in optimum f-number as turbulence increases.

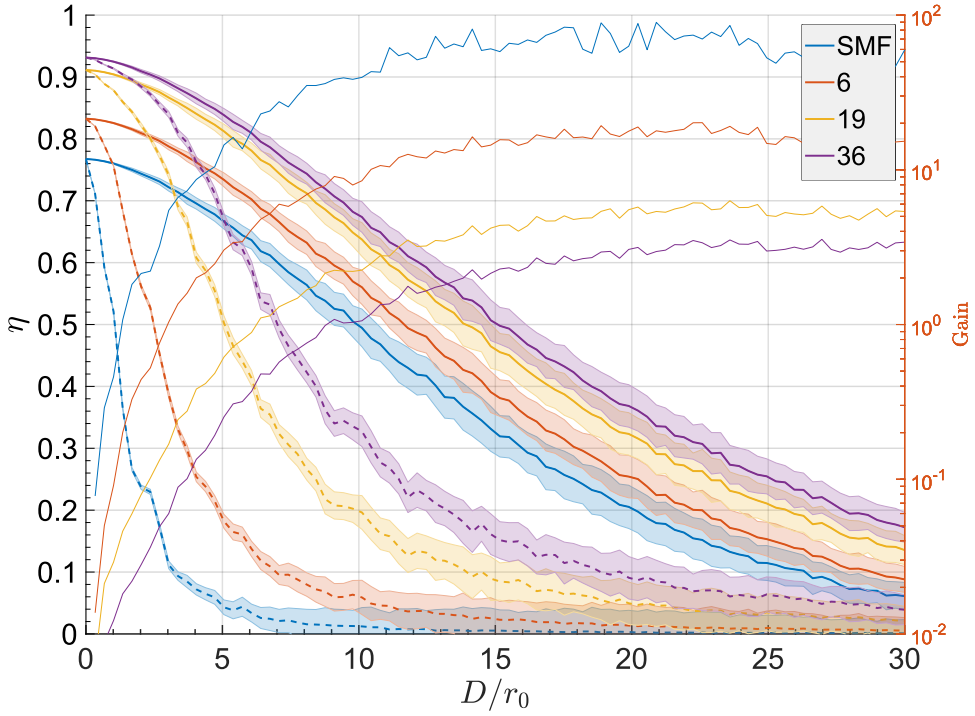

Figure 5.12: Coupling efficiency dependence on D/r_0 for $NA = 0.1$ SMF, 6, 19, and 36 modes FMFs. Solid line: for AO-corrected wavefronts, dashed-line: for uncorrected wavefronts with the shaded bands 2σ wide centered on the average value. Light solid line: gain in coupling with the log ordinate on the right.

coupling into the fibers is computed by Eq. (5.8). For a 4 m telescope at $r_0 = 0.2$ m, $D/r_0 = 20$ and the level of correction that the LOAO system attains is only partial. The coupling efficiency into the SMF is increased a 100 fold to about 20 per cent as depicted in Fig. 5.12. A comparable boost in η between 20 and 3 is attained for the 6 and 36 FMFs at $D/r_0 = 20$, respectively. The operation regime for an LOAO assisted SMF- or FMF-fed astrophotonic instrument can therefore be determined from curves like those in Fig. 5.12.

SNR dependence on turbulence and modes count

In the absence of detector noise as a consideration, maximum throughput could be obtained by using a multi-channel astrophotonic instrument with the highest available number of channels q, in order to maximize flux collection. Detectors are however always noisy. Splitting the total flux into small shares by a photonic lantern and detecting them separately by a noisy detector before accumulating all

the signals in post-processing would only result in a better SNR than using an SMF if the number of channels in the instrument is optimized to the photon flux and the detector's RON. Consequently, the SNR is taken here as a figure of merit to decide on the optimal size of a photonic lantern for a given telescope aperture, seeing condition, target magnitude, AO degrees of freedom, and detector's noise. Sources of noise relevant here are photon shot noise and RON. In a photon-starved application like astronomy, photon shot noise σ_{ph} dominates ($SNR = \sqrt{N_{ph}}$, where N_{ph} is the photons count) and delivering more photons via larger FMFs is thus beneficial. Moreover, the electronic circuit of the detector used to sense the starlight introduces a constant RON independent of photons count every time a pixel is read out. With the total signal distributed into multiple channels and detected at the outputs of the photonic devices over more pixels, every output signal has an RON component and in the aggregated signal the noise accumulates. The multiplexing approach using a photonic lantern can only yield a better SNR than a standalone SMF-fed device for detectors with minimal RON and bright objects under relatively good seeing conditions.

Astronomy-grade NIR detectors typically have RON values in orders of few electrons (Finger et al., 2014) and improved designs for amplifier circuits with sub-electron RON continue to come out (Feautrier et al., 2016). The case for a multiplexed H-band astrophotonic device fed by a photonic lantern is therefore driven by the technological advancements of both integrated optics and NIR detectors along with AO.

A two parameter calculation of SNR variation with D/r_0 and the number of detection channels q is performed to decide on the optimum configuration for the multiplexed astrophotonic instrument. With both photon noise and RON considered, SNR for the accumulated signal is

$$SNR = \frac{\eta \cdot N_{ph}}{\sqrt{\sigma_{ph}^2 + q \cdot \sigma_{RON}^2}}, \tag{5.10}$$

where η is the coupling efficiency and q is the number of channels. Fig. 5.13 shows the SNR as a function of q for the example cases of a faint ($N_{ph} = 10^2$) and a bright ($N_{ph} = 10^8$) sources detected with a $\sigma_{RON} = 3$ e$^-$ detector. For the fainter object, the maximum SNR is attained using a single channel ($q = 1$) device for both cases with and without LOAO correction ([a] and [d] in Fig. 5.13). For the brighter objects on the other hand, SNR grows linearly with the number of channels q for

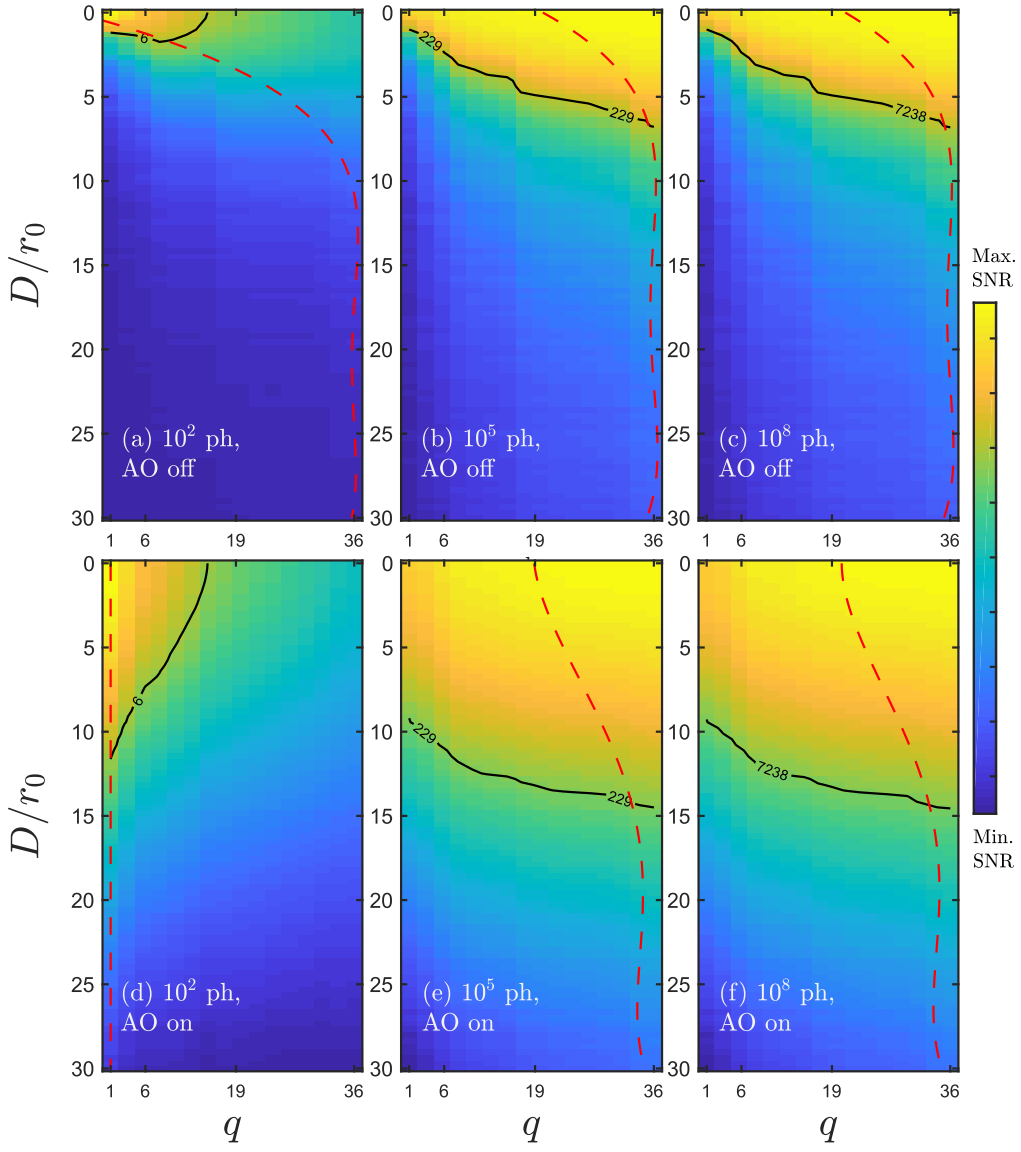

Figure 5.13: SNR dependence on turbulence strength D/r_0 and number of channels q for a detector with RON $\sigma = 3$ e$^-$. Photons count $= 10^2$ photons (left panels), 10^5 photons (middle panels) and 10^8 photons (right panels). Without AO correction (upper panels) and in the presence of AO correction (lower panels). Black contours are isolines of constant SNR at 0.75 of the maximum achievable for the scenario in question. Dashed red lines are polyfits that trace along the 0.99 of the maximum SNR values for each D/r_0 case.

all turbulence scenarios in the uncorrected case ([c] in Fig. 5.13) but saturates at around $q = 19$ channels for the LOAO-corrected case ([f] in Fig. 5.13).

Scrambling

While all MMFs experience modal noise, FMFs are particularly affected due to the wider separation in terms of effective refractive indices between their supported modes. Scrambling the modes to minimize modal noise might be crucial depending on the application, e.g. high precision radial velocity spectroscopy. For a multiplexed astrophotonic instrument, modal noise entails that different replicas of the IO component at the SMFs of the delivery photonic lantern will receive different amounts of light.

Diffraction-limited and partially AO-corrected PSFs, with most of the optical power in a central disk, excite azimuthally-symmetric (LP_{0m}) modes only. As D/r_0 increases, more light is present in speckles away from the PSF core and higher, non-circularly symmetric, LP modes are excited with higher probability. Fig. 5.14 shows the coupling efficiency into each mode of a 6 modes FMF as a function of turbulence strength for the AO-corrected and the seeing-limited cases. This suggests that shifting the corrected PSF away from the center of the FMF in a controlled manner, akin to the speckles in a seeing-limited focal pattern, can improve scrambling (at the cost of efficiency) as is planned for the NIRPS spectrograph (Wildi et al., 2017). Mechanical agitation (Baudrand et al., 2001) and stretching (Chen et al., 2006) on the other hand scrambles the light by transferring the optical power that is coupled dominantly in LP_{0m} modes into the other modes along the fiber. Static scrambling strategies, e.g. octagonal fibers, have also been studied (Chazelas et al., 2010).

At the diffraction limit, the IO replica connected to the central SMF (in a hexagonal pack configuration) will get most of the power. Depending on the application, an astrophotonic instrument might be able to deliver a good performance with an unequal distribution of power between the replicas as long as enough light to achieve an $SNR \gg 1$ reaches every replica. Other applications that require an equal splitting of the total flux would require that the light is scrambled among the SMFs using one of the techniques mentioned above. For applications sensitive to modal noise, further investigation of the suitability of the MMFs modelling and scrambling methods for FMFs is needed since the statistical treatment of the fiber noise in large MMFs (Grupp, 2003) is not appropriate for modelling FMFs.

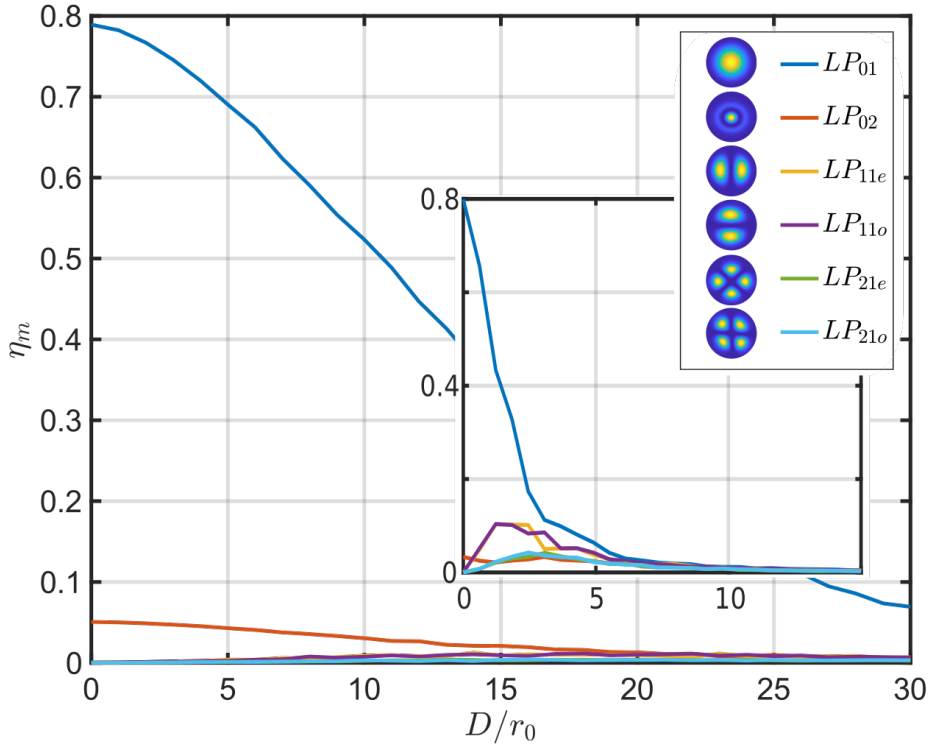

Figure 5.14: Contribution of individual modes to coupling efficiency into a 6 modes FMF. Inset shows the uncorrected case. Notice the different ranges on the abscissae.

The substantial contribution of LP_{0m} modes to coupling as compared to the other modes presents an opportunity for mode-selective photonic lanterns (MSPL). By breaking the symmetry between the SMFs in a photonic lantern, a one-to-one definitive mapping can be enforced between the excited modes and the SMFs (Leon-Saval et al., 2014). This results in the optical power coupled into the multimode port being guided dominantly to a subset of all the SMFs present, reducing the number of channels and alleviating the effect of the detector's RON. The natural scrambling that takes place due to the atmospheric turbulence limits the utilization of MSPLs for the uncorrected wavefronts case (see Fig. 5.14).

5.2.5 Experiments

To validate the aforementioned coupling models, the experimental testbed in Fig. 5.15 is built around an LOAO system. The measurements are performed using two light sources, one of which is the science beam at 1550 nm that simulates star light and a second beam at 785 nm as guide star for the AO system. The coupling models are tested by recreating the simulated scenarios and measuring the cou-

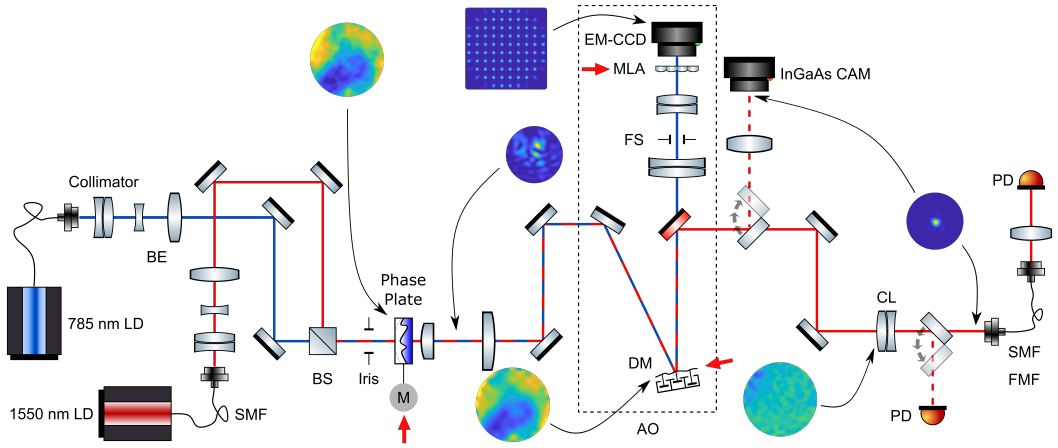

Figure 5.15: Experimental setup. BE: beam expander, BS: beam splitter, M: stepper motor, CL: coupling lens. Red arrows indicate conjugated pupil planes.

pling efficiency. The main parts of the experimental testbed are described in the following subsections, including the LOAO system (Sec. 5.2.5), the atmospheric emulator (Sec. 5.2.5), the relay and coupling optics (Sec. 5.2.5), and the fiber optics (Sec. 5.2.5), with the experimental results presented in Sec. 5.2.5.

Atmosphere emulator - Phase screen

The two beams that emulate the astronomical science target and the guide star are provided by a 1550 and a 785 nm fiber-coupled laser diodes, respectively. The beams are collimated by doublet achromats and enlarged by Galilean beam expanders to 24 mm diameters. Light polarization is not maintained. The beams are reflected off folding mirrors that steer them toward a beam splitter where the visible beam is transmitted and the NIR beam is reflected onto a common axis (c.f. Fig. 5.15). The combined beams are passed through a phase screen mounted on a rotary stage. The phase screen from LEXITEK is a 100 mm diameter plate of two polymers of similar but unequal refractive indices bonded together (Ebstein, 1996). The near index match between the two materials means that the physical profile variation across the screen to produce a given optical path difference is coarser than that for an air-glass interface. This relaxation results in a profile difference as high as 75 μm being required to introduce a phase shift of only 1 wave on an incoming planar wavefront at 1550 nm. This allows for engraving the phase pattern using typical CNC machining techniques. The sandwich is itself cemented between two $\lambda/10$ BK-7 windows with AR coating. All materials are transparent between 600 nm and 1600 nm and the dispersion in the refractive index difference Δn of the two polymers

is less than 0.001 between 785 nm and 1550 nm. The phase pattern is impressed on an outer annulus of width 24 mm and thus a maximum beam diameter of 24 mm can be passed through the plate. The plate is mounted off-center to overlap the outer annulus with the beam path, and different pattern realizations can be attained by rotating the plate about its axis. The phase screen engraved has Kolmogorov statistics with an $r_0 = 0.6$ mm. The beams emerging from the phase plate are truncated by an iris to allow the emulation of different telescope aperture sizes. With the fixed Fried parameter of the screen, varying the turbulence strength up to a maximum of $D/r_0 = 40$ is possible by changing the iris opening diameter.

Low-order adaptive optics

The LOAO system from ALPAO has a 13.5 mm DM with 97 actuators, that can achieve a flatness of 2.89 nm rms in closed loop. It can be driven up to a frequency of 1 kHz before the first resonance sets in. Wavefront sensing is performed downstream of the DM in a closed-loop architecture by a Shack-Hartmann type sensor that consists of a 16×16 MLA with an electron-multiplying CCD (EM-CCD) camera. The EM-CCD from Nüvü has a quantum efficiency $QE > 75\%$ between 500 and 800 nm and a full frame rate of 1 kHz. The LOAO system features a dichroic mirror to split the science beam from the guide star beam which in turn is resized by a beam reducer (a Keplerian telescope of 2 achromats) to match the size of the lenslet array (2.75 mm). The beam reducer also conjugates the DM pupil to the lenslet array that is placed at the exit pupil of the system. A field stop at the image plane between the telescope lenses allows for blocking the light from all sources other than the guide star beam. The loop is controlled with a PC driven by an Intel i5-8500, 3.0 GHz, 6 cores processor and 16 GB RAM running a Matlab-based engine developed by ALPAO. The pure delay, i.e. the time it takes the PC to have the DM commands ready after the end of an exposure, is 1.38 ms. The loop can be closed at 500 Hz with the WFS camera operating at maximum frame rate with sufficient photons available for each frame to guarantee a high signal-to-noise ratio (camera requires 3 photons/frame/subaperture for SNR = 1). The rejection (correction) bandwidth, i.e. the maximum Greenwood frequency that can be corrected for, is the figure of merit most important for our purposes and for this system it is about 20 Hz. The partial correction nature of the LOAO system is clear from the limited number of modes (97) it can correct for (spatial limitation) and the maximum Greenwood frequency it can track (temporal limitation) compared to the needs of large and very large

telescopes.

Relay optics and coupling setup

After passing the phase screen and the iris, the clipped beams are then passed through a Keplerian telescope that resizes the beam diameter to match the DM aperture. The secondary lens of the telescope also images the phase screen at the primary lens, i.e. the entrance pupil, onto the DM when the telescope is kept at the correct image distance from the DM. The telescope lenses are uncoated singlets, and lens pairs that produce the minimum total Seidel aberrations were selected from off-the-shelf catalogues using Zemax. The exit pupil position is also calculated by Zemax.

The combined beams are then folded towards the DM, where the wavefront is actively controlled. After reflection off the DM, the AO-corrected beams are split by a dichroic beam splitter (c.f. Fig. 5.15). While the guide star beam goes to the WFS, the science beam is reflected out of the AO setup toward a coupling lens with an SMF or FMF aligned at its focus. The same $f = 75$ mm lens is used for all fibers. With the beam diameter at the lens equal to the DM aperture, i.e. $d = 13.5$ mm, an $f/5.56$ beam results which is close to the optimum for coupling into an $NA = 0.1$ SMF at $\lambda = 1550$ nm as shown in Fig. 5.11. The optimum $f/\#$ for coupling into SMFs of a different NA or FMFs is different, but 5.5 is roughly the midpoint where sufficient coupling is expected for all the cases considered.

To measure the total power coupled, the output end of the fiber is connected to a fiber port where the facet is imaged onto a free-space photodetector (PD) by a singlet lens. Such an arrangement is necessary because the femto-watt PD has a small active area (0.2 mm^2), which makes it difficult to completely capture the diverging beam directly after the fiber. The highly sensitive InGaAs PD has a noise equivalent power $NEP = 7.5$ fW and bandwidth $BW = 25$ Hz.

The NIR beam is intercepted at two points by flip mirrors. First, before the coupling lens, the beam can be sent toward a C-RED2 InGaAs camera (Feautrier et al., 2017) through a long focal length lens $f = 1000$ mm to image the PSF and measure its Strehl ratio and encircled energy. Second, after the coupling lens and before the fiber, the beam can be reflected towards a free-space highly sensitive PD to measure the total power available at the pupil for coupling. The two PDs were calibrated against each other using the fiber port-lens-PD setup across their dynamic range 10 fW - 100 pW.

Table 5.1: Properties of the fibers used.

Fiber	Core diameter [μm]	*NA*	Sustained modes [1]
SMF[2]	8.2	0.14[3]	1
FMF	25 ± 1	0.08 ± 0.005	6

Flip mirrors are used instead of beamsplitters after separating the guide star beam from the science beam to reduce the number of surfaces that may give rise to non-common path aberrations (NCPA) between the AO setup and the fiber. To align the fiber at the focus of the coupling lens, a 6-axis kinematic precision stage is used. The nanopositioning stage used can achieve a resolution of less than 50 nm for x, y, and z. Pitch and yaw have a 0.2 arcsec resolution.

A feedback loop is closed between the C-RED2 camera and the DM (on top of the main AO loop) to correct for temperature-induced tip and tilt in the IR arm only and hence not seen by the WFS. Wavefront error, temperature and humidity are logged for the open loop case to make sure that creep and memory effects as reported by Bitenc et al. (2014) do not introduce measurement artifacts.

Coupling is measured for an SMF and an FMF. A coated SMF-28 patch cable from Corning is used as the SMF. For the FMF, a THORLABS FG025LJA MMF is used. Table 5.1 lists the properties of the fibers used. Short fibers (< 2 m) are used to minimize attenuation in the fibers and cladding modes are removed by having the fibers bent at radii (> 30mm) larger than their macrobend loss thresholds.

Experimental results

Fig. 5.16 shows the measured coupling efficiencies and gain for an SMF and a 6-modes fiber using the setup described above. The maximum efficiency measured at the diffraction limit for both fibers is lower than that theoretically predicted in Fig. 5.11 by $\sim 25\%$, for which we identify three causes: 1. Coupling in the testbed is done at $f/5.56$, the optimum for the SMF but slightly faster than the $f/6.8$ required to maximally couple into a 6-mode fiber. 2. The aberrations in the optical train amount to an rms wavefront error of $80 - 120$ nm depending on the telescope in place and can only be flattened down to a minimum of 20 nm rms error by closing the loop. The reduction of the theoretical limit (at an open loop) due to aberrations

[1] Per polarization and accounting for degeneracies at $\lambda = 1550$ nm
[2] Fiber is AR-coated at one end
[3] Measured at 1 per cent power level

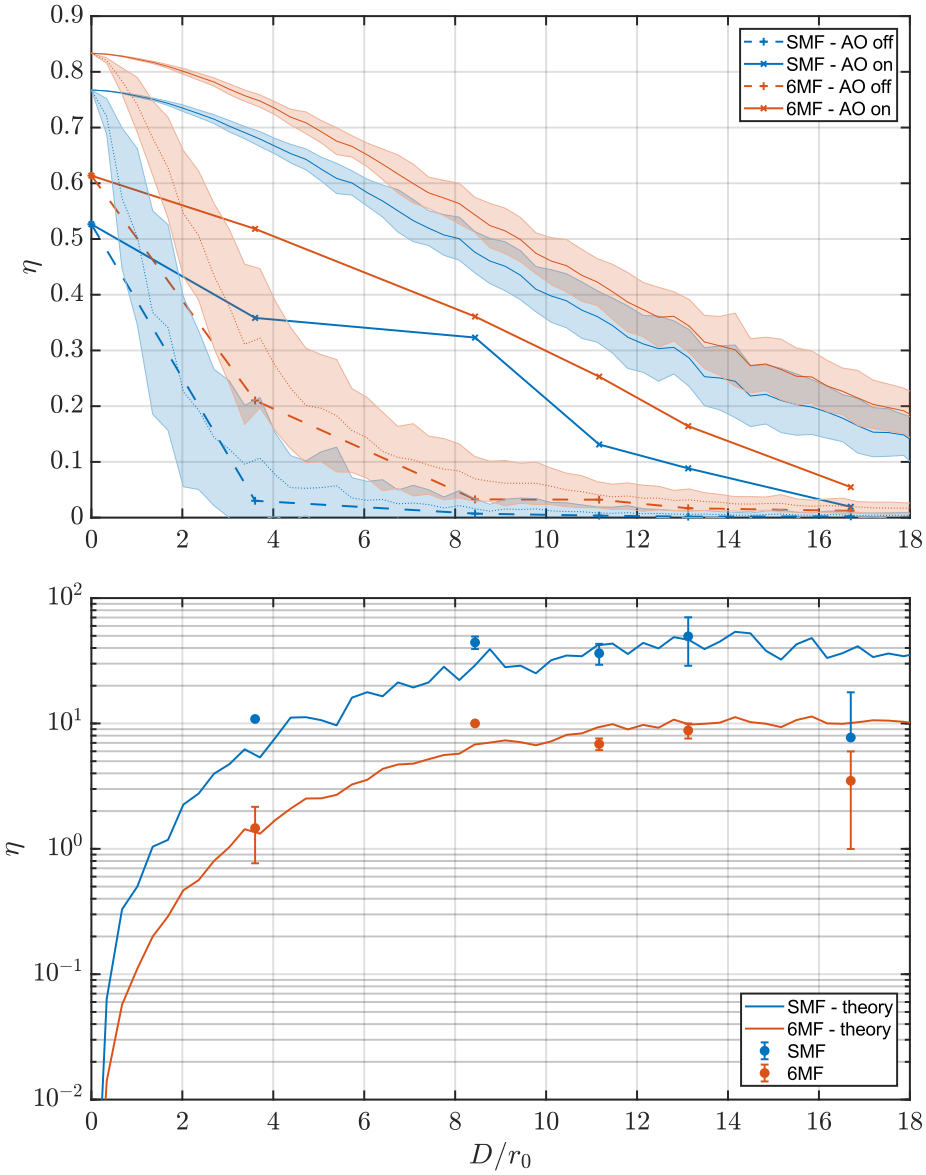

Figure 5.16: Top: measured coupling efficiency into SMF and 6 modes FMF. For reference, the simulation results are plotted (light lines with shaded areas indicating uncertainties). Bottom: measured gain in coupling upon application of AO correction. The line plots going through the data are the simulation results.

was confirmed by modelling the trains in Zemax where a physical optics module can calculate the overlap between the fundamental mode and the deformed PSF. Alignment was improved until those theoretical limits were reached. 3. Insertion and transmission losses in the fibers introduce a small reduction in the measured efficiencies as compared to the other factors.

The reasons mentioned for the mismatch above cancel out for the gain curves and

therefore we choose to qualify the models using them. At higher D/r_0 values the theoretical gain remains constant but a drop is seen in the experimental values for $D/r_0 > 16$. This is a result of filtering the high-order eigenmodes of the DM to calculate the command matrix in Eq. (5.5) when closing the loop. The high-order eigenmodes have smaller eigenvalues and therefore cause the actuator commands to saturate and the loop to diverge when high spatial frequency shapes are requested of the DM. Only 3 eigenmodes are filtered for the cases where $D/r_0 < 10$ but more are filtered dynamically by the control code as D/r_0 is increased and the loop starts to diverge. Moreover, the phase screen of the testbed was calculated as a Fourier series (FS) expansion over an area equal to the size of the screen while the phase screen realizations for the model were calculated over an area $40\times$ larger to minimize the inherited periodicity in the FS-generated phase. The testbed screen therefore has a structure function (Eq. (5.2)) that deviates from Kolmogorov's $5/3$ law at greater separations while the model's screens adhere to the law more closely. The underrepresented low frequencies in the testbed screen cause a higher coupling efficiency into the fibers for the uncorrected case while the AO-corrected case remain unaffected (c.f. Fig. 5.17). Furthermore, a large ensemble of unique screens cannot be achieved for larger beam diameters due to the finite size of the phase screen.

Fig. 5.18 shows the drop in the Strehl ratio (SR) and the increase in the encircled energy (EE) as D/r_0 increases. The resemblance between the η curves for the SMF in Fig. 5.12 (when normalized to have $\eta = 1$ at the diffraction limit) and the SR curves in Fig. 5.18 is a result of the SMF being nearly a point-like sampler of the center of the PSF as first noticed by Coudé du Foresto et al. (2000). The knee in the EE curve for the AO corrected case at $D/r_0 \sim 9$ indicates the transition between the total and the partial correction regimes where r_0 projected on the DM becomes smaller than the inter-actuator spacing. The PSF is no longer contained by the LOAO system and starts to broaden at a rate equal to that of the uncorrected case. Strehl ratio drops linearly throughout both regimes for the corrected wavefronts since a central core is always present in the PSF for $D/r_0 < 18$ as shown in the images at the top of Fig. 5.18. The deviation of the data points at $D/r_0 = 16.7$ from the theoretical prediction is again due to the periodicity of the phase screen as discussed above.

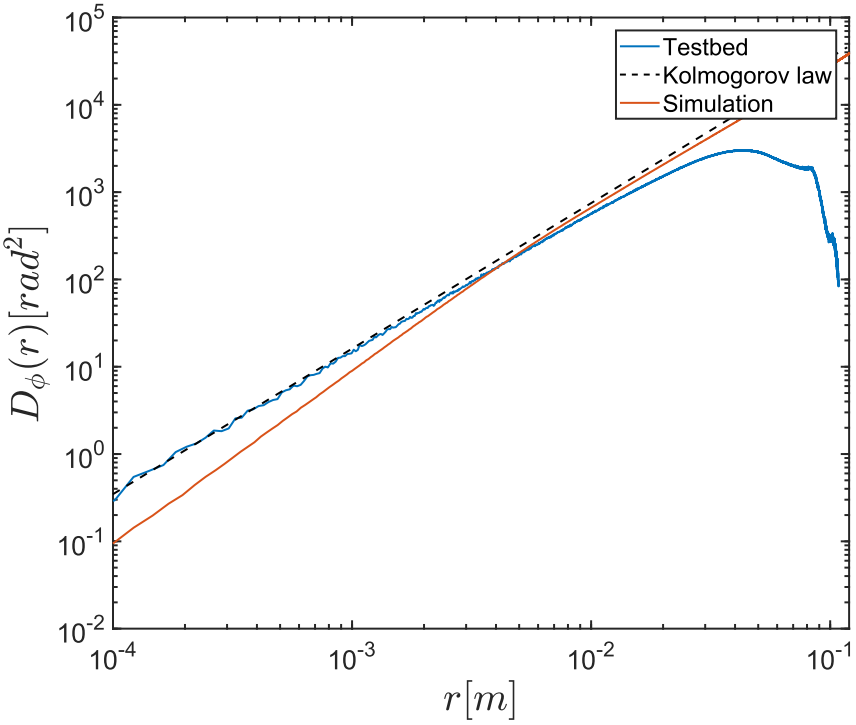

Figure 5.17: Structure functions of the testbed phase screen (blue line) and the model realizations (orange line). Plotted also is Kolmogorov's $5/3$ law of turbulence (dashed line).

5.2.6 Discussion

The results for the effect of the $f/\#$ of the telescope on coupling in Fig. 5.11 match those reported by Horton et al. (2007) for the diffraction-limited case. The extension into the seeing limit and the study here of how the optimum geometry varies with turbulence was necessary to confirm that diffraction-limited values remain valid for all cases. FMFs coupling curves (see Fig. 5.12) for the uncorrected case can be cross-checked against a number of references that studied coupling for FSO communication. Tedder et al. (2020) measured coupling for a 15-modes fiber up to $D/r_0 = 8.6$ and the 6 dB loss reported is comparable to the 0.22 coupling efficiency for the 19 modes fiber we calculated. Zheng et al. (2016) simulated and measured received power into SMFs and their results can be directly compared to the drop in efficiency and increase of the standard deviation with D/r_0. For example, the 1.25% efficiency they reported for $D/r_0 = 10$ matches the calculated $\eta = 1.24\%$ in Fig. 5.12. The addition here is the inclusion of AO correction and the focus on the modal counts most relevant to tapered photonic lanterns.

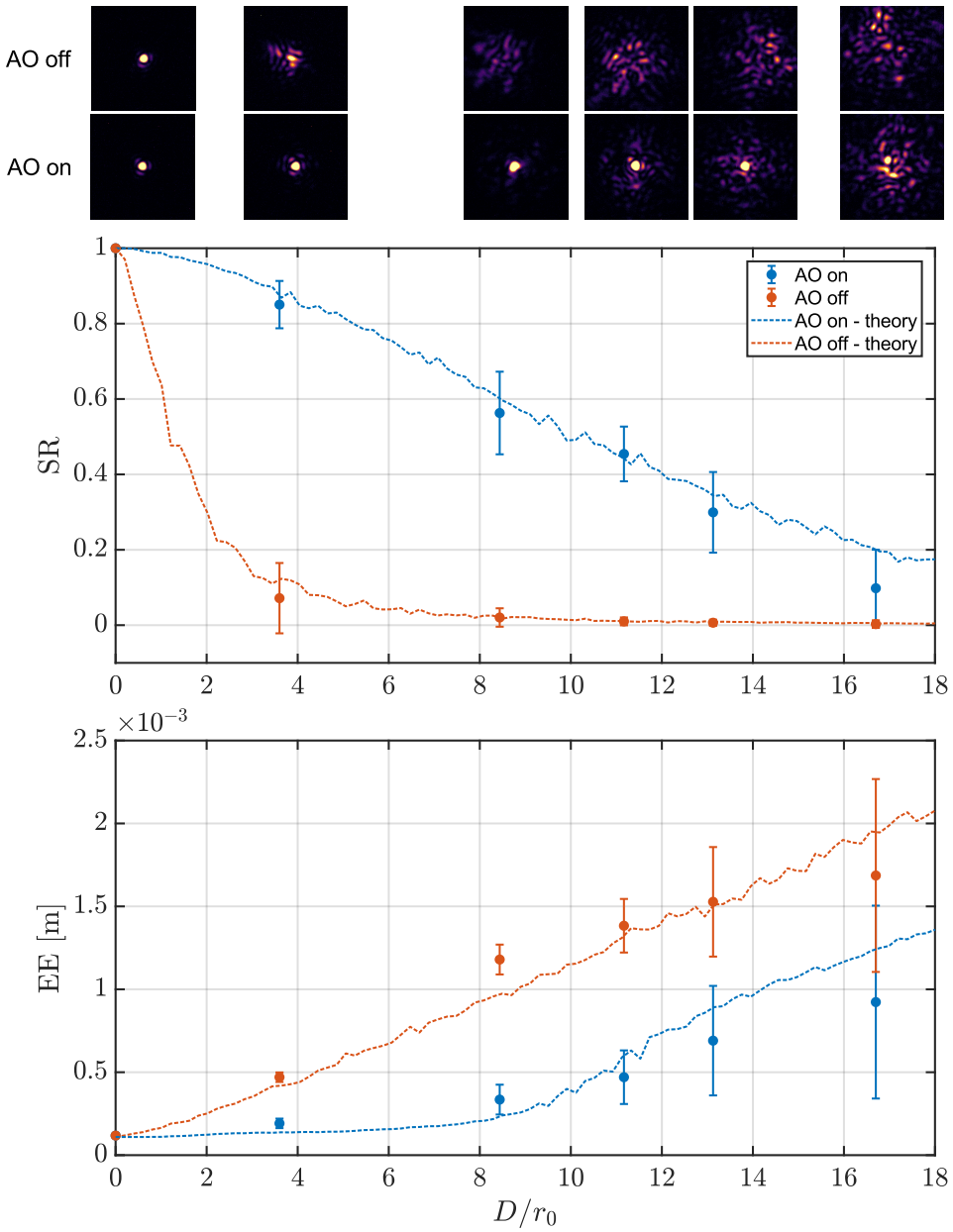

Figure 5.18: Top: Short exposure PSF images taken with the loop open and then closed for increasing D/r_0. Middle: SR dependence on D/r_0 for the corrected and the uncorrected cases. Bottom: PSF 50% encircled energy at $f/74$ dependence on D/r_0. Simulation results from the theoretical model are also plotted for reference.

With an experimentally-verified model like the pipeline detailed in this work, one has the tool to decide if a multiplexed photonic instrument fed by an LOAO-assisted photonic lantern provides an advantage over a single device in terms of SNR. A typical scenario is a telescope equipped with an AO system that has a maximum number of modes and a temporal bandwidth it can correct for but can also function at decreased capabilities in the absence of a bright enough guide star. A photonic lantern can then be appropriately sized given the source brightness, the available exposure time and the detector specifications. The availability of photonic components (lantern and IO devices) in different sizes and quantities for a quick exchange should be feasible although packaging and alignment techniques need to be perfected to minimize losses and downtime.

Turnkey, general-purpose AO systems are now available from a variety of vendors. The use of pre-engineered hardware and software make such solutions affordable ($\sim \$10^5$) for midsize telescopes where astrophotonic technologies could be employed first. This is in contrast to the custom-made, large-scale AO projects currently existing or being considered for the very and extremely large telescopes. FSO communication applications in particular are set to benefit from the anticipated ubiquity of low-cost AO systems (Leonhard et al., 2016).

Once a verified model for coupling through turbulence in the presence of AO compensation is available, color maps like those in Fig. 5.13 can be generated for any given celestial target and scientific camera. A quick multi parameter scan shows the regime (D/r_0, N_{ph}, and σ_{RON}) under which multiplexing becomes beneficial and the optimum number of channels that one should opt for to get the most cost-efficient, i.e. least number of channels, that maximizes the SNR above a certain threshold.

The study done here concerns H-band astronomy as this is the band where the operating ranges of current AO and photonic technologies overlap. Results from simulations and the experiment detailed above are for $\lambda = 1550$ nm but a recalculation at a different wavelength between 1500 and 1800 nm is possible without modification as, in principle, the physics and the assumptions made remain valid. In general, Fried parameter is smaller towards the blue $r_0 \propto \lambda^{6/5}$ (c.f. Eq. (5.4)) effectively squeezing the curves in Fig. 5.12 to the left as the wavelength decreases. however the number of modes supported by a given waveguide increases approximately as $\sim \lambda^{-2}$, hence increasing the total coupling efficiency. The general case of an unobscured circular aperture was considered for the simulations and the experi-

ments reported here but obscurations, spiders and segmented pupils can be readily included in the models when necessary. An on-sky test of fully packaged photonic lanterns of different sizes assisted by an LOAO shall complement this work.

5.2.7 Conclusions

We presented a feasibility study and made the case for H-band multiplexed astrophotonic instruments fed by AO-assisted photonic lanterns. A numerical simulation was completed to find the compromise between the complexity of the AO system and the size of the photonic lantern to maximize sensitivity. Photonic lanterns sustain few modes at their multimode ports and the optimum f-numbers for coupling into FMFs deviate from the geometric predictions as Fig. 5.11 depicts. An LOAO system can boost the coupling of atmospherically-distorted starlight into FMFs and photonic lanterns manyfold ($2 \sim 100$, c.f. Fig. 5.12). The SNR of an accumulated signal detected at the output of a multiplexed instrument depends on the photons flux that can be coupled into the instrument, the number of channels over which they are split by a photonic lantern and the RON of the detector used (c.f. Fig. 5.13). The realm where such an approach offers an advantage over singular standalone devices fed by SMFs is therefore defined by the aperture size, the science target, and the detector capability.

With the prevalence of LOAO systems, the continuing improvement of low noise infrared detectors, and the imminent adoption of photonic technologies by astronomy, multiplexed photonic instruments will soon become advantageous for midsize and large telescopes. Immediate applications for extremely large telescopes could be considered for AO-supported multi-object spectrographs that are currently being designed for the next generation of ELTs, such as MOSAIC for the ELT (Jagourel et al., 2018; Morris et al., 2018).

Acknowledgements

The author is most thankful to Stefano Minardi for his valuable guidance during the early stages of this work. The author is also thankful to Peter Tuthill for suggestions on applying mode-selective photonic lanterns, to Sergio Leon-Saval for comments on scrambling and the geometric considerations of lanterns design, to Alan Günther for help with thermal effects in the lab, and to the anonymous reviewer for useful remarks about modal noise in fibers.

The authors acknowledge financial support from the Federal Ministry of Education and Research (BMBF) under grant number 03Z22AN11.

Data Availability

The data underlying this article will be shared on reasonable request to the corresponding author.

Chapter 6

MODE-SELECTIVE PHOTONIC LANTERNS FOR STARLIGHT COUPLING

This chapter was published as

Diab, M., Tripathi, A., Davenport, J., Dinkelaker, A. N., Madhav, K., & Roth, M. M. (2021). Simulations of mode-selective photonic lanterns for efficient coupling of starlight into the single-mode regime. *Applied Optics*, *60*(19), D9–D14. https://doi.org/10.1364/AO.421799

6.1 Abstract

In ground-based astronomy, starlight distorted by the atmosphere couples poorly into single-mode waveguides but a correction by adaptive optics, even if only partial, can boost coupling into the few-mode regime allowing the use of photonic lanterns to convert into multiple single-mode beams. Corrected wavefronts result in focal patterns that couple mostly with the circularly symmetric waveguide modes. A mode-selective photonic lantern is hence proposed to convert the multimode light into a subset of the single-mode waveguides of the standard photonic lantern, thereby reducing the required number of outputs. We ran simulations to show that only two out of the six waveguides of a 1×6 photonic lantern carry $> 95\%$ of the coupled light to the outputs at $D/r_0 < 10$ if the wavefront is partially corrected and the photonic lantern is made mode-selective.

6.2 Introduction

Although starlight arrives at the top of Earth's atmosphere with planar wavefronts that would form Airy patterns when focused by unobscured circular apertures, atmospheric turbulence distorts the wavefronts before they are collected by ground-based telescopes. Such distortion introduce random information into the wavefront which translates into the point spread function (PSF) breaking up into a speckle pattern that couples poorly with single-mode waveguides. Photonic lanterns can be used to couple atmospherically-distorted starlight into single-mode integrated optics and fibers, where the multimode speckle pattern at the focal plane is converted into multiple single-mode beams. This conversion is however only lossless if the degrees

of freedom are conserved, i.e. the number of single-mode channels is at least equal to the number of supported modes at the multimode input (Leon-Saval et al., 2005). Since the modal content of the seeing-limited PSF increases as the telescope aperture grows or as seeing worsens, hundreds, if not thousands, of modes are required to efficiently couple all the starlight into the multimode port of the lantern which results in the signal getting split among an equal number of single-mode channels. To minimize the size of the lantern, adaptive optics (AO) may be used to first correct the received wavefront and hence reduce the modal content of the PSF to the point where only $\sim$ 10s of modes are required to efficiently couple the PSF of a ground-based large telescope into a multiplexed photonic device (Diab et al., 2021).

Partially AO-corrected wavefronts result in PSFs that have a prominent core on top of a background halo (Hardy, 1998). The near symmetry of such PSFs means that they have a stronger overlap with the circularly symmetric of the linearly polarized (LP) modes of step-index circular fibers. By breaking the degeneracy between the single-mode waveguides, a mode-selective photonic lantern (MSPL) like the one depicted in Fig. 6.1 can be designed that converts the light coupled into a certain spatial mode to one specific output waveguide (Leon-Saval et al., 2014). For the case of partially AO-corrected PSFs, this can be exploited to transform most of the coupled multimode starlight into a subset of the total number of modes supported by the photonic lantern. Specifically, most of the light can be coupled into the waveguides associated with the circularly symmetric modes ($LP_{0m}, m = 1, 2, ...$) and thus reduce the number of single-mode channels, i.e. waveguides, that needs to be handled at the output of the photonic lantern without significant loss of light.

While conventional photonic lanterns were originally invented to accommodate fiber Bragg grating-based sky emission filters for H-band astronomy (Bland-Hawthorn et al., 2011), MSPLs were first used as spatial division multiplexers (SDMs) to increase the capacity of optical communication channels (Leon-Saval et al., 2014). They have since been proposed to multiplex orbital angular momentum modes (Zeng et al., 2018) and to selectively amplify spatial modes in doped fibers (Wittek et al., 2016). MSPLs also found applications as bending sensors (Newkirk et al., 2015), as differential group delay compensator (Huang et al., 2015) and made a comeback to astronomy as a way of mitigating focal ratio degradation (Benoit et al., 2020).

In this work, we present simulation results that demonstrate the potential of MSPLs as a method of reducing the number of single-mode channels for the various astronomical applications that photonic lanterns have been suggested for so far, e.g.

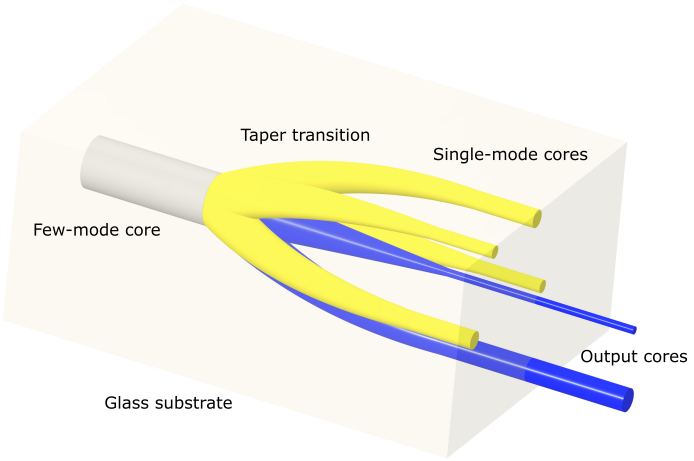

Figure 6.1: Layout of a 1×6 MSPL inscribed in a glass substrate. Corrected starlight coupled into the few-mode core (grey) will predominantly route towards the two single-mode cores (blue) that correspond to the LP_{0m} modes of the input.

OH suppression (Bland-Hawthorn et al., 2011), reformatting (J. J. Davenport et al., 2020), multiplexed spectrographs (Bland-Hawthorn et al., 2010), and beam combiners (Diab et al., 2019; Minardi, 2012). First, the working principle and the design of the MSPL we considered are given. Next, we show how the modal content of starlight PSFs depends on the turbulence strength and the degree of correction. We finally present the expected performance results of using a 1×6 and a 1×15 MSPLs to convert AO corrected PSFs into few single-mode beams and discuss the limits beyond which this approach becomes less beneficial.

6.3 Concept and MSPL design

Conventional photonic lanterns guide the light from a multimode core through an adiabatic transition to an array of identical single-mode cores (Leon-Saval et al., 2010). A one-to-one mapping between the spatial modes of the multimode end and the single-mode waveguides of the array can be achieved with an MSPL that has dissimilar diameters or refractive indices for the array cores. The fundamental modes supported by the single-mode waveguides will consequently have different propagation constants leading to the modes of the input port orderly coupling with the dissimilar cores one by one. Single-mode waveguides support only the fundamental mode LP_{01}. Higher-order circularly symmetric modes, LP_{02} and LP_{03}, are supported by 6 and 15 modes waveguides, respectively. Disregarding geometry, one could directly assign different diameters or refractive indices to the cores in

descending order within the allowed range. The modes from the multimode core would then occupy the single-mode cores in succession. Opting for dissimilar core sizes rather than varying the refractive indices and since the selectivity of the device can be improved by optimizing the diameters to the cores arrangement (Fontaine et al., 2012; Shen et al., 2018), we carried out an optimization of the geometry parameters using the beam propagation solver BeamPROP (Synposys and RSoft Design Group, 1993-2018) on CAD models of the structures. The designs assume a device written using ultrafast laser inscription (ULI) (Thomson et al., 2011) in a block of GLS or Eagle glass (Spaleniak et al., 2013) with refractive index contrast $\Delta = (n_{core} - n_{cladding})/n_{core} = 4.138 \times 10^{-3}$ (Tepper et al., 2017).

To avoid mode coupling along the transition, the adiabaticity criterion (Snyder et al., 2012; Yerolatsitis et al., 2014)

$$\left| \frac{2\pi}{\beta_1 - \beta_2} \frac{\mathrm{d}\rho}{\mathrm{d}z} \int_A \psi_1 \frac{\partial \psi_2}{\partial \rho} \mathrm{d}A \right| \ll 1, \tag{6.1}$$

must be fulfilled. The criterion demands that the propagation constants β_1 and β_2 of neighboring modes ψ_1 and ψ_2 that evolve slowly along the taper to be well separated if the taper length is to remain short enough for the simulations to conclude in a reasonable time. In Eq. 6.1, ρ is the local core size and z is the longitudinal coordinate, making $\mathrm{d}\rho/\mathrm{d}z$ a measure of the taper ratio, while A is the structure cross-sectional area. The range of propagation constants to be filled $(\beta_{max} - \beta_{min})$ is limited by the wavelength and the normalized frequency (V-number) of the single-mode waveguides. It has an upper limit determined by the requirement for the largest waveguide in the array (corresponding to the fundamental mode of the multimode core) to remain single-mode and the smallest (corresponding to the highest order mode of the multimode core) to be 3.6 times larger than the longest operating wavelength to have a V-number of at least 1.5 for good field confinement of the field within the core. The minimum separation to have the output waveguides decoupled is ~ 30 μm. With a device length of 50 mm, the taper angle is 0.03°and therefore the taper is gradual enough to guarantee adiabaticity.

In addition to the bounds set by the propagation constants range, the maximum diameter for the single-mode cores and the minimum diameter for the multimode core depend on the operating wavelength range. The diameters are chosen such that the device will operate across the H-band (1550 - 1800 nm) while keeping the number of supported modes at both ends the same.

Two MSPLs were designed within the constraints given above, a 1×6 and a 1×15. The anatomy of both devices consists of three segments. The input at the front facet of the glass substrate is a straight, uniform, few-mode core that can be readily spliced to a fiber. The tapered cores start at the end of the few-mode core with a matching diameter and then taper over a 5 mm length down to the designated final diameter while fanning out from the center to form a pentagon with a central core for the 1×6 MSPL. The 1×15 MSPL has the remaining 9 cores fanning into an outer nonagon and thus meeting the geometric requirement for lossless transition (Fontaine et al., 2012). The last segment has cores of uniform diameters that continue to fan out at the same angle for 22 mm to a maximum separation of 30 μm from the center where the cores are decoupled. These segments can be identified by the jumps in the effective refractive index curves in Fig. 6.2b.

For the 1×6 MSPL (cf. Fig. 6.1), the multimode core has a diameter of 18.58 μm and $NA = 0.13177$ and therefore supports the 6 modes (12 vector modes): LP_{01}, $2 \times LP_{11}$, $2 \times LP_{21}$, and LP_{02} between $\lambda = 1550$ and 1800 nm. The diameters for the 6 single-mode waveguides found by the optimization are 8.5, 7.5, 7.5, 5.8, 5.8, and 5.6 μm, respectively. While the MSPL is highly selective for all modes, only the waveguides for LP_{0m} modes are of interest here. Fig. 6.2a shows the light spatial distribution corresponding to excitations with pure modes and Fig. 6.2c shows the selectivity matrix of the device, where the rows indicate how much of the total power launched into a given mode ends up at each core.

A similar procedure is followed for the 1×15 MSPL except that the diameters for the waveguides associated with the degenerate higher-order modes (LP_{1m}, LP_{2m}, ...) are all set to the same value to narrow the parameter space of the optimization, as only LP_{01}, LP_{02} and LP_{03} are relevant for this application.

6.4 Starlight coupling into few-mode waveguides

The atmospherically induced distortion of starlight, particularly in the field's phase, precludes efficient coupling into single-mode photonic devices, but a combination of AO and photonic lanterns can help couple light efficiently into astrophotonic instruments that allow multiplexing. Without any correction, the number of modes that the photonic lantern would need to support, p, (and in turn the number of channels of the device) depends on the aperture of the telescope, D, and the seeing

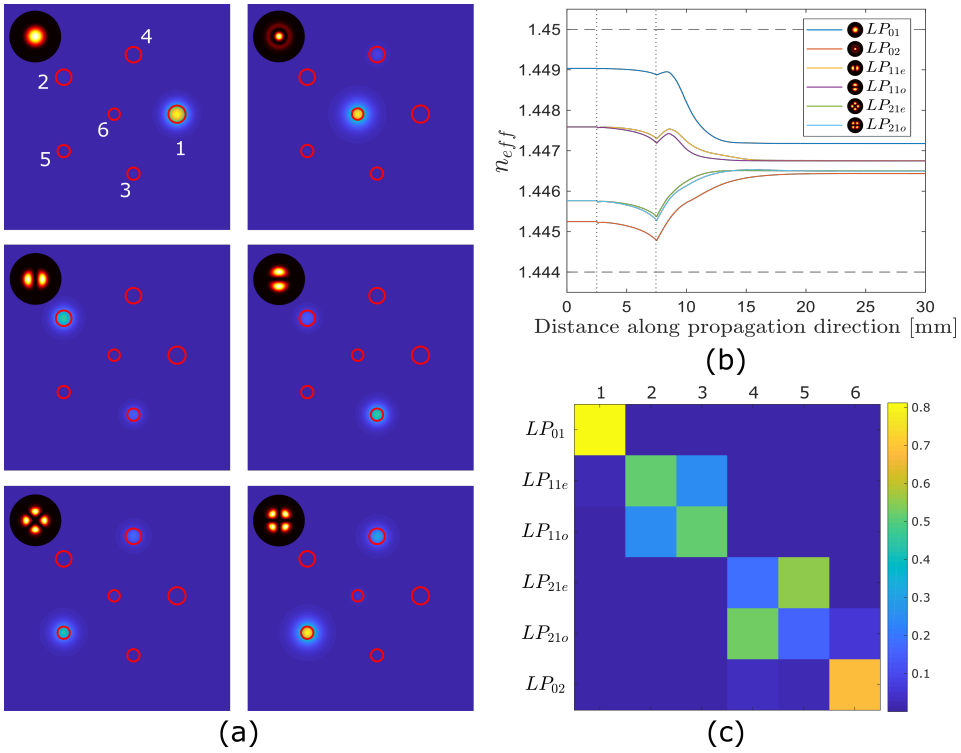

Figure 6.2: (a) Output patterns of the 1×6 MSPL due to excitations by a pure mode. The insets show the launched mode. (b) Variation of the effective index along the propagation direction. Horizontal dashed lines indicate the cladding and the core refractive indices and the vertical dotted lines indicate the interfaces between the segments of the device. (c) Selectivity matrix illustrating the power shares of the output cores with a pure mode launched.

condition gauged by Fried's parameter r_0 (Minardi et al., 2020):

$$p \approx \frac{\pi^2 D^2}{4 r_0^2}. \tag{6.2}$$

A 4 m telescope at median seeing conditions, $r_0 = 20$ cm, in the NIR would require $\sim$ 1000 channels to couple the light efficiently into a multiplexed single-mode integrated optic. To fully correct such a wavefront, an AO system that has a comparable $\sim$ 1000 degrees of freedom, i.e. count of the wavefront sensor (WFS) subapertures and the deformable mirror (DM) actuators, is required. However, a partial correction with only a $\sim$ 100 actuators low-order system can already boost the coupling efficiency into single-mode fibers a 100-fold and decrease the number of channels required of the photonic lanterns for full coupling to only $\sim$ 10s (Diab et al., 2021).

Through scrambling, AO-assisted photonic lanterns can redistribute the light, more

or less, equally among the single-mode channels (Baudrand et al., 2001) and therefore one would need to process the beams at all output ports if the flux collected by the telescope is to be fully utilized. Without scrambling, the redistribution is not equal but rather highly dependent on the time-varying environmental and atmospheric conditions, meaning again that all the channels must be used. An MSPL can help reduce the number of channels by routing most of the light coupled into the multimode core to only 2 of the total 6 channels of a 1×6 MSPL.

Fig. 6.3 shows the contribution of each mode to coupling into a 6 modes waveguide as the turbulence strength D/r_0 is increased for both, the uncorrected and the AO-corrected cases. For this computation, 20 seeing-limited PSFs, ψ_E, at each D/r_0 point are calculated from Kolmogorov's phase screens (Welsh, 1997) and the overlap with the LP modes of a weakly-guiding, step-index circular waveguide, ψ_i, is evaluated to find the coupling contributions η_i

$$\eta_i = \frac{|\langle \psi_i | \psi_E \rangle|^2}{\langle \psi_i | \psi_i \rangle \langle \psi_E | \psi_E \rangle}. \tag{6.3}$$

To compute the LP modes analytically, an ansatz that satisfies the symmetry boundary conditions of the cylindrical, step-index waveguide is substituted in the Helmholtz equation, $\nabla^2\psi + n^2 k_0^2 \psi = 0$ (Snyder et al., 2012). The resulting differential equations have solutions in the family of Bessel functions. Imposing the weak guidance condition, $\Delta \ll 1$, a characteristic equation is obtained that may be solved graphically to determine the parameters of the modes and subsequently their spatial distribution.

AO correction is applied to the distorted phase screens by simulating a Shack-Hartmann WFS and a DM that has 97 actuators (Gorkom et al., 2018). A modal reconstruction is performed to calculate the wavefront from the local slopes sensed by the WFS and find the commands for the DM (Hardy, 1998).

For the uncorrected case, the contributions of LP_{01} and LP_{02} are initially highest, but drop for increasing turbulence, with higher-order modes quickly contributing similar amounts. In the case where partial AO correction is applied on the distorted wavefronts, contributing the most are the LP_{01} and LP_{02} modes. The same calculation was performed for the 1×15 MSPL, where we still find LP_{01} and LP_{02} carry the largest fraction of light. LP_{03}, however, does not contribute.

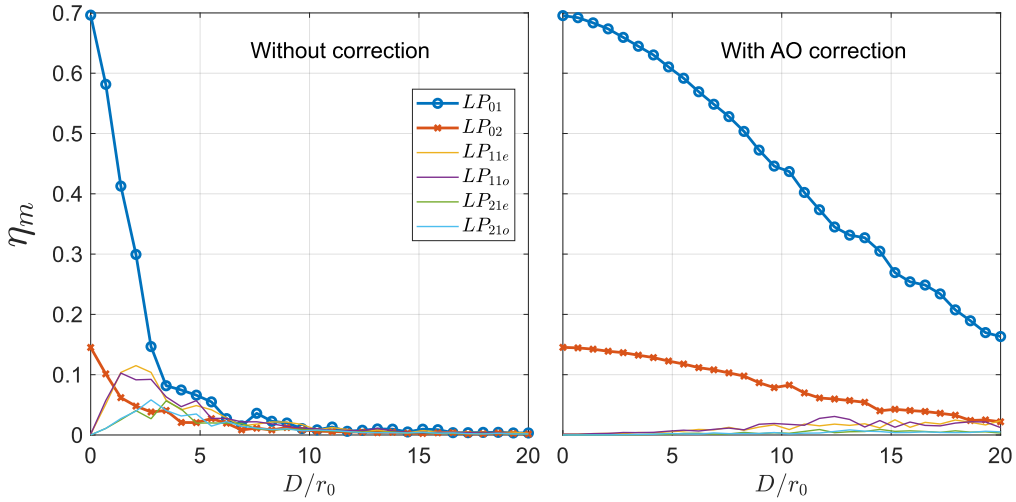

Figure 6.3: Contribution of the modes to coupling from an unobscured circular aperture at the optimum $f/\# = 4.83$ at $\lambda = 1550$ nm as D/r_0 is increased for a 6 modes waveguide. Left: Without AO correction. Right: with partial AO correction.

6.5 Starlight coupling into MSPLs

To demonstrate the MSPL ability to convert the multimode starlight to a few of its single-mode outputs, focal fields of AO-corrected wavefronts at the optimum coupling $f/\#$ are computed and launched into the multimode waveguide of a model of a 1×6 MSPL. The beam propagation method is then used to evolve the launch field along the MSPL and calculate the output fields at the tips of the single-mode waveguides. Fig. 6.4 shows the dependence of the power at the outputs on D/r_0 for the corrected and the uncorrected cases at $\lambda = 1550$ nm.

As the overlap of the corrected PSF with the LP_{01} mode is higher than the overlap with LP_{02}, the 1×6 MSPL will always redistribute the light unequally between the two output waveguides. Without further scrambling, this may prove problematic for certain applications, e.g. high-resolution spectroscopy, and would require a redistribution among the channels using a scrambling device for the outputs.

Of the total optical power coupled from free space into the 1×6 MSPL, $> 99\%$ is delivered to the two cores associated with LP_{0m} at the diffraction limit. The preference for the light to steer toward those cores decreases as turbulence strength is increased but the share of the power remains $> 85\%$ at all $D/r_0 < 20$ for the unobscured telescope. Fig. 6.5 shows how the share of the power in the two LP_{0m} cores of a 1×6 MSPL depends on D/r_o and the obscuration ratio of the telescope. At the diffraction limit, a central obscuration effectively redistributes part of the power from the Airy disk into the rings and thus increases the coupling into the

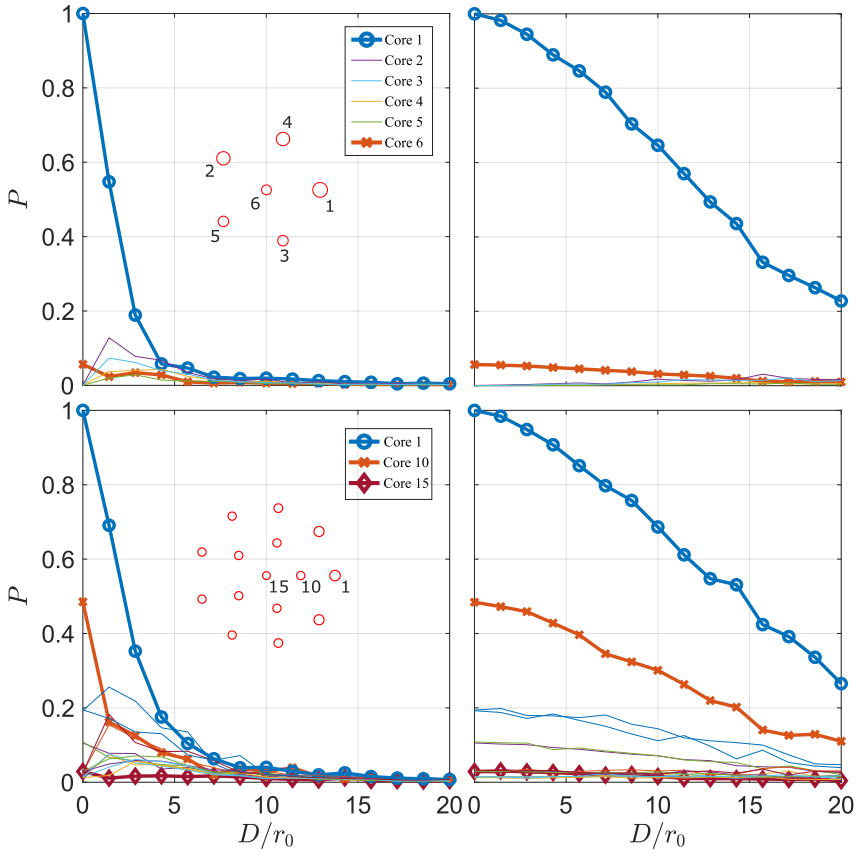

Figure 6.4: Normalized optical power at the single-mode output cores as turbulence strength increases for unobscured circular apertures. Insets show the cores arrangement at the output. Top: 1×6 MSPL. Bottom: 1×15 MSPL. Left: No correction. Right: With AO correction

higher-order LP_{0m} modes. The total share of the power remains the same in these circularly symmetric modes as seen in Fig. 6.5.

6.6 Conclusion and future outlook

We have run simulations to demonstrate the potential of MSPLs to coupling starlight into the single-mode regime upon introducing AO correction to atmospherically distorted wavefronts. MSPLs can reduce the number of output beams that one needs to consider as compared to conventional photonic lanterns for an equal total flux delivered. For multiplexed photonic devices (Watson, 1995), fewer channels also mean that the signal-to-noise ratio is improved by requiring the stacking of fewer signals in post-processing after detection (Diab et al., 2021). The MSPL is selective across the H-band where the modal count of both ports remains the same.

Several methods can be considered to fabricate MSPLs. For the simulations pre-

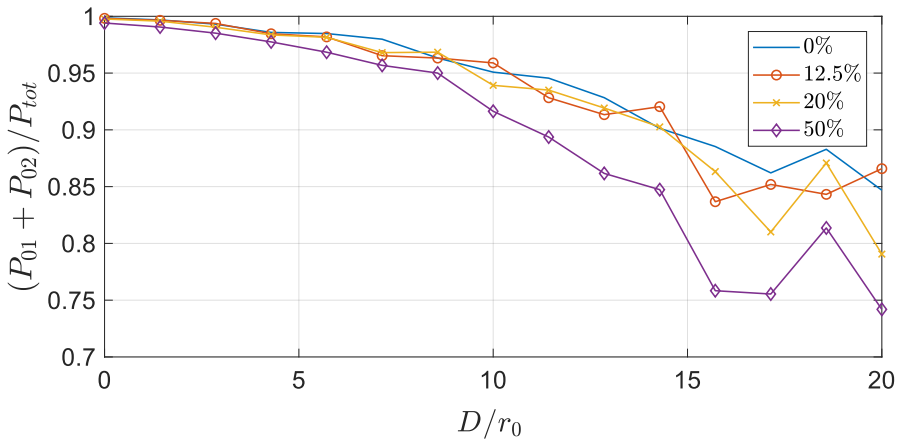

Figure 6.5: Share of light contained in the two LP_{0m} cores for the 1×6 MSPL. Curves are shown for obscuration ratio $= 0, 12.5, 20$, and 50%.

sented here, we have assumed the ULI technique. With ULI, 3D structures can be written into bulk glass by moving the substrate in all three dimensions relative to a focused short-pulse laser beam. The refractive index is modified at the focus, thereby producing waveguide structures. By combining laser parameters, focusing optics, and sample movement appropriately, the position, shape, and size of each waveguide can be changed. ULI has already been used to write single-mode waveguides, directional couplers and interferometers (Piacentini et al., 2021), Bragg-gratings (Brown et al., 2012), photonic reformatters (MacLachlan et al., 2016; Pike et al., 2020), as well as photonic lanterns (Spaleniak et al., 2013; Thomson et al., 2011). MSPLs, however, have not yet been fabricated using ULI. High positional precision and repeatability will be required to shape the individual waveguides, especially for the lowest MFD difference of 200 nm between mode-selective waveguides in our simulations. Here, the substrate motion will be crucial. For systems utilizing air-bearing translation stages, (e.g. Brown et al., 2012; MacLachlan et al., 2016), hardware specifications from the manufacturers state positioning repeatability of $\pm 25 - 100$ nm. While we expect the precision to be sufficient, experimental tests should be conducted to verify MFD and selective coupling of ULI-manufactured devices. The effect of position uncertainty might be mitigated when using the multiscan technique, where the combined index change of several displaced scans accumulates to form the final waveguide, e.g. Brown et al., 2012.

Furthermore, photonic lanterns can be produced by tapering stacks of optical fibers. Many single-mode fibers fuse together to form the multi-mode waveguide (J. J. Davenport et al., 2020). MSPLs can be produced by this method, either by using

optical fibers of varying sizes (Yerolatsitis et al., 2014), with similar cladding diameters but different cores (Leon-Saval et al., 2014), or using a multicore fiber (Benoit et al., 2020).

With a fabricated device, the simulation results reported here can be verified on an AO testbed where D/r_0, the degree of correction, and the obscuration ratio can be changed (Diab et al., 2020). After initial proof-of-concept experiments in the lab, subsequent on-sky tests would be required. As losses in the laser-written devices can accumulate to cancel any signal advantage from the MSPL, the throughput has to be evaluated. Optimization might be required to reduce losses. However, if the throughput is too low, a similar MSPL could be fabricated from a fiber stack for testing on an astronomical telescope. Both techniques can be used complementally to find suitable MSPL configurations for different telescopes and AO systems in order to improve light coupling in photonic devices under the effect of turbulence.

Funding

German Federal Ministry of Education and Research (BMBF) (03Z22AN11).

Disclosures

The authors declare no conflicts of interest.

Acknowledgments

The authors would like to thank the Photonic Instrumentation (PHI) Group at Heriot-Watt University, especially Aurélien Benoit, for fruitful discussions on the ULI technique.

Chapter 7

PHOTONIC WAVEFRONT SENSING AND MODAL ANALYSIS

This chapter was published as

Diab, M., & Minardi, S. (2019). Modal analysis using photonic lanterns coupled to arrays of waveguides. *Optics Letters*, *44*(7), 1718–1721. https://doi.org/10.1364/OL.44.001718

7.1 Abstract

We present a new concept of an integrated optics component capable of measuring the complex amplitudes of the modes at the tip of a multimode waveguide. The device uses a photonic lantern to split the optical power carried by an N-modes waveguide among a collection of single-mode waveguides that excite a periodic array of at least N^2 single-mode evanescently-coupled waveguides. The power detected at each output of the array is a linear combination of the products of the modal amplitudes—a relation that can, under suitable conditions, be inverted allowing the derivation of the amplitudes and relative phases of the modal mixture at the input. The expected performance of the device is discussed and its application to the real-time measurement of modal instability in high power fiber lasers is proposed.

7.2 Article

The decomposition of the optical field carried by a multimode fiber into its supported modes is a requirement for several applications in the photonic industry ranging from spatial division multiplexing communication protocols (Li et al., 2017) to management of modal instability in high power fiber lasers (Eidam et al., 2011). However, while modal decomposition of an optical field is a straightforward numerical task, it is usually a rather complex one from the experimental viewpoint. Free space modal characterization techniques often use phase holograms as multiplexed mode matched filters (Goodman, 2004) to retrieve amplitude and phase from optical cross-correlations of the mode functions with the fiber field (Kaiser et al., 2009). Direct field measurement by means of a wavefront sensor (Paurisse et al., 2012) or by means of a spatial-spectral scan of the mode profile (Nicholson et al., 2008) are other free

space methods used to estimate the modal coefficients in an excited fiber. A common feature of free space methods is the requirement of extended setups and slow data processing, making them unsuitable for high speed applications. Integrated optics mode-division multiplexer/demultiplexer can offer devices with smaller footprints and a fast measurement of the modulus of the modal (complex) amplitude. In this respect, asymmetric couplers in 2 (Narevicius et al., 2005) and 3 dimensions (Hanzawa et al., 2014; Riesen et al., 2014) and asymmetric photonic lanterns (Leon-Saval et al., 2014) have been used to multiplex/demultiplex up to 3 modes in rectangular multimode waveguides. While the speed of the modal decomposition in demultiplexers is limited by the speed of the light detector at the output, an integrated device measuring the relative phase between the excited modes has not been reported so far. The measurement of the modal phase is an essential requirement to determine the exact optical pattern at the output plane of the multimode fiber, information that could find application in the active control of modal instability in high power fiber lasers (Otto et al., 2013).

In this letter we present the concept of a new integrated optics device designed to accomplish a complete measurement of the complex modal amplitudes at the input of a multimode waveguide (Minardi et al., 2019). The proposed device combines a photonic lantern (Leon-Saval et al., 2005) with a discrete beam combiner (Minardi et al., 2010), as sketched in Fig. 7.1. After describing the operating principle, we present the results of a numerical optimization of the device and discuss estimates of the precision of the modal complex amplitude retrieval relative to detection noise.

As known, the photonic lantern is a tapered waveguide that transforms adiabatically the modes supported by its multimode end into the supermodes of an array of single-mode waveguides. The output of the lantern can be used to excite an array of coupled single-mode waveguides, designed to act as an interferometric beam combiner, i.e., the discrete beam combiner. We show here below that by choosing appropriately the interface between the photonic lantern and the discrete beam combiner, it is possible to relate linearly the power carried by each output of the beam combiner with the square moduli and mutual products of the input modal amplitudes.

We begin by describing our system in terms of a linear operator $\hat{\psi}$ from the N-dimensional functional space spanned by the transverse modes $U_i(x, y)$ of the multimode end of the lantern to an M-dimensional functional space describing the excitations of the M waveguides of the discrete beam combiner. In the frame of the coupled-mode approximation, the fields supported by the array of evanescently-

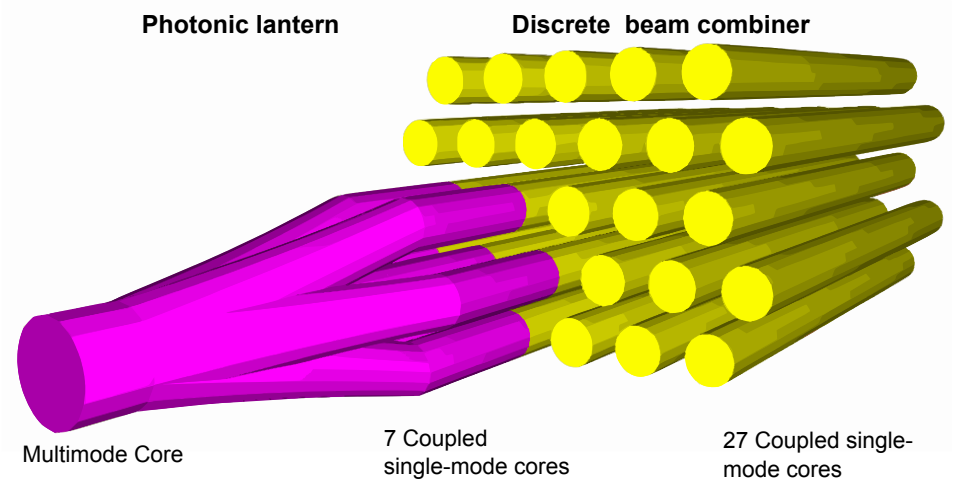

Figure 7.1: Layout of a photonic mode analyzer designed to retrieve the complex amplitudes of the modes excited at its multimode input. The scale in the propagation direction is reduced by 200x relative to the transverse coordinates and the cladding of the waveguides is hidden for clarity.

coupled waveguides are written in terms of the mode profile $u_0(x,y)$ of the isolated single-mode waveguide, each centered at the coordinates (x_n, y_n) of the nth waveguide axis. With this approximation, we can choose as a base of the M-dimensional space, fields composed of single waveguide excitations at the output of the array $u_n(x,y) = u_0(x-x_n, y-y_n)$. We can thus rewrite the operator $\hat{\psi}$ as an $M \times N$ complex matrix $\psi_{n,i} = \langle u_n | \hat{\psi} U_i \rangle$, where the norm $\langle \cdot | \cdot \rangle$ is the usual overlap integral. Notice that $\psi_{n,i}$ represents the complex amplitude of the mode of the nth waveguide at the output of the array due to an excitation of the photonic lantern input with mode U_i. If the transition from multimode end to array output is lossless and the chosen bases are normalized we clearly have that $\sum_{n=1}^{M} |\psi_{n,i}|^2 = 1$ for every $i = 1, ..., N$. A generic superposition of the input modes U_i with weights $c_i \in \mathbb{C}$ will therefore map into the output amplitude

$$\phi_n = \sum_{i=1}^{N} c_i \psi_{n,i}, \qquad n = 1, ..., M. \tag{7.1}$$

We now consider that powers rather than fields are measured at the output waveguides, i.e., with a detector array aligned with the waveguides. Because we assume that the chosen base is orthonormal, the signal I_n of the detector is

$$I_n = \left| \sum_{i=1}^{N} c_i \psi_{n,i} \right|^2, \tag{7.2}$$

which can be written in the following expanded form:

$$I_n = \sum_{i=1}^{N} |c_i|^2 |\psi_{n,i}|^2 + 2 \sum_{i=1}^{N-1} \sum_{j=1}^{N} [\mathrm{Re}(c_i c_j^*)\,\mathrm{Re}(\psi_{n,i}\psi_{n,j}^*) - \mathrm{Im}(c_i c_j^*)\,\mathrm{Im}(\psi_{n,i}\psi_{n,j}^*)], \quad (7.3)$$

where the operators $\mathrm{Re}(z)$ and $\mathrm{Im}(z)$ denote the real and imaginary parts of z, respectively. For all output waveguides, the equations in Eq. (7.3) can be arranged in a matrix form:

$$\vec{I} = \boldsymbol{V} \cdot \vec{J}. \quad (7.4)$$

By choosing the N^2-dimensional vector $\vec{J}$ as

$$\vec{J} = [|c_1|^2, \ldots, |c_N|^2, \mathrm{Re}(c_1 c_2^*), \ldots, \mathrm{Re}(c_{N-1} c_N^*), \mathrm{Im}(c_1 c_2^*), \ldots, \mathrm{Im}(c_{N-1} c_N^*)]^T, \quad (7.5)$$

the matrix $\boldsymbol{V}$ can be divided into three sub-matrices $\boldsymbol{V} = [\boldsymbol{A} : \boldsymbol{B} : \boldsymbol{C}]$ where $\boldsymbol{A}$ is an $M \times N$ matrix that contains the squared moduli of $\psi_{n,i}$ while $\boldsymbol{B}$ and $\boldsymbol{C}$ are matrices of size $M \times N(N-1)/2$ that contain the real and imaginary parts of all possible pair products $\psi_{n,i}\psi_{n,j}^*$, respectively. The entries of $\boldsymbol{A} = [\alpha_{i,j}]$, $\boldsymbol{B} = [\beta_{i,j'}]$ and $\boldsymbol{C} = [\gamma_{i,j'}]$ are given explicitly by

$$\begin{aligned} \alpha_{i,j} &= |\psi_{i,j}|^2, \\ \beta_{i,j'} &= 2\,\mathrm{Re}(\psi_{i,p(j')}\psi_{i,q(j')}^*), \\ \gamma_{i,j'} &= -2\,\mathrm{Im}(\psi_{i,p(j')}\psi_{i,q(j')}^*), \end{aligned} \qquad \begin{aligned} i &= 1, \cdots, M, \\ j &= 1, \cdots, N, \\ j' &= 1, \cdots, N(N-1)/2, \end{aligned} \quad (7.6)$$

where $p(j')$ and $q(j')$ are given by

$p(j') = m$, for $m \in \mathbb{N}$ that satisfies

$$(m-1)\left(N - \frac{m}{2}\right) < j' \leqslant m\left(N - \frac{m+1}{2}\right),$$

$$q(j') = p(j') + j' + [p(j') - 1]\left[\frac{1}{2}p(j') - N\right]. \tag{7.7}$$

Now $\boldsymbol{V}$ in Eq. (7.4) has a generalized inverse provided that its number of rows $M \geqslant N^2$, i.e., the discrete beam combiner section of the device must at least have a number of coupled waveguides equal to the square of the number of modes to be analyzed.

While the numerical determination of the matrix $\boldsymbol{V}$ is straightforward, in a real experiment a calibration procedure is required. This can be accomplished with a method similar to the one used for the calibration of integrated optics interferometers for astronomical use (see for instance Saviauk et al., 2013). In the present case, a spatial light modulator is required to excite selectively the modes of the multimode end of the device and perform the calibration. In particular, the columns of the sub-matrix $\boldsymbol{A}$ are obtained from the power delivered by each output waveguide resulting from the excitation of individual modes of the photonic lantern. The sub-matrices $\boldsymbol{B}$ and $\boldsymbol{C}$ are obtained by exciting the device with a superposition of modes with a linearly increasing phase delay between them.

The column vector $\vec{J}$ [Eq. (7.5)] contains the square moduli of the coefficients c_i and the real and imaginary parts of all possible pair products of the modal amplitudes. Since only the relative phase between the modes matter to retrieve the input pattern of light, only the real and imaginary parts of the products of the amplitudes of a reference mode (*e.g.* the fundamental one) by the conjugate of the amplitudes of the other modes are indeed necessary to solve the modal decomposition problem. Solving for $\vec{J}$ is equivalent to solving an overdetermined system of equations, which is possible by left multiplying the vector $\vec{I}$ by the Moore-Penrose pseudoinverse of $\boldsymbol{V}$: $\boldsymbol{V}^+ = (\boldsymbol{V}^T\boldsymbol{V})^{-1}\boldsymbol{V}^T$ (Press et al., 1992). An important feature of this solution algorithm is to gauge the sensitivity of the solution to the inevitable measurement noise of the elements of $\vec{I}$. This is possible by estimating the condition number of $\boldsymbol{V}$, which is defined as the ratio of the maximum to the minimum singular values of the matrix (Press et al., 1992).

The condition number (which we denote with the symbol κ) can be interpreted as the ratio of the maximal to minimal stretching ratios of the matrix $\boldsymbol{V}$ along specific directions in the space of the $\vec{J}$ vector. Thus, an ill-conditioned matrix (large κ) would stretch the vectors much more in one direction than another meaning that small perturbations of the vector $\vec{J}$ chosen along certain directions would be

amplified greatly by the mapping operation. Therefore, a small κ is required to ensure the numerical stability of the transformation $\boldsymbol{V}$ and its pseudoinverse.

As it has been already shown in the past (Minardi, 2012; Minardi, 2015), the conditioning of the transfer matrix $\boldsymbol{V}$ of a discrete beam combiner significantly depends on the geometric parameters of the waveguide array and its excitation configuration. To optimize the modal analyzer, we considered not only the geometry of the array of waveguides, but we also carried out tests to find a convenient injection geometry from the photonic lantern to the discrete beam combiner. A thorough verification of all injection configurations would become very rapidly an intractable problem due to their factorial scaling with the number of waveguides in the photonic lattice. We therefore used a heuristic method to guide our optimization process, which was based on the requirement of a field transfer function $\psi_{\mathrm{i,j}}$ with aperiodic phases evenly distributed on the $0 - 2\pi$ interval (Minardi, 2015). The optimization was carried out by means of an RSoft CAD (Synposys and RSoft Design Group, 1993-2018) model of the mode analyzer. The $\boldsymbol{V}$ matrices of the studied designs were constructed according to Eq. (7.6) from the peak amplitudes of the fields at the waveguides centers $\psi_{\mathrm{i,j}}$ calculated by the beam propagation solver BeamPROP (Synposys and RSoft Design Group, 1993-2018). The multimode end of the device has an 8 μm core diameter and a numerical aperture of 0.17 and hence supports 3 LP modes (the fundamental LP_{01} and the doubly-degenerate LP_{11}) at $\lambda = 1.5\ \mu m$ (see Fig. 7.1). The single-mode fibers emerging from the multimode core and the array's waveguides have a 5 μm core diameter each with a similar numerical aperture. The lattice constant of the hexagonal array is 7.5 μm which gives a coupling length of $L_C = 1\ mm$. The lantern's taper angle is taken shallow enough for it to be adiabatic.

Figure 7.2 shows the dependence of κ on the array's length for some of the configurations we studied while attempting to optimize the device. This optimization strategy was supported by the observation that an input configuration where the output waveguides of the photonic lantern are symmetrically distributed across the array give rise to highly ill-conditioned $\boldsymbol{V}$ matrices (one example of this case is the configuration shown by green dashed line in Fig. 7.2). For those configurations the modes of the photonic lantern excite with high efficiency the analogous real-valued supermodes of the photonic lattice, which allow only two possible phases separated by π. On the contrary, by restricting the injection sites to contiguous sites of the photonic lattice (see brown circle in Fig. 7.2), the field propagating in the array is in general a complex-valued superposition of different supermodes, allowing the

transfer function $\psi_{i,j}$ to take arbitrary phase values. An off-center excitation of the array provided a smoother dependence of κ on the device's length (cf. purple dotted-dashed line and black solid circle in Fig. 7.2) as more phase diversity is introduced thanks to the broken symmetry of the system in agreement with previous results (Minardi, 2015). Additionally, the array needed to be compatible with the symmetry of the modes of the photonic lantern to avoid modal losses (Birks et al., 2015). For this reason, we chose a 1×7 photonic lantern supporting $N = 3$ linearly polarized (LP) modes coupled to 7 neighboring sites of a hexagonal photonic lattice featuring more than 9 waveguides (see red open square in Fig. 7.2). We thus significantly restricted the number of configurations to be tested with a beam propagation method to a bare minimum. We confirmed that, even though the minimal number of waveguides required in the photonic lattice is $M = N^2$ (in this case, 9 for the 3 modes), an oversized device with more waveguides leads to better conditioned matrices $\boldsymbol{V}$ (cf. red open square and blue solid line in Fig. 7.2). The phases at output waveguides corresponding to each of the supported modes for two of the configurations we studied are counted in the histograms in Fig. 7.3. The oversized hexagonal configuration (shown by the blue solid line in Fig. 7.2 and by dotted

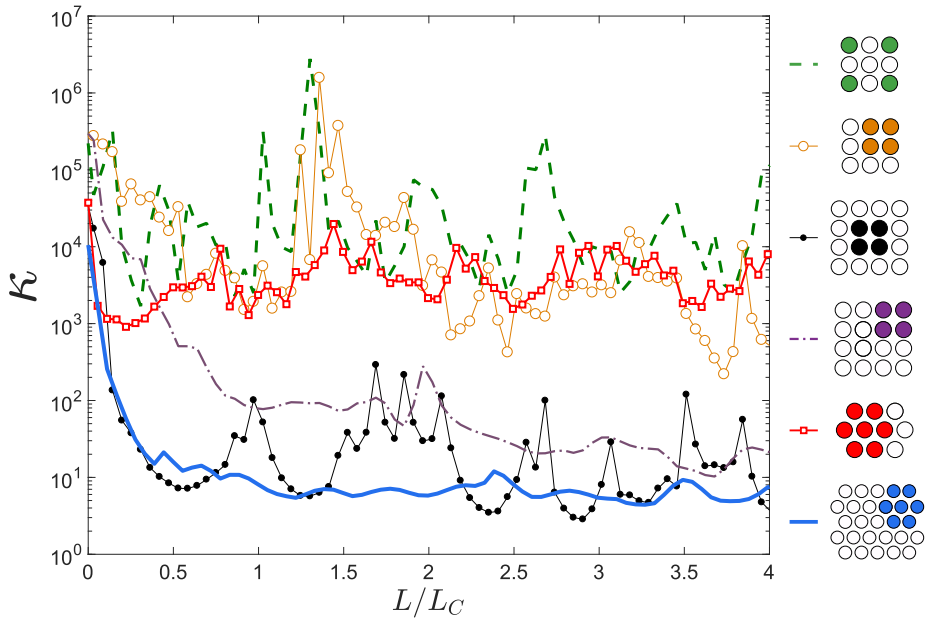

Figure 7.2: Variations of the condition number κ of $\boldsymbol{V}$ along the array in units of coupling lengths for different geometries. A hexagonal oversized array with an off-center 1×7 lantern (blue solid curve) provides the best performance as it has a low condition number that is fairly insensitive to length.

outline, blue fill in Fig. 7.3) which possesses all the attributes we deemed beneficial to lowering κ has its phases more evenly distributed in the interval $[-\pi, \pi]$ than the phases of the square configuration (shown by green dashed line in Fig. 7.2 and by solid outline, green fill box in Fig. 7.3), which lacks those attributes.

Figure 7.1 illustrates the layout of a device with an optimized configuration. The device has been designed for an input lantern supporting 3 modes and has a minimal condition number of $\kappa = 4.4$ (at array length $L = 3.3\,mm$) as a result of the oversized array (27 waveguides). Interestingly, the condition number varies smoothly along the length of the device (Fig. 7.2, blue solid line curve), so that the performance of a real device is relatively tolerant to uncertainties in the coupling coefficient of the waveguide array.

The performance of the same device was evaluated numerically by calculating the impact of an additive random noise in the intensity measurement (*e.g.* dark current of a single pixel detector) on the retrieval of the complex amplitudes of the input modes. The algorithm computes the intensity signal at the output of the mode analyzer $\vec{I}$ from an array of different input vectors $\vec{J}$, each one with unitary modal amplitude and a phase covering all possible combinations of relative phases between modes 1-2 and 1-3 sampled on the $[0, 2\pi]$ interval. We added to each element of the

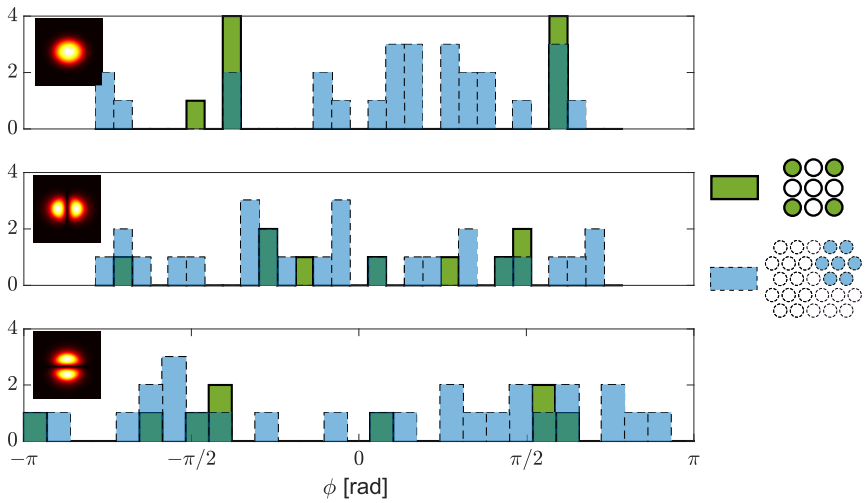

Figure 7.3: Histogram of the phase of the field transfer matrix $\psi_{n,i}$ for i = 1, 2 and 3 (excitation of the device with the 3 modes supported by the lantern and shown in the insets) in a 9 waveguides square array (solid outline, green fill, $\kappa = 2 \times 10^6$) and a 27 waveguides hexagonal array with an off-center lantern (dotted outline, blue fill, $\kappa = 4.4$). Greater phase diversity of the field transfer matrix yields $\boldsymbol{V}$ matrices with lower condition numbers.

calculated $\vec{I}$ vectors a random number with zero mean and Gaussian distribution of amplitude ϵ. The noisy vector was transformed back to the modal amplitude vector $\vec{J}_\epsilon$ by means of the pseudoinverse of $\boldsymbol{V}$ and its average distance χ from the input vector $\vec{J}$ was calculated:

$$\chi = \sqrt{\frac{\sum_{i=1}^{N^2}[J_\epsilon(i) - J(i)]^2}{N^2}}. \tag{7.8}$$

The average of χ over 1000 noise realization was calculated for each input vector. Because of the chosen normalization, χ can be seen as the average relative error of the retrieved elements of vector $\vec{J}$. Figure 7.4 shows the averaged χ as a function of the relative phases differences 1-2 and 1-3 for $\epsilon = 0.1$. We notice that there is no preferential phase combination. The phase-averaged χ grows linearly with the noise ϵ with a slope of 0.7.

The fidelity of the modal analysis depends ultimately on how well the modes of the multimode waveguide describe the input field. A numerical estimate shows that a lateral shift of the input field by 1/32 of the waveguide diameter will change the projected amplitudes of the modes by $\sim$10%. We notice, however, that solid state lasers can feature a pointing stability better than 1/100 of the beam divergence.

To conclude, we proposed a fast and computationally inexpensive method for determining the complex amplitudes of the excited modes in a waveguide by means

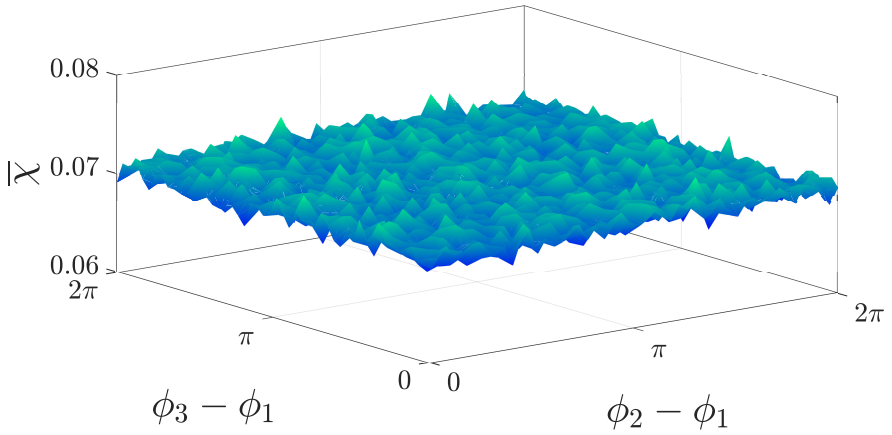

Figure 7.4: The expected average relative error of the retrieved vector $\vec{J}$ from a noisy measurement of the output signal with the device depicted in Fig. 7.1. The horizontal axes represent the relative phase between modes 1-2 and 1-3. Only an additive Gaussian noise with standard deviation $\epsilon = 0.1$ was considered in the calculation (see text for details).

of intensity measurements. A single matrix multiplication is required to retrieve the sought-after coefficients, which implies that the method can be as fast as the photo-detection is. The method is, in principle, applicable to any number of modes; however, the array must have a number of waveguides that is at least equal to the square of the number of modes. The geometry of the lantern's SMFs, the geometry of the array, the manner by which the lantern is connected to the array, and the array's length all have an impact on how the modes evolve into the supermodes of the array. This, in turn, determines the condition number of the device's transfer matrix, which must be low to have a system that is relatively insensitive to measurement noise. The optimal configuration, shown by blue solid line in Fig. 7.2, has a low κ over a wide length range, which makes it suitable for broadband operation and makes it more tolerant to fabrication defects. A device like the one described here may be fabricated using 3D micro-fabrication techniques such as ultrafast laser inscription in glasses (Thomson et al., 2009) or laser two-photon polymerization (Woods et al., 2014).

The device can be used to monitor the transverse modes in lasers for control purposes. The integrated mode analyzer could be matched directly to multimode fiber lasers or through free space optics to conventional laser cavities. The possibility to operate the device in real time opens its application in the control of the beam quality of fiber lasers (Otto et al., 2013) or of the oscillating mode in transverse multi-stable lasers (Tamm et al., 1990).

Funding. German Federal Ministry of Education and Research (BMBF) (03Z22AN11).

Chapter 8

CONCLUSIONS AND OUTLOOK

Conceptually, when starlight travels from the top of the atmosphere to a detector behind a telescope, all information is conserved as long as no losses occur in between. Part of that information is the sought-after properties of the science object, while the rest is noise introduced by the atmosphere, the telescope optics, the delivery waveguide, and other instrumentation artifacts. In interferometry, for example, SMFs are used to couple only the desired fundamental mode that carries information about the unresolved source and intentionally filter the higher-order modes that carry information about the atmosphere's temporal and spatial states. The filtered modes, in this case, are valuable stellar flux that was corrupted by atmospheric noise but may be recovered if the added information can be measured and thus isolated. This is, in principle, what AO and fringe tracking systems do. Still, the correction can only be performed to an extent, mainly limited by the brightness of the available reference. Photonic lanterns, either on their own or assisted by AO, can also be used to avoid the losses that direct coupling into an SMF involves. In this case, the atmospheric noise is not filtered but instead passively rearranged, and it is now represented by the differences in amplitude and phase between the single-mode outputs of the photonic lantern. For spectroscopy, since the spectral content of the starlight is unaltered by turbulence, all the output channels carry the same spectral signal and might be used to maximize the sensitivity. Compared to MMFs, SMFs can be used to feed photonic components and are immune from modal noise that encodes additional information about the mechanical state of the delivery fiber.

The photonic approach to starlight processing has the potential of addressing some of the major challenges that astronomical instruments will face as telescope apertures grow into the extremely large phase and beyond. Many of the benefits such an approach offers, e.g., multiplexability, also extend to current smaller observatories and telescope arrays, allowing better utilization of the collected light while simplifying the instrument design. To large telescopes, AO systems are indispensable, making it possible to couple light into the waveguide intakes of astrophotonic devices. However, efficient coupling into the single-mode regime requires an extensive level of turbulence correction as is offered by ExAO systems, but that is only available under tightly limited conditions of brightness and FoV. Photonic lanterns

can be brought in to bridge the gap between the few-mode regime that conventional AO setups can achieve and the single-mode regime that astrophotonic components require. Nonetheless, as most of these novel technologies remain under development, midsize telescopes seem like the stage where astrophotonic instruments will be demonstrated first before they are fully deployed on larger observatories as facility instruments. With the continuing drop in the costs of AO systems, particularly those that are LOAO, a photonic solution can arrive at the telescope together with its AO system for on-sky testing and proofs of concept.

Quantifying the level of coupling possible via a photonic lantern into a given photonic component is imperative for deciding on the suitability of a candidate telescope and choosing science targets. This is because splitting signals inevitably impacts the SNR of the aggregate signal. Therefore, finding the best combination requires end-to-end simulations that take into account the physics of atmospheric turbulence (see Sec. 2.1.2) and imaging (see Sec. 2.1.3), the principles of AO correction (see Sec. 2.2), and the theory of optical waveguides (see Ch. 3).

For Kolmogorov's turbulence, simulating atmospheric layers requires an efficient algorithm that can generate a library of phase screens promptly since only statistical metrics taken from a large sample of such screens carry meaningful information (see Sec. 4.3). The challenge with simulating AO systems, on the other hand, is the large variety of configurations these systems could take. A general-purpose script, like the one presented in Sec. 4.5 for Matlab or the recently published open-source AOtools (Townson et al., 2019) for Python, are adjustable, to a certain degree, as required by the science case. In its current form, the script developed for this work simulates an SCAO system since the focus is on LOAO for enabling photonics, but an expansion to add more DMs or WFSs as required by the more advanced AO architectures should be straightforward. The effect of scintillation may also be included when higher turbulence layers are to be modeled, but this typically comes at a computational cost (see Sec. 2.1.2). Moreover, scenarios other than astronomical observations, e.g., laser communication, where light propagation might be upward towards a satellite or horizontal between ground stations, can also be simulated with some changes to the models of Sec. 4.3.

Multiple methods are available to solve Maxwell's equations in dielectric media and thus simulate optical phenomena in waveguides. The brute-force BPM, calculates light propagation in slowly varying waveguides by solving the Helmholtz equation on a discretized grid. However, when the interest is on circular step-index fibers that

are weakly guiding, analytical solutions exist, and the propagation into an idealized straight fiber is easily calculated using the LP modes as is done in Sec. 4.1. This technique's rapidness compared to BPMs is crucial for large FMFs with modes > 20. For astrophotonic devices with non-circular cores, e.g., trench waveguides in planar structures, analytical solutions for the modes do not exist. However, the results obtained for their closest circular analogs can prove helpful, especially when these results are read together with the geometrical optics approximation of Eq. (3.66).

With these simulators, computer models can then be run to solve the equations acquired (see Ch. 4) and gain insight into the dependence of coupling on geometry, turbulence, and degree of correction (see Sec. 5.2). The trade-off between the number of degrees of freedom needed at the side of the AO system and the side of the photonic lantern is accordingly calculated given the target brightness and the quality, i.e., the noise characteristics, of the detectors available. Experimental verification is consequently essential to assess the impact of the approximations made in the models on the accuracy of the simulation results (see Sec. 5.1 and Sec. 5.2).

Results on what configuration (of AO and photonic lantern) to use are highly dependent on the circumstances of the science case, and one needs to run a simulation before a configuration is favored. The criterion chosen here is to maximize the cost function that expresses the SNR in terms of those variables. The color maps in Fig. 5.13 are only valid for a 97 elements AO system and a 3 e^- RON detector but a rerun of some parts of the calculations pipeline is immediately possible if different inputs are desired. Such maps reveal the regimes where an SMF produces a higher SNR than a photonic lantern solution. When an AO correction is applied, this is the case for faint sources under weak or strong turbulence (see Fig. 5.13d). A photonic lantern is superior for brighter sources, and the optimum size depends on the turbulence strength, as Fig. 5.13e and f show. These results assume equal splitting of optical power by the photonic lantern among its outputs which is, strictly speaking, only true when a scrambling technique is successfully employed (see Sec. 5.2.4). To account for the unequal splitting, BPMs must be used to simulate the photonic lantern, which again comes at a computational cost. Neural networks have also been used recently to model photonic lanterns, including fabrication defects when trained with *in situ* measurements of a physical lantern (Sweeney et al., 2021). Separately, the different parts of these numerical models are useful to calculate dis-

torted and corrected wavefronts, PSFs, modes, coupling coefficients, output fields, among other physical parameters.

Photonic lanterns, being relatively new, continue to be designed and configured in different manners other than the one originally proposed for suppressing telluric lines. One way they can help reduce the multiplicity of a multiplexed instrument is by breaking the symmetry between their SMFs to get mode selectivity whereby, if AO is utilized, many of the output channels can be discarded (see Ch. 6) leading to accumulated signals with a better SNR. Such an approach will further strengthen the case for multiplexed astrophotonic devices. Experimental work and on-sky testing are clearly the next milestones for this concept of applying AO-assisted MSPLs to astrophotonics.

Furthermore, when combined with a DBC, a photonic lantern can be used to analyze the modes at its multimode input (see Ch. 7). This represents a focal plane, all-photonic WFS. For astronomy, the integrated nature of such devices does not outweigh their need for a large number of subapertures leading to them requiring even brighter guide stars than their pupil plane analogs, e.g., SH-WFS. Convolutional neural networks may, however, help in the future tip the scale in favor of the photonic mode analyzer if post-processing of the outputs of an undersized device, with fewer waveguides than theoretically required, can be done fast enough (Norris et al., 2020) but this is yet to be studied. They can, however, be used for measuring NCPAs that dictate the achievable contrast in exoplanet imaging. NCPAs arise from the path mismatch between the WFS and the science arm and are therefore quasi-static in general, with changes only occurring due to mechanical creep and temperature variations. The long-time scales allow the implementation of post-processing computations to overcome the lack of measurements of an undersized sensor and for longer exposures to overcome the low photons count in an oversized sensor (Orban de Xivry et al., 2021). At their current state, photonic mode analyzers comprised of photonic lanterns and DBCs offer an integrated WFS for industries where the brightness of the illumination source is ample, e.g., FSO communication (Calvo et al., 2019), photolithography, directed energy applications, and vision sciences. For high-power fibered lasers used in metal processing, the mode analyzer could be used as a feedback sensor for the control loop that suppresses the excitation of higher-order modes in LMA fibers. In ophthalmology, the photonic WFS is well suited for integration in handheld ophthalmoscopes (DuBose et al., 2018) being developed to visualize retinal structures *in vivo*.

Space is also one more frontier where integrated optics may find applications in the near future. Photonic WFSs could, to give one example, be used to correct phasing errors in segmented space telescopes (Potier et al., 2021). Generally, the multiplexing approach, that photonic lanterns enable, can help recover the last 20 per cent of starlight that is otherwise lost, even under diffraction-limited conditions, when light is directly focused onto an SMF. Qualifying integrated optics for space applications to ensure they can endure vacuum and radiation is an active area of research of several groups (Piacentini et al., 2021).

Appendix A

KOLMOGOROV'S LAW

An alternative derivation of Kolmogorov's law that also uses a dimensional analysis argument is given here. Again, the goal is to find the share of energy in every length scale in the continuum of vortices between the outer and the inner scales. Instead of working in real space, it is convenient to work in the reciprocal space k and find the number of vortices in a unit length.

If the energy stored in each mode k per unit mass is $\Phi(k)$, the quantity $\Phi(k)\mathrm{d}k$ has the dimension $\mathrm{J{\cdot}kg^{-1}}$ in SI units. Since $\mathrm{J = kg{\cdot}m^2{\cdot}s^{-2}}$, one gets $[\Phi(k)] = \mathrm{m^3{\cdot}s^{-2}}$ and $[\varepsilon] = \mathrm{m^2{\cdot}s^{-3}}$. Kolmogorov's assumption is that, in the inertial subrange, the energy is governed only by the scale size k and the energy injection rate ε, i.e., $\Phi(k) \propto \varepsilon^a k^b$. The constant of proportionality of this relation must be dimensionless since the equation does not depend on the choice of units. This leads to $\mathrm{m^3} = \mathrm{m^{2a}{\cdot}m^{-b}}$ and $\mathrm{s^2} = \mathrm{s^{3a}}$. For the dimensions to match, $a = 2/3$ and $b = -5/3$ giving

$$\Phi(k) \propto \varepsilon^{2/3} k^{-5/3}, \tag{A.1}$$

which is Kolmogorov's 5/3rds law. The subrange $\mathcal{L}_0/l_0$ where the law is valid grows as the turbulence develops ($Re \to \infty$), and it increases with Re as $Re^{3/4}$. The dimensionless constant of proportionality depends on Re and needs to be determined from experiments. In general, it has values $\in (1.4, 1.8)$.

One shortcoming of the Kolmogorov theory is that it is not consistent with the *intermittency* of the small-scale eddies in fully developed turbulence. The velocity signal exhibits short bursts in time because the small scales are not space-filling as Kolmogorov assumed since the number of generated eddies N by one parent eddy in each step in the cascade is not necessarily as much space-filling as the parent, i.e., $N < 2^3$ for a second generation of eddies that are each half the size of the primary one. The power law (Eq. A.1) holds for the spectrum in the inertial range but the exponent must be modified (Frisch, 1980)

$$\Phi(k) \propto \varepsilon^{2/3} k^{-5/3} (k l_0)^{-(3-\log_2 N)/3}. \tag{A.2}$$

Experimental results show that $N \sim 2^{2.5}$ and not 2^3 like Kolmogorov assumed.

Appendix B

DIFFRACTION THEORY

The derivation of the Fraunhofer diffraction integral from Huygens' principle is given here. The special case of planar waves passing through a circular aperture is also calculated.

A typical scenario (see Fig. B.1) has the aperture at the $z = 0$ plane centered on the coordinate system's origin with a point source on the z axis at $z = -\infty$. The waves arriving from the source are, therefore, planar and normally incident at the aperture. According to the Huygens-Fresnel principle (Born et al., 2013), every elemental area dS within the aperture emits spherical wavelets. At an arbitrary point P on the observation plane, a distance r_s away, the contribution to the field from the element dS is

$$\mathrm{d}E(x', y') = \frac{A}{r_s} e^{i(\omega t - k r_s)} \mathrm{d}S, \tag{B.1}$$

where $E(x', y')$ is the field at the observation plane $z' = 0$, A is the constant amplitude of the field over the aperture plane, ω is the temporal angular frequency, and $k = 2\pi/\lambda$ is the wavenumber. For astronomical telescopes, the observation plane is the far field, i.e., the focal plane. There, the aperture is small compared to the distance between the two planes, and all elemental areas can be assumed to be at the same distance from the observation point. Specifically, all area elements are

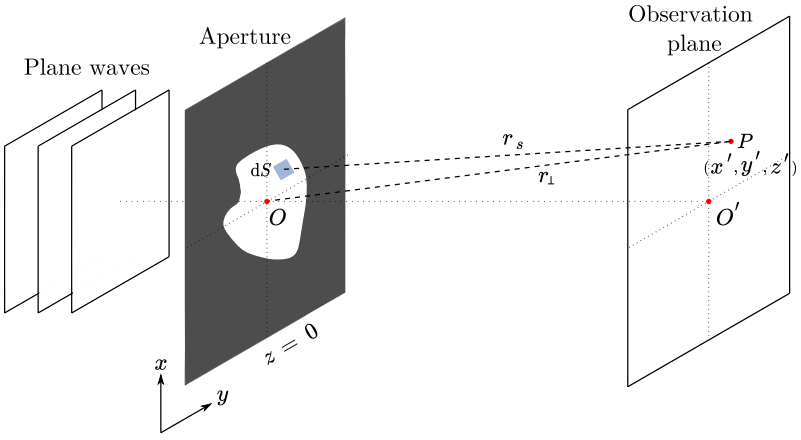

Figure B.1: Geometry of a diffracting aperture and an observation plane.

assumed to be at the origin, a distance $r_\perp = (x' + y' + z')^{1/2}$ away. Equation (B.1) is thus simplified by replacing r_s with $r_\perp$ in the amplitude term, i.e., $A/r_s \approx A/r_\perp$. The wavenumber k has a large magnitude at short wavelengths, which causes the phase to be more sensitive to path differences between different area elements than amplitude (Hecht, 2002) and therefore cannot be simplified in a similar manner . The distance between the observation point P and the element dS is

$$r_s = \left[z'^2 + (x' - x)^2 + (y' - y)^2\right]^{1/2}. \tag{B.2}$$

Expanding the squares

$$r_s = r_\perp \left[1 + \frac{x^2 + y^2}{{r_\perp}^2} - \frac{2(x'x + y'y)}{{r_\perp}^2}\right]^{1/2}, \tag{B.3}$$

where use was made of the formula for $r_\perp$. The term $(x^2 + y^2)/{r_\perp}^2$ is negligible when the distance $r_\perp$ is very large compared to the size of the aperture. Keeping only two terms of the binomial expansion

$$r_s \approx r_\perp \left[1 - \frac{x'x + y'y}{{r_\perp}^2}\right]. \tag{B.4}$$

Substituting in Eq. (B.1) and integrating one gets

$$E(x', y') = \frac{Ae^{i(\omega t - kr_\perp)}}{r_\perp} \iint_S e^{ik(x'x + y'y)/r_\perp} \mathrm{d}S, \tag{B.5}$$

This is the optical field at the focal plane of an arbitrary aperture when illuminated by a monochromatic plane wave of constant amplitude and phase throughout. In general, this need not be the case. Both amplitude and phase can vary over the aperture, and the amplitude in Eq. (B.5) can be rewritten as a complex amplitude

$$A(x, y) = A_0(x, y)e^{i\phi(x,y)}, \tag{B.6}$$

where $A_0(x, y)$ represents the amplitude over the aperture while $\phi(x, y)$ represents the phase. The optical field due to a general wavefront passing the aperture is then

$$E(x', y') = \int_{-\infty}^{+\infty}\!\!\iint A(x, y)e^{ik(x'x + y'y)/r_\perp} \mathrm{d}x\mathrm{d}y, \tag{B.7}$$

where the limits on the integral were extended to $\pm\infty$ since the aperture function $A(x, y)$ is zero outside the aperture and the differential area element $\mathrm{d}S$ was replaced by its Cartesian representation $\mathrm{d}x\mathrm{d}y$. The time-dependant factor $e^{i\omega t}$, the constant phase factor $e^{-ikr_\perp}$ and the amplitude factor $1/r_\perp$, all are necessary to compute the absolute field value relative to the magnitudes at the aperture but do not affect the relative intensity distribution on the observation plane, i.e., the form of the image. Therefore, they were dropped in Eq. (B.7) and an energy conservation argument can always be applied later to normalize the field. If a parameters substitution is now introduced as

$$k_{x'} = \frac{kx'}{r_\perp}, \tag{B.8a}$$

$$k_{y'} = \frac{ky'}{r_\perp}, \tag{B.8b}$$

the field at the observation plane can simply be written as the Fourier transform of the aperture function $A(x, y)$.

$$E(k_{x'}, k_{y'}) = \iint_{-\infty}^{+\infty} A(x, y) e^{ik(k_{x'}x + k_{y'}y)} \mathrm{d}x\mathrm{d}y = \mathcal{F}\left\{A(x, y)\right\}, \tag{B.9}$$

where $\mathcal{F}(\cdot)$ denotes a Fourier transform. A special case of particular importance is the Fraunhofer diffraction of a plane wave at a circular aperture since most telescopes have round primary mirrors and observe distant point sources. Switching to cylindrical coordinates with

$$x = \rho\cos\phi, \qquad y = \rho\sin\phi \tag{B.10a}$$

$$x' = \rho'\cos\phi', \qquad y' = \rho'\sin\phi', \tag{B.10b}$$

and using Eq. (B.7) instead of the Fourier transform since an analytical solution exists for this case

$$E(\rho', \phi') = \frac{Ae^{i(\omega t - kR)}}{r_\perp} \int_0^a \int_0^{2\pi} e^{i(i\rho\rho'/r_\perp)\cos(\phi - \phi')} \rho\mathrm{d}\rho\mathrm{d}\phi. \tag{B.11}$$

Axial symmetry suggests that the field at the observation plane must be independent of ϕ'. Setting $\phi' = 0$, the inner integral

$$\int_0^{2\pi} e^{i(k\rho\rho'/R)\cos\phi}\mathrm{d}\phi, \tag{B.12}$$

is, apart from a factor of 2π, recognized as the Bessel function of the first kind of order zero $J_0(k\rho\rho'/R)$. Equation (B.11) is then

$$E(\rho',\phi') = \frac{2\pi A e^{i(\omega t-kR)}}{r_\perp}\int_0^a J_0\left(\frac{k\rho\rho'}{r_\perp}\right)\rho\mathrm{d}\rho. \tag{B.13}$$

Using the recurrence property of Bessel functions,

$$\int_0^u u' J_0(u')\mathrm{d}u' = uJ_1(u), \tag{B.14}$$

and substituting with $w = k\rho\rho'/r_\perp$, this becomes

$$\begin{aligned} E(\rho',\phi') &= \frac{Ae^{i(\omega t-kr_\perp)}}{r_\perp}2\pi\left(\frac{r_\perp}{k\rho'}\right)^2\int_0^{ka\rho'/R} J_0(w)w\mathrm{d}w \\ &= \frac{Ae^{i(\omega t-kr_\perp)}}{r_\perp}2\pi a^2\left(\frac{r_\perp}{ka\rho'}\right)J_1\left(\frac{ka\rho'}{r_\perp}\right). \end{aligned} \tag{B.15}$$

The intensity distribution associated with this field is given by $(1/2)EE^*$ as

$$I(\rho',\phi') = \frac{2A^2(2\pi a^2)^2}{{r_\perp}^2}\left[\frac{J_1(ka\rho'/r_\perp)}{ka\rho'/r_\perp}\right]^2. \tag{B.16}$$

This is the Airy pattern. It has a central circular lobe, i.e., the Airy disk, surrounded by an infinite succession of bright rings of ever-decreasing intensity. The radius of the Airy disk is of importance since 84% of the light falls within that disk and for most applications, the resolution and quality of the formed images are conventionally determined by the disk rather than the surrounding rings. The Bessel function in Eq. (B.16) can be evaluated numerically or using mathematical tables. One finds that the first zero is at a distance

$$\rho' = 1.22\frac{r_\perp\lambda}{2a}, \tag{B.17}$$

from the center.

To derive the formula for the Strehl ratio, the Fresnel-Kirchhoff diffraction integral is required (Born et al., 2013).

$$E(P) = -\frac{iAa^2}{\lambda {r_\perp}^2} \exp\left[iu\left(\frac{r_\perp}{a}\right)^2\right] \int_0^1 \int_0^{2\pi} \rho \mathrm{d}\rho \mathrm{d}\theta \exp\left[i\left(\psi(\rho,\theta) - v\rho\cos(\theta-\psi) - \frac{1}{2}u\rho^2\right)\right], \quad \text{(B.18)}$$

where $u = k(a/r_\perp)^2 z$ and $v = k(a/r_\perp)\sigma$ (Hardy, 1998). For a circular aperture, the Strehl ratio is

$$SR = \frac{I(0,0)}{I_0(0,0)} = \frac{1}{\pi^2}\left|\int_0^1 \int_0^{2\pi} \rho \mathrm{d}\rho \mathrm{d}\theta e^{ik\Lambda(\rho,\theta)}\right|^2, \quad \text{(B.19)}$$

where $\Lambda(\rho.\theta)$ is the aberration function in OPD units. $I(0)$ and $I_0(0)$ are the central intensities of the seeing-limited and diffraction-limited PSFs, respectively. The central intensity is given by integrating the OTF since the OTF is the Fourier transform of the PSF

$$I_0(0,0) = \int \mathrm{d}\vec{f} T_{tele}(\vec{f}). \quad \text{(B.20)}$$

Using Eq. (2.46)

$$\begin{aligned} SR = \frac{I(0,0)}{I_0(0,0)} = \frac{\int \mathrm{d}\vec{f} T_{tele}(\vec{f}) B_\psi(\vec{f})}{\int \mathrm{d}\vec{f} T_{tele}(\vec{f})} &= \frac{\int \mathrm{d}\vec{f} \exp\left[-\left(\frac{D_\phi}{2}\right)\right] T_{tele}(\vec{f})}{\int \mathrm{d}\vec{f} T_{tele}(\vec{f})} \\ &= \frac{\int \mathrm{d}\vec{f} \exp\left[-B_\phi(0) + B_\phi(\vec{f})\right] T_{tele}(\vec{f})}{\int \mathrm{d}\vec{f} T_{tele}(\vec{f})} \\ &= \exp\left[-B_\phi(0)\right] \frac{\int \mathrm{d}\vec{f} \exp\left[B_\phi(\vec{f})\right] T_{tele}(\vec{f})}{\int \mathrm{d}\vec{f} T_{tele}(\vec{f})}. \end{aligned} \quad \text{(B.21)}$$

An approximation is possible for wavefronts with small variance $B_\phi(\vec{f}) \ll 1$. The quotient becomes close to unity, and since $B_\phi(0)$ is by definition the ensemble average of the square variations in phase, i.e., the phase variance over the aperture σ_ϕ^2.

When ψ is random and only its statistics are known, the following approximation

$$SR \approx e^{-\sigma_\phi^2}, \tag{B.22}$$

known as the *extended Maréchal approximation* (Maréchal, 1947; Ross, 2009) holds for rms phase errors $\sigma_\phi = \langle(\phi - \overline{\phi})^2\rangle < 2$ rad. The phase rms, σ_ϕ, is related to the rms OPD error by $\sigma_\phi \equiv k\sigma_\psi$. The Strehl ratio, therefore, takes values $SR \in [0, 1]$. For a plane wavefront with $\phi = const.$, $SR = 1$. Equation B.22 shows how the image quality degrades exponentially with the mean square error of the phase.

Appendix C

MAXWELL'S EQUATIONS

In the electromagnetic theory of light, the field is described by two temporally and spatially varying vector fields, i.e., the electric $\vec{\mathcal{E}}(\vec{r},t)$ and the magnetic $\vec{\mathcal{H}}(\vec{r},t)$ fields. Maxwell formulated four partial differential equations that relate the functions of these fields in space and time to each other. In free space

$$\nabla \times \mathcal{H} = \epsilon_0 \frac{\partial \mathcal{E}}{\partial t}, \tag{C.1}$$

$$\nabla \times \mathcal{E} = -\mu_0 \frac{\partial \mathcal{H}}{\partial t}, \tag{C.2}$$

$$\nabla \cdot \mathcal{E} = 0, \tag{C.3}$$

$$\nabla \cdot \mathcal{H} = 0, \tag{C.4}$$

where ϵ_0 and μ_0 are the electric permittivity and the magnetic permeability of free space, respectively. For electromagnetic waves, $\mathcal{E}$ and $\mathcal{H}$ are the oscillating quantities in time and space. Taking the curl of Eq. (C.2) one gets

$$\nabla \times \nabla \times \mathcal{E} = -\mu_0 \frac{\partial(\nabla \times \mathcal{H})}{\partial t}, \tag{C.5}$$

where the order of the two differential operators could be interchanged as one is acting on space while the other is acting on time. Applying the identity $\nabla \times \nabla \times u = \nabla(\nabla \cdot u) - \nabla^2 u$ yields

$$\nabla(\nabla \cdot \mathcal{E}) - \nabla^2 \mathcal{E} = -\mu_0 \frac{\partial(\nabla \times \mathcal{H})}{\partial t}. \tag{C.6}$$

Substituting for $\nabla \cdot \mathcal{E}$ and $\nabla \times \mathcal{H}$ from Eq. (C.3) and Eq. (C.1), respectively

$$\nabla^2 \mathcal{E} - \frac{1}{{c_0}^2} \frac{\partial^2 \mathcal{E}}{\partial t^2} = 0, \tag{C.7}$$

where $\mathcal{E}$ is any of the three components of $\vec{\mathcal{E}}$ and $c_0 = (\epsilon_0 \mu_0)^{-1/2}$ is the speed of light in free space. A similar approach will produce the wave equation of $\mathcal{H}$ in

free space. In a source-free medium, the electric and magnetic properties of the medium play a role in shaping the fields, and two additional fields are required, i.e., the electric flux density $\mathcal{D}(\vec{r},t)$ and the magnetic flux density $\mathcal{B}(\vec{r},t)$. Maxwell's equations in such media are

$$\nabla \times \mathcal{H} = \frac{\partial \mathcal{D}}{\partial t}, \tag{C.8}$$

$$\nabla \times \mathcal{E} = \frac{\partial \mathcal{B}}{\partial t}, \tag{C.9}$$

$$\nabla \cdot \mathcal{D} = 0, \tag{C.10}$$

$$\nabla \cdot \mathcal{B} = 0. \tag{C.11}$$

The types of media of interest in waveguide optics are linear, nondispersive, homogeneous, and isotropic. Maxwell's equations, in this case, are similar to those in free space except that the free space permittivity and permeability are replaced by the relative permittivity ϵ and the relative permeability μ. The scalar wave equation of the electric field, therefore, is

$$\nabla^2 \mathcal{E} - \frac{1}{c^2}\frac{\partial^2 \mathcal{E}}{\partial t^2} = 0, \tag{C.12}$$

where $c = (\epsilon\mu)^{-1/2}$ is the speed of light in the medium. To proceed further, one needs to restrict one's self to the monochromatic case where the components $\mathcal{E}$ and $\mathcal{H}$ are harmonic in time and can be factored into a space-dependent part and a time-dependent part, i.e.,

$$\mathcal{E}(\vec{r},t) = \mathrm{Re}\{E(\vec{r})e^{i\omega t}\} \tag{C.13}$$

$$\mathcal{H}(\vec{r},t) = \mathrm{Re}\{H(\vec{r})e^{i\omega t}\}, \tag{C.14}$$

where the space-dependent factors $E(\vec{r})$ and $H(\vec{r})$ are the electric field and magnetic field complex amplitudes, respectively. The partial time derivatives are simplified in this case, and the monochromatic Maxwell's equations of the complex amplitudes are

$$\nabla \times H = i\omega\epsilon E, \tag{C.15}$$

$$\nabla \times E = -i\omega\mu H, \tag{C.16}$$

$$\nabla \cdot D = 0, \tag{C.17}$$

$$\nabla \cdot B = 0. \tag{C.18}$$

Differentiating Eq. (C.13) twice with respect to time and substituting in the wave equation Eq. (C.12), the *Helmholtz equation* (Born et al., 2013) is obtained

$$\nabla^2 U(\vec{r}) + k^2 U(\vec{r}) = 0, \tag{C.19}$$

where $U(\vec{r})$ can be the complex amplitude of any of the components of $\vec{E}$ or $\vec{H}$ and $k = \omega\sqrt{\epsilon\mu} = nk_0$ is the wavenumber in the medium. The factor by which light slows down in a medium, $n = c_0/c$, is recognized as the refractive index of that medium.

In Cartesian coordinates, the transverse fields distributions $U(x, y)$ propagates in the z direction with propagation constant β without change (Buck, 2004)

$$U(x, y, z) = U(x, y)e^{-i\beta z}. \tag{C.20}$$

The Helmholtz equation applies to both transverse components

$$\nabla^2 U_{x,y} + k_0^2 n^2 U_{x,y} = 0 \tag{C.21}$$

For the ansatz in Eq. (C.20), the z derivative is

$$\partial_{zz} U_{x,y} = \beta^2 U_{x,y} \tag{C.22}$$

Substituting in Eq. (C.21) yields

$$\nabla_T^2 U_{x,y} + \left(k_0^2 n^2(x, y) - \beta^2\right) U_{x,y} = 0, \tag{C.23}$$

where $\nabla_T^2 = \partial_{xx} + \partial_{yy}$ is the transverse Laplacian. The weak guidance approximation $\Delta \ll 1$ and the requirement for β to lay between the core and cladding wavenumbers yield $|k_0^2 n^2 - \beta^2| \ll \beta^2$ with $\beta = k_0 n_{eff}$ where $n_2 < n_{eff} < n_1$.

For the weakly guiding fiber, only knowledge of two of the six field components is required to know the rest. If e_x and e_y are known, Maxwell equation Eq. (3.4) can be used to obtain h_z as follows

$$h_z = -\frac{1}{i\omega\mu_0}\left(\partial_x e_y - \partial_y e_x\right) \tag{C.24}$$

Now utilizing Eq. (3.3), e_x and e_y can be determined from

$$e_x = \frac{1}{i\omega\epsilon_0 n^2}\left(\partial_y h_z + i\beta h_y\right) \tag{C.25}$$

$$e_y = \frac{1}{i\omega\epsilon_0 n^2}\left(-\partial_x h_z - i\beta h_x\right). \tag{C.26}$$

Note that $\partial_z h_y$ and $\partial_z h_x$ were directly calculated from Eq. (C.20). Furthermore, from the weak guidance condition, $|\nabla_T^2| \ll \beta^2$ yielding $|\partial_x|, |\partial_y| \ll \beta$. Therefore, $\partial_y h_z$ and $\partial_x h_z$ can be dropped from Eq. (C.25) and (C.26), respectively, to get

$$e_x \approx \frac{\beta}{\omega\epsilon_0 n^2} h_y \tag{C.27}$$

$$e_y \approx \frac{-\beta}{\omega\epsilon_0 n^2} h_x. \tag{C.28}$$

Again by means of Maxwell equation Eq. (3.3) and the weak guidance approximation

$$e_z = \frac{1}{i\omega\epsilon_0 n^2}\left(\partial_x h_y - \partial_y h_x\right) \approx \frac{1}{i\beta}\left(\partial_x e_x - \partial_y e_y\right). \tag{C.29}$$

Thus knowledge of the two transverse components of one field is enough to determine all six components for a weakly guiding fiber.

BIBLIOGRAPHY

Abuter, R., Amorim, A., Bauböck, M., Berger, J. P., Bonnet, H., Brandner, W., Clénet, Y., Coudé du Foresto, V., Zeeuw, P. T. d., Deen, C., Dexter, J., Duvert, G., Eckart, A., Eisenhauer, F., Schreiber, N. M. F., Garcia, P., Gao, F., Gendron, E., Genzel, R., . . . Yazici, S. (2018). Detection of orbital motions near the last stable circular orbit of the massive black hole SgrA*. *Astronomy & Astrophysics*, *618*, L10. https://doi.org/10.1051/0004-6361/201834294

Alefeld, G. (1981). On the Convergence of Halley's Method. *The American Mathematical Monthly*, *88*(7), 530–536. https://doi.org/10.1080/00029890.1981.11995308

Babcock, H. W. (1953). The possibility of compensating astronomical seeing. *Publications of the Astronomical Society of the Pacific*, *65*(386), 229–236. Retrieved April 13, 2021, from https://www.jstor.org/stable/40672682

Baudrand, J., & Walker, G. A. H. (2001). Modal Noise in High-Resolution, Fiber-fed Spectra: A Study and Simple Cure. *Publications of the Astronomical Society of the Pacific*, *113*(785), 851–858. https://doi.org/10.1086/322143

Bechter, A., Crass, J., Ketterer, R., Crepp, J. R., King, D., Zhao, B., Reynolds, R., Hinz, P., Brooks, J., & Bechter, E. (2015). Design of the iLocater acquisition camera demonstration system. *Techniques and Instrumentation for Detection of Exoplanets VII*, *9605*, 96051U. https://doi.org/10.1117/12.2188426

Beckers, J. M. (1988). Increasing the Size of the Isoplanatic Patch with Multiconjugate Adaptive Optics [Conference Name: Very Large Telescopes and their Instrumentation, Vol. 2], *30*, 693. Retrieved April 13, 2021, from http://adsabs.harvard.edu/abs/1988ESOC...30..693B

Belle, G. T. v., Meinel, A. B., & Meinel, M. P. (2004). The scaling relationship between telescope cost and aperture size for very large telescopes. *Ground-based Telescopes*, *5489*, 563–570. https://doi.org/10.1117/12.552181

Benoit, A., Yerolatsitis, S., Harrington, K., Birks, T. A., & Thomson, R. R. (2020). A focal-ratio-degradation resistant multimode fiber link using mode-selective photonic lantern. In R. Navarro & R. Geyl (Eds.), *Advances in Optical and Mechanical Technologies for Telescopes and Instrumentation IV* (pp. 408–413). SPIE. https://doi.org/10.1117/12.2561438

Birks, T. A., Gris-Sánchez, I., Yerolatsitis, S., Leon-Saval, S. G., & Thomson, R. R. (2015). The photonic lantern. *Adv. Opt. Photon., AOP*, *7*(2), 107–167. https://doi.org/10.1364/AOP.7.000107

Bitenc, U., Bharmal, N. A., Morris, T. J., & Myers, R. M. (2014). Assessing the stability of an ALPAO deformable mirror for feed-forward operation. *Opt. Express, OE*, *22*(10), 12438–12451. https://doi.org/10.1364/OE.22.012438

Black, R. J., & Ankiewicz, A. (1985). Fiber-optic analogies with mechanics. *American Journal of Physics*, *53*(6), 554–563. https://doi.org/10.1119/1.14237

Black, R. J., & Gagnon, L. (2010). *Optical Waveguide Modes: Polarization, Coupling and Symmetry*. McGraw Hill Professional.

Bland-Hawthorn, J., Ellis, S. C., Leon-Saval, S. G., Haynes, R., Roth, M. M., Löhmannsröben, H.-G., Horton, A. J., Cuby, J.-G., Birks, T. A., Lawrence, J. S., Gillingham, P., Ryder, S. D., & Trinh, C. (2011). A complex multi-notch astronomical filter to suppress the bright infrared sky. *Nature Communications*, *2*(1), 581. https://doi.org/10.1038/ncomms1584

Bland-Hawthorn, J., & Horton, A. (2006). Instruments without optics: An integrated photonic spectrograph. *Ground-based and Airborne Instrumentation for Astronomy*, *6269*, 62690N. https://doi.org/10.1117/12.670931

Bland-Hawthorn, J., & Kern, P. (2009). Astrophotonics: A new era for astronomical instruments. *Optics Express*, *17*(3), 1880. https://doi.org/10.1364/OE.17.001880

Bland-Hawthorn, J., Lawrence, J., Robertson, G., Campbell, S., Pope, B., Betters, C., Leon-Saval, S., Birks, T., Haynes, R., Cvetojevic, N., & Jovanovic, N. (2010). PIMMS: Photonic integrated multimode microspectrograph. *Ground-based and Airborne Instrumentation for Astronomy III*, *7735*, 77350N. https://doi.org/10.1117/12.856347

Blind, N., Coarer, E. L., Kern, P., & Gousset, S. (2017). Spectrographs for astrophotonics. *Optics Express*, *25*(22), 27341–27369. https://doi.org/10.1364/OE.25.027341

Born, M., & Fock, V. (1928). Beweis des Adiabatensatzes. *Zeitschrift für Physik*, *51*(3), 165–180. https://doi.org/10.1007/BF01343193

Born, M., & Wolf, E. (2013). *Principles of Optics: Electromagnetic Theory of Propagation, Interference and Diffraction of Light*. Elsevier.

Bouquin, J.-B. L., Berger, J.-P., Beuzit, J.-L., Cottalorda, E., Delboulbe, A., Egner, S. E., Gonte, F. Y. J., Guieu, S., Haguenauer, P., Jocou, L., Magnard, Y., Moulin, T., Rochat, S., Vérinaud, C., & Woillez, J. (2018). Characterization of ALPAO deformable mirrors for the NAOMI VLTI Auxiliary Telescopes adaptive optics. *Adaptive Optics Systems VI*, *10703*, 1070371. https://doi.org/10.1117/12.2313442

Breckinridge, J. B., & Voelz, D. G. (2011). *Computational Fourier Optics: A MATLAB Tutorial*. SPIE Press.

Brown, G., Thomson, R. R., Kar, A. K., Psaila, N. D., & Bookey, H. T. (2012). Ultrafast laser inscription of Bragg-grating waveguides using the multiscan technique. *Optics Letters*, *37*(4), 491–493. https://doi.org/10.1364/OL.37.000491

Buck, J. A. (2004). *Fundamentals of Optical Fibers*. John Wiley & Sons.

Calvin, B., Jovanovic, N., Ruane, G., Pezzato, J., Colborn, J., Echeverri, D., Schofield, T., Porter, M., Wallace, J. K., Delorme, J.-R., & Mawet, D. (2021). Enhancing Direct Exoplanet Spectroscopy with Apodizing and Beam Shaping Optics. *Publications of the Astronomical Society of the Pacific*, *133*(1020), 024503. https://doi.org/10.1088/1538-3873/abdace

Calvo, R. M., Poliak, J., Surof, J., Reeves, A., Richerzhagen, M., Kelemu, H. F., Barrios, R., Carrizo, C., Wolf, R., Rein, F., Dochhan, A., Saucke, K., & Luetke, W. (2019). Optical technologies for very high throughput satellite communications. *Free-Space Laser Communications XXXI*, *10910*, 109100W. https://doi.org/10.1117/12.2513819

Chazelas, B., Pepe, F., Wildi, F., Bouchy, F., Perruchot, S., & Avila, G. (2010). New scramblers for precision radial velocity: Square and octagonal fibers. *Modern Technologies in Space- and Ground-based Telescopes and Instrumentation*, *7739*, 773947. https://doi.org/10.1117/12.856874

Chen, C.-H., Reynolds, R. O., & Kost, A. (2006). Origin of spectral modal noise in fiber-coupled spectrographs. *Applied Optics*, *45*(3), 519. https://doi.org/10.1364/AO.45.000519

Colavita, M. M. (1990). Design considerations for very long baseline fringe-tracking interferometers. *Amplitude and Intensity Spatial Interferometry*, *1237*, 80–86. https://doi.org/10.1117/12.19284

Coudé du Foresto, V. (1994). Integrated Optics in Astronomical Interferometry. In J. G. Robertson & W. J. Tango (Eds.), *Very High Angular Resolution Imaging* (pp. 261–271). Springer Netherlands. https://doi.org/10.1007/978-94-011-0880-5_46

Coudé du Foresto, V., Faucherre, M., Hubin, N., & Gitton, P. (2000). Using single-mode fibers to monitor fast Strehl ratio fluctuations: Application to a 3.6 m telescope corrected by adaptive optics. *Astronomy and Astrophysics Supplement Series*, *145*(2), 305–310. https://doi.org/10.1051/aas:2000351

Coudé du Foresto, V., Perrin, G. S., Ruilier, C., Mennesson, B. P., Traub, W. A., & Lacasse, M. G. (1998). FLUOR fibered instrument at the IOTA interferometer. *Astronomical Interferometry*, *3350*, 856–863. https://doi.org/10.1117/12.317153

Coudé du Foresto, V., & Ridgway, S. T. (1992). Fluor - a Stellar Interferometer Using Single-Mode Fibers [Conference Name: European Southern Observatory Conference and Workshop Proceedings ISBN: 9783923524426], *39*, 731. Retrieved April 22, 2021, from http://adsabs.harvard.edu/abs/1992ESOC...39..731C

Crank, J., & Nicolson, P. (1947). A practical method for numerical evaluation of solutions of partial differential equations of the heat-conduction type. *Mathematical Proceedings of the Cambridge Philosophical Society*, *43*(1), 50–67. https://doi.org/10.1017/S0305004100023197

Davenport, J., Diab, M., Deka, P., Tripathi, A., Madhav, K., & Roth, M. (2021). Photonic lanterns: A practical guide to filament tapering. *Optical Materials Express*. https://doi.org/10.1364/OME.427903

Davenport, J. J., Diab, M., Madhav, K., & Roth, M. M. (2021). Optimal SMF packing in photonic lanterns: Comparing theoretical topology to practical packing arrangements. *JOSA B*, *38*(7), A7–A14. https://doi.org/10.1364/JOSAB.413640

Davenport, J. J., Diab, M., Tripathi, A., Madhav, K., & Roth, M. M. (2020). Optical fibre pseudo-slits for astronomy. *Advances in Optical and Mechanical Technologies for Telescopes and Instrumentation IV*, *11451*, 1145123. https://doi.org/10.1117/12.2562652

Diab, M., Dinkelaker, A. N., Davenport, J., Madhav, K., & Roth, M. M. (2020). Testbed for coupling starlight into fibers and astrophotonic instruments. *Advances in Optical and Mechanical Technologies for Telescopes and Instrumentation IV*, *11451*, 114516G. https://doi.org/10.1117/12.2564720

Diab, M., Dinkelaker, A. N., Davenport, J., Madhav, K., & Roth, M. M. (2021). Starlight coupling through atmospheric turbulence into few-mode fibres and photonic lanterns in the presence of partial adaptive optics correction. *Monthly Notices of the Royal Astronomical Society*, *501*(2), 1557–1567. https://doi.org/10.1093/mnras/staa3752

Diab, M., & Minardi, S. (2019). Modal analysis using photonic lanterns coupled to arrays of waveguides. *Optics Letters*, *44*(7), 1718–1721. https://doi.org/10.1364/OL.44.001718

Dikmelik, Y., & Davidson, F. M. (2005). Fiber-coupling efficiency for free-space optical communication through atmospheric turbulence. *Applied Optics*, *44*(23), 4946–4952.

DuBose, T., Nankivil, D., LaRocca, F., Waterman, G., Hagan, K., Polans, J., Keller, B., Tran-Viet, D., Vajzovic, L., Kuo, A. N., Toth, C. A., Izatt, J. A., & Farsiu, S. (2018). Handheld adaptive optics scanning laser ophthalmoscope. *Optica*, *5*(9), 1027–1036. https://doi.org/10.1364/OPTICA.5.001027

Ealey, M. A., & Wellman, J. A. (1992). Deformable mirrors: Design fundamentals, key performance specifications, and parametric trades. *Active and Adaptive Optical Components*, *1543*, 36–51. https://doi.org/10.1117/12.51167

Ebstein, S. M. (1996). Nearly index-matched optics for aspherical, diffractive, and achromatic-phase diffractive elements. *Optics Letters*, *21*(18), 1454–1456. https://doi.org/10.1364/OL.21.001454

Edlén, B. (1966). The Refractive Index of Air. *Metrologia*, *2*(2), 71–80. https://doi.org/10.1088/0026-1394/2/2/002

Eidam, T., Wirth, C., Jauregui, C., Stutzki, F., Jansen, F., Otto, H.-J., Schmidt, O., Schreiber, T., Limpert, J., & Tünnermann, A. (2011). Experimental observations of the threshold-like onset of mode instabilities in high power fiber amplifiers. *Opt. Expr.*, *19*, 13218. https://doi.org/10.1364/OE.19.013218

Eisenhauer, F., Perrin, G., Brandner, W., Straubmeier, C., Richichi, A., Gillessen, S., Berger, J. P., Hippler, S., Eckart, A., Schöller, M., Rabien, S., Cassaing, F., Lenzen, R., Thiel, M., Clénet, Y., Ramos, J. R., Kellner, S., Fédou, P., Baumeister, H., … Rousset, G. (2008). GRAVITY: Getting to the event horizon of Sgr A*. *Optical and Infrared Interferometry*, *7013*, 70132A. https://doi.org/10.1117/12.788407

Ellis, S. C., Bland-Hawthorn, J., Lawrence, J., Horton, A. J., Trinh, C., Leon-Saval, S. G., Shortridge, K., Bryant, J., Case, S., Colless, M., Couch, W., Freeman, K., Gers, L., Glazebrook, K., Haynes, R., Lee, S., Löhmannsröben, H.-G., O'Byrne, J., Miziarski, S., … Zheng, J. (2012). Suppression of the near-infrared OH night-sky lines with fibre Bragg gratings – first results. *Monthly Notices of the Royal Astronomical Society*, *425*(3), 1682–1695. https://doi.org/10.1111/j.1365-2966.2012.21602.x

Ellis, S. C., Leon-Saval, S. G., & Bland-Hawthorn, J. (2019). Astrophotonics: A promising arena for silicon photonics. *Silicon Photonics XIV*, *10923*, 109230M. https://doi.org/10.1117/12.2511917

Everhart, E., & Kantorski, J. W. (1959). Diffraction patterns produced by obstructions in reflecting telescopes of modest size. *The Astronomical Journal*, *64*, 455. https://doi.org/10.1086/107973

Faddeev, L. D. (2019). *V.A. Fock - Selected Works: Quantum Mechanics and Quantum Field Theory*. Routledge.

Feautrier, P., Gach, J.-L., & Bério, P. (2016). Fast sub-electron detectors review for interferometry. *Optical and Infrared Interferometry and Imaging V*, *9907*, 990715. https://doi.org/10.1117/12.2234143

Feautrier, P., Gach, J.-L., Greffe, T., Clop, F., Lemarchand, S., Carmignani, T., Stadler, E., Doucouré, C., & Boutolleau, D. (2017). C-RED One and C-RED 2: SWIR advanced cameras using Saphira e-APD and Snake InGaAs detectors. *Image Sensing Technologies: Materials, Devices, Systems, and Applications IV*, *10209*, 102090G. https://doi.org/10.1117/12.2261082

Fienup, J. R. (1982). Phase retrieval algorithms: A comparison. *Applied Optics*, *21*(15), 2758–2769. https://doi.org/10.1364/AO.21.002758

Finger, G., Baker, I., Alvarez, D., Ives, D., Mehrgan, L., Meyer, M., Stegmeier, J., & Weller, H. J. (2014). SAPHIRA detector for infrared wavefront sensing. *Adaptive Optics Systems IV*, *9148*, 914817. https://doi.org/10.1117/12.2057078

Fontaine, N. K., Ryf, R., Bland-Hawthorn, J., & Leon-Saval, S. G. (2012). Geometric requirements for photonic lanterns in space division multiplexing. *Optics Express*, *20*(24), 27123. https://doi.org/10.1364/OE.20.027123

Foy, R., & Labeyrie, A. (1985). Feasibility of adaptive telescope with laser probe. *Astronomy and Astrophysics*, *152*, L29–L31. Retrieved April 13, 2021, from http://adsabs.harvard.edu/abs/1985A%26A...152L..29F

Fried, D. L. (1965). Statistics of a Geometric Representation of Wavefront Distortion. *JOSA*, *55*(11), 1427–1435. https://doi.org/10.1364/JOSA.55.001427

Fried, D. L. (1966). Optical Resolution Through a Randomly Inhomogeneous Medium for Very Long and Very Short Exposures. *Journal of the Optical Society of America*, *56*(10), 1372. https://doi.org/10.1364/JOSA.56.001372

Frisch, U. (1980). Fully Developed Turbulence and Intermittency. *Annals of the New York Academy of Sciences*, *357*(1), 359–367. https://doi.org/10.1111/j.1749-6632.1980.tb29703.x

Frisch, U. (1995). *Turbulence: The Legacy of A. N. Kolmogorov*. Cambridge University Press.

Garcia, H. R., & Brooks, L. D. (1978). Characterization Techniques For Deformable Metal Mirrors. *Adaptive Optical Components I*, *0141*, 74–81. https://doi.org/10.1117/12.956515

Gavel, D. T. (2003). Suppressing anomalous localized waffle behavior in least squares wavefront reconstructors. *Adaptive Optical System Technologies II*, *4839*, 972–980. https://doi.org/10.1117/12.459686

Glindemann, A. (1997). Beating the seeing limit - adaptive optics on large telescopes. *Beating the seeing limit - adaptive optics on large telescopes., by Glindemann, A.. Heidelberg Univ. (Germany). Naturwissenschaftlich-Mathematische Gesamtfakultät, 1997, 91 p.,* retrieved May 13, 2021, from http://adsabs.harvard.edu/abs/1997bsl..book.....G

Gloge, D. (1971). Weakly Guiding Fibers. *Applied Optics*, *10*(10), 2252–2258. https://doi.org/10.1364/AO.10.002252

Goodman, J. W. (2004). *Introduction to Fourier Optics* (3rd edition). W. H. Freeman.

Gorkom, K. V., Miller, K. L., Males, J. R., Guyon, O., Rodack, A. T., Lumbres, J., & Knight, J. M. (2018). Characterization of deformable mirrors for the MagAO-X project. *Adaptive Optics Systems VI*, *10703*, 107035A. https://doi.org/10.1117/12.2323450

Greenwood, D. P. (1977). Bandwidth specification for adaptive optics systems*. *Journal of the Optical Society of America*, *67*(3), 390. https://doi.org/10.1364/JOSA.67.000390

Gross, H., Dörband, B., & Müller, H. (2012). Non-Interferometric Wavefront Sensing. *Handbook of Optical Systems* (pp. 181–302). John Wiley & Sons, Ltd. https://doi.org/10.1002/9783527699230.ch2

Grupp, F. (2003). The nature of the fiber noise with the FOCES spectrograph - Nature, modeling and a way to achieve S/N. *Astronomy & Astrophysics*, *412*(3), 897–902. https://doi.org/10.1051/0004-6361:20031432

Guyon, O. (2018). Extreme Adaptive Optics. *Annual Review of Astronomy and Astrophysics*, *56*(1), 315–355. https://doi.org/10.1146/annurev-astro-081817-052000

Haffert, S. Y. (2021). Fundamental limit of single-mode integral-field spectroscopy. *JOSA B*, *38*(7), A27–A35. https://doi.org/10.1364/JOSAB.421326

Hanzawa, N., Saitoh, K., Sakamoto, T., Matsui, T., Tsujikawa, K., Koshiba, M., & Yamamoto, F. (2014). Mode multi/demultiplexing with parallel waveguide for mode division multiplexed transmission. *Opt. Expr.*, *22*, 29321. https://doi.org/10.1364/OE.22.029321

Hardy, J. W. (1998). *Adaptive Optics for Astronomical Telescopes*. Oxford University Press.

Harris, R. J., MacLachlan, D. G., Choudhury, D., Morris, T. J., Gendron, E., Basden, A. G., Brown, G., Allington-Smith, J. R., & Thomson, R. R. (2015). Photonic spatial reformatting of stellar light for diffraction-limited spectroscopy. *Monthly Notices of the Royal Astronomical Society*, *450*(1), 428–434. https://doi.org/10.1093/mnras/stv410

Haynes, D. M., Gris-Sanchez, I., Birks, T. A., & Haynes, R. (2018). Optical fiber modal noise suppression in the NIR region using multicore fiber and photonic lanterns [Conference Name: Advances in Optical and Mechanical Technologies for Telescopes and Instrumentation III ISBN: 9781510619654], *0706*, 1070665. https://doi.org/10.1117/12.2314224

Hecht, E. (2002). *Optics*. Addison-Wesley.

Herrmann, J. (1980). Least-squares wave front errors of minimum norm. *JOSA*, *70*(1), 28–35. https://doi.org/10.1364/JOSA.70.000028

Horton, A. J., & Bland-Hawthorn, J. (2007). Coupling light into few-mode optical fibres I: The diffraction limit. *Optics Express*, *15*(4), 1443. https://doi.org/10.1364/OE.15.001443

Huang, B., Fontaine, N. K., Ryf, R., Guan, B., Leon-Saval, S. G., Shubochkin, R., Sun, Y., Lingle, R., & Li, G. (2015). All-fiber mode-group-selective photonic lantern using graded-index multimode fibers. *Optics Express*, *23*(1), 224–234. https://doi.org/10.1364/OE.23.000224

Hubin, N., Arsenault, R., Conzelmann, R., Delabre, B., Le Louarn, M., Stroebele, S., & Stuik, R. (2005). Ground Layer Adaptive Optics. *Comptes Rendus Physique*, *6*(10), 1099–1109. https://doi.org/10.1016/j.crhy.2005.10.005

Hunsperger, R. (2009). *Integrated Optics: Theory and Technology* (6th ed.). Springer-Verlag. https://doi.org/10.1007/b98730

Jagourel, P., Fitzsimons, E., Hammer, F., Frondat, F. D., Puech, M., Evans, C. J., Sanchez, R., Guinouard, I., Chemla, F., Frotin, M., Yang, Y., Parr-Burman, P., Morris, T., Dubbeldam, M., Close, M., Middleton, K., Rousset, G., Gendron, É., Kelz, A., ... Fèvre, O. L. (2018). MOSAIC: The ELT multi-object spectrograph. *Ground-based and Airborne Instrumentation for Astronomy VII*, *10702*, 10702A4.

Jovanovic, N., Cvetojevic, N., Norris, B., Betters, C., Schwab, C., Lozi, J., Guyon, O., Gross, S., Martinache, F., Tuthill, P., Doughty, D., Minowa, Y., Takato, N., & Lawrence, J. (2017). Demonstration of an efficient, photonic-based astronomical spectrograph on an 8-m telescope. *Optics Express*, *25*(15), 17753. https://doi.org/10.1364/OE.25.017753

Jovanovic, N., Schwab, C., Guyon, O., Lozi, J., Cvetojevic, N., Martinache, F., Leon-Saval, S., Norris, B., Gross, S., Doughty, D., Currie, T., & Takato, N. (2017). Efficient injection from large telescopes into single-mode fibres: Enabling the era of ultra-precision astronomy. *Astronomy & Astrophysics*, *604*, A122. https://doi.org/10.1051/0004-6361/201630351

Kaiser, T., Flamm, D., Schröter, S., & Duparré, M. (2009). Complete modal decomposition for optical fibers using CGH-based correlation filters. *Opt. Expr.*, *17*, 9347. https://doi.org/10.1364/OE.17.009347

Kelly, D. P. (2014). Numerical calculation of the Fresnel transform. *JOSA A*, *31*(4), 755–764. https://doi.org/10.1364/JOSAA.31.000755

Kolmogorov, A. N. (1991). The Local Structure of Turbulence in Incompressible Viscous Fluid for Very Large Reynolds Numbers. *Proceedings: Mathematical and Physical Sciences*, *434*(1890,), 9–13. http://www.jstor.org/stable/51980

Kronig, R. D. L., Penney, W. G., & Fowler, R. H. (1931). Quantum mechanics of electrons in crystal lattices. *Proceedings of the Royal Society of London. Series A, Containing Papers of a Mathematical and Physical Character*, *130*(814), 499–513. https://doi.org/10.1098/rspa.1931.0019

Labadie, L., Berger, J.-P., Cvetojevic, N., Haynes, R., Harris, R., Jovanovic, N., Lacour, S., Martin, G., Minardi, S., Perrin, G., Roth, M., & Thomson, R. R. (2016). Astronomical photonics in the context of infrared interferometry and high-resolution spectroscopy. *Optical and Infrared Interferometry and Imaging V*, *9907*, 990718. https://doi.org/10.1117/12.2230889

Ladouceur, F., & Love, J. D. (1990). Multiport single-mode fibre splitters. *Optical and Quantum Electronics*, *22*(5), 453–465. https://doi.org/10.1007/BF02113969

Lane, R. G., Glindemann, A., & Dainty, J. C. (1992). Simulation of a Kolmogorov phase screen. *Waves in Random Media*, *2*(3), 209–224. https://doi.org/10.1088/0959-7174/2/3/003

Leonhard, N., Berlich, R., Minardi, S., Barth, A., Mauch, S., Mocci, J., Goy, M., Appelfelder, M., Beckert, E., & Reinlein, C. (2016). Real-time adaptive optics testbed to investigate point-ahead angle in pre-compensation of Earth-to-GEO optical communication. *Optics Express*, *24*(12), 13157–13172. https://doi.org/10.1364/OE.24.013157

Leon-Saval, S. G., Birks, T. A., Bland-Hawthorn, J., & Englund, M. (2005). Multimode fiber devices with single-mode performance. *Optics Letters*, *30*(19), 2545. https://doi.org/10.1364/OL.30.002545

Leon-Saval, S. G. (2015). Photonic Lantern. *Advanced Photonics 2015*, NeS2D.2. https://doi.org/10.1364/NETWORKS.2015.NeS2D.2

Leon-Saval, S. G., Argyros, A., & Bland-Hawthorn, J. (2010). Photonic lanterns: A study of light propagation in multimode to single-mode converters. *Optics Express*, *18*(8), 8430–8439. https://doi.org/10.1364/OE.18.008430

Leon-Saval, S. G., Betters, C. H., & Bland-Hawthorn, J. (2012). The Photonic TIGER: A multicore fiber-fed spectrograph. *Modern Technologies in Space- and Ground-based Telescopes and Instrumentation II*, *8450*, 84501K. https://doi.org/10.1117/12.925254

Leon-Saval, S. G., Fontaine, N. K., Salazar-Gil, J. R., Ercan, B., Ryf, R., & Bland-Hawthorn, J. (2014). Mode-selective photonic lanterns for space-division multiplexing. *Optics Express*, *22*(1), 1036–1044. https://doi.org/10.1364/OE.22.001036

Li, J., Ren, F., Hu, T., Li, Z., He, Y., Chen, Z., Mo, Q., & Li, G. (2017). Recent progress in mode-division multiplexed passive optical networks with low modal crosstalk. *Opt. Fib. Techn.*, *35*, 28–36. https://doi.org/10.1016/j.yofte.2016.08.001

Little, B. E., & Huang, W.-P. (1995). Coupled-Mode Theory for Optical Waveguides. *Progress In Electromagnetics Research*, *10*, 217–270. Retrieved April 19, 2021, from http://www.jpier.org/PIER/pier.php?paper=9403215

Louthain, J. A., & Welsh, B. M. (1998). Fourier-series-based phase and amplitude optical field screen generator for weak atmospheric turbulence. *Airborne Laser Advanced Technology*, *3381*, 286–296. https://doi.org/10.1117/12.323950

MacLachlan, D. G., Harris, R. J., Choudhury, D., Simmonds, R. D., Salter, P. S., Booth, M. J., Allington-Smith, J. R., & Thomson, R. R. (2016). Development of integrated mode reformatting components for diffraction-limited spectroscopy. *Optics Letters*, *41*(1), 76–79. https://doi.org/10.1364/OL.41.000076

Maeda, J., & Murata, K. (1981). Retrieval of wave aberration from point spread function or optical transfer function data. *Applied Optics*, *20*(2), 274–279. https://doi.org/10.1364/AO.20.000274

Maire, J., Ziad, A., Borgnino, J., & Martin, F. (2007). Measurements of profiles of the wavefront outer scale using observations of the limb of the Moon. *Monthly Notices of the Royal Astronomical Society*, *377*(3), 1236–1244. https://doi.org/10.1111/j.1365-2966.2007.11681.x

Marcuse, D. (1978). Gaussian approximation of the fundamental modes of graded-index fibers. *JOSA*, *68*(1), 103–109. https://doi.org/10.1364/JOSA.68.000103

Maréchal, A. (1947). Mechanical Integrator for Studying the Distribution of Light in the Optical Image. *JOSA*, *37*(5), 403_1–404. https://doi.org/10.1364/JOSA.37.0403_1

Martínez-Garaot, S., Muga, J. G., & Tseng, S.-Y. (2017). Shortcuts to adiabaticity in optical waveguides using fast quasiadiabatic dynamics. *Optics Express*, *25*(1), 159–167. https://doi.org/10.1364/OE.25.000159

Mayor, M., & Queloz, D. (1995). A Jupiter-mass companion to a solar-type star. *Nature*, *378*(6555), 355–359. https://doi.org/10.1038/378355a0

McMahon, D. H. (1975). Efficiency limitations imposed by thermodynamics on optical coupling in fiber-optic data links*. *JOSA*, *65*(12), 1479–1482. https://doi.org/10.1364/JOSA.65.001479

Miller, J., & Friedman, E. (2003). *Photonics Rules of Thumb: Optics, Electro-Optics, Fiber Optics and Lasers* (2 edition). McGraw-Hill Education.

Minardi, S. (2012). Photonic lattices for astronomical interferometry. *Mon Not R Astron Soc*, *422*(3), 2656–2660. https://doi.org/10.1111/j.1365-2966.2012.20832.x

Minardi, S., Harris, R., & Labadie, L. (2020). Astrophotonics: Astronomy and modern optics. *arXiv:2003.12485 [astro-ph]*. Retrieved October 26, 2020, from http://arxiv.org/abs/2003.12485

Minardi, S., Harris, R. J., & Labadie, L. (2021). Astrophotonics: Astronomy and modern optics. *The Astronomy and Astrophysics Review*, *29*(1), 6. https://doi.org/10.1007/s00159-021-00134-7

Minardi, S. (2015). Nonlocality of coupling and the retrieval of field correlations with arrays of waveguides. *Phys. Rev. A*, *92*(1), 013804. https://doi.org/10.1103/PhysRevA.92.013804

Minardi, S., & Diab, M. (2019). *Device for analyzing modes of multimode optical fibers* (EP3572857A1). Retrieved May 7, 2021, from https://patents.google.com/patent/EP3572857A1/en

Minardi, S., & Pertsch, T. (2010). Interferometric beam combination with discrete optics. *Optics Letters*, *35*(18), 3009. https://doi.org/10.1364/OL.35.003009

Morris, T., Basden, A., Calcines-Rosario, A., Dohlen, K., Dubbeldam, C., Hadi, K. E., Fitzsimons, E., Fusco, T., Gendron, É., Hammer, F., Jagourel, P., Jenkins, D., Morel, C., Morris, S., Rousset, G., Townson, M., Vola, P., & Younger, E. (2018). Phase A AO system design and performance for MOSAIC at the ELT. *Adaptive Optics Systems VI*, *10703*, 1070316. https://doi.org/10.1117/12.2313562

Narevicius, E., Narevich, R., Berlatzky, Y., Shtrichman, I., Rosenblum, G., & Vorobeichik, I. (2005). Adiabatic mode multiplexer for evanescent-coupling-insensitive optical switching. *Opt. Lett.*, *30*, 3362–3364. https://doi.org/10.1364/OL.30.003362

Neumann, E.-G. (2013). *Single-Mode Fibers: Fundamentals*. Springer.

Newkirk, A. V., Antonio-Lopez, J. E., Velazquez-Benitez, A., Albert, J., Amezcua-Correa, R., & Schülzgen, A. (2015). Bending sensor combining multicore fiber with a mode-selective photonic lantern. *Optics Letters*, *40*(22), 5188–5191. https://doi.org/10.1364/OL.40.005188

Newton, I. (1730). *Opticks:: Or, A Treatise of the Reflections, Refractions, Inflections and Colours of Light*. William Innys at the West-End of St. Paul's.

Nicholson, J. W., Yablon, A. D., Ramachandran, S., & Ghalmi, S. (2008). Spatially and spectrally resolved imaging of modal content in large-mode-area fibers. *Opt. Expr.*, *16*, 7233. https://doi.org/10.1364/OE.16.007233

Noll, R. J. (1976). Zernike polynomials and atmospheric turbulence. *Journal of the Optical Society of America*, *66*(3), 207. https://doi.org/10.1364/JOSA.66.000207

Noordegraaf, D., Skovgaard, P. M. W., Sandberg, R. H., Maack, M. D., Bland-Hawthorn, J., Lawrence, J. S., & Lægsgaard, J. (2012). Nineteen-port photonic lantern with multimode delivery fiber. *Optics Letters*, *37*(4), 452–454. https://doi.org/10.1364/OL.37.000452

Noordegraaf, D., Skovgaard, P. M., Nielsen, M. D., & Bland-Hawthorn, J. (2009). Efficient multi-mode to single-mode coupling in a photonic lantern. *Optics Express*, *17*(3), 1988. https://doi.org/10.1364/OE.17.001988

Norris, B. R. M., Wei, J., Betters, C. H., Wong, A., & Leon-Saval, S. G. (2020). An all-photonic focal-plane wavefront sensor. *Nature Communications*, *11*(1), 5335. https://doi.org/10.1038/s41467-020-19117-w

Orban de Xivry, G., Quesnel, M., Vanberg, P.-O., Absil, O., & Louppe, G. (2021). Focal Plane Wavefront Sensing using Machine Learning: Performance of Convolutional Neural Networks compared to Fundamental Limits. *Monthly Notices of the Royal Astronomical Society*, (stab1634). https://doi.org/10.1093/mnras/stab1634

Osborn, J. (2015). Scintillation correction for astronomical photometry on large and extremely large telescopes with tomographic atmospheric reconstruction. *Monthly Notices of the Royal Astronomical Society*, *446*(2), 1305–1311. https://doi.org/10.1093/mnras/stu2175

Otto, H.-J., Jauregui, C., Stutzki, F., Jansen, F., Limpert, J., & Tünnermann, A. (2013). Controlling mode instabilities by dynamic mode excitation with an acousto-optic deflector. *Optics Express*, *21*, 17285. https://doi.org/10.1364/OE.21.017285

Parry, I. (1998). The Astronomical Uses of Optical Fibers [Conference Name: Fiber Optics in Astronomy III], *152*, 3. Retrieved April 20, 2021, from http://adsabs.harvard.edu/abs/1998ASPC..152....3P

Paurisse, M., Lévèque, L., Hanna, M., Druon, F., & Georges, P. (2012). Complete measurement of fiber modal content by wavefront analysis. *Opt. Expr.*, *20*, 4074. https://doi.org/10.1364/OE.20.004074

Perraut, K., Jocou, L., Berger, J. P., Chabli, A., Cardin, V., Chamiot-Maitral, G., Delboulbé, A., Eisenhauer, F., Gambérini, Y., Gillessen, S., Guieu, S., Guerrero, J., Haug, M., Hausmann, F., Joulain, F., Kervella, P., Labeye, P., Lacour, S., Lanthermann, C., . . . Straubmeier, C. (2018). Single-mode waveguides for GRAVITY: I. The cryogenic 4-telescope integrated optics beam combiner. *Astronomy & Astrophysics*, *614*, A70. https://doi.org/10.1051/0004-6361/201732544

Piacentini, S., Vogl, T., Corrielli, G., Lam, P. K., & Osellame, R. (2021). Space Qualification of Ultrafast Laser-Written Integrated Waveguide Optics. *Laser & Photonics Reviews*, *15*(2), 2000167. https://doi.org/https://doi.org/10.1002/lpor.202000167

Pike, F. A., Benoit, A., MacLachlan, D. G., Ross, C. A., Harris, R. J., Haffert, S. Y., Gris-Sánchez, I., Birks, T. A., & Thomson, R. R. (2020). Multicore fiber–fed integral field spectrograph (MCIFU) – III: An ultrafast laser inscribed photonic reformatter and mask. *Advances in Optical and Mechanical Technologies for Telescopes and Instrumentation IV*, *11451*, 1145166. https://doi.org/10.1117/12.2559197

Potier, A., Ruane, G., Chen, P., Chopra, A., Dewell, L., Parramon, R. J., Nordt, A., Pueyo, L., Redding, D., Riggs, A. E., & Sirbu, D. (2021). LUVOIR-ECLIPS closed-loop adaptive optics performance and contrast predictions. *Techniques and Instrumentation for Detection of Exoplanets X*, *11823*, 118231L. https://doi.org/10.1117/12.2595116

Press, W. H., Flannery, B. P., Teukolsky, S. A., & Vetterling, W. T. (1992). *Numerical Recipes in C: The Art of Scientific Computing* (2 edition). Cambridge University Press.

Rahman, A., Madhav, K., & Roth, M. M. (2020). Complex phase masks for OH suppression filters in astronomy: Part I: Design. *Optics Express*, *28*(19), 27797–27807. https://doi.org/10.1364/OE.402989

Richardson, L. F. (1922). *Weather Prediction by Numerical Process*. University Press.

Riesen, N., Gross, S., Love, J. D., & Withford, M. J. (2014). Femtosecond direct-written integrated mode couplers. *Opt. Expr.*, *22*, 29855. https://doi.org/10.1364/OE.22.029855

Rigaut, F., Rousset, G., Kern, P., Fontanella, J. C., Gaffard, J. P., Merkle, F., & Léna, P. (1991). Adaptive optics on a 3.6-m telescope - Results and performance. *Astronomy and Astrophysics*, *250*, 280–290. Retrieved April 13, 2021, from http://adsabs.harvard.edu/abs/1991A%26A...250..280R

Roddier, F. (1981). V The Effects of Atmospheric Turbulence in Optical Astronomy. In E. Wolf (Ed.), *Progress in Optics* (pp. 281–376). Elsevier. https://doi.org/10.1016/S0079-6638(08)70204-X

Roddier, F. (Ed.). (1999). *Adaptive Optics in Astronomy*. Cambridge University Press. https://doi.org/10.1017/CBO9780511525179

Roddier, F., & Roddier, C. (1986). National Optical Astronomy Observatories (NOAO) Infrared Adaptive Optics Program II: Modeling Atmospheric Effects In Adaptive Optics Systems For Astronomical Telescopes. *Advanced Technology Optical Telescopes III*, *0628*, 298–304. https://doi.org/10.1117/12.963545

Roddier, F. (2008). *Adaptive Optics in Astronomy* (Revised edition). Cambridge University Press.

Roddier, N. A. (1990). Atmospheric wavefront simulation and Zernike polynomials. *Amplitude and Intensity Spatial Interferometry*, *1237*, 668–679. https://doi.org/10.1117/12.19346

Roggemann, M. C., & Welsh, B. M. (2018). *Imaging Through Turbulence*. CRC Press.

Ross, T. S. (2009). Limitations and applicability of the Maréchal approximation. *Applied Optics*, *48*(10), 1812–1818. https://doi.org/10.1364/AO.48.001812

Roth, M. M., Kelz, A., Fechner, T., Hahn, T., Bauer, S.-M., Becker, T., Böhm, P., Christensen, L., Dionies, F., Paschke, J., Popow, E., Wolter, D., Schmoll, J., Laux, U., & Altmann, W. (2005). PMAS: The Potsdam Multi-Aperture Spectrophotometer. I. Design, Manufacture, and Performance. *Publications of the Astronomical Society of the Pacific*, *117*(832), 620–642. https://doi.org/10.1086/429877

Roth, M. M., Sandin, C., Kamann, S., Husser, T.-O., Weilbacher, P. M., Monreal-Ibero, A., Bacon, R., Brok, M. d., Dreizler, S., Kelz, A., Marino, R. A., & Steinmetz, M. (2018). MUSE crowded field 3D spectroscopy in NGC 300 - I. First results from central fields. *Astronomy & Astrophysics*, *618*, A3. https://doi.org/10.1051/0004-6361/201833007

Ruilier, C. (1998). A Study of Degraded Light Coupling Into Single-Mode Fibers. *Proc. SPIE 3350, Astronomical Interferometry*, *3350*, 319–329. https://doi.org/10.1117/12.317094

Saleh, B. E. A., & Teich, M. C. (2019). *Fundamentals of Photonics*. John Wiley & Sons.

Saviauk, A., Minardi, S., Dreisow, F., Nolte, S., & Pertsch, T. (2013). 3d-integrated optics component for astronomical spectro-interferometry. *Applied Optics*, *52*(19), 4556. https://doi.org/10.1364/AO.52.004556

Schimpf, A., Micallef, M., & Charton, J. (2014). 1500Hz adaptive optics system using commercially available components. *Adaptive Optics Systems IV*, *9148*, 914851. https://doi.org/10.1117/12.2056395

Shaklan, S., & Roddier, F. (1988). Coupling starlight into single-mode fiber optics. *Applied Optics*, *27*(11), 2334–2338.

Shen, L., Gan, L., Huo, L., Yang, C., Tong, W., Fu, S., Tang, M., & Liu, D. (2018). Design of highly mode group selective photonic lanterns with geometric optimization. *Applied Optics*, *57*(24), 7065–7069. https://doi.org/10.1364/AO.57.007065

Snyder, A. W., & Love, J. (2012). *Optical Waveguide Theory*. Springer Science & Business Media.

Snyder, A. W. (1974). Leaky-ray theory of optical waveguides of circular cross section. *Applied physics*, *4*(4), 273–298. https://doi.org/10.1007/BF00928381

Snyder, A. W., & Mitchell, D. J. (1974). Leaky mode analysis of circular optical waveguides. *Opto-electronics*, *6*(4), 287–296. https://doi.org/10.1007/BF01423378

Southwell, W. H. (1980). Wave-front estimation from wave-front slope measurements. *JOSA*, *70*(8), 998–1006. https://doi.org/10.1364/JOSA.70.000998

Spaleniak, I., Jovanovic, N., Gross, S., Ireland, M. J., Lawrence, J. S., & Withford, M. J. (2013). Integrated photonic building blocks for next-generation astronomical instrumentation II: The multimode to single mode transition. *Optics Express*, *21*(22), 27197. https://doi.org/10.1364/OE.21.027197

Spanò, P., Zerbi, F. M., Norrie, C. J., Cunningham, C. R., Strassmeier, K. G., Bianco, A., Blanche, P. A., Bougoin, M., Ghigo, M., Hartmann, P., Zago, L., Atad-Ettedgui, E., Delabre, B., Dekker, H., Melozzi, M., Snÿders, B., Takke, R., & Walker, D. D. (2006). Challenges in optics for Extremely Large

Telescope instrumentation. *Astronomische Nachrichten*, *327*(7), 649–673. https://doi.org/10.1002/asna.200610610

Spanò, P., Delabre, B., Dekker, H., & Avila, G. (2008). New design approaches for a very high resolution spectrograph for the combined focus of the VLT. *Ground-based and Airborne Instrumentation for Astronomy II*, *7014*, 70140M. https://doi.org/10.1117/12.789283

Stoll, A., Wang, Y., Madhav, K., & Roth, M. (2020). Integrated echélle gratings for astrophotonics. *Advances in Optical Astronomical Instrumentation 2019*, *11203*, 112030Z. https://doi.org/10.1117/12.2541554

Sweeney, D., Norris, B. R. M., Tuthill, P. G., Scalzo, R., Wei, J., Betters, C. H., & Leon-Saval, S. G. (2021). Learning the lantern: Neural network applications to broadband photonic lantern modeling. *Journal of Astronomical Telescopes, Instruments, and Systems*, *7*(2), 028007. https://doi.org/10.1117/1.JATIS.7.2.028007

Synposys and RSoft Design Group. (1993-2018). *RSoft, CAD & BeamPROP*. Synopsys Inc. CA, USA. https://rsoftdesign.com

Tallon, M., & Foy, R. (1990). Adaptive telescope with laser probe - Isoplanatism and cone effect. *Astronomy and Astrophysics*, *235*, 549–557. Retrieved April 13, 2021, from http://adsabs.harvard.edu/abs/1990A%26A...235..549T

Tamm, C., & Weiss, C. O. (1990). Bistability and optical switching of spatial patterns in a laser. *J. Opt. Soc. Am. B, JOSAB*, *7*(6), 1034–1038. https://doi.org/10.1364/JOSAB.7.001034

Tatarski, V. I. (2016). *Wave Propagation in a Turbulent Medium*. Courier Dover Publications.

Taylor, G. I. (1938). The Spectrum of Turbulence. *Proceedings of the Royal Society A: Mathematical, Physical and Engineering Sciences*, *164*(919), 476–490. https://doi.org/10.1098/rspa.1938.0032

Tedder, S. A., Floyd, B., Chahine, Y. K., Croop, B., Vyhnalek, B. E., Betters, C., & Leon-Saval, S. G. (2020). Measurements of few-mode fiber photonic lanterns in emulated atmospheric conditions for a low earth orbit space to ground optical communication receiver application. *Free-Space Laser Communications XXXII*, *11272*, 112720U. https://doi.org/10.1117/12.2542848

Tepper, J., Labadie, L., Diener, R., Minardi, S., Pott, J.-U., Thomson, R., & Nolte, S. (2017). Integrated optics prototype beam combiner for long baseline interferometry in the L and M bands. *Astronomy & Astrophysics*, *602*, A66. https://doi.org/10.1051/0004-6361/201630138

Thomson, R. R., Birks, T. A., Leon-Saval, S. G., Kar, A. K., & Bland-Hawthorn, J. (2011). Ultrafast laser inscription of an integrated photonic lantern. *Optics Express*, *19*(6), 5698–5705. https://doi.org/10.1364/OE.19.005698

Thomson, R. R., Kar, A. K., & Allington-Smith, J. (2009). Ultrafast laser inscription: An enabling technology for astrophotonics. *Opt. Express, OE*, *17*(3), 1963–1969. https://doi.org/10.1364/OE.17.001963

Townson, M. J., Farley, O. J. D., Xivry, G. O. d., Osborn, J., & Reeves, A. P. (2019). AOtools: A Python package for adaptive optics modelling and analysis. *Optics Express*, *27*(22), 31316–31329. https://doi.org/10.1364/OE.27.031316

Traub, J. F. (1982). *Iterative Methods for the Solution of Equations*. American Mathematical Soc.

Valley, G. C. (1980). Isoplanatic degradation of tilt correction and short-term imaging systems. *Applied Optics*, *19*(4), 574. https://doi.org/10.1364/AO.19.000574

Watson, F. G. (1995). Multifiber waveguide spectrograph for astronomy. *Fiber Optics in Astronomical Applications*, *2476*, 68–74. https://doi.org/10.1117/12.211840

Welsh, B. M. (1997). A Fourier series based atmospheric phase screen generator for simulating anisoplanatic geometries and temporal evolution. *Proc. SPIE*, *3125*, 327–338.

Wildi, F., Blind, N., Reshetov, V., Hernandez, O., Genolet, L., Conod, U., Sordet, M., Segovilla, A., Rasilla, J. L., Brousseau, D., Thibault, S., Delabre, B., Bandy, T., Sarajlic, M., Cabral, A., Bovay, S., Vallée, P., Bouchy, F., Doyon, R., ... Saddlemyer, L. (2017). NIRPS: An adaptive-optics assisted radial velocity spectrograph to chase exoplanets around M-stars. *Techniques and Instrumentation for Detection of Exoplanets VIII*, *10400*, 1040018. https://doi.org/10.1117/12.2275660

Wittek, S., Ramirez, R. B., Zacarias, J. A., Eznaveh, Z. S., Bradford, J., Galmiche, G. L., Zhang, D., Zhu, W., Antonio-Lopez, J., Shah, L., & Correa, R. A. (2016). Mode-selective amplification in a large mode area Yb-doped fiber using a photonic lantern. *Optics Letters*, *41*(10), 2157–2160. https://doi.org/10.1364/OL.41.002157

Woods, R., Feldbacher, S., Zidar, D., Langer, G., Satzinger, V., Schmidt, V., Pucher, N., Liska, R., & Kern, W. (2014). 3d optical waveguides produced by two photon photopolymerisation of a flexible silanol terminated polysiloxane containing acrylate functional groups. *Opt. Mater. Express*, *4*(3), 486–498. https://doi.org/10.1364/OME.4.000486

Yang, B., Duan, J., Xie, Z., & Xie, Z. (2013). Evaluation of Mode Field Diameter of Step-Index Fibers and Comparison Analysis. *Research Journal of Applied Sciences, Engineering and Technology*, *6*(3), 382–386. https://doi.org/10.19026/rjaset.6.4090

Yerolatsitis, S., Gris-Sánchez, I., & Birks, T. A. (2014). Adiabatically-tapered fiber mode multiplexers. *Optics Express*, *22*(1), 608–617. https://doi.org/10.1364/OE.22.000608

Zeng, X., Li, Y., Feng, L., Wu, S., Yang, C., Li, W., Tong, W., & Wu, J. (2018). All-fiber orbital angular momentum mode multiplexer based on a mode-selective photonic lantern and a mode polarization controller. *Optics Letters*, *43*(19), 4779–4782. https://doi.org/10.1364/OL.43.004779

Zernike, F., & Stratton, F. (1934). Diffraction Theory of the Knife-Edge Test and its Improved Form, The Phase-Contrast Method. *Monthly Notices of the Royal Astronomical Society*, *94*(5), 377–384. https://doi.org/10.1093/mnras/94.5.377

Zheng, D., Li, Y., Chen, E., Li, B., Kong, D., Li, W., & Wu, J. (2016). Free-space to few-mode-fiber coupling under atmospheric turbulence. *Optics Express*, *24*(16), 18739. https://doi.org/10.1364/OE.24.018739

Ziad, A., Schöck, M., Chanan, G. A., Troy, M., Dekany, R., Lane, B. F., Borgnino, J., & Martin, F. (2004). Comparison of measurements of the outer scale of turbulence by three different techniques. *Applied Optics*, *43*(11), 2316–2324. https://doi.org/10.1364/AO.43.002316